Stress Developments within a Backfilled Mine Stope and the Lateral Loading on the Barricade

By

Sankha Darshanath Widisinghe B.Sc.(Eng) Hons

This thesis submitted for the

Degree of Doctor of Philosophy

School of Engineering and Physical Sciences

James Cook University

December 2014

STATEMENT OF ACCESS

I, the undersigned, the author of this thesis, understand that James Cook University will make it available for use within the University Library and, by microfilm or other means, allow access to users in other approved libraries.

All users consulting this thesis will have to sign the following statement:

In consulting this thesis, I agree not to copy or closely paraphrase it in whole or in part without the written consent of the author; and to make proper public written acknowledgement for any assistance which I have obtained from it.

Beyond this, I do not wish to place any restriction on access to this thesis.

01/12/2014

…….

Date

STATEMENT OF ORIGINAL AUTHOURSHIP

DECLARATION

I declare that this thesis is my own work and has not been submitted in any form of another degree or diploma at any university or other institution of tertiary education. Information derived from the published or unpublished work of others has been acknowledged in the text and a list of references is given.

01/12/2014

…….

Date

PUBLICATIONS DURING CANDIDATURE

Journals

- Widisinghe, S. and Sivakugan, N. (2014). Vertical Stress Isobars for Trenches and Mine Stopes Containing Granular Backfills. International Journal of Geomechanics, 14(2), 313-318. doi: 10.1061/(ASCE)GM.1943-5622.0000321
- Widisinghe, S. and Sivakugan, N. (2014). Vertical stresses within granular materials in containments International Journal of Geotechnical Engineering, 8(4), 431-435. doi: 10.1179/1939787913Y.0000000031
- Widisinghe, S. and Sivakugan, N. (2014). Vertical stress isobars for silos and square backfilled mine stopes. International Journal of Geomechanics. (accepted manuscript)
- Sivakugan, N. and Widisinghe, S. (2013). Stresses Within Granular Materials Contained Between Vertical Walls. Indian Geotechnical Journal, 43(1), 30-38. doi: 10.1007/s40098-012-0029-z
- Sivakugan, N., Widisinghe, S. and Wang, V. (2014). Vertical Stress Determination within Backfilled Mine Stopes. International Journal of Geomechanics, 14(5), 06014011. doi: 10.1061/(ASCE)GM.1943-5622.0000367

Refereed Conference Proceedings

- Widisinghe, S. and Sivakugan, N. (2012). Vertical Stresses within Granular Materials in Silos. In Narsilio, G., Arulrajah, A. & Kodikara, J. (Ed.), Ground Engineering in a Changing World: 11th Australia - New Zealand Conference on Geomechanics (pp. 590-595). Melbourne, Australia: Australian Geomechanics Society and New Zealand Geotechnical Society.
- Widisinghe, S., Sivakugan, N. and Wang, V. Z. (2013). Laboratory investigations of arching in backfilled mine stopes. In Leung, C. F., Goh, S. H. & Shen, R. F.

(Ed.), 18th Southeast Asian Geotechnical Conference Cum Inaugural AGSSEA Conference (pp. 741-746). Singapore: Research Publishing.

- Widisinghe, S., Sivakugan, N. and Wang, V. Z. (2014). Loads on barricades in hydraulically backfilled underground mine stopes. In Potvin, Y. & Grice, T. (Ed.), MineFill 2014: 11th International Symposium on Mining with Backfill (pp. 123-134). Perth, WA, Australia: Australian Centre for Geomechanics, University of Western Australia.

ACKNOWLEDGEMENTS

Firstly I would like to acknowledge the support of my wonderful family and relatives throughout the period of my studies. To my parents as well as sister and brothers who understood my intentions to pursue for PhD and supported back from home, I'm forever grateful their support and the understanding throughout this long journey.

To my supervisor Associate Professor Nagaratnam Sivakugan, indeed a professor in the way he would interpret the complex aspects in Geomechanics with fundamental knowledge. Thank you Professor Siva, for being a real mentor and providing continuous support from the beginning till the end of my thesis. My co-supervisor, Dr. Vincent Z. Wang, whose guidance into numerical simulation aspects were very helpful throughout. Thanks to all academic and technical staff in School of Engineering and Physical Sciences, especially to senior engineering laboratory technicians Mr. Warren O'Donnell and Mr. Tony Skalecki for their ongoing patience with my style of test design and testing within the laboratory. Thanks to Ms. Kellie Johns at Teaching and Learning development for the discussions provided on my research proposal and to the graduate research school and Dr. Liz Tynan on organising academic writing workshops.

Also, my university colleagues (Chana, Dushyanth, Peter, Manish, Om, Satheesh, Niroshan, Dhanya, Shaun, Rhys, Mohammad and Sepideh) and the school support staff (Melissa and Alison) provided support as well as company during my candidature. Also the friends and families at Townsville (the home away from home) should be thanked for their love, company and laughs during my stay. Bhanuka, Dinusha, Chamila, Samanthi, Chana, Susanthi, Muditha, Niranjan, Sudarshana, Nilanthi, Tony, Asanka and Udeshika, I feel very fortunate to spend with you guys during my stay in Townsville.

I wish to acknowledge the JCU postgraduate research scholarship, which provided a living allowance during my studies as well as the financial support received from my

school (Student Support Account) and the Graduate Research Scheme funds to support my academic and conference travel expenses.

Finally, I also wish to express my sincere love and gratitude to my beloved wife, Nadeesha, for her understanding and endless love throughout the duration of my studies and keeping me fed during long hours of writing. Thank you for being a great companion on this journey.

ABSTRACT

Mine backfilling, filling of underground mined voids with processed tailings, is an integral process within the mining cycle and brings multiple benefits. Engineered barricades are constructed, to retain the backfill within the mined void (stope), across the horizontal drives before backfilling. Failure of such a slurry retaining barricade not only endangers the miners' lives but also has led to many financial losses. Correct engineered design of barricade would bring safety and efficiency to the mining operation. The purpose of this thesis is to critically assess the arching and stress developments within backfilled stopes and drives and to develop a methodology to estimate the loads onto barricades, synthesizing analytical, numerical and laboratory studies.

The arching theory is revisited and analytical equations are established, with limit equilibrium analysis method, for the vertical stress determination within the stope, considering the stope perimeter to the cross sectional areas as the basis. Numerical simulations were carried out to record the vertical stress at the bottom of the stope, which is a unique way of stress recording and has not been identified by previous studies. Although the lateral variation of vertical stress is well understood, there is a lack of simplified models to estimate the vertical stress at any point within the backfilled structure. Vertical stress isobars, were created with the use of numerical simulations, enable to estimate the vertical stress at any point within a backfilled structure up to a depth of six times the width. This has been extended to axisymmetric situations that can represent grain storage silos.

A novel laboratory model was developed to identify the factors affecting lateral load on barricade as well as to measure the variation of the barricade loads with the change of barricade location within the drive (offset distance) and the effect of barricade width. Transducers were used to measure the horizontal normal stress on the barricade and the vertical stress at the stope centre and the stope corner. With laboratory tests, it is

observed that the barricade stress decreased with the offset distance and increased with the drive width. Then the barricade stress is estimated with modified analytical equation, which considers the equilibrium of a vertical layer element. Additionally, three dimensional numerical simulations were carried out to replicate the laboratory tests. The barricade stress estimated from analytical equations, numerical simulations and laboratory tests varied within a narrow range for all three approaches but the stress estimations were deviated at the stope entrance because of the continuum approach. Finally, an empirical equation to estimate the barricade stress in full scale mine backfilling situations was proposed with the test results, considering the offset distance, the drive width and the vertical stress at the stope centre.

In order to improve the understanding of the stress variation within a backfilled stope, the previous laboratory models were modified to measure the average vertical stress and the horizontal stress on the stope wall. The vertical stress variations from laboratory model tests showed two distinct regions of vertical stress deviation, the upper region showing an exponential variation followed by a linear variation in the lower region of the stope. In contrast, the arching theory as well as finite difference numerical simulations use the continuum approach and predict an asymptotic vertical stresses achieved at large depths. Additionally, laboratory model tests revealed that the lateral pressure coefficient is not a constant along the depth. The deviations occurred as the cohesionless granular material differs from the concept of continuum approach considered in arching theory as well as in finite difference numerical simulations. Therefore, an alternative analytical solution, considering the particulate approach and inter-particle forces, was proposed. The vertical stress variation within a backfilled stope or silo, as studied through laboratory model test, could successfully match the new analytical solution which considered the presence of intermediate arching conditions with the packing of cohesionless granular material.

Table of Contents

Abstract viii
List of Figures xiii
List of Tables xxi
Abbreviations xxii
List of Symbols xxiii
Chapter 1 1
Introduction 1
1.1 General 2
1.1.1 Mining 2
1.1.2 Geomechanics in underground mining 5
1.1.3 Mine backfilling 6
1.2 Problem statement 9
1.3 Objectives and scope of research 10
1.4 Relevance of research 11
1.5 Thesis overview 12
Chapter 2 15
Literature Review 15
2.1 Overview of mine backfill literature 16
2.2 Hydraulic fills – properties 17
2.2.1 Friction angle 19
2.2.2 Interfacial friction angle 20
2.3 Barricade types and failures 21
2.3.1 Brick barricades 22
2.3.2 Shotcrete barricades 23
2.3.3 Barricade failure and mechanisms 23
2.3.4 Numerical modelling of barricade 27
2.4 Numerical simulations for backfilling and estimations of loads onto the barricade 28
2.5 Arching within backfills 32
2.5.1 In situ and model stress measurements 37
2.5.2 Assumption of uniform stress 39
2.5.3 Lateral pressure coefficient 40

2.5.4 The use of $K\tan\delta$ as a measure of arching 42
Chapter 3 44
Vertical Stresses in Vertical Containments 44
3.1 General 45
3.2 Generalised Marston's equation 46
3.3 Setup and material description 50
3.4 Data interpretation 53
3.4.1 Shear stresses along the wall: 54
3.4.2 Average normal stress at the base: 55
3.5 Numerical simulation of laboratory scale backfilled stope 58
3.5.1 FLAC/FLAC^{3D} simulation packages and capabilities 58
3.5.2 Modelling methodology 60
3.6 Vertical stress variation while filling and after filled 63
3.7 Results from laboratory tests and FLAC for backfilled mine stopes 67
3.7.1 Vertical stress variation 68
3.7.2 Vertical and shear stress variation within region 1 70
3.7.3 Vertical and shear stress variation within region 2 71
3.7.4 Sand and hydraulic fills - vertical stress variation 72
3.7.5 Vertical stress variation with the size of the stope 74
3.8 Calculated lateral pressure coefficient (K_{calc}) 76
3.9 Estimation of vertical stress variation for plane strain conditions 77
3.10 Summary and conclusions 80
Chapter 4 84
Vertical Stress Isobars for Backfilled Structures 84
4.1 General 85
4.1 Sensitivity study for parameters used with simulations 88
4.1.1 Influence of friction angle 90
4.1.2 Young's modulus and Poisson's ratio 92
4.1.3 Interfaces and interfacial friction angle 97
4.1.4 Dilation angle and cohesion 100
4.2 FLAC simulation procedure 101
4.3 Stress isobars for plane strain conditions and validation 103
4.4 Stress isobars for axisymmetric conditions and validation 108
4.5 Summary and conclusions 117

Chapter 5 119
Stress Developments within a Backfilled Drive and the Lateral Loading on the Barricade 119
5.1 General 120
5.2 Laboratory test design 122
5.2 Earth pressure cells – installation and calibration 125
5.2.1 Earth pressure cells installation 125
5.2.2 Calibration of earth pressure cells 126
5.3 Laboratory test methodology 130
5.3.1 Methodology to evaluate the variation of vertical stress 130
5.3.2 Methodology to evaluate the barricade stress variation with offset distance 130
5.3.3 Methodology to evaluate the barricade stress variation with drive dimensions 130
5.3.4 Methodology to evaluate the barricade stress variation with drive shape 131
5.4 Analytical equations to estimate stresses on barricade 131
5.4.1 Derivation of analytical equation to estimate the barricade stress 133
5.5 Numerical ($FLAC^{3D}$) simulations for laboratory tests 135
5.6 Results and analysis 138
5.6.1 Variation of vertical stress at bottom and lateral stress ratio 139
5.6.2 Barricade stress variation with offset distance 141
5.6.3 Variation of barricade stress with drive dimensions 144
5.6.4 Variation of barricade stress with drive shape 145
5.6.5 Comparison of barricade stress estimated with analytical equations, numerical simulations and laboratory tests 146
5.7 Extension of simulations to full scale mine stopes 150
5.8 Summary and conclusions 153
Chapter 6 155
Estimation of Stresses within Backfilled Containments: An Analytical Approach 155
6.1 General 156
6.1 Theoretical assumptions with continuum approach 157
6.1.1 Horizontal layer element and uniform vertical stress 157
6.1.2 The lateral pressure coefficient -K 158
6.2 Modified Butterfield (1969) solution for particulate approach 159
6.2.1 Contacts and contact angle 160
6.2.2 Arching factor- *F* 162

6.2.3 Derivation of analytical solution 163
6.3 Analytical equations for inter-disk forces 165
6.4 Sensitivity of the model 169
6.4.1 Vertical stress outputs and comparison with arching theory 171
6.4.2 Lateral variation of vertical stress 173
6.4.3 Variation of lateral pressure coefficient 175
6.5 Comparison of laboratory tests with analytical solution 176
6.7 Advantages and limitations of proposed numerical approach 178
6.8 Summary and conclusions 180
Chapter 7 183
Summary, Conclusions and Recommendations for Future Research 183
7.1 Summary 184
7.2 Conclusions 189
7.3 Recommendations for future research 192
References 195
APPENDICES 211
APPENDIX A 212
The FLAC3D code used to simulate laboratory studies 222
APPENDIX B 235

List of Figures

Figure 1.1. Idealised infrastructure in an underground mine, showing the basic elements around a stope (source: www.wikipedia.com) 3

Figure 1.2. Open stoping sequence with backfilling showing the barricade 4

Figure 1.3. Fatalities in Australian mining industry, as reported by Mineral Council of Australia for 1999 to 2009; (a) fatalities breakdown due to cause and (b) geomechanically caused fatalities are categorised based on the location 5

Figure 1.4. Plan view related to egg crater pattern stoping sequence at Mount Isa Mines (reproduced from Simpson (2007)) 8

Figure 2.1. Grain size distribution of Australian backfills that were tested at James Cook University (Sivakugan et al. 2006) 18

Figure 2.2. Failure profiles as identified by previous researchers; (a) flexural failure or diagonal cracks, (b) punching failure and (c) shear failure 24

Figure 2.3. Flexural failure pattern of a brick barricade (Grice 1989) 24

Figure 2.4. Shear failure appears on the barricade top (Revell and Sainsbury 2007b) 25

Figure 2.5. The punching failure is shown with failed brick barricade (Grice 1998) 26

Figure 2.6. The barricade load variation with centrifuge tests (Mitchell 1992), analytical equations (Li and Aubertin 2009) and numerical simulations ($FLAC^{3D}$); (a) set back distance of 0 mm and (b) set back distance of 100 mm 31

Figure 2.8. Vertical stress variation on a corn filled silo, as measured by Janssen 1895 . 34

Figure 2.9. Maximum vertical stress variation from Handy (1985) and Singh et al. (2011) equations 36

Figure 2.10. Lateral stress measurement within silos; (a) when filled with coal and (b) when filled with barley 37

Figure 2.11.The Laboratory test setup to model the average stress variation used by Ting et al. 2012; (a) photograph and (b) schematic diagram (Ting 2011) 38

Figure 2.12. Average vertical stress variation for a rectangular stope backfilled with sand, as obtained by Ting (2011) 39

Figure 2.13. The use of Mohr's circle to define the lateral pressure coefficient as suggested by Krynine (1945) 42

Figure 3.1. Schematic diagram to derive analytical equations for stress within a backfilled stope; (a) backfilled stope dimensions and (b) isolated horizontal layer element 47

Figure 3.2. Laboratory test setup; (a) photograph and (b) schematic diagram 51

Figure 3.3. Grain size distribution for sand and HFs, obtained from Malvern Mastersizer-X instrument 52

Figure 3.4. Detailed interpretation of calculations: (a) one layer, (b) after 6 layers, (c) after 7 layers, and (d) after all 10 layers 54

Figure 3.5. Variation of normalised vertical, shear and horizontal stress according to Table 3.2 56

Figure 3.6. Vertical stress variation along centre with number of elements across the half-width ; E = 50 MPa, ν =0.2 and γ = 14.675 kN/m³ 62

Figure 3.7. Vertical stress variation along centre with number of layers used; E = 50 MPa, ν =0.2 and γ = 14.675 kN/m³ 63

Figure 3.8. Vertical stress at centre versus depth, for a narrow stope of 4B deep: E = 50 MPa, ν = 0.2 and γ = 14.675 kN/m³ 64

Figure 3.9. Maximum vertical stress variation for vertical aspect ratios with depth H = 2B, 3B, 4B, 5B and 6B.:: E = 50 MPa, ν = 0.2 and γ = 17.65 kN/m³ 66

Figure 3.10. Maximum vertical stress variation for horizontal cross sections, B/L=1 - square stope, B/L= 0 - narrow stope: E = 50 MPa, ν = 0.2 and γ = 14.675 kN/m³ 66

Figure 3.11. Variation of $K\tan\delta$ with when definitions for K_o and K_a is considered for rough walls 67

Figure 3.12. Vertical stress variation from laboratory tests and FLAC simulations are compared with analytical equations; a) circular 150 mm diameter stope with medium

rough walls, b) circular 150 mm diameter stope with rough walls, c) square 150 mm wide stope with medium rough walls and d) square 150 mm wide stope with rough walls 69

Figure 3.13. Stress variation from laboratory tests are compared with analytical equations for circular and square stope of 150 mm width; (a) shear stress variation and (b) horizontal stress variation 71

Figure 3.14. Variation of stress for sand and HFs, when filled to a 150 mm wide square stope; (a) vertical stress and (b) shear stress 73

Figure 3.15. Grain shape analysis through SEM; (a) highly angular grains in HFs and (b) rounded to sub-rounded grains in sand 74

Figure 3.16. Vertical stress variation from laboratory tests and FLAC simulations are compared with analytical equations; (a) circular 100 mm diameter stope with medium rough walls, (b) circular 100 mm diameter stope with rough walls, (c) circular 150 mm diameter stope with medium rough walls and (d) circular 150 mm diameter stope with rough walls 75

Figure 3.17. Calculated K value (K_{calc}) from laboratory tests; (a) sand and (b) HFs..... 76

Figure 3.18. Vertical stress variations for square and rectangular stopes, and a linear regression is indicted for region 2 79

Figure 3.19. Regression for region 1; for (a) B/L = 1 (square stopes) and (b) B/L = 0.2 (rectangular stopes) 79

Figure 3.20. Estimated vertical stress variation for plane strain conditions, based on laboratory test results 80

Figure 4.1. Orientation of principal stress directions for a narrow backfilled structure, as output with FLAC simulations..... 86

Figure 4.2. Variation of average vertical stress with depth for various friction angles E = 20 MPa, ν = 0.20, and γ = 17.65 kN/m³ 90

Figure 4.3. Vertical stresses for selected 15 points within the fill for friction angles 30° to 50° and E = 20 MPa, ν = 0.20, and γ = 17.65 kN/m^3; (a) width 0.15B from the centre, (b) width 0.25B from the centre and (c) width 0.35B from the centre. 91

Figure 4.4. Error distribution when 40° selected as the reference friction angle to estimate vertical stress within a backfilled structure 92

Figure 4.5. Vertical stress variation along centre with Young's modulus, when the model filled in layers; ν = 0.25 and γ = 17.65 kN/m³ 93

Figure 4.6. Stress variations for different Poisson's ratio, when the model filled in layers, E = 50 MPa and γ = 17.65 kN/m³; (a) vertical stress at centre, (b) horizontal stress at wall and (c) horizontal stress at wall to vertical stress at centre ratio 94

Figure 4.7.Variation of 'elastic K_o', with Poisson's ratio 95

Figure 4.8. Variation of average vertical stress for Mohr-Coulomb material and for elastic material. Analytical equation estimations are also included with K_o, K_a and 'elastic K_o' 97

Figure 4.9. A photograph showing the wall roughness in a mine stope (courtesy of Mr. Patrick Wilson, Ravenswood mine, Queensland). 98

Figure 4.10. Vertical stress variation along the centreline for different values of interfacial friction angle (E = 50 MPa, ν =0.20 and γ = 17.65 kN/m³) 99

Figure 4.11. Vertical stress variation along the centreline for different values of dilation angle (ψ) and cohesion (c) of the fill (E = 50 MPa, ν = 0.20 and γ = 17.65 kN/m³)..... 100

Figure 4.12. Stress isobars for plane strain conditions- trenches for (a) z = 0-2B, and (b) z = 2B-4B 104

Figure 4.12. Stress isobars for plane strain conditions- trenches for (c) z = 4B-6B..... 105

Figure 4.13. Comparison of vertical stresses estimated for selected random cases in Table 4.3 with plane strain stress isobar charts and individual FLAC simulations 106

Figure 4.14. Vertical stress variation at x = 0, B/4 and B/2 for square and circular structures filled with granular materials (E = 50 MPa, ν = 0.20 and γ = 17.65 kN/m³).. 108

Figure 4.15. Axisymmetric vertical stress isobars for $\delta = \varphi$; (a) z = 0 - 2$B$and (b) z = 2B - 4B 110

Figure 4.15. Axisymmetric vertical stress isobars for $\delta = \varphi$; (c) z = 4B - 6B 111

Figure 4.16. Vertical stress isobars for δ = 0.5 φ; (a) z = 0 - 2B, (b) z = 2B - 4B, and (c) z = 4B - 6B 112

Figure 4.16. Vertical stress isobars for $\delta = 0.5\ \varphi$; (a) $z = 0$ - $2B$, (b) $z = 2B$ - $4B$, and (c) $z = 4B$ - $6B$ 113

Figure 4.17. Comparison of vertical stresses estimated for selected random cases with axisymmetric stress isobars and individual FLAC simulations 114

Figure 4.18. Error of estimation, when stress isobar charts were used to estimate vertical stresses for scenarios; (a) plane strain stress isobars chart used for scenarios given on Table 4.3 and (b) axisymmetric stress isobars chart used for scenarios for given on Table 4.4 116

Figure 5.1. Arrangement of the test setup; (a) with square drive, (b) with circular drive, (c) EPC arrangement and (d) schematic of UDL application from MTS 124

Figure 5.2. The calibration charts by Ramirez et al. (2010) and a linear calibration drawn for readings of 'deadweights and wheat' 127

Figure 5.3. The mould and setup used to calibrate EPCs; (a) close-up view with the mould and the EPC, (b) EPC loaded with dead weights after placing a fine layer and (c) details of the setup 128

Figure 5.4. EPC Calibration results shown with calibration coefficients s and R-squared values for; (a) EPC1-200 kPa, (b) EPC2-500 kPa and (c) EPC3-1 MPa 129

Figure 5.5. The notation showing the barricade height and offset distance along with other parameters 133

Figure 5. 6.FLAC^{3D} model to simulate the tests conducted with MTS; (a) numerical modelling parameters and boundary conditions, and (b) interfaces used in model 137

Figure 5.7. The lateral stress variation when the SD_125_75 model stope is subjected to a surcharge of 913 kPa 137

Figure 5.8. The repeatability of tests, conducted with MTS, as analysed with four trials; (a) CD150_0 test results (b) CD150_75 test results 138

Figure 5.9. Vertical stress recorded at stope centre and stope edge with applied surcharge; (a) square drive attached, (b) circular drive attached, and (c) comparison of stress at centre to stress at edge 139

Figure 5.10. The theoretical and calculated lateral pressure coefficient values are compared; (a) 75 mm wide square drive attached and (b) 75 mm wide circular drive attached 141

Figure 5.11. Barricade stress variation with offset distance and the best fit curve; (a) and (b) 75mm wide square drive, (c) and (d) 75 mm wide circular drive 142

Figure 5.12. Barricade stress variations, highlighting few increased stresses, as the offset distance increased; (a) for SD125 tests and (b) for CD150 tests 143

Figure 5.13. Barricade stress variation with barricade width, for offset distance of 25 mm; (a) square drives and (b) circular drives 144

Figure 5.14. Barricade stress variation when shape of the drive is changed and the offset of 25 mm: (a) for surcharges of 36 kPa and 68 kPa, and (b) surcharges of 393 kPa and 523 kPa..... 145

Figure 5.15. Variation of barricade stress with offset distance as compared in different surcharges; (a) q = 36 kPa, (b) q = 394 kPa and (c) q = 913 kPa 147

Figure 5.16. The variation of barricade stresses with the drive width from analytical, numerical and laboratory test results; (a) q = 394 kPa and L = 0, (b) q = 913 kPa and L = 0, (c) q= 394 kPa and L = 75 mm and (d) q =913 kPa and L = 75 mm..... 149

Figure 5.17. The normalised barricade stress, with respect to the offset distance, from all laboratory tests with drives of 75 mm, 100 mm, 125 mm and 150 mm widths 151

Figure 6.1. The forces in the disk assembly; (a) forces from surrounding disks and (b) the weight represented with two equal forces f 162

Figure 6.2. The force transmission at walls, when $\alpha < 60°$..... 163

Figure 6.3. Disk arrangement in 2D space and relevant parameters 164

Figure 6.4. Disk arrangement to calculate (a) the vertical stress and (b) the horizontal stress..... 165

Figure 6.5. The disk arrangement highlighting the cases considered for calculations; each disk is identified with the respective i,j location..... 166

Figure 6.6. Sensitivity of F on average vertical stress variation 169

Figure 6.7. Variation of vertical stress with number of disks used in the model..... 170

Figure 6.8. Variation of vertical stress from the proposed analytical equation is compared with arching theory 172

Figure 6.9. Variation of vertical stress along the width, for various arching factors, at a depth of 6B..... 173

Figure 6.10. Lateral variation of average stress at depths of 2*B*, 4*B* and 6*B*; (*F* = 0.002) 174

Figure 6.11. Variation of calculated lateral pressure coefficient (K_1) with depth for different *F* values 175

Figure 6.12. The laboratory test results for B/L = 0.2 model are compared with the proposed analytical solution 176

Figure 6.13. The proposed analytical solution is matched with laboratory model test results with *B*/*L* = 0.2 177

Figure 6.14. The derived vertical stress variation with laboratory tests is matched with the proposed analytical solution 178

Figure A1. Load plate displacement results for tests with square drives for 75 mm and 100 mm wide drives..... 212

Figure A2. Load plate displacement results for tests with square drives for 125 m and 150 mm wide drives..... 213

Figure A3. The calculated lateral pressure coefficient values are compared with theoretical values; (a) 100 mm wide square drive is attached, (b) 100 mm wide circular drive is attached 214

Figure A4. The calculated lateral pressure coefficient values are compared with theoretical values; (a) 125 mm wide square drive is attached, (b) 125 mm wide circular drive is attached 215

Figure A5. The calculated lateral pressure coefficient values are compared with theoretical values; (a) 150 mm wide square drive is attached, (b) 150 mm wide circular drive is attached 216

Figure A6. Barricade stress variation with drive width at zero offset distance on square drives 217

Figure A7. Barricade stress variation with drive width at zero offset distance on circular drives 218

Figure A8. Barricade stress variation with drive width, for offset distance of 25 mm on square drives 219

Figure A9. Barricade stress variation with drive width, for offset distance of 50 mm on square drives 220

Figure A10. Barricade stress variation with drive width, for offset distance of 50 mm on circular drives 221

Figure B1. Forces arrangements around a disk, for contact angle of 60; (a) forces from surrounding disks and (b) force transmission at walls 236

List of Tables

Table 1.1. Reported backfill barricade failures in Australia 9

Table 2.1. Density, Young's modulus and Poisson's ratio values used with numerical simulations 19

Table 3.1.Geotechnical properties for hydraulic fills and sand 53

Table 3.2. Laboratory model test data and derived vertical, shear and horizontal stress values for 150 mm x 150 mm x 900 mm stope..... 57

Table 3.3. Material properties for backfill and Perspex, used in FLAC simulations 61

Table 4.1. Summary of material properties used in the sensitivity study 89

Table 4.2. Parameters used with FLAC simulations to generate stress isobars..... 102

Table 4.3. Scenarios used for verification of plane strain stress isobar charts 107

Table 4.4. Scenarios used for verification of axisymmetric stress isobar charts 115

Table 5.1. Geomechanical properties used with FLAC^{3D} model for barricade bricks, rock surrounding, HF and interface 136

Table 5.2. The parameters considered for the calculation of barricade stress from the proposed empirical equation (Equations 5.18 and 5.19)..... 152

Table 6.1. The maximum average vertical stress compared with the number of disks used in the model..... 171

Abbreviations

EPC	Earth Pressure Cells
TPC	Total Pressure Cell
CPB	Cemented Paste Backfills
UDL	Uniformly Distributed Load
DSM	Discrete Stiffness Model
DEM	Discrete Element Model
HF	Hydraulic Fills
USCS	Unified Soil Classification System
UCS	Unconfined Compressive Strength
FLAC	Fast Lagrangian Analysis of Continua
$FLAC^{3D}$	Fast Lagrangian Analysis of Continua in three dimensions
JCU	James Cook University
SEM	Scanning Electron Microscope
PFC	Particle Flow Code

List of Symbols

h'	A height considered on the barricade
c_a	Adhesion
F	Arching factor for disk model
σ_v	Average vertical normal stress
K_{calc}	Calculated lateral pressure coefficient
C_c	Coefficient of curvature
C_u	Coefficient of uniformity
c	Cohesion
A_d	Cross sectional area of the drive/barricade
A	Cross sectional area of the stope
ρ	Density of the fill
z	Depth to a particular point, within the stope
ψ	Dilation angle
d	Disk diameter
f	Disk weight components
D_{10}	Effective grain size
n	Fill load measured by the balance
m	Fill load measured by the load cell
φ	Friction angle
H	Height of the stope or structure
x	Horizontal distance from centre

σ_{hB0}	Horizontal stress at base of the stope entrance
σ_{hT0}	Horizontal stress at top of the stope entrance
σ_h	Horizontal stress from backfill to walls
δ	Interfacial friction angle
$K_{krynine}$	Krynine's lateral pressure coefficient at rest
K	Lateral pressure coefficient
K_0	Lateral pressure coefficient at rest
K_{dl}	Lateral pressure coefficient in longitudinal direction within the drive
K_{dt}	Lateral pressure coefficient in transverse direction within the drive
σ_b	Lateral stress on barricade
L	Length of the stope or structure
D_{50}	Median grain diameter
MTS	MTS Universal Testing Machine
K_n	Normal stiffness for the interface in FLAC
p	Number of disks along the height
s	Number of disks along the width
L	Offset distance of barricade from the stope entrance
P_d	Perimeter of the drive/barricade
P	Perimeter of the horizontal layer element
v	Poisson's ratio
K_a	Rankine's active earth pressure coefficient
D_r	Relative density
K_s	Shear stiffness for the interface in FLAC

C_w	Solids by weight
$n_{i,j}$	The force directed horizontally from left side to the disk
$N_{i,j}$	The force directed horizontally from right side to the disk
$L_{i,j}$	The force directed on an angle α from bottom left side to the disk
$M_{i,j}$	The force directed on an angle α from bottom right side to the disk
$m_{i,j}$	The force directed on an angle α from top left side to the disk
$l_{i,j}$	The force directed on an angle α from top right side to the disk
α	The inclination of the line connecting the centres of disks to the horizontal
τ	The shear stress at the wall
H_d	Total height of the drive
q	Uniform surcharge
γ	Unit weight of the fill
$\sigma_{v,\phi}$	Vertical stress computed at friction angle of ϕ
$\sigma_{v,40}$	Vertical stress computed at friction angle of 40°
A_w	Wall-fill contact area in a backfilled structure
w	Weight of the disk
B	Width of the stope or structure
E	Young's Modulus

Chapter 1

Introduction

1.1 General

Underground mining is the process of extracting mineral ore deposits. The massive ore bodies are divided into blocks or stopes, and the ore is mined from those stopes sequentially. The processed mineral waste is called tailings and the disposal of tailings in a safe, stable and economical manner is very important and beneficial to all stakeholders. Tailings were earlier disposed to surface impoundments, but limited availability of land area motivates one to find alternative means of tailings disposal. The void generated after mining the ore from underground is backfilled with a mixture including the processed mineral waste. The interest in mine backfilling is increasing and in some instances regulations were implemented for mandatory backfilling of mined voids considering the environmental impact from releasing mine waste to land or sea (Nantel 1998; Keen et al. 2007). For example, Jabiluka Uranium mine situated in Kakadu National Park, Australia had to direct all the tailings to underground due to lack of space for surface tailings facilities (ERA 2003).

1.1.1 Mining

Mining is a major industry in Australian economy and can be classified into two categories based on the location: underground and open pit mining. Underground mining extracts the valuable ore from deep ore bodies and the ore body is accessed through ramps, shafts and tunnels (Figure 1.1). In contrast, open pit mining extracts the mineral ore from the earth by removal of ore from an open pit or open cut mining, where the overburden is relatively thin. Mineral distribution, ore grade, ore deposit dimensions, prevailing rock conditions and dilution rates decide the optimum mining method to be adopted in underground mining (Brady and Brown 1985). Deep massive ore bodies can be mined through open stoping methods (sublevel open stoping, secondary or tertiary stoping and vertical crater retreat) with the use of backfilling.

In open stoping method, the ore body is divided into sections or stopes to carry out the mining operations. Often rectangular, square or narrow sections or stopes are mined such that the previously mined stopes are filled before mining the next stope (Figure 1.2). Open stoping mining method accounts for 60% of total underground tonnage in Canada (De Souza et al. 2003) and also a significant quantity in Australia (Grice 2001). Stope widths range from 2.7 m to 25 m and heights range from 11 m to 180 m (Evans et al. 2007). In open stoping, there are two production methods: (1) short hole mining, which is similar to development mining, except that it occurs in ore, and (2) long hole mining, which requires two accesses within the ore at different elevations to drill holes between the two levels and then production is carried out.

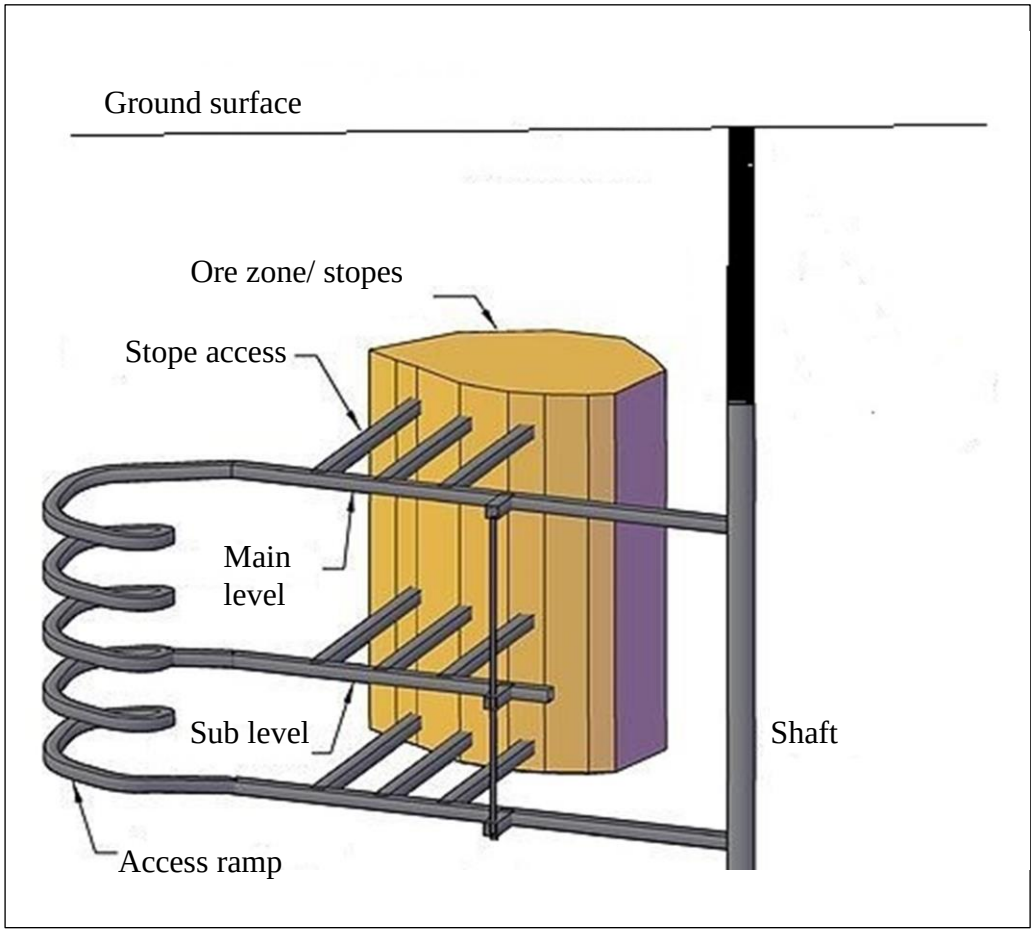

Figure 1.1. Idealised infrastructure in an underground mine, showing the basic elements around a stope (source: www.wikipedia.com)

The blasted ore is removed from the bottom level via drives or drifts used as machinery paths and providing the link between stopes and other underground facilities (Figure 1.2). Usually drives are created only to cater to the underground traffic, and are barricaded before backfilling the stope. As it is required to support the host rock after exploitation the stope, backfill can be used as a bulking agent. When backfill is used with underground mining, a number of extraction strategies are available to optimize pillar recovery. In general, a stoping sequence is driven by ore grade requirements, operational issues such as existing development and fill availability, as well as induced stress considerations (Villaescusa 2003).

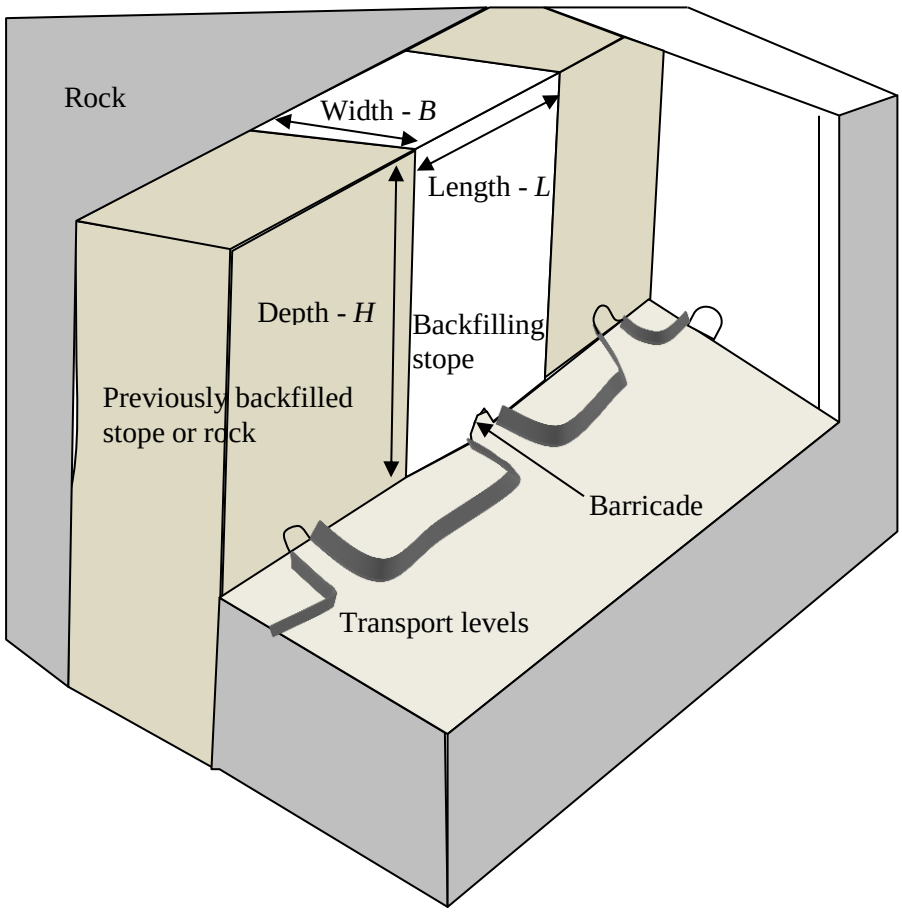

Figure 1.2. Open stoping sequence with backfilling showing the barricade

1.1.2 Geomechanics in underground mining

The underground in situ rock stress conditions are affected by mining because the confinement conditions are changed in the stope vicinity. However, managing the host rock stress conditions is essential to maintain the safety and operational efficiency. The importance of underground geomechanics related to mining can be highlighted further with Figure 1.3, which summarises the fatalities related to Australian mining as reported by Mineral Council Australia's annual safety and performance reports from

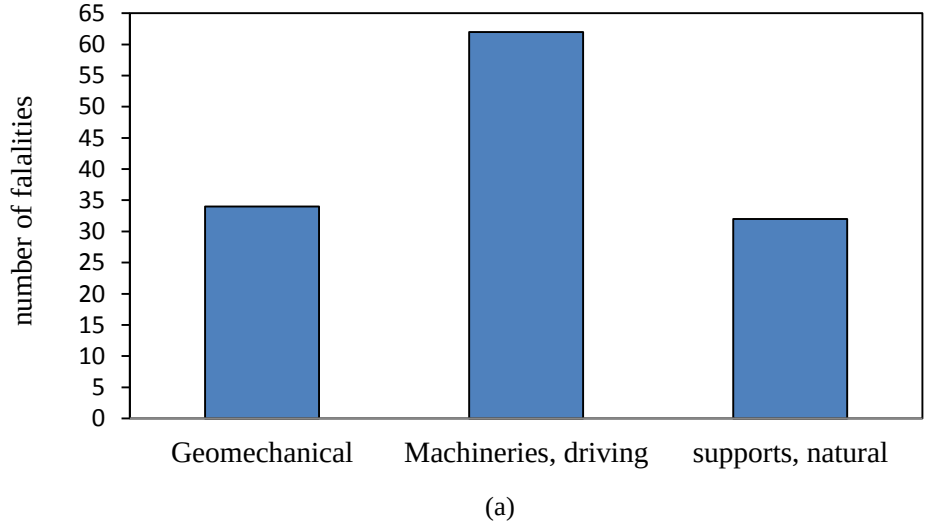

(a)

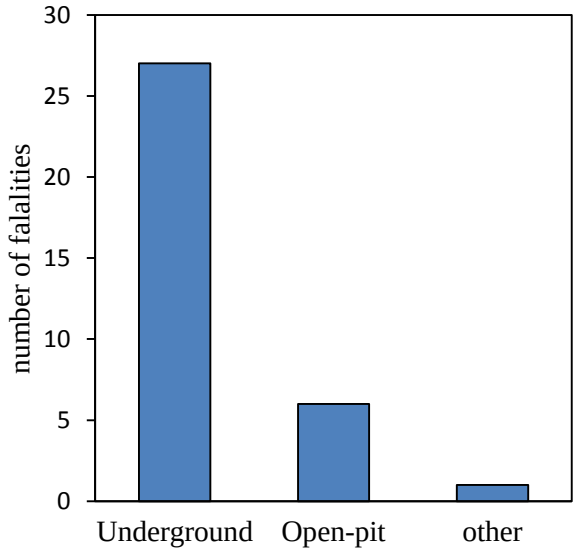

(b)

Figure 1.3. Fatalities in Australian mining industry, as reported by Mineral Council of Australia for 1999 to 2009; (a) fatalities breakdown due to cause and (b) geomechanically caused fatalities are categorised based on the location

1999 - 2009.

In Figure 1.3, any cause of fatality related to geomechanics, such as rock falls, rock bursts and fill barricade failures are considered as geomechanical. Any fatality originated with machinery manoeuvring and repair activities is counted under ‘machineries, driving’. The other causes, such as inadequate handling of instrument and natural causes are categorised into ‘supports, natural’ category. Almost a quarter of the fatalities during 1999 - 2009, were caused by geomechanical issues (Figure 1.3). Further, fatalities due to geomechanical causes are classified with the location in Figure 1.3b, which highlights that 80% of the geomechanically caused fatalities occurred within underground operations. Several fatalities are counted from backfill runoffs occurring with barricade failures. Therefore, the underground geomechanics especially related to mine backfilling needs to be well understood for safe and efficient mining operations.

1.1.3 Mine backfilling

Though the backfill system is often expensive, typically covering about 30% of total mining costs, reliability and flexibility of the backfill system greatly support the mining operation (Bloss 2014). Backfill is an integral part of the mining cycle and brings production, safety and financial performance benefits (Evans et al. 2007). Backfill offers a versatile solution for waste disposal and sometimes uses surface pit waste or quarried aggregates as constituents to enhance the strength and flow properties of the backfill. In every backfilling situation, there may be one or more drives needing barricading to isolate the stope (Figure 1.2). Backfilling is a concurrent operation with mining and cannot be delayed as the next mining cycle depends on backfilling the stopes. Thus, development of the efficient backfill system can lower the cost of mining and bring operational benefits to the mining process.

The main purposes of mine backfilling are as follows.

- To achieve local and regional ground support
- To maximise ore extraction
- To control the ore dilution
- To dispose waste in an effective and environmentally friendly manner
- To reduce the need and maintenance of surface tailings ponds
- To improve ventilation and fire control aspects
- To control ground subsidence
- To acts as a working floor for the next mining cycle

The backfill quantities used per annum are high in Australia. For instance, the backfilled tonnage is two million tonnes or greater per annum (Grice 2003). The choice of materials that are utilized for fill preparation depends on the location of backfilling, availability of materials for a particular fill and prevailing ground conditions (Grice 1998a). Therefore, classified or total stream of tailings is processed and directed to mined out stopes. According to fill properties and preparation method, backfills can be divided into;

- Hydraulic fills (HF)
- Paste fill
- Aggregate / Rock fill

When free standing walls are not expected when mining adjacent stopes, the stopes can be filled with uncemented or slightly cemented HFs, just as a bulking agent to fill the void. Therefore, in stoping methods, the tertiary stope is usually filled with HFs. The backfilling in underground massive ore body mining is further illustrated with the egg crate pattern stope planning for 1100 ore body in Mount Isa Mines, Australia (Figure 1.4). In preparing HFs, fines (i.e., the clay fraction) are removed from total stream tailings through hydrocyclones (de-sliming) to increase the permeability to facilitate fast drainage. After preparation at surface fill plants, the fill is pumped or allowed to gravitate to underground. HF possess low to moderate in situ strength and

HF placement rates can be as high as 100 – 200 t/h. Moreover, sufficient time should be left to allow draining the excessive water.

Total mill tailings are used to process paste fills and about 50 - 200 t/h placement rates can be achieved. Negligible water run-offs are encountered as the water is used internally for the cementation process and often no provision is left for drainage with CPB. Higher free standing walls can be achieved with paste fills, in which the rheology is modified at the paste fill plant. However, paste fill has a more difficult rheology to manage than lower density hydraulic fill due to a higher pressure loss per unit length of pipe and a higher angle of repose when placed in a stope (Potvin 2005).

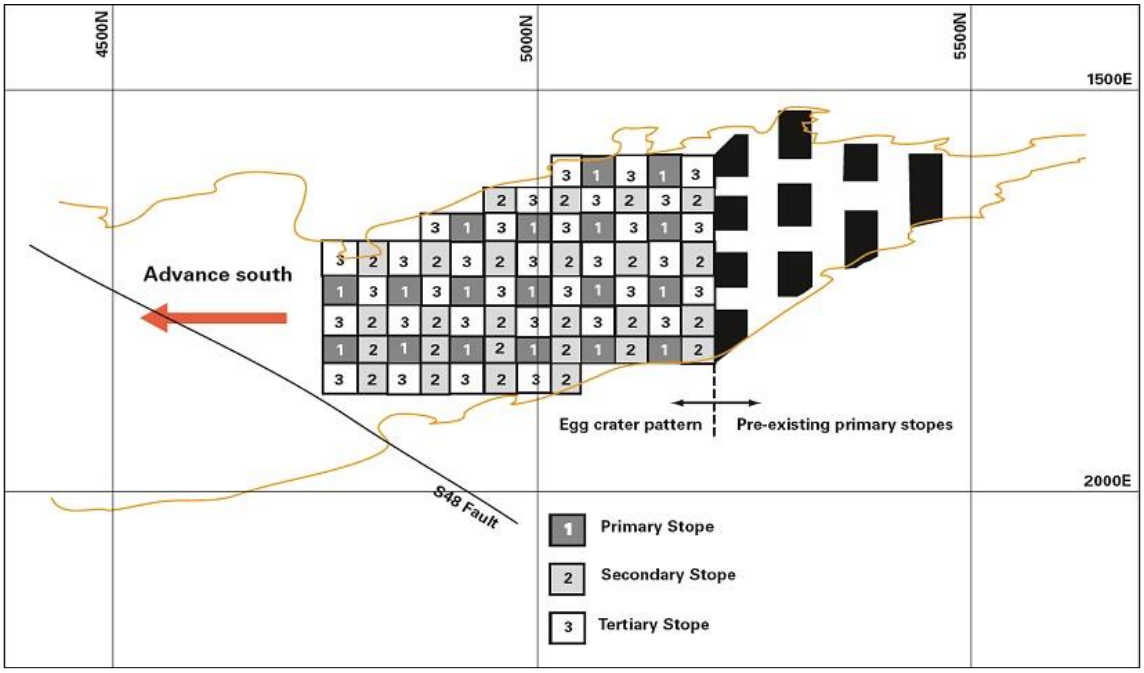

Figure 1.4. Plan view related to egg crater pattern stoping sequence at Mount Isa Mines (reproduced from Simpson (2007))

Aggregates are usually gravel size materials, which are produced in screening and pre-concentration processes. Rock fill is the crushed and screened product from the quarry or the fragments of host rock where mine developments were taking place (for example, crosscuts or development drives). Often, rock or aggregate fills are used when high strength fill is required especially for severe in situ stress conditions. Rock fill placement in stopes carried out with truck dumping for small operations, and for large

operations conveyors are used to manage the placement costs. Additionally, de-slimed tailings are used solely or combined with aggregates, rock, or cement to prepare the required backfill composition.

1.2 Problem statement

Engineered barricades are built across horizontal drives to retain the backfill slurry in the stopes. Failure of such a slurry retaining barricade not only endangers the miners' lives but also has led to many financial losses such as damage to mining equipment, underground rehabilitation due to flooding and cessation of operations for a considerable amount of time (Duffield et al. 2003; Sivakugan et al. 2006a; Yumlu and Guresci 2007). A catastrophic failure, the collapse of a hydraulic fill barricade at Bronzewing mine in Western Australia has resulted in three fatalities (Celeste 2000; Torlach 2000). Several other examples are presented in Table 1.1. Although most of the barricade failures are not reported in detail, it was evident that there is increased rate of backfill barricade failures. After all, the need to understand the stress developments within the mine stope and the need for the correct engineered design of barricade are increasing.

Table 1.1. Reported backfill barricade failures in Australia

Year	Incident/ Mine	Location	Consequences	References
2003-2006	Twelve barricade failures	Not reported	Not reported	Helinski et al. (2011)
1998	Two barricade failures	Not reported	Not reported	Grice (1998b)
2000	Bronzewing Mine	Western Australia	Three fatalities	Torlach (2000), Celeste (2000)
2000	Osborne Mine	Queensland	Rehabilitation	Duffield et al (2003)
2007	Two mines-five barricade failures	Not reported	Not reported	Revell and Sainsbury (2007b)

1.3 Objectives and scope of research

The aim of this research is to critically assess the arching and stress developments within backfilled stopes and drives and to develop a methodology to estimate the loads onto barricades synthesizing analytical, numerical and laboratory studies.

The following objectives are set in order to estimate loads onto backfilled barricades.

1. To revisit the stress transfer mechanisms in hydraulic backfilled stopes
2. To identify the factors that affect the lateral load on barricade and develop suitable analytical expressions
3. To measure the variation of the barricade loads with the change of barricade location within the drive and the effect of barricade dimension on stresses in laboratory tests
4. To develop three dimensional numerical models to verify the laboratory model tests
5. To measure vertical stress in backfilled stopes and develop alternative analytical solutions to verify the test results

The analytical, numerical and laboratory studies are conducted concurrently and the outcome for the barricade stress is compared for all three techniques. The agreements or deviations among the results will generate:

- Improvement in the current state-of-the-art related to stress developments within backfilled mine stopes and drives,
- The concept of vertical stress isobars, and simple design charts to determine the vertical stress variations within backfilled structures including silos and stopes, and
- An alternative analytical methodology to address the stress developments within backfilled stopes.

1.4 Relevance of research

Backfilling facilitates the optimization of the performance of the chosen mining method. There are numerous examples where mine production is directly related to the effectiveness and speed of filling empty stopes (Henderson et al. 1997). The overall productivity is severely constrained by the individual stope cycle times as stopes must be mined, filled and cured before an adjacent stope can be extracted. Barricades are temporary structures that need to support the loading from the backfill placed onto the stope. The water introduced into the stope, especially with hydraulic fill, can lead to higher hydraulic heads and the safety of the barricade can be jeopardized. Fill retaining barricades are normally constructed to isolate the backfilling stope. There are several methods available to estimate the vertical stresses within the backfilled stopes and the loads on the barricade, such as analytical, in situ stress measurements, physical modelling and numerical simulations. Analytical methods allow a preliminary assessment of the anticipated loads onto the barricade. However, the assumptions and simplifications to the geometry, barricade or rock interface properties, and the properties of the barricade limit the confidence in these design estimations for field application.

Barricades vary in thickness, which is determined by the drive dimensions and loadings from backfill. However, when there is lack of understanding of the geomechanics related to backfill, barricade stresses are overestimated, and thus there is a tendency to construct larger barricades than necessary. For example, one metre thick heavily reinforced concrete barricades have been built (Mitchell et al. 1975). Construction of a such large barricade is not only expensive, but also causes considerable delays in the mining cycle due to time taken for the construction and curing of the barricade (Mitchell et al. 1975). Therefore, correct estimates of loads onto the barricades would lead to the optimum barricade design and favour the speed of the mining cycle.

Therefore, while it is necessary to optimize the thickness of the barricade and to minimize time taken for the construction, the barricade needs to be able to sustain the loads induced by backfill. This study will investigate the forces acting on barricades in order to quantify the requirements for the barricade dimensions. Dry, uncemented hydraulic fills are considered in this study. Realistic determination of the vertical stresses within the mine stope and drives can pave the way to improving the design of barricades as well as minimise the risks associated with underground mining. Therefore, optimising of the design of barricades will balance the performance and safety concerns in underground mining. Furthermore, the stress developments onto bulkheads when the stope is filled with CPB would be different to the stresses from this study.

1.5 Thesis overview

Chapter 1 provides the introduction to mine backfilling and discusses the significance of studying the stress developments within backfilled mines and drives to enhance the understanding on loads acting on the barricades.

Chapter 2 reviews the literature related to mine backfilling and barricade failures. The latter section of Chapter 2 reviews the analytical equations used with arching theory and reliability of the assumptions.

Chapter 3 focusses on understanding the in situ stress state within a backfilled mine stope. First section summarises the laboratory tests carried out with square, circular and rectangular model stopes and identifies that the vertical stress variation from laboratory model tests shows a linear increase with depth without reaching an asymptotic vertical stress even at large depths. Next, finite difference numerical simulations were used to replicate the backfilling into model stopes and at the end of Chapter 3, vertical stresses calculated from analytical, numerical and laboratory test approaches were compared and the implications are discussed.

Chapter 4 emphasizes the lateral variation of vertical stress within backfilled structures, which is not generally estimated by analytical equations. Numerical simulations were used to carry out a sensitivity analysis of the fill parameters that influence the vertical stress within a stope. The vertical stress contours within the backfill are presented as isobar charts. The proposed plane strain stress isobars can be used to estimate stresses in plane strain backfill situations, such as backfilled narrow mine stopes and backfilled trenches. Also, the proposed axisymmetric stress isobars can be used to estimate stresses in circular structures and the axisymmetric stress variation closely matches the vertical stress variation in backfilled structures with square cross section in plan. Additionally, an equation is proposed with interpolation to estimate vertical stresses in mine stopes with other cross sectional shapes such as rectangles.

After the understanding of the stresses within the backfilled stope, the load distribution from stope to the drive is studied in Chapter 5. A laboratory test apparatus is designed and manufactured with provisions to insert drives of different widths as well as to vary the distance from stope to the barricade. This study focused on stress developments through drives towards the barricade in a stope filled with hydraulic fills. The analytical solutions available in literature are generally based on a continuum approach, and often underestimate the stresses within the fill. Therefore a laboratory model was used to investigate the stress distributions within stope and drive filled with dry hydraulic fill material under higher stresses. Earth pressure cells are used on the barricade and also within the stope to record the stress variation when a uniformly distributed load is applied from the top of the model stope. Also, three dimensional numerical simulations were used to compare the results from laboratory model tests. Finally, an empirical relationship for barricade stress was constructed based on laboratory test results.

Chapter 6 presents an alternative analytical solution, as the observed vertical stress variation with laboratory models related to backfilled stopes is not successfully predicted by the arching theory. The mine fills are granular materials, which may show

deviations in vertical stress estimations when assumed as continuum. Therefore, alternative analytical equations are developed considering a particulate medium consisting of two dimensional regular disk array and the summation of inter-particle forces. The proposed analytical equation is capable of estimating the vertical stresses close to those obtained from laboratory tests.

Chapter 7, the final chapter, synthesises the conclusions drawn in each chapter and concludes the thesis. Furthermore, recommendations on future research are presented at the end of Chapter 7.

Chapter 2

Literature Review

2.1 Overview of mine backfill literature

Mine backfilling is an integral process within the mining cycle and often the backfilling speed dictates the speed of overall mining cycle. “One cannot mine faster than he fills” is a famous quote among the miners (Bloss 2014). The use of backfill has brought many advantages and provides the option to select the optimum ore extraction technique with mining methods such as sublevel open stoping, vertical crater retreat and cut and fill mining. Hydraulic fills (HF), among many other fill types, are widely used with backfilling operations, and are popular due to their low cost and relatively easy preparations. Barricades are constructed in place, blocking the drives, to retain the backfills and contain them within the stope. A proper understanding of the loadings on the barricades is necessary to design them with confidence, thus ensuring safe and reliable mining practices.

In situ stress measurements have been reported for backfills within the stope (Knutsson 1981; Grice 1989; Belem et al. 2004; Thompson et al. 2009; Thompson et al. 2012). However, in situ measurements of barricade stress when the stope is filled with hydraulic fills are limited. Grice (1989) loaded the brick barricades under undrained conditions with cemented aggregate fills at Mount Isa Mines and recorded the stresses experienced by the barricades. Mitchell (1992), studied the resultant force variation for a barricade within a 200 mm × 200 mm wide drive via a centrifuge model, locating the barricade at two offset distances of 0 and 100 mm.

Understanding the stress development within the backfilled mine stopes is necessary for estimating the loads on the barricade. The barricade stress variation is analytically expressed by Kuganathan (2002) and Li and Aubertin (2009b), assuming elastic behaviour considering a vertical layer element along the drive. Also numerical modelling has been carried out for studying the stress developments within the stope as well as the loads acting on the barricade (Aubertin et al. 2003; Li and Aubertin 2009b; Helinski et al. 2010). Moreover, laboratory model studies provide an insight to the behaviour of the backfill as well (Pirapakaran 2008; Ting 2011). Therefore, analytical,

numerical and laboratory tests are used in this dissertation to shed light on the understanding of loads onto the barricades considering the arching and stress propagation, thus enabling development of competent designs for barricades.

The aspects such as drainage, loading on barricade and filling procedures are to be considered when mine stopes are backfilled with uncemented tailings. Comprehensive tests on properties and behaviour of emplace fills were undertaken by Thomas (1969) for Mount Isa Mines. Grice (1998) identified a few operations that use lower slurry densities than generally accepted and reported a few barricade failures while indicating recorded slurry densities of 53% solids by weight. Recent studies by Rankine (2005), Sivakugan et al. (2006b) and Helinski (2007) have led to improved understanding of the drainage within backfilled mine stopes.

2.2 Hydraulic fills – properties

The hydraulic fills are the coarse fraction from mine tailing streams. The specific gravity of mine fills is high, compared with general soils, as they are end products from heavy mineral ores. Sivakugan et al. (2006b) have reported that the specific gravity is ranging from 2.8 to 4.4 for HFs, after tests conducted for 20 different Australian hydraulic fills. The grain size distribution is an essential component in the backfill and the grain size distributions for common Australian backfills are given in Figure 2.1. The grain size parameters C_u and C_c vary in a range of 3.7 to 13.3 and 0.6 to 2.0, respectively (Sivakugan 2008). Removal of finer fraction, de-sliming, leads to a major characteristic of hydraulic fills as “less than 10% to be finer than 10 μm” (Grice 1998). This implies that D_{10} of a HF is expected to be greater than 10 μm.

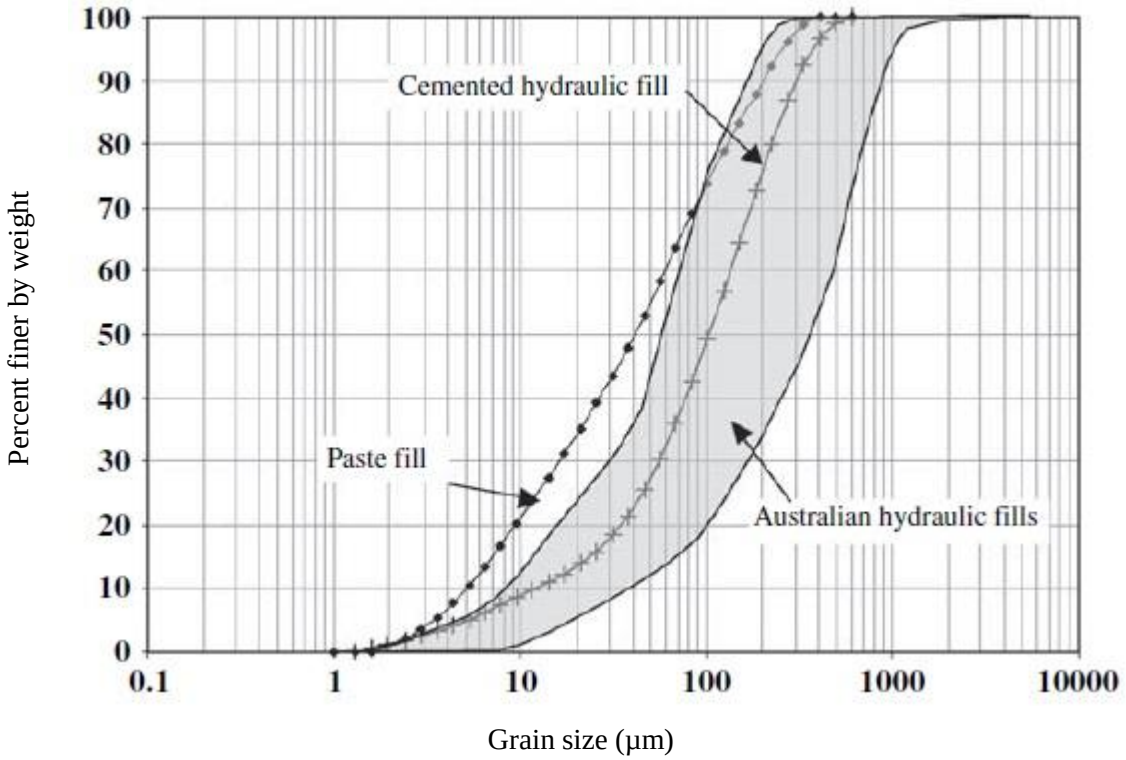

Figure 2.1. Grain size distribution of Australian backfills that were tested at James Cook University (Sivakugan et al. 2006)

When a large quantity of water enters the stopes, it may not be able to drain through the barricade and may induce hydrostatic loading conditions to the barricade. Therefore, maintaining the slurry density as specified is important. Usually the slurry density of HF, ranges from 50 - 70% solids by weight (C_w). The quantity of drainage resulting from slurry densities of around 70% C_w is as little as a quarter of the drainage resulting from 55% C_w slurries (Grice 1998). Often, it is recommended to maintain 70% or higher solids by weight in the slurry to minimize the water placed underground.

Water, being the main constituent of distribution and placement of backfill, enters the stope in considerable amount. The excess water needs to be removed from the stope as quickly as possible because of the instability caused by hydrostatic conditions (Sivakugan et al. 2005). The rate of drainage is a function of the permeability of the backfill and the driving head (Grice 1998). Rough surfaced and angular shaped HF particles produce a greater resistance to the movement of fluid through the voids and therefore permeability is lowered within the backfill. Permeability controls the rate of

fill dewatering and if it has not been adequately dewatered, the fill is not ready to accept loads (Thomas 1969). HFs have permeability of 9.1 to 37.8 mm/h (Berndt et al. 2007). Therefore dewatering characteristics were improved by de-sliming with classification systems such as hydrocyclones. Hence HFs are also called as classified tailings and categorised as sandy silts or silty sand (SM or ML), according to Unified Soil Classification System (USCS) (Sivakugan 2008).

Backfill comprises crushed and milled mine waste, and is usually less stiff than the surrounding host-rock. Uncemented HFs possess Young's modulus of 10 to 50 MPa. The surrounding rock mass is two orders stiffer than the fill material (Table 2.1). This difference of stiffness characteristics leads to shearing along the walls and then to arching. A summary of the geotechnical properties used in the numerical simulations related to backfills is given in Table 2.1.

Table 2.1. Density, Young's modulus and Poisson's ratio values used with numerical simulations

Material	**Density (ρ)**	**Young's modulus**	**Poisson's ratio**	**Reference**
Rock	2700 kgm^{-3}	30 GPa	0.3	Li et al. (2003)
Minefill	2038 kgm^{-3}	10 MPa	0.2	Fahey et al. (2009)
Minefill	1834 kgm^{-3}	300 MPa	0.2	Aubertin et al. (2003)
Minefill	1834 kgm^{-3}	100 MPa	0.25	Mkadmi et al. (2011)
Minefill	1800 kgm^{-3}	300 MPa	0.2	Ting (2011)
Sand	2038 kgm^{-3}	50 MPa	0.35	Jayasree et al. (2012)

2.2.1 Friction angle

The friction angle *(φ)* of a granular soil or fully drained HF is primarily influenced by the material density or the degree of particle packing. Tailing particles are generated from crushing and milling and are angular in shape. Because of this angular shape, the internal friction angle of HF is higher. This angular shapes of HF is also

evident from scanning electron micrographs (Rankine 2005; Singh 2009). Interlocking is greatly influenced by gradation and densification of the material (Spangler and Handy 1973). Therefore, the friction angle ranges between 30^o and 47^o for HFs (Bloss 1992). Rankine (2005) has conducted direct shear tests on HF samples and found that friction angle is 38^o for relative density of 52% and it is 49^o for relative density of 93% and proposed Equation 2.1, in which the friction angle varies with the relative density of the fill.

$$\varphi^o = 0.19{D_r}^2 + 33^o \tag{2.1}$$

where D_r is the relative density of backfill material.

Pirapakaran (2008) has conducted direct shear tests and identified that the friction angle varies from 30^o to 49^o for very loose to very dense packing in HFs. Many internal friction angles are reported and used in literature for HFs, such as 30^o to 35^o (Li et al. 2003), 20^o and 15^o (Kuganathan 2002), and 35^o (Helinski 2007). Considering the analytical equations, Singh et al. (2010) have suggested that the average vertical stress within a backfill is insensitive to friction angle in the range of 25^o to 45^o.

2.2.2 Interfacial friction angle

The shear strength is a key component for arching to consider with mine backfilling. Interfacial friction angle (δ) is the friction component along the contact surface between two different materials, i.e., the interface. Singh et al. (2010) showed that the average vertical stress at a certain depth within a backfill is dependent on wall roughness condition, which essentially reflects the δ/φ ratio. Full mobilization of interfacial friction leads to the maximum force transfer though the walls. Usually, the interfacial friction angle is close to zero for very smooth walls and the maximum is equal to the material friction angle for rough surfaces. Singh et al. (2010) suggested that the interfacial friction angle can be taken as being equal to the material friction angle in mine backfilling because of the highly uneven walls in actual mine stopes after blast

operations. Here, any slip occurs a few grains away from the rough wall and hence the failure surface is entirely within the minefill. This shear strength property is equally important along the drives where wall friction is mobilized in the drives, and influences the lateral stress conditions and finally the load on the barricade. However, the interfacial friction angle is considered to be the same in the stope walls and within the drive walls. Direct shear tests between cemented paste backfill (CPB) against concrete and porous brick have showed that peak interfacial friction angles were 28.4^{o} and 24.3^{o} respectively (Fall and Nasir 2010).

2.3 Barricade types and failures

The barricade design and construction techniques have evolved with the research related to mine backfilling. Australian mining practice often refers to barricades as a fill retaining structure that provides free drainage of excess water and bulkhead as an impermeable fill retaining structure. With this study, both the fill retaining structure types are considered as barricades. Currently, the following barricade types were used with HF applications;

- Planar concrete brick masonry barricade
- Arched concrete brick masonry barricade
- Fibrecrete, aquacrete or shotcrete barricade
- Foamcrete barricade

Although many forms of barricades are encountered in mining, the main features and the loading mechanisms are often the same. However, each design of barricade is applicable to a specific mine environment and may depends on the fill type, cementation of the fill, mining dimensions and time allowed for barricade construction in mining cycle. Loadings on the barricade depend on the shear strength of the fill material and stress transfer with arching (Grice 1989). Stress redistribution within the backfill and also between backfill and stope walls induces loads on the barricade

jeopardising the structural integrity of barricades (Bridges 2003; Duffield et al. 2003). The strength achieved with design and construction of barricades as well as the operational stresses of barricades is not yet completely comprehended (Berndt et al. 2007).

2.3.1 Brick barricades

Brick masonry barricades are made of specially manufactured porous bricks (Berndt et al. 2007). Brick barricades are mostly used with HF applications and a high duration of time is required before the next mining cycle, when compared with impermeable barricades. The brick barricade should be capable of the following for a successful operation (Grice 1998);

- Have the strength to withstand initial hydrostatic slurry loading,
- Be more permeable than the hydraulic backfill and
- Act as an efficient filter to retain all fines.

Specially manufactured porous bricks are used for the construction of brick barricades. Mortar is composed of gravel, sand, cement and water in a ratio of 40:40:5:1 by weight (Berndt et al. 2007). Brick dimensions have evolved from 460×200×115 mm to 400×200×100 mm (Duffield et al. 2003). Typical barricade bricks were tested to show porosities between the values 18% and 24%, and a specific gravity range of 2.39 to 2.59 (Berndt et al. 2007). Moreover, unconfined compressive strength (UCS) was approximately 7.0 MPa in dry conditions (Berndt et al. 2007). The porous brick barricade is saturated with draining water when the stope is backfilled and this saturation reduces the compressive strength of bricks significantly (Duffield et al. 2003; Berndt et al. 2007). As tested, when the bricks are wetted like in the actual situations, the UCS decreased by 25% (Berndt et al. 2007). Rankine (2005) proposed a permeability testing apparatus for barricade bricks and determined permeability of the bricks in the range of 32.8 mm/h to 126.0 mm/h. Therefore, barricade bricks are

significantly more permeable than the fill and permit free draining and ensure negligible excess pore pressures within the fill.

2.3.2 Shotcrete barricades

Over-sprayed concrete was used around reinforcement meshes as barricades and its thickness varied from 20 cm to 50 cm (Archibald et al 2009). Reinforcements were gabion basket structural supports where sheeting was a welded mesh (Archibald et al. 2009). Horizontal or angle drains with 150 mm diameter perforated PVC pipes are installed towards the fill from the barricade, as the bulkhead is impermeable (Sivakugan 2008). Installation of drains extending into the stope helps to cease the mobilization of fill in drives with impermeable bulkheads (Kuganathan 2001). With the reported failures of aquacrete barricades, barricade quality control (for example, specified thickness, restrict of water pooling at the bottom of the bulkhead) must be maintained when backfilling (Revell and Sainsbury 2007b).

Barricade technology has evolved over time and recently curved shape barricades have been used to enable better transmission of loads to anchored host-rock. An arched shaped barricade can withstand large spans with lower thickness (Kuganathan 2005). Therefore, curved shaped brick barricades keyed to host-rock are becoming a common practice (Kuganathan 2001; Berndt et al. 2007).

2.3.3 Barricade failure and mechanisms

Barricade stability is one of the main considerations in hydraulic mine backfilling as the stope is filled with hydraulic fill material (Sivakugan 2008). The following failure mechanisms were identified in the previous studies.

1. Flexural failure; cracks starting from corners and extending to centre in 45^{o} inclination
2. Shear failure; contact surface of rock around the barricade is failed

3. Punching failure; punched hole at the centre of the barricade

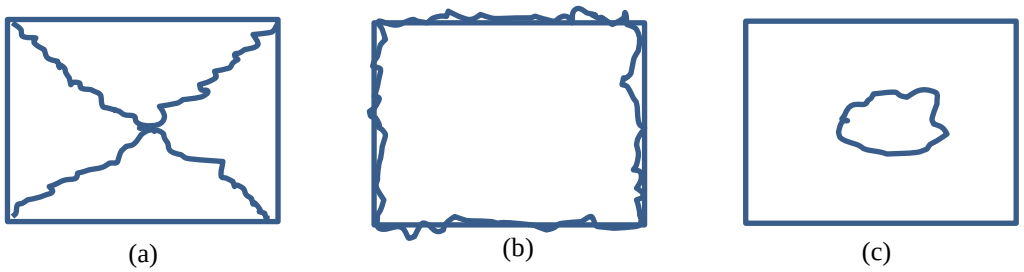

Figure 2.2. Failure profiles as identified by previous researchers; (a) flexural failure or diagonal cracks, (b) punching failure and (c) shear failure

Flexural failure

The HF load can be considered as a flexural load applied on the barricade, which is constrained at the walls along the perimeter. The Failure mechanism would be as shown in Figure 2.2a. The reinforced concrete would fail in flexure when loaded, while fixed at ends. Similar to those flexural crack lines of reinforced concrete, failed barricades also showed diagonal cracks (Grice 1989).

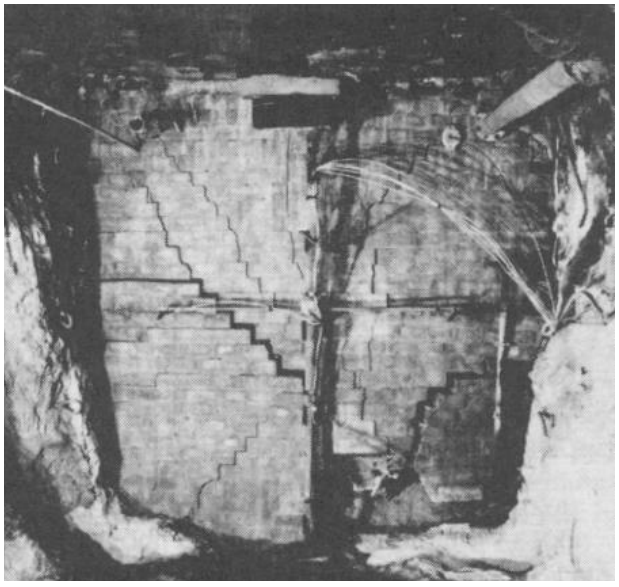

Figure 2.3. Flexural failure pattern of a brick barricade (Grice 1989)

A cracked barricade that shows the failure profile is shown in Figure 2.3, in which the barricade is subjected to undrained conditions with the cemented aggregate fills (Grice 1989).The barricade had cracked in tension along the diagonal line as shown in Figure 2.3 (Grice 2001). The assumed failure profile for the barricade was a linear crack starting at corners and extending to the centre making a 45° inclination (Duffield et al. 2003; Rankine 2004). Revell and Sainsbury (2007a) noted that there is no theoretical basis for applying yield line theory which is used to analyse the flexural failure in reinforced concrete slabs, to an unreinforced masonry wall. However, Grabinsky et al. (2014) have successfully modelled the failure of reinforced shotcrete barricades with laboratory tests and numerical simulations, considering this failure mechanism. The barricade failure may occur when the barricade is keyed to host rock and the force from the backfill is larger than the designed load on the barricade.

Shear failure

The insufficient shear strength at the barricade drive interface may lead to removal of the barricade from walls, with the load on the barricade. Grice (1989) reported model barricade testings, where three barricades were sealed and equipped

Figure 2.4. Shear failure appears on the barricade top (Revell and Sainsbury 2007b)

with pressure and displacement transducers, and filled with cemented aggregate fills till the failure occured. Furthermore, Grice 1989 reported from the video related to the bulkhead 3, which failed at 750 kPa, that the initial failure occurred due to shearing around the perimeter. The shear dislocation of the barricade at a drive was observed with recently reported paste fill bulkhead failures (Revell and Sainsbury 2007b). Figure 2.4 shows a barricade failure that occurred in Australia. Therefore, additional supports and keying to host rock, such as, rock bolts, rock pins were required to ensure the barricade safety.

Punching failure

Escape of finer particles through the barricade would lead to the formation of erosion pipes (Potvin et al. 2005). The erosion pipes may appear on the fill surface as a sinkhole (Grice 1989). If water ponds on the fill surface, the erosion pipe may induce hydrostatic loads onto the barricade and leads to a highly concentrated load at the centre of the barricade, like a punching force (Figures 2.2c and 2.5).

Figure 2.5. The punching failure is shown with failed brick barricade (Grice 1998)

Cracks can be initiated with bulkhead deflection and further movement leads to barricade failure at the centre, making a circular hole (Kuganathan 2001). Barricades have been observed failing according to this mechanism (case 2 of Grice 1998 paper).

Additionally, the importance of preventing the formation of erosion pipe was emphasized by Grice (1989) and Cowling et al. (1989), with studies conducted at Mount Isa mines. These barricade failures observed in the mines also emphasizes the need to avoid piping with cessation of the escape of HF fines from the stope.

The dynamic effects around the saturated fill need to be controlled, as the liquefaction due to blasting and piping actions results the failure not the build-up of excess pore water pressure (Bloss and Chen 1998; Grice 1998a). Liquefaction and piping can impose a substantial load on the barricade (Kuganathan 2001). Therefore, it is important to control the amount of fines entering the stope with HF. Overall, the erosion pipe leading to hydrostatic loading, dynamic effects (blast damages, rock fall off) as well as poor construction of the barricade can be the major causes of failures.

2.3.4 Numerical modelling of barricade

Numerical modelling approach has been proposed as the appropriate method of paste fill bulkhead design (Bridges 2003). When the problem scenario is complex and three dimensional, the analytical solutions are not capable of reliable estimates. Additionally, with difficulties of obtaining in situ measurements of vertical stresses in this type of backfilling situations, numerical simulations provide a viable alternative to estimate the lateral variation of vertical stresses. This becomes a three dimensional problem when drive and barricade are added, which would be difficult to simplify into a two dimensional system. However, the stress state near the barricade was modelled in plane strain by Li and Aubertin (2009a) and Fahey et al. (2009) with two dimensional numerical packages, assuming evenly distributed drive along the bottom of the stope. Revell and Sainsbury (2007a) have simulated three dimensional numerical models of barricades with backfilling for studying the load variations. A three dimensional numerical model can be developed to incorporate realistic bulkhead shapes, non-linear material properties and an interface between the bulkhead and the wall. However, there still remains a substantial amount of uncertainty in simulating representative barricade

material properties and loading conditions. Therefore Fast Lagrangian Analysis of Continua for three dimensions ($FLAC^{3D}$), a finite difference simulation software, was used to simulate the stope, drive and the barricade in this study. Moreover, in free draining barricades the pore pressure is not the major contributor to the failure (Cowling et al. 1988). As free draining barricades related to HFs are considered in this study, the study is limited to analyse the dry conditions considering laboratory limitations. The stress distribution within the backfilled stope and drives and the lateral loads on the barricade were studied in this thesis.

2.4 Numerical simulations for backfilling and estimations of loads onto the barricade

Numerical simulations on the fill stability of exposed fill masses were reported by Trollope et al. (1965) and Barrett et al. (1978). The first numerical model to simulate the hydraulic filling operation was developed by Isaacs and Carter in 1983 in ISAACS two dimensional package (Bloss 1992). Sivakugan et al. (2005) have verified the ISAACS numerical model for both two and three dimensional numerical modelling. Although Li and Aubertin (2008) have discussed the effect of stope width, stope height and material internal friction angle on the vertical stress variation, they have not included the effect of Poisson's ratio, which is not often considered in limit equilibrium analysis.

After the ore is removed, significant deformations would occur around the underground stope, under the ground stress conditions. These can be higher, where large horizontal stresses are experienced (For example Canadian shield possess horizontal stress of twice the vertical stress (Aubertin et al. 2003)). However it is considered that most of the ground deformations have occurred before backfilling and therefore a negligible amount of surrounding deformations may occur after backfilling as backfill acts as a bulking agent too. Veenstra (2013) has modelled the stope backfilling with paste fills and rock was modelled as a single layer in the simulations to match the pore

pressure variation with cement desiccation process. Therefore the surrounding rock boundary was assumed to be not deforming and the sliding boundary conditions were used to simulate symmetry axes.

The rock and backfill interface is the force transfer medium considered in arching and also with limit equilibrium analysis. Therefore, the realistic simulation of this boundary condition is essential. Fixed or hinged boundary condition between the fill and rock or interface elements can be used to simulate the rock and backfill interaction. Both fixed boundary conditions (Aubertin et al. 2003; Li and Aubertin 2009b), and the interface elements (Pirapakaran and Sivakugan 2007a; Fahey et al. 2009), have been used for numerical simulations of backfill. Veenstra (2013) has not included the interface reactions and assumed that the shear strength of paste is lower than the shear stress between the paste and rock. However, El Mkadmi et al. (2014) have confirmed that the interface elements would model the interaction at the interface with deformations. Although the shear failure occurs a tiny distance away from rock walls (Singh et al. 2010), the failure surface can be modelled with linear interface elements available in numerical simulation packages.

Degree of arching is dependent on the mobilization of shear stress. The stress reduction due to arching varies with the height and more specifically with height to width ratio. Arching greatly influences the stress states in filled stopes and sometimes the vertical stress reduces by 29.5% of the total overburden stress for narrow stopes (Fahey et al. 2009), and also by 60% of overburden stress in circular stopes (Pirapakaran and Sivakugan 2007a). Arching does not influence the stress state at undrained conditions or partially drained conditions. i.e. water needs to be drained and the effective stresses need to be developed to lower the vertical stress (Fahey et al. 2009). HFs are typically well drained and pore pressure becomes zero after few days (Mitchell et al. 1982), and hence they are expected to follow drained loading conditions, giving lower stress values than expected with overburden stress on a certain structure like barricade.

The loads in barricades can be estimated with analytical, numerical simulations and laboratory tests. Limit equilibrium of a vertical layer element is used in deriving the analytical equations and exponential reduction of barricade load with offset distance was observed with analytical equations (Kuganathan 2001; Li and Aubertin 2009a). Li and Aubertin (2009b) have presented a comprehensive analytical equation for the stress onto the barricade as,

$$\sigma_b = \left[\frac{h'}{H_d}.\sigma_{hT0} + \left(1 - \frac{h'}{H_d}\right).\sigma_{hB0}\right]\left\{exp - L.\frac{2\,tan\delta}{K_{dl}}\left(\frac{1}{H_d} + \frac{K_{dt}}{h'}\right)\right\} \qquad (2.2)$$

where, σ_b - lateral stress on barricade

σ_{hB0} , σ_{hT0} - horizontal stress at base and top of the stope entrance, respectively

h', H_d - height considered and total height of the drive respectively

L - offset distance of barricade from the stope entrance

K_{dl} - lateral pressure coefficient in longitudinal direction within the drive

K_{dt} - lateral pressure coefficient in transverse direction within the drive

Mitchell (1992) has conducted centrifuge tests to study the variation of barricade stresses and obtained the barricade stress variation when the barricade was at two different offset distances. Mitchell (1992) has modelled a stope of 0.2 m, 0.2 m and 0.35 m, wide, long and high respectively within a centrifuge. Mitchell (1992) tests are replicated in FLAC^{3D} and results from above three approaches are compared in Figure 2.6.

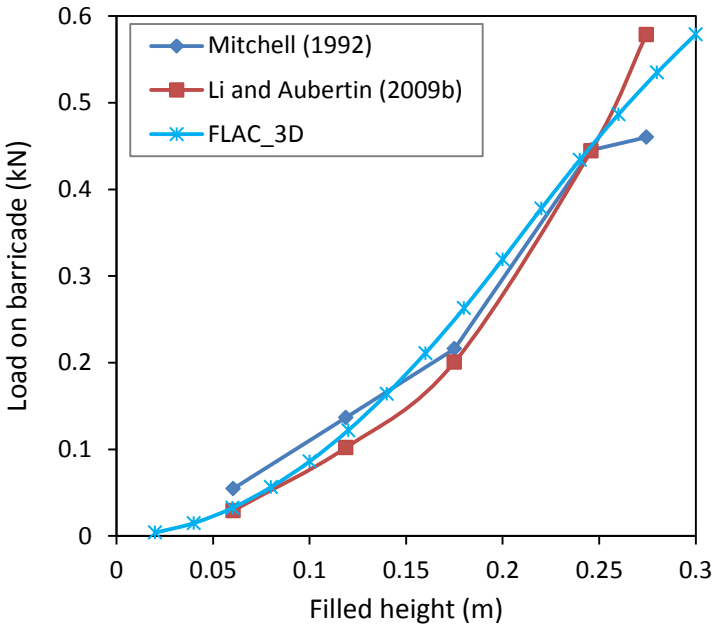

(a)

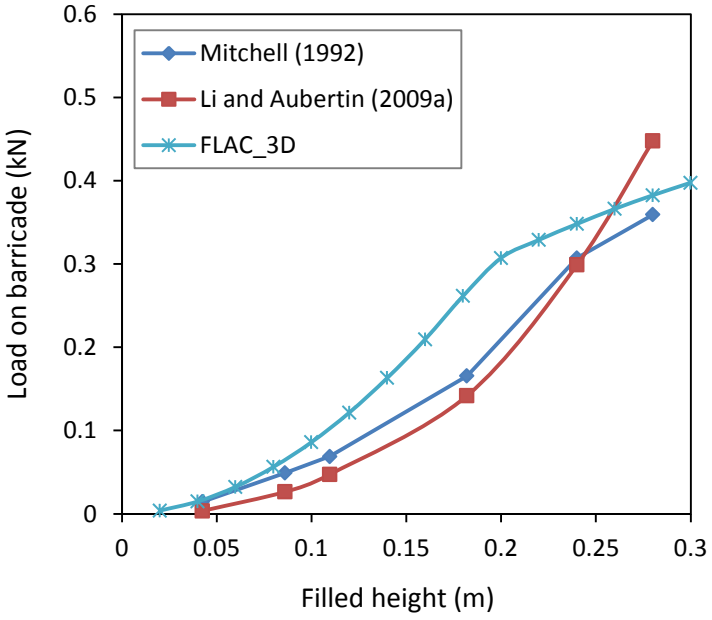

(b)

Figure 2.6. The barricade load variation with centrifuge tests (Mitchell 1992), analytical equations (Li and Aubertin 2009) and numerical simulations ($FLAC^{3D}$); (a) set back distance of 0 mm and (b) set back distance of 100 mm

In situ stress measurements of barricade stress have been conducted by researchers at University of Toronto (Thompson et al. 2009, Thompson et al. 2012) and one result is given on Figure 2.7. These measurements are valuable to understand the stress development mechanisms, but applicability is limited as these stress measurements are site and backfill specific.

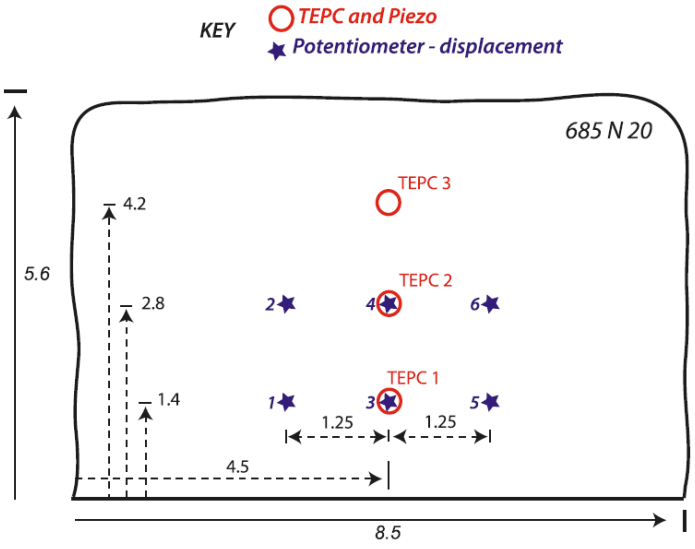

(a)

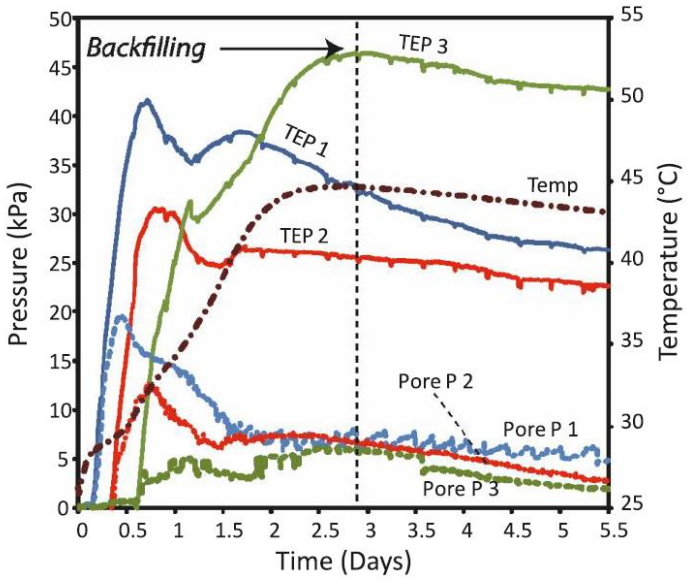

(b)

Figure 2.7. In situ measurements of barricade stresses at Cayeli Mine, when filled with CPB (from Thompson et al. 2012); (a) Total earth pressure cell and potentiometer locations and (b) Total earth pressure (TEP), pore-water pressure (Pore P) and temperature results

2.5 Arching within backfills

Arching can be interpreted as the reduction of stress due to relative movement of frictional material and as an opposing reaction to restrict the material movement (Handy 1985). The interaction of different materials with stiffness differences generates shearing with relative movements. Terzaghi (1943) explained arching by trap door experiments, observing a load increase on adjoining sand layers when trap door was released. When a granular material is placed in rigid containers or behind retaining walls, the shear stress between the wall and the granular material interface leads to arching and results in lower vertical stresses at any depth. Arching is beneficial to engineers since it reduces the effective stress acting on the structure (Mitchell et al. 1975; Take and Valsangkar 2001; Pirapakaran and Sivakugan 2007a).

Janssen (1985) conducted tests to measure the vertical load when a rectangular silo was filled with corn. The force from filling corn was counter-balanced with a scale at base and the weight indicated on scale is considered to be the vertical force felt at the bottom. Here, Janssen observed that the vertical stress reaching an asymptote and would not increase further after placing a surcharge on top of the structure. Janssen's results are summarised in Figure 2.8, and the unit weights and friction angles of corn were taken from Moya et al. (2002) results to normalise Janssen results. The Janssen's equation for vertical stress (σ_v) is given in Equation 2.3.

$$\sigma_v = \frac{\gamma B}{4Ktan\delta}\left[1 - exp\left(-\frac{4Ktan\delta\, z}{B}\right)\right] \tag{2.3}$$

where, γ – unit weight of the fill

B – width/ diameter of the structure

δ – interfacial friction angle

K - lateral pressure co-efficient

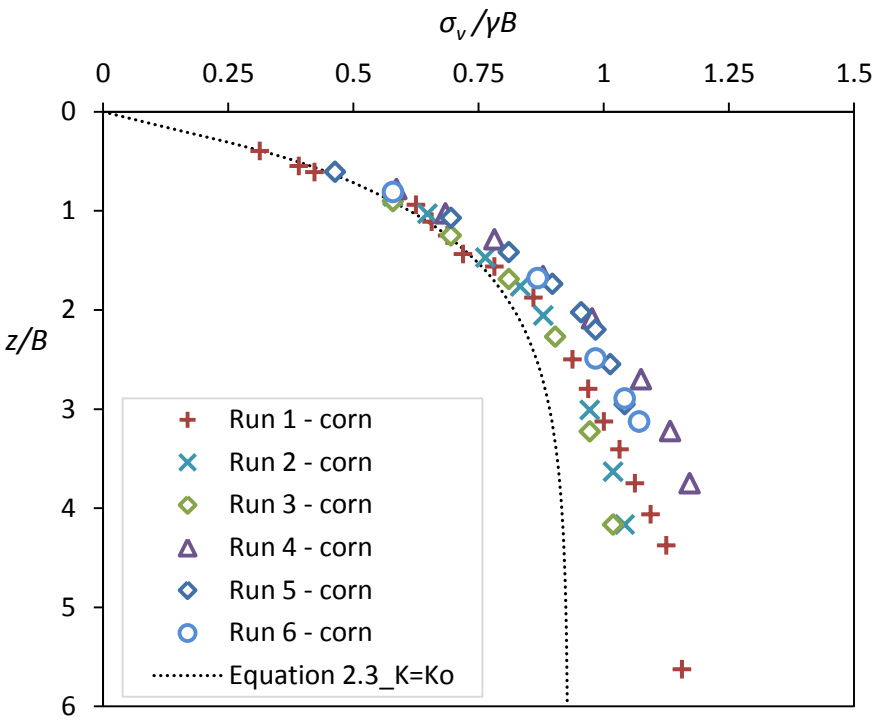

Figure 2.8. Vertical stress variation on a corn filled silo, as measured by Janssen 1895

The need to measure the loads onto ceramic drain pipes in backfilled trenches was increased with reported failures of clay drain pipes and therefore tests were carried out at Iowa College Engineering Experiment Station. Marston and Anderson (1913) have developed the equation on vertical stresses in backfilled tranches, acknowledging that Janssen (1895) has published the same equation (Equation 2.4).

Vertical stress (σ_v) at height z in a narrow backfilled trench or narrow filled structure is given by:

$$\sigma_v = \frac{\gamma B}{2Ktan\delta}\left[1 - exp\left(-\frac{2Ktan\delta\, z}{B}\right)\right] \qquad (2.4)$$

Marston and Anderson (1913) carried out tests with a shearing apparatus for clay, yellow clay and mixed clay to measure the interfacial friction. The cohesion was later highlighted by Scarino (2003) with re-calculations of shear test data from Marston and Anderson (1913). The cohesion would result in particle bonding as well as higher shear strength those lead to arching and ultimately for a vertical stress asymptote. Although Anderson and Marston (1913) observed a vertical stress asymptote with depth

for backfills in trenches, filling with a granular material will not have a considerable cohesion and the vertical stresses may be different from the Equation 2.4 proposed by Marston and Anderson (1913).

Janssen (1895) as well as Marston and Anderson (1913) made two assumptions that (1) the vertical stress is distributed uniformly over the horizontal cross section and (2) the vertical and horizontal stresses are principal stresses. In order to address the error of the first assumption, the uniform stress distribution, Walker (1966) introduced a distribution factor, which was defined as the ratio of the vertical stress at the wall to the average vertical stress over the horizontal layer element. Handy (1985) proved that the vertical and lateral stresses at a depth behind the retaining wall vary with the distance from the wall, friction angle (φ) and interface friction angle (δ). The inter-dependence of φ and δ, was incorporated by Singh et al. (2011) to formulate a circular arch condition in mine stopes and the relation between δ and φ was highlighted in their analytical derivation. The equation proposed by Handy (1985) could be used to calculate the vertical stress at the centre and the average vertical stress when a structure (a retaining wall or a bin silo) is backfilled. The second assumption considering the vertical and horizontal stresses as the principal stresses is incorrect as the shear stresses must be zero at the principal planes. This has been addressed by Jaky (1944) and Krynine (1945) and will be further discussed later in this chapter.

Handy (1985) considered that minor principal direction of a horizontal layer element forms a catenary shaped arch. Also, Singh et al. (2011) developed an analytical equation to calculate the vertical stress at a point using a circular arch for the minor principal stress. Moreover, Singh et al. (2011) showed that the proposed analytical equation matched Handy's (1985) equation and hence the effect of considering the minor principal stress directions as circular or as a catenary of a horizontal layer element is negligible. However, with further analysis it is noticed that Singh et al. (2011) analytical equation matches Handy's (1985) equation if the δ is less than φ. But

Singh et al. (2011) equation shows a deviation from Handy's (1985) equation when $\delta = \varphi$ (fully rough walls) (Figure 2.9).

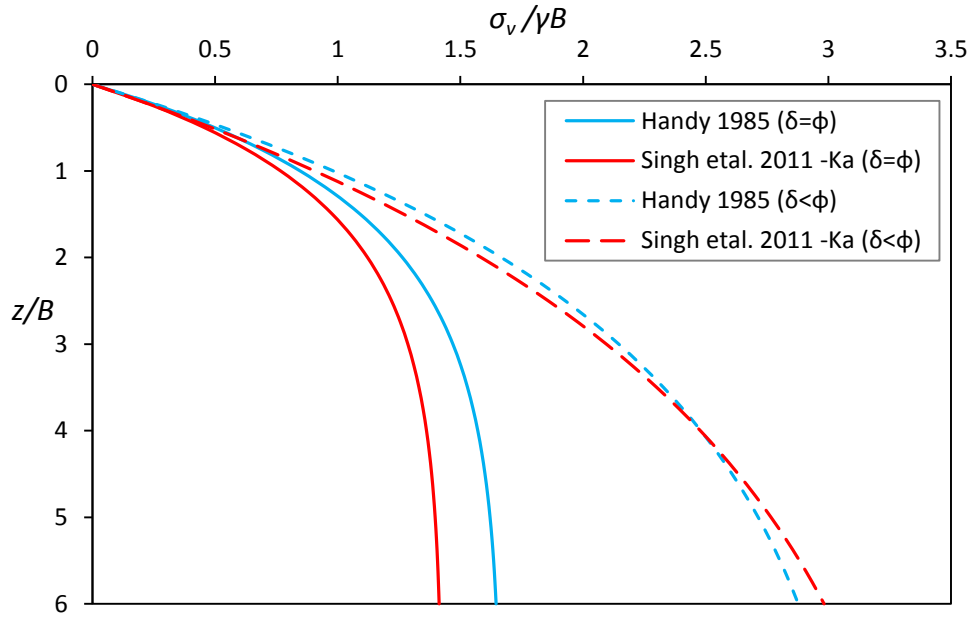

Figure 2.9. Maximum vertical stress variation from Handy (1985) and Singh et al. (2011) equations

Later, Ting et al. (2012b) assumed that a fixed portion of fill load from the overlying layer is transferred to walls and the rest of the load is transferred to the layer below. The summation of vertical loads was calculated with Simpson's triangle method and Equation 2.5 was proposed by Ting et al. (2012b);

$$\sigma_v = \gamma h \frac{(1-x)}{x}[1-(1-x)^m] + q(1-x)^m \tag{2.5}$$

where the fill is divided into m layers of thickness h, and q is the surcharge pressure at the top of the fill. The value of x is given by;

$$x = \frac{\psi}{1+\psi} \tag{2.6}$$

where $\psi = \frac{2Kh\tan\delta}{B}$ for long strips or narrow stopes.

The Equation 2.5 proposed by Ting et al. (2012b) converges to Marston's equation (Marston and Anderson 1913) when a large number of layers are considered.

The Equation 2.3, Equation 2.4 and modifications to those equations are based on the limit equilibrium analysis and are considered as the arching theory herein.

2.5.1 In situ and model stress measurements

A few lateral stress measurement results related to coal (Blight 1986) and barley filled silos (Hartlen et al. 1984) are given in Figure 2.10 along with estimations from arching theory when $K = K_0$ and $K = K_a$.

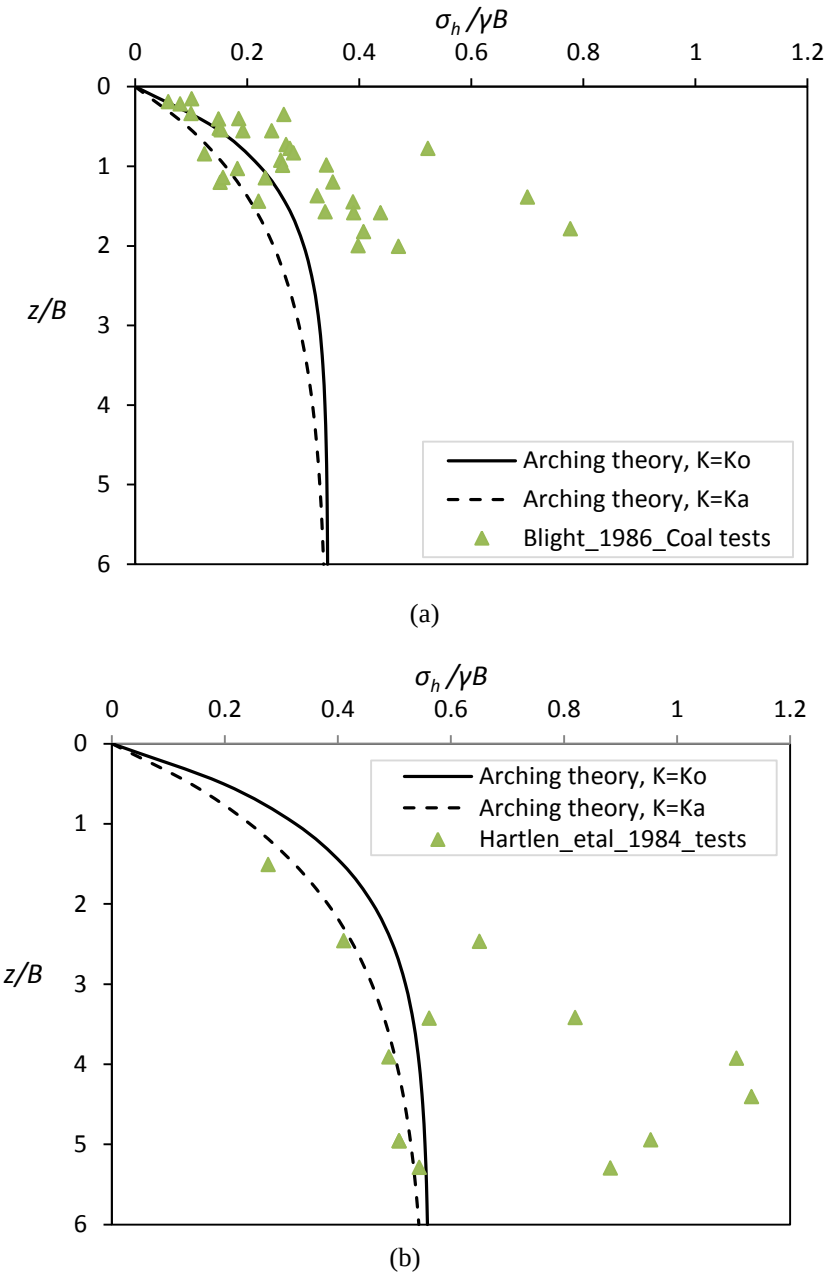

Figure 2.10. Lateral stress measurement within silos; (a) when filled with coal and (b) when filled with barley

Laboratory models to study arching have been developed for vertical structures (Pirapakaran and Sivakugan 2007b) as well as for inclined structures (Ting et al. 2012a). Pirapakaran and Sivakugan (2007b) filled 100 mm and 150 mm wide square and circular stopes with minefills and the average vertical stress at bottom was obtained as the stope is filled. In contrast, Ting (2011) filled a 100 mm wide and 500 mm long inclined rectangular stope and obtained the average vertical stress variation when the stope is filled with sand. The schematic of the stope used by Ting (2011) is shown in Figure 2.11. Also the vertical stress variation obtained by Ting (2011) for a vertical stope with rough walls is given in Figure 2.11.

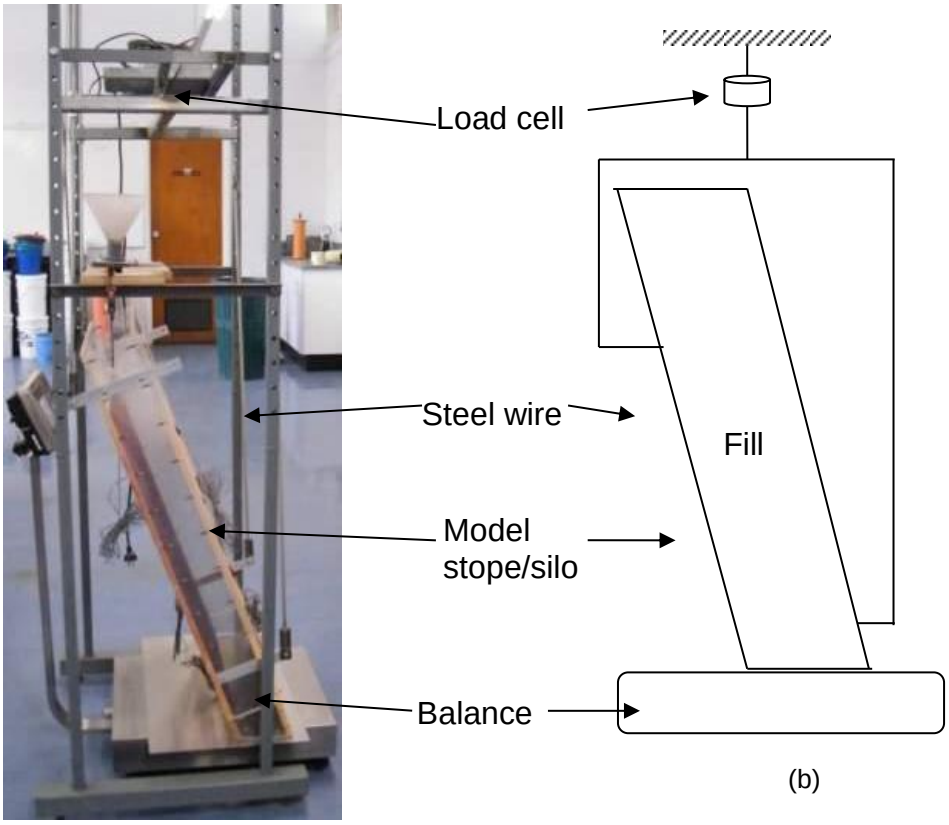

Figure 2.11. The Laboratory test setup to model the average stress variation used by Ting et al. 2012; (a) photograph and (b) schematic diagram (Ting 2011)

The average vertical stress for a sand filled rectangular stope varies within the estimates of the arching theory ($K = K_a$ and $K = K_0$ (Figure 2.12)). Additionally, the

average vertical stress in a backfilled rectangular stope seems to increase with the depth, not reaching an asymptote as estimated by the arching theory (Figure 2.12).

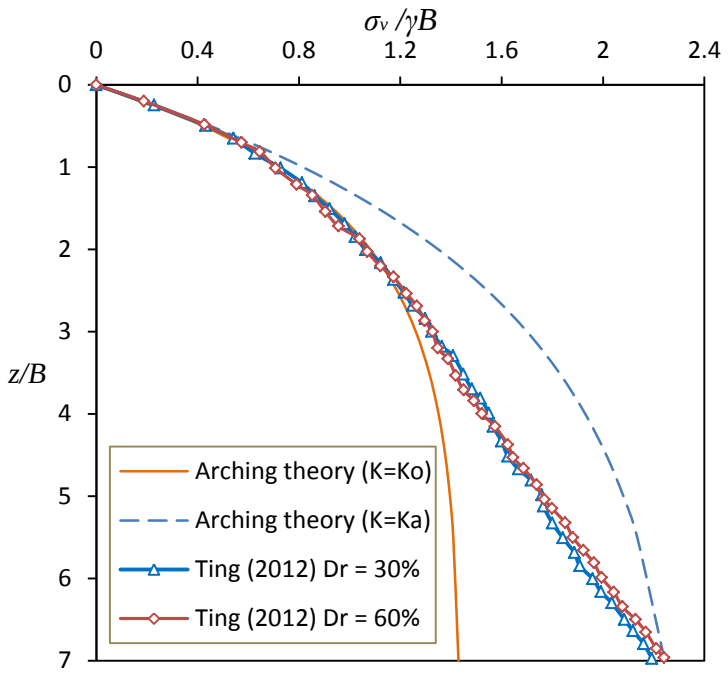

Figure 2.12. Average vertical stress variation for a rectangular stope backfilled with sand, as obtained by Ting (2011)

The vertical stress as well as horizontal stress within a granular filled structure varies in a range, which is not often estimated with the arching theory (Figure 2.9 and Figure 2.11). Although many theoretical improvements were suggested to the arching theory, the widely scattered pressure measurements could not be explained (Vanel and Clément 1999). The assumptions used in the arching theory and the continuum approach are the leading causes to these deviations and the factors are discussed in next sections in this chapter.

2.5.2 Assumption of uniform stress

The arching theory tends to underestimate the vertical loads (Lenczner 1963; Pirapakaran and Sivakugan 2007b). Shear stresses result in greater load transfered to walls and therefore the vertical stress is minimized near the wall and maximised at the centre. Hence, the predicted average vertical stress with these analytical expressions may be less than the actual vertical stress at centre, and this was noted by Janssen

(1895) and many others. For example, Talesnick (2005) measured the vertical stress and showed that if a uniform pressure of 100 kPa was applied, the vertical stress at the centre was 95 kPa, but at a distance of 300 mm, the vertical stress was 66 kPa. Therefore, the lateral variation of vertical stress needs to be considered.

2.5.3 Lateral pressure coefficient

Theoretically, the lateral pressure coefficient is defined for a point within a soil mass. But with classical equations, the ratio of the horizontal stress at wall to the average vertical stress at bottom was taken as *K*, which is not defined at a point. Bishop (1958) defined the lateral pressure coefficient at rest, K_0 as "the ratio of the lateral to the vertical effective stresses in a soil consolidated under the condition of no lateral deformation, the stresses being principal stresses with no shear stress applied to the planes on which these stresses act". El-Sohby and Andrawes (1972) have modified this definition to remove any effects due to the history by expressing the horizontal to vertical stress ratio in terms of stress increments.

The backfill is defined to be in "at rest condition" when there are no lateral strains within a backfill, and the lateral pressure coefficient for this condition is K_0. K_0 reflects soil characteristics and stress history. Higher K_0 values are observed in loose soils (Mesri and Hayat 1993). Jaky (1944) considered earth pressures in granular piles and suggested that for cohesionless soils the earth pressure coefficient at rest is given by $Ko = 1 - sin\varphi$. Sometimes 'at rest condition' is not applicable to the backfills, as the 'at rest condition' is defined for zero lateral strain. However, Take and Valsangkar (2001) assumed K_0 to be independent of mobilized interfacial friction angle, and observed that K_0 matched Jaky's (1944) equation. Later, Brooker and Ireland (1965) have shown that this K_0 ratio is more suitable to be used for cohesionless materials. On the contrary, the expression for the stress ratio in backfilled situations has not been verified and also Federico et al. (2008) noted that there is no satisfactory method that has been developed to measure K_0 in soil, either from in situ or reconstituted samples.

Moreover, so far no experimental evidence to support Jaky's (1944) formula has been presented that are related to cohesionless granular material stored between vertical walls (Michalowski 2005).

When a material is filled between rigid walls, sometimes the fill produces significant strains causing the walls to move outwards. Rankine's active earth pressure coefficient (K_a) value applies to the backfills, mostly in retaining walls and retaining structures, where a significant lateral movement to outward of wall is experienced. However, backfills within rigid walls may not generate large lateral strains that can develop active or passive states. K_a has proven to be successful in estimating stresses with cantilever retaining walls (Bentler and Labuz 2006). Moreover, Li and Aubertin (2009b) have observed that $K = K_a$ in arching theory gives reasonable estimates of vertical stresses when the backfilling is numerically simulated with FLAC.

Krynine (1945) derived a formula for horizontal to vertical stress ratio using Mohr's circle (Figure 2.13). The lateral pressure coefficient suggested by Krynine (1945) is termed as $K_{krynine}$ herein. Trapdoor experiments with a centrifuge conducted by Iglesia et al. (2014) suggested that the horizontal and vertical stresses are not to be considered as the principal stresses. Also, Iglesia et al. (2014) have endorsed the $K_{krynine}$ expression (Equation 2.6).

$$K_{krynine} = \frac{1}{1+2\tan^2\phi} = \frac{1-\sin^2\phi}{1+\sin^2\phi} \tag{2.6}$$

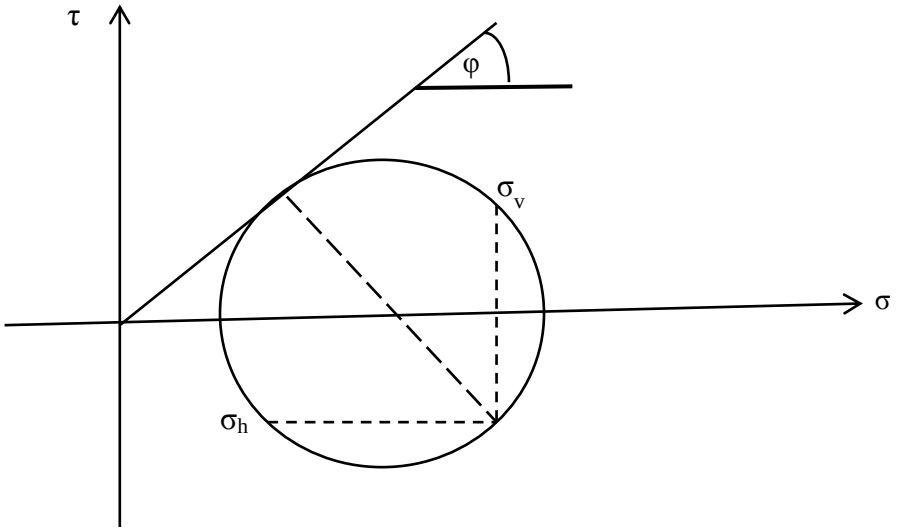

Figure 2.13. The use of Mohr's circle to define the lateral pressure coefficient as suggested by Krynine (1945)

A significant lateral strain is required to mobilise active or passive state in soil mechanics (Blight 1990; Das 2010). Moreover, the filling to the containment with rigid walls would not induce any horizontal strains, rather only vertical strains as the granular material rearrange with the pressure from overlying materials. Therefore, often a range of $K\tan\delta$ is used with the arching theory.

2.5.4 The use of $K\tan\delta$ as a measure of arching

$K\tan\delta$ provides a good measurement and both terms are derived from the internal friction angle. Janssen (1895) measured the $K\tan\delta$ in the range of 0.21 to 0.23. Marston and Anderson (1913) mentioned that the calculated values for $K_a\tan\delta$ varies between 0.190 to 0.193. Additionally, Singh et al. (2010) showed that the $K\tan\delta$ value does not vary with the friction angle. The use of K_a with stress estimations with backfills has been subjected to arguments over the years, as significant displacement is required to achieve the active lateral pressures and therefore it is erroneous to assume the material filled in silos or mine stopes are neither in active conditions nor passive conditions. However, $K\tan\delta$ varies in a narrow range because when friction angle

increases the lateral earth pressure coefficient K decreases and tan δ increases such that there is very little change in K tanδ. Therefore, the use of Ktanδ is suitable with backfilling applications.

The K value has posed a question for designers who estimate the stress on backfilled structures whether to use K_0 or K_a or any other value. Sometimes a range of K values are recommended (For example K = 0.33- 0.5 (Butterfield 1969)). Most likely these theoretical K values would give lower bound estimation of the vertical stress (Butterfield 1969). For most uncemented tailings the K varies in the range of 0.3 to 0.5 (Helinski 2007). For loosely packed granular material, K_0 ranges from 0.5 to 0.6, while for dense granular material K_0 varies from 0.3 to 0.5 (McCarthy 2007). Also Pirapakaran and Sivakugan (2007a) suggested that considering $K = K_0$ with $\delta = 0.67\ \varphi$ in arching theory would match the average vertical stress variation obtained from FLAC numerical simulations. Furthermore, Ting (2011) suggested that either $K = K_0$ with $\delta = 0.67\ \varphi$ or $K = K_a$ with $\delta = \varphi$ in analytical equations would match the numerical simulation results related to inclined backfilled structures.

Chapter 3

Vertical Stresses in Vertical Containments

3.1 General

In underground mining, granular backfills such as hydraulic fills (HF) are placed in square or rectangular stopes, where the stress variation with depth is similar to that in a silo. Understanding the vertical as well as horizontal stress distribution, in vertical containments, is necessary for sound geotechnical designs. Proper understanding of vertical stresses will improve design criteria for above mentioned containments and related structures. Terzaghi (1920) mentioned that these earth pressure problems are better solved experimentally than analytically and also the simplifications made in analytical formulations are too unrealistic and therefore might have an impact on the stress estimations. This study aims to identify the vertical stress variation when a container of uniform cross section filled with granular material and how the variation is influenced by the width, shape of the container and wall roughness conditions. The laboratory setup was developed such that filling can be conducted in layers and the average vertical stress at the bottom and horizontal stress on walls could be obtained. Model laboratory tests, were undertaken and test results were compared to arching theory and numerical simulations. Additionally, numerical simulations related to backfilling are discussed in detail and two ways of interpreting vertical stresses from numerical simulations are discussed.

Determining the vertical stresses within the HFs is necessary for designing the barricades that block the drives, when underground mine stopes are backfilled. Noting the difficulties associated with the in situ measurement of stresses within backfills, numerical modelling appears to be an effective tool in understanding the stress conditions within the backfill. Laboratory models have been used in the past for validating the numerical models and analytical equations.

3.2 Generalised Marston's equation

The well established analytical equations, derived with shear plane method, are introduced by Janssen (1895) for silos and Marston and Anderson (1913) for backfilled narrow trenches. Thereafter, Terzaghi (1943) included cohesion to the arching equation. The equation has been applied for trap door problem (Ladanyi and Hoyaux 1969), backfilled narrow trenches (Handy 1985; Harrop-Williams 1989), retaining walls (Frydman and Keissar 1987; Take and Valsangkar 2001), backfilled narrow mine stopes (Aubertin et al. 2003) and modified for square and rectangular mine stopes (Li et al. 2005; Pirapakaran and Sivakugan 2007a). The approach presented herein can be used to estimate stress for any stope shape without additional equations.

An analytical expression for the average vertical normal stress (σ_v), for incompressible, backfill contained within vertical walls, is derived from the first principles. For generality, the fill is assumed to have both cohesive and frictional properties, and a uniform surcharge (*q)* is included at the top of the fill. The fill-wall interface has friction angle of δ and adhesion of c_a. The fill wall interface friction is assumed to be fully mobilised on entire height in this derivation. The general expression (Equation 3.11) is further simplified into special cases with different cross sections and for cohesionless granular fills ($c_a = 0$).

Fill contained within four vertical walls is shown in Figure 3.1a. The dimensions of the container are *B*, *L* and *H* for width, length and depth respectively. Depth is measured from the top of the fill, and a thin layer element of thickness *dz* at a depth of *z* is isolated showing the free body diagram (Figure 3.1b). Let the perimeter length of the element be *P* and the horizontal cross- sectional area be *A*, for the considered layer element.

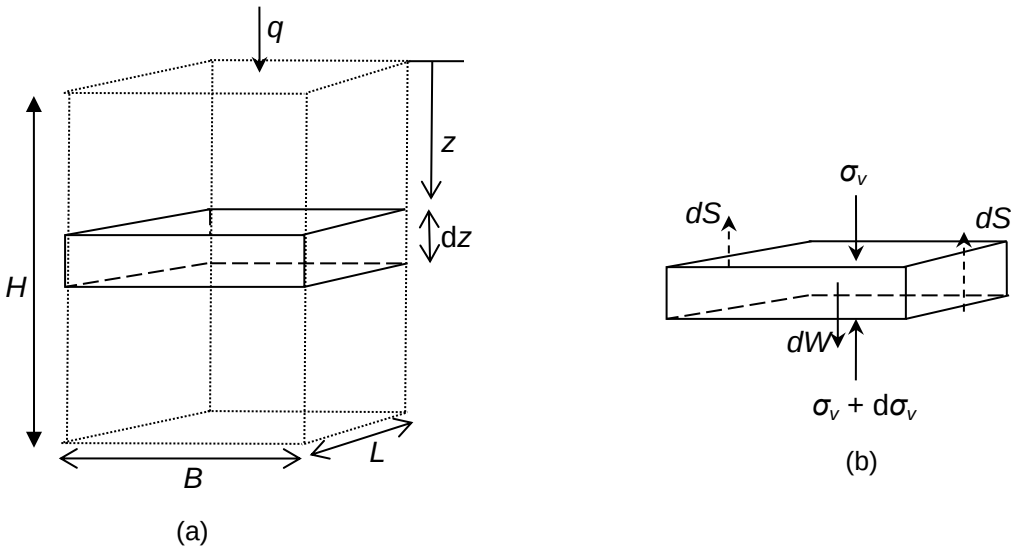

Figure 3.1. Schematic diagram to derive analytical equations for stress within a backfilled stope; (a) backfilled stope dimensions and (b) isolated horizontal layer element

The weight of the layer element, $dW = \gamma A\, dz$ (3.1)

The shear load on the layer element, $dS = (K\sigma_v \tan\delta + c_a)\, Pdz$ (3.2)

For equilibrium of layer element (Figure 3.1b),

$$\sigma_v\, A + \gamma A\, dz = (\sigma_v + d\sigma_v)A + (K\ \sigma_v \tan\delta + c_a)P\, dz \quad (3.3)$$

$$d\sigma_v = \gamma\, dz - (K\ \sigma_v \tan\delta + c_a)\frac{P}{A}dz \quad (3.4)$$

$$\frac{d\sigma_v}{dz} = \left(\gamma - \frac{P}{A}c_a\right) - \left(K\tan\delta\frac{P}{A}\right)\sigma_v \quad (3.5)$$

Let $X = \gamma - \frac{P}{A}c_a$ and $Y = K\ tan\delta\frac{P}{A}$, both of which are constants that depend on the dimensions and fill parameters, to simplify next few steps.

Therefore,

$$\frac{d\sigma_v}{dz} = X - Y\sigma_v \tag{3.6}$$

$$\int_q^{\sigma_v} \frac{d\sigma_v}{X - Y\sigma_v} = \int_0^z dz \tag{3.7}$$

$$\left[-\frac{1}{Y}\ln(X - Y\sigma_v)\right]_q^{\sigma_v} = [z]_0^z \tag{3.8}$$

$$\therefore \frac{X - Y\sigma_v}{X - Y\,q} = e^{-Yz} \tag{3.9}$$

$$\sigma_v = \frac{X}{Y}(1 - e^{-Yz}) + \; q\, e^{-Yz} \tag{3.10}$$

i.e., the general expression for the average vertical stress at depth *z* becomes:

$$\sigma_v = \frac{\left(\gamma - \frac{P}{A}c_a\right)}{\left(K\tan\delta\frac{P}{A}\right)}\left(1 - e^{-K\,tan\delta\frac{P}{A}z}\right) + \; q\, e^{-K\,tan\delta\frac{P}{A}z} \tag{3.11}$$

where, the first component on the right hand side of the equation comes from the self-weight of the fill and the second component comes from the surcharge. The terms A and P depend on the cross section of the stope. Analytical equations for often used cross sectional shapes are simplified from Equation 3.11 as follows;

Case 1: Rectangular cross section, $P = 2(L + B)$, and $A = LB$

For the rectangular stope shown in Figure 3.1a, *A* = *BL* and *P* = 2(*B*+*L*). Substituting these values in Equation 3.11;

$$\sigma_v = \left(\frac{\gamma BL - 2c_a(B + L)}{2K(B + L)\tan\delta}\right)\left(1 - e^{-K\,tan\delta\left[\frac{2(B+L)}{BL}\right]z}\right) + \; q\, e^{-K\,tan\delta\left[\frac{2(B+L)}{BL}\right]z} \tag{3.12}$$

When the backfill is cohesionless (i.e. c_a = 0) and if there is no surcharge;

$$\sigma_v = \left(\frac{\gamma BL}{2K(B+L)\tan\delta}\right)\left(1 - e^{-K\tan\delta\left[\frac{2(B+L)}{BL}\right]z}\right) \quad (3.13)$$

Case 2: Square cross section, where L = B, A = B^2

$P = 4B$, and $A = B^2$, $\frac{P}{A} = \frac{4}{B}$

$$\sigma_v = \left(\frac{\gamma B - 4c_a}{4K\tan\delta}\right)\left(1 - e^{-K\tan\delta\left[\frac{4}{B}\right]z}\right) + q\, e^{-K\tan\delta\left[\frac{4}{B}\right]z} \quad (3.14)$$

When the backfill is cohesionless and if there is no surcharge,

$$\sigma_v = \left(\frac{\gamma B}{4K\tan\delta}\right)\left(1 - e^{-K\tan\delta\left[\frac{4}{B}\right]z}\right) \quad (3.15)$$

Case 3: For a circular cross section with diameter B

$P = \pi B$and $A = \pi\left(\frac{B}{2}\right)^2$, $\frac{P}{A} = \frac{4}{B}$

$$\sigma_v = \left(\frac{\gamma B - 4c_a}{4K\tan\delta}\right)\left\{1 - e^{-K\tan\delta.\left(\frac{4}{B}\right)z}\right\} + q.e^{-K\tan\delta.\left(\frac{4}{B}\right)z} \quad (3.16)$$

The Equation 3.16 for the average vertical stress in circular containment is same as, for circular cross sections with diameter of *B* (Equation 3.14).

Case 4: Narrow trench where L >> B, A = BL and P = 2(B+L) and P/A ≈2/B

$P = 2(B+L) \sim 2L$, and $A = LB$. Therefore, $\frac{P}{A} = \frac{2}{B}$

$$\sigma_v = \left(\frac{\gamma B - 2c_a}{2K\tan\delta}\right)\left(1 - e^{-K\tan\delta\left[\frac{2}{B}\right]z}\right) + q\, e^{-K\tan\delta\left[\frac{2}{B}\right]z} \quad (3.17)$$

When the backfill is cohesionless and if there is no surcharge,

$$\sigma_v = \left(\frac{\gamma B}{2K\tan\delta}\right)\left(1 - e^{-K\tan\delta\left[\frac{2}{B}\right]z}\right) \quad (3.18)$$

The main contributors to vertical stress in cohesionless granular filled containments are γ, K, δ, B, and z as in Equations 3.13, 3.15 and 3.18. The vertical stress can be expressed in dimensionless form ($\sigma_v/\gamma B$), after normalizing with the overburden stress, and the normalized vertical stress is a function of K, δ and z/B.

$$\frac{\sigma_v}{\gamma B} = \left(\frac{1}{2K\tan\delta}\right)\left(1 - e^{-2K\,tan\delta\left[\frac{z}{B}\right]}\right) \tag{3.19}$$

3.3 Setup and material description

A simple laboratory model stope is developed at James Cook University (JCU) geomechanics laboratory to study the effects of arching and vertical stresses within the granular fill by Pirapakaran and Sivakugan (2007b). That setup was used with the tests described herein and few modifications were introduced, such as calculation of shear forces and horizontal stresses on wall after each layer of fill was added. A container of uniform cross section, referred to as 'the stope' from here onwards, was made out of Perspex. Figure 3.2a shows the photograph of the laboratory model stope/silo setup and a schematic diagram is shown in Figure 3.2b. The stope was held vertically by three equally spaced supports (Figure 3.2). The supports were attached to a load cell (Revere Transducers, type 9363-D3-100kg_20T1; precision 0.001 kg), which was connected to the frame. Therefore, the load of the setup was measured with the load cell. The model was lowered until it just touches the balance, without registering any load on the electronic balance (maximum reading 60 kg, precision 0.005 kg). There was a tiny gap (less than a grain size) between the bottom of the model walls and the balance. When the model stope was filled, a part of the fill mass is carried by the base (i.e., the balance) and the rest is transferred to the wall (i.e. the load cell). In other words, the load cell registers the initial mass of the setup and the mass of the fill transferred to the walls. The apparatus has been described in detail by Pirapakaran and Sivakugan (2007b). Tests

were performed on circular, square and rectangular cross sectional stopes, with widths of 100 mm and 150 mm in this dissertation.

The weight of sand (relative density = 30%) required to fill the model structure was calculated and the model was filled in 12 layers. The maximum and minimum dry densities were calculated with relevant Australian standards (AS1289.5.5.1 1998) and tabulated in Table 3.1. The filling was carried out by keeping the funnel at a fixed height, to maintain uniform relative density and replicate the filling conditions on field. After each stage of filling, the readings from the balance and load cell were checked, whether the sum of the load on the load cell and bottom scale, matches the weight of poured sand. As the fill load was shared by the balance and the load cell, this check confirmed the performance of the apparatus after each stage of filling.

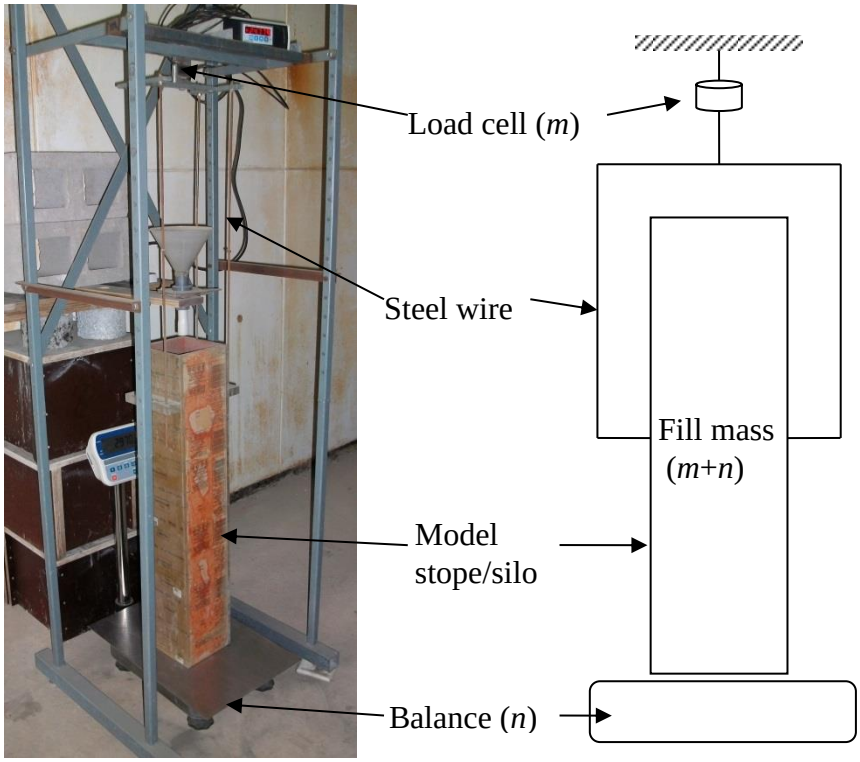

Figure 3.2. Laboratory test setup; (a) photograph and (b) schematic diagram

The grain size distribution of sand and HFs was determined from Malvern Mastersizer X instrument and the shown in Figure 3.3. The median grain diameter (D_{50}), effective grain size (D_{10}), coefficient of uniformity (C_u) and coefficient of curvature (C_c), are also tabulated in Table 3.1. According to USCS, the sand would be classified as poorly graded uniform sand, with symbol of *SP*, and the HF can be categorised as silty sand with symbol of *SM*.

The interface characteristics depend on wall roughness and internal friction angle of the material being stored. The effective friction angle of sand was determined with direct shear test (AS1289.6.2.2 1998) in the laboratory at a relative density of 30% (Table 3.1). Two different wall roughness conditions were used to study the wall roughness as: (i) medium rough walls - Perspex, (ii) rough walls - glued sandpaper [KMCA Garnet G62 P40 Garnet electro coated dry sanding abrasive paper]. Interfacial friction angles were determined in laboratory by replacing the lower half of the direct shear box by a Perspex block or sand paper glued to Perspex block (Ting et al. 2012a). The interfacial friction angles, for selected wall roughness conditions, are also tabulated in Table 3.1.

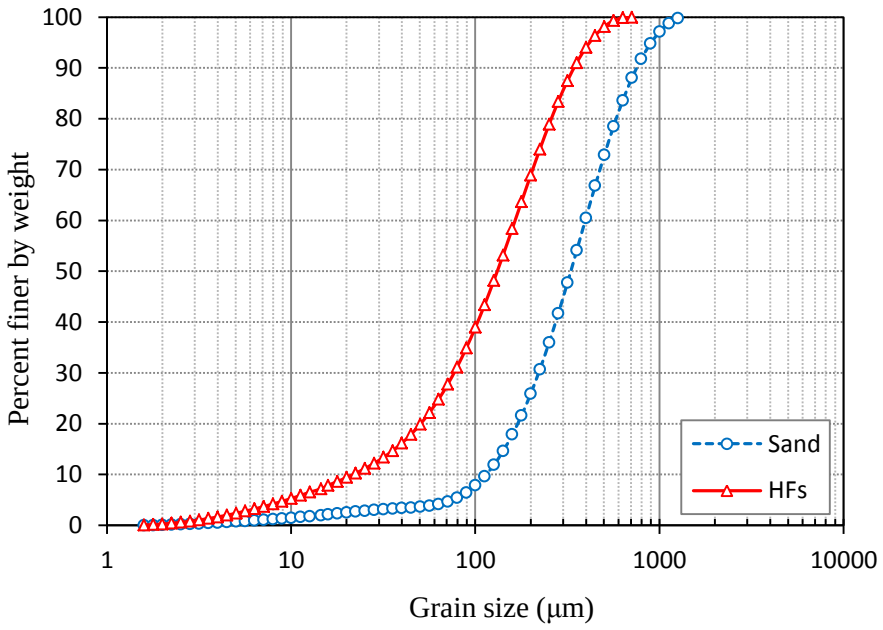

Figure 3.3. Grain size distribution for sand and HFs, obtained from Malvern Mastersizer-X instrument

Table 3.1.Geotechnical properties for hydraulic fills and sand

Property	**Hydraulic Fills**	**Sand**
Median grain diameter, D_{50} (mm)	0.132	0.335
Effective grain size, D_{10} (mm)	0.021	0.115
Coefficient of uniformity (C_u)	7.71	3.43
Coefficient of curvature (C_c)	1.69	1.08
Minimum dry density (kg/m^3)	1540	1430
Maximum dry density (kg/m^3)	2175	1676
Specific gravity	3.12	2.58
Peak friction angle, φ (°)	39.3	38.2
Interfacial friction angle, medium rough walls, δ (°)	23.1	22.9
Interfacial friction angle, rough walls, δ (°)	38.8	37.5

3.4 Data interpretation

Filling of a new layer into the model, will incur the load to be transferred to the wall and to the bottom. When the model is filled with a granular fill of weight $m+n$, the load cell reads the fill load transferred to the wall (m) and the balance reads the fill load transferred to the bottom (n) (Figure 3.4). At any stage of filling, m and n can be measured separately through this setup. The layers are numbered from the top to bottom at any stage of filling, such that subsequent changes to the system with additional layers are represented by lower layers. The test procedure and the interpretation of the shear and normal stresses are discussed below.

To explain the interpretation, a simple example is considered where a model with vertical walls is being filled in 10 equal layers (Figure 3.4). Each layer has a wall-fill contact area of A_w and inner cross sectional area of A as shown in Figure 3.4a. Figure 3.4b shows that first six layers filled and m_6 and n_6 are the fill loads transferred to the wall and the base, respectively, as recorded from the load cell and the balance. The total weight of the fill contained within the six layers is $m_6 + n_6$. Figure 3.4c shows the first seven layers, where m_7 and n_7 are the fill loads transferred to the wall and the base,

respectively. As the addition of a new layer spreads the further load to the wall, it is expected that $m_7 > m_6$.

3.4.1 Shear stresses along the wall:

When the first six layers are placed, m_6 is the wall load carried by the six wall segments attached to layers 1 to 6 (Figure 3.4b). When the next layer is placed, m_7 is the wall load carried by the seven wall segments attached to layers 1 to 7 (Figure 3.4c). Therefore, $m_7 - m_6$ is the load on wall with the addition of 7th layer, and this load has to be carried entirely by the wall section next to layer 7.i.e. the shear force generated from layer 7 is $m_7 - m_6$. Therefore, the shear stress τ_7 at the wall surrounding the layer 7 can be determined as:

$$\tau_7 = \frac{m_7 - m_6}{A_w} \tag{3.20}$$

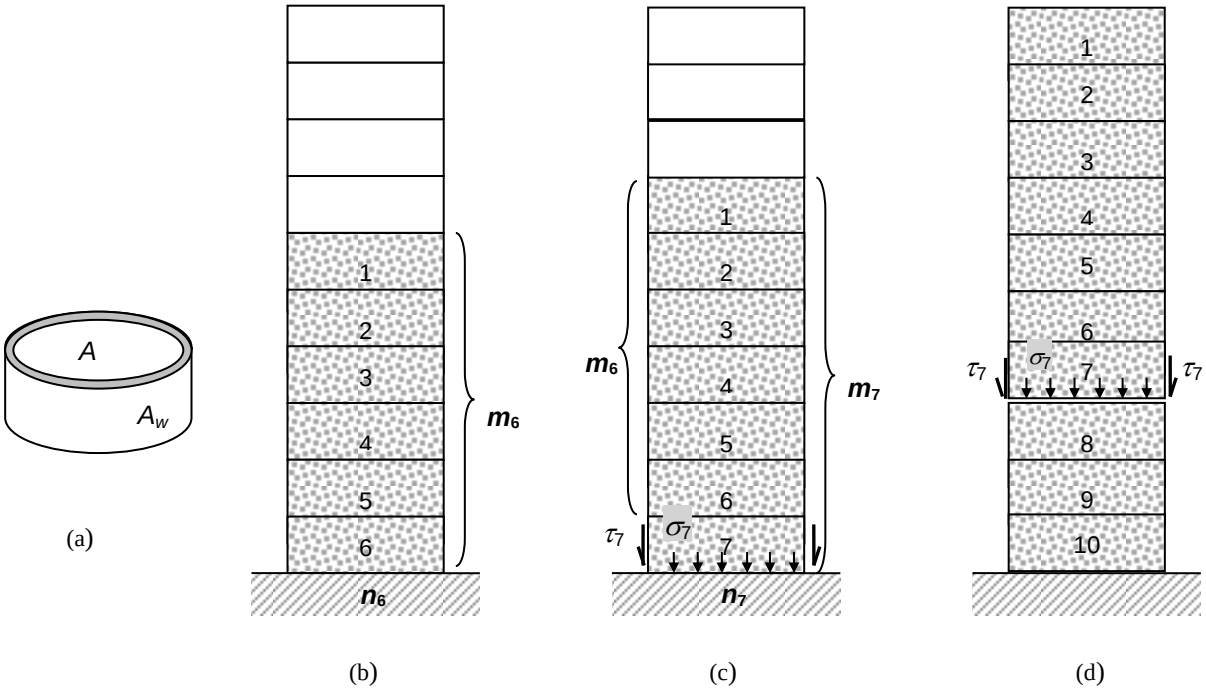

Figure 3.4. Detailed interpretation of calculations: (a) one layer, (b) after 6 layers, (c) after 7 layers, and (d) after all 10 layers

The shear stresses on each wall section can be obtained experimentally with this procedure as τ_1, τ_2, τ_3, τ_4 and others. Therefore, if the layer number is taken as i, the following generalised equation can be used to calculate the shear stress for each layer.

$$\tau_i = \frac{m_i - m_{i-1}}{A_w} \tag{3.21}$$

Additionally, if the interfacial friction angle is δ and the wall friction is fully mobilised, the horizontal stress on walls can be calculated as:

$$\sigma_{hi} = \frac{\tau_i}{\tan \delta} \tag{3.22}$$

3.4.2 Average normal stress at the base:

While the total effective wall area changes with addition of layers, the A remains the same for computing the normal stress at the base. From Figures 3.4b and 3.4c, it can be seen that n_7- n_6 is the load from layer 7 transferred to the base. The total load from the layers 1 to 7, to the base, is n_7. Therefore, the normal stress at the bottom, after filling the layer 7, is given by:

$$\sigma_7 = \frac{n_7}{A} \tag{3.23}$$

This is the same for the layer 7 within the filled vessel shown in Figure 3.3d. Accordingly, the normal stress at the bottom can be calculated with addition of each layer as σ_1, σ_2, σ_3 and the others. Therefore, the generalised equation for normal stress at the base is:

$$\sigma_i = \frac{n_i}{A} \tag{3.24}$$

The normal and shear stress values can be determined at any depth of the model, when the model is filled in layers. The model is considered to be vertical and the equations are valid for shapes other than circular and rectangular cross sections. The computations of normal and shear stresses in a laboratory model test are illustrated

through a numerical example (Table 3.2). Furthermore, Figure 3.5 details the variation of normalised vertical, horizontal and shear stress variation as calculated in Table 3.2. Note that this scheme can be extended for inclined stopes, but the Equations 3.21, 3.22 and 3.24 need to be modified.

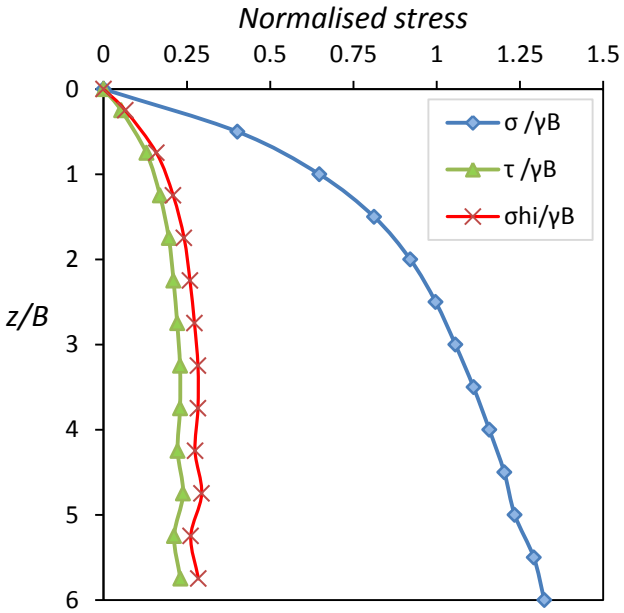

Figure 3.5. Variation of normalised vertical, shear and horizontal stress according to Table 3.2

Table 3.2. Laboratory model test data and derived vertical, shear and horizontal stress values for 150 mm x 150 mm x 900 mm stope

Filling step, i	Load cell reading	Mass on load cell (kg)	Initial mass of setup (kg)	Mass on walls, m_i (kg)	Mass on base, n_i (kg)	σ_i (kPa)	τ_i (kPa)	$\sigma_i/\gamma B$	$\tau_i/\gamma B$	$\sigma_{hi}/\gamma B$
0	-20.08	9.77	9.77	0.00	0	0.00	0.00	0.00	0.00	0.00
1	-19.26	10.33	9.77	0.56	2.11	0.93	0.12	0.40	0.05	0.07
2	-17.27	11.67	9.77	1.91	3.4	1.50	0.30	0.65	0.13	0.16
3	-14.65	13.45	9.77	3.68	4.26	1.87	0.39	0.81	0.17	0.21
4	-11.62	15.50	9.77	5.74	4.83	2.13	0.45	0.92	0.20	0.24
5	-8.37	17.71	9.77	7.94	5.23	2.30	0.49	1.00	0.21	0.26
6	-4.95	20.03	9.77	10.26	5.54	2.44	0.51	1.06	0.22	0.27
7	-1.4	22.43	9.77	12.66	5.825	2.56	0.53	1.11	0.23	0.28
8	2.15	24.84	9.77	15.07	6.075	2.67	0.53	1.16	0.23	0.28
9	5.59	27.17	9.77	17.40	6.31	2.78	0.51	1.20	0.22	0.28
10	9.28	29.67	9.77	19.90	6.475	2.85	0.55	1.24	0.24	0.29
11	12.56	31.90	9.77	22.13	6.775	2.98	0.49	1.29	0.21	0.26
12	16.13	34.32	9.77	24.55	6.94	3.05	0.53	1.32	0.23	0.29

3.5 Numerical simulation of laboratory scale backfilled stope

Geomechanical behaviour related to underground mining are often predicted with numerical simulations. However, due to the level of uncertainty of model predictions and level of simplification, simulations are often questioned (Bloss 1992). The simulation error can be minimized by the use of appropriate boundary conditions, constitutive models, input parameters, and correct modelling procedures (Pirapakaran and Sivakugan 2007a). Not only laboratory tests, but also numerical simulations can be used to assist to understand the stress transfer mechanisms related to backfilling of mine stopes or granular filling of industrial silos. FLAC, a finite difference numerical package was used in this dissertation to simulate the laboratory scale model filling, in order to compare with model test results. Pirapakaran and Sivakugan (2007a) numerically simulated the in situ stress measurements on HF backfilled stope by Knutsson (1981). A basic two-dimensional modelling package allows to simulate the plane strain conditions (for example, narrow long stopes) and axisymmetric occurrences, such as circular stopes. However, when the drives and barricades are considered with the stope, the stope environment becomes three-dimensional and calculations need to be performed with FLAC^{3D}.

3.5.1 FLAC/FLAC^{3D} simulation packages and capabilities

FLAC is an explicit solution technique, in which the system equilibrium is computed using a time-stepping numerical integration within the model (Itasca 2011). FLAC uses an explicit, Lagrangian calculation scheme and a mixed-discretization zoning technique and is well recognised in simulations with geomechanical applications. Coulthard (1999) suggested that FLAC and FLAC^{3D} are the best numerical codes to model mine backfilling, after comparing all the available numerical programmes.

The required geometry is divided into a grid with several zones in FLAC. When the code is executed, the unbalanced forces and displacements, for each grid point, are calculated through a time marching mechanism. An important feature of this numerical software is the built-in programming language "FISH", which can be used to include additional variables or properties over time and adjust the external or internal conditions/ parameters accordingly. Moreover, stepwise excavations and filling activities can be implemented with codes written in FISH. In explicit calculations, the stress state is determined by considering the previous stress state and time advancements via iterative calculations. A key advantage of finite difference method, over the implicit finite elements method, is that the governing equations for the mechanics are not based on an initial assumption that the system is in equilibrium (Coulthard 1999). However, the disadvantage of finite difference method is that the timestep is tiny and large number of timesteps must be taken to reach the equilibrium. Additionally, explicit mechanism (FLAC) is very efficient in modelling non-linear, large strain problems rather than solving linear, small-strain problems (Itasca 2011).

The stress conditions in backfilled mine stopes have been simulated numerically (Aubertin et al. 2003) and proved with laboratory test data (Pirapakaran and Sivakugan 2007b; Ting et al. 2012a). Li et al.(2003) used FLAC to simulate narrow stope backfilling but observed an anomalous variation of vertical stress, which exceeds the overburden stress. Later, Pirapakaran and Sivakugan (2007a) suggested a layer wise filling to overcome this vertical stress anomaly. Understanding the stress conditions within the stope is required to simulate the stress conditions within drives. Though the stress state near the barricade is modelled by Li and Aubertin (2009b) and Fahey et al. (2009) with two-dimensional numerical packages, it is difficult to represent the barricade environment under two-dimensional configurations. Because when the drive and barricade are added to the model, the problem becomes three-dimensional. Therefore, the stress distributions in circular and narrow stopes were estimated with FLAC and square stopes with FLAC^{3D} in this dissertation.

In simulations herein, the rock mass was considered as a homogeneous, isotropic material and behaves in a linear elastic manner allowing the use of a 'linear elastic' constitutive model. Also the granular backfill was modelled with Mohr-Coulomb constitutive model (Brinkgreve et al. 2004). Interface elements were used to model the effect of the shearing between stope wall and backfill. Though previous studies suggested that the interface elements have a negligible effect on the stress state (Li and Aubertin 2009), there is a need to simulate interface shearing more realistically, especially when replicating the laboratory tests with numerical models. Furthermore, a significant relative movement between the rock mass and the backfill is witnessed in FLAC simulations and this validates the use of interface elements.

3.5.2 Modelling methodology

For simplicity, it is assumed that the HF is granular with no cohesion and is dry. Since the numerical modelling approach discussed herein is for a continuum, which does not consider grain size, the simulation results applicable to other cohesionless fill types too. Axisymmetric configuration was used to model cylindrical containments in FLAC. Dimensions of the FLAC models were the same as those of the model containments tested in the laboratory, where the outer diameters of 100 mm and 150 mm with a wall thickness of 3 mm. Height of each model was taken as 6*D*. The model consisted of 1 mm × 1 mm grid. Most of the geotechnical properties of HFs were chosen from the literature and the material parameters used for modelling are tabulated in Table 3.3. The model walls were fixed for both *y* and *x*-displacement. *Y*-displacement was fixed at the bottom of the model. Medium rough Perspex interface and rough sand paper interface were modelled with appropriate interface parameters (Table 3.3). The interface stiffness parameters K_n and K_s were empirically calculated as suggested by FLAC manual (Itasca 2011). A low Young's modulus was used in FLAC model, as the confining stresses are low (maximum 3.5 kPa) in the laboratory models. In real-life

applications, a higher Young's modulus appropriate to the stress levels needs to be considered.

Table 3.3. Material properties for backfill and Perspex, used in FLAC simulations

Properties	**Backfill**	**Perspex wall**
Young's Modulus, *E* (MPa)	0.42	3200
Poisson's ratio, *v*	0.2	0.3
Density, ρ (kg/m^3)	1496*	1190
Effective friction angle, (°)	39	-
Interface friction angle – medium wall roughness, (°)	23	-
Interface friction angle – high wall roughness, (°)	38	-

* - Vertical stress results were normalised with density and width of stope

The effect of model zone size on vertical stress is considered to select the optimum mesh size. As FLAC treats the fill as a continuum, the finest zone size is desired. However, the optimum of zone size is required to identify considering the calculation time and memory limitations. Therefore few simulations were carried out to analyse the sensitivity of mesh size. Here, a half width was modelled with 10, 15, 20, 24, 30, 40, 48 and 60 zones, respectively and results are shown in Figure 3.6. As shown in results, a reasonable number of zones needs to be included within the stope and very low number of zones would over-estimate the vertical stress.

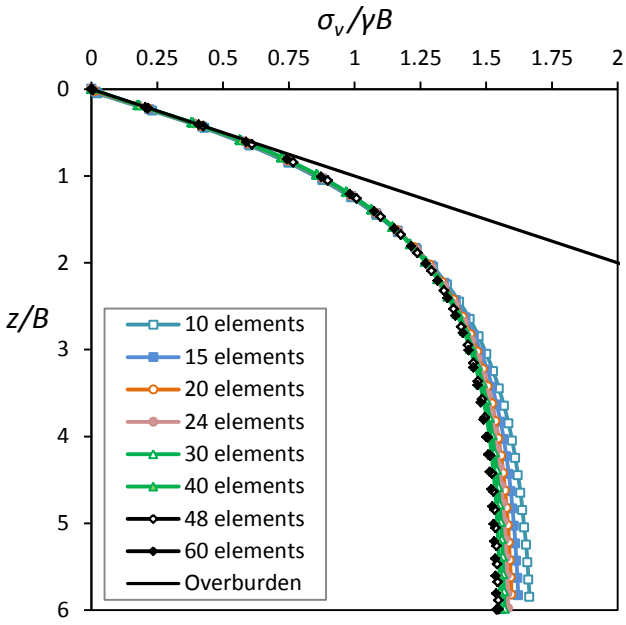

Figure 3.6. Vertical stress variation along centre with number of elements across the half-width ; E = 50 MPa, ν =0.2 and γ = 14.675 kN/m³

The number of layers, used to fill the model, may affect the vertical stress results in numerical models. Few models were simulated to study the effect of number of layers (8, 48 and 240 layers) that used to fill a particular stope (Figure 3.7). As in Figure 3.7, a small number of layers still model the stress variation but a considerable under-estimation of vertical stresses is observed. If a small number of layers are used to model backfilled stopes, then the layer height is large. As the layer height is increasing, the stress distribution is different because of the inertial effects are higher with addition of large mass into the previously solved system as high inertial effects are generated (Itasca 2011). Li and Aubertin (2009) observed this effect and expressed the phenomenon as a shock load. Furthermore, when the number of layers is increased from 48 to 240, a small increase in the vertical stresses was observed (Figure 3.7). The addition of a small layer generates less inertial effects and makes solution scheme effective. Therefore, in the simulations carried out for modelling laboratory model tests, the stope/silo was filled with maximum number of layers, 240 layers, to reduce the inertial effects.

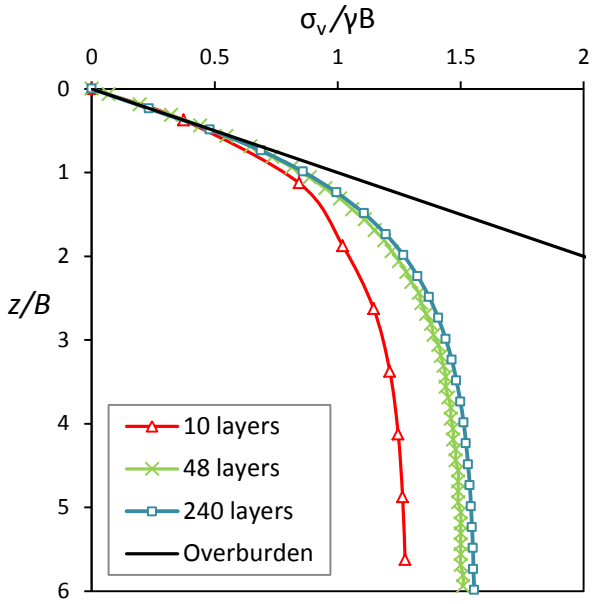

Figure 3.7. Vertical stress variation along centre with number of layers used; E = 50 MPa, ν =0.2 and γ = 14.675 kN/m³

FLAC^{3D} was used to simulate the filling of the model square stope, which is 150 mm × 150 mm × 900 mm. The stope was filled in 30 equal layers, as 3D model consumes a considerable time to solve one layer. Only one quadrant of the problem was modelled, using 5 mm × 5 mm × 5 mm brick elements in the mesh, because of the symmetry. The stresses were initialized to zero before filling starts in numerical calculations and fill was subjected to its own weight. The surrounding Perspex wall was included as a single zone and displacements of the Perspex is fixed.

3.6 Vertical stress variation while filling and after filled

Two different ways of presenting the variation of the vertical stresses with depth in numerical simulations are available and, these two methods output different stress profiles (Sivakugan et al. 2014). Understanding the differences between the two approaches is necessary to determine the required vertical stress profile for particular application. As the filling was conducted in layers or stages, two stress recording choices; either to record stress at the bottom after each layer is placed or to record the stress variation with depth once the whole stope is filled, are available and must be used accordingly. The vertical stress recording methods detailed as:

Method 1 – Plotting the vertical stress *at the bottom* against the fill height, after addition of each layer, mimicking the model laboratory test, or

Method 2 – Plotting the vertical stresses with depth, determined on the completion of filling.

Method 2, requires more instrumentation to conduct the model tests in the laboratory for measuring the vertical stresses at various depths within the fill, making the laboratory model more complex. On the other hand, one transducer is required at bottom in method 1, like most of the laboratory tests as well as in situ stress measurements. Figure 3.8 shows the $\sigma_v/\gamma B$ versus z/B variation for the two methods, where the difference is significant. Only at the top and the bottom the vertical stresses are the same. The difference is attributed to the zero-displacement bottom boundary, which is assumed in numerical modelling. In method 1, where the vertical stress is monitored only at the bottom when the fill accrues, the fixed bottom boundary effect (i.e. partial mobilisation of shear stresses) applies to every reading and hence no such sharp increase in vertical stress near the bottom is observed.

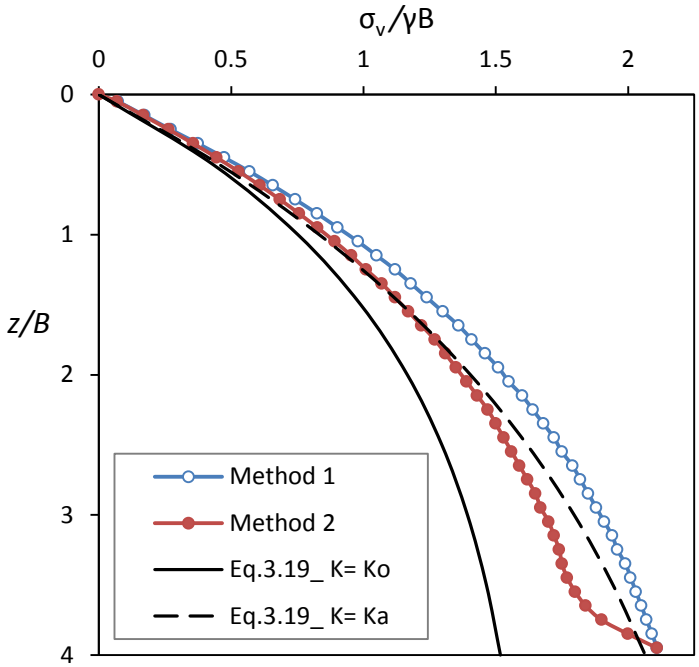

Figure 3.8. Vertical stress at centre versus depth, for a narrow stope of 4*B* deep: E = 50 MPa, ν = 0.2 and γ = 14.675 kN/m³

In method 2, for all layers except for the bottom one, the downward movement is not restricted and hence the friction along the wall is fully mobilised. However, at the bottom layer, the downward movement is fully restricted and therefore, the friction along the wall is not fully mobilised. Hence, vertical stress was increased close to the bottom of the stope (Figure 3.8). The effect is present to a lesser extent in the few layers above the bottom boundary. This is evident in the "kink" seen in the plot corresponding to method 2 near the bottom. In most of the numerical modelling work reported in the literature (Kuganathan 2005; Pirapakaran and Sivakugan 2007a; Fahey et al. 2009; Li and Aubertin 2009b; Ting et al. 2011), method 2 has been adopted which clearly shows the sharp increase in the vertical stress near the bottom, caused by the zero-displacement bottom boundary. To quantify the vertical stresses within the fill at any depth, on completion of the filling, method 2 is applicable. Although, a considerable deviation is observed with respect to Equation 3.19, the method 1 appears to follow the analytical curve trend (Figure 3.8).

Figure 3.9 shows the $\sigma_v / \gamma B$ versus z/B variations as determined by the two methods, for narrow stopes (i.e. plane strain conditions) of different vertical aspect ratios (height to width ratio) with the depth $H = 2B$, $3B$, $4B$, $5B$ and $6B$. The plots generated by method 1 are the same for all aspect ratios, enabling the use of a single curve to estimate the vertical stress for a stope of any aspect ratio (Figure 3.9). On the other hand, the plots generated by method 2 follow a curve that is different to that determined from method 1, but deviate at the bottom. Therefore, the stress estimations for locations close to the bottom are need to be corrected when method 2 is used.

Figure 3.10 shows the $\sigma_v / \gamma B$ versus z/B variations as determined by the two methods, for stopes of different horizontal cross sections, varying from a square ($B/L = 1$) to a strip ($B/L = 0$). The trend is similar to what is seen in Figure 3.10 for all B/L ratios.

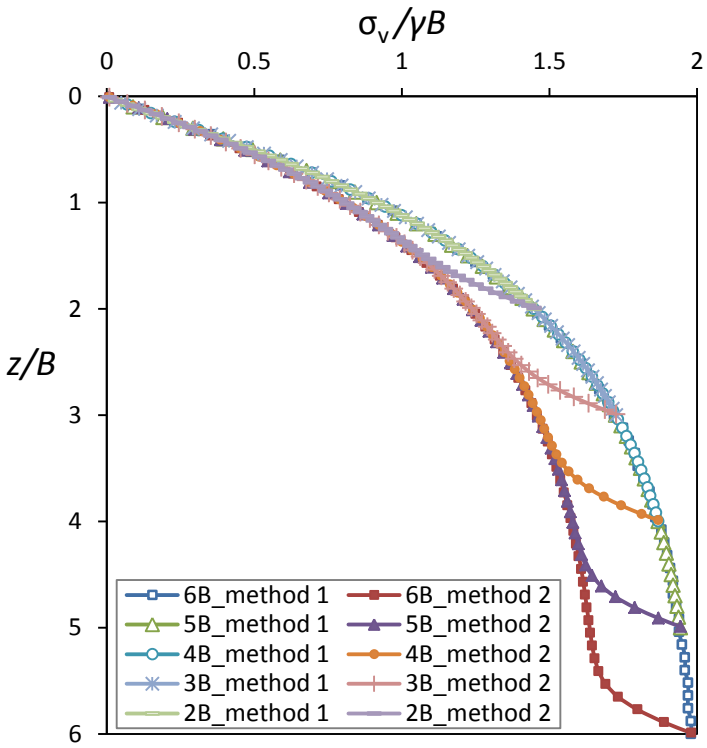

Figure 3.9. Maximum vertical stress variation for vertical aspect ratios with depth H = 2B, 3B, 4B, 5B and 6B.:: E = 50 MPa, ν = 0.2 and γ = 17.65 kN/m³

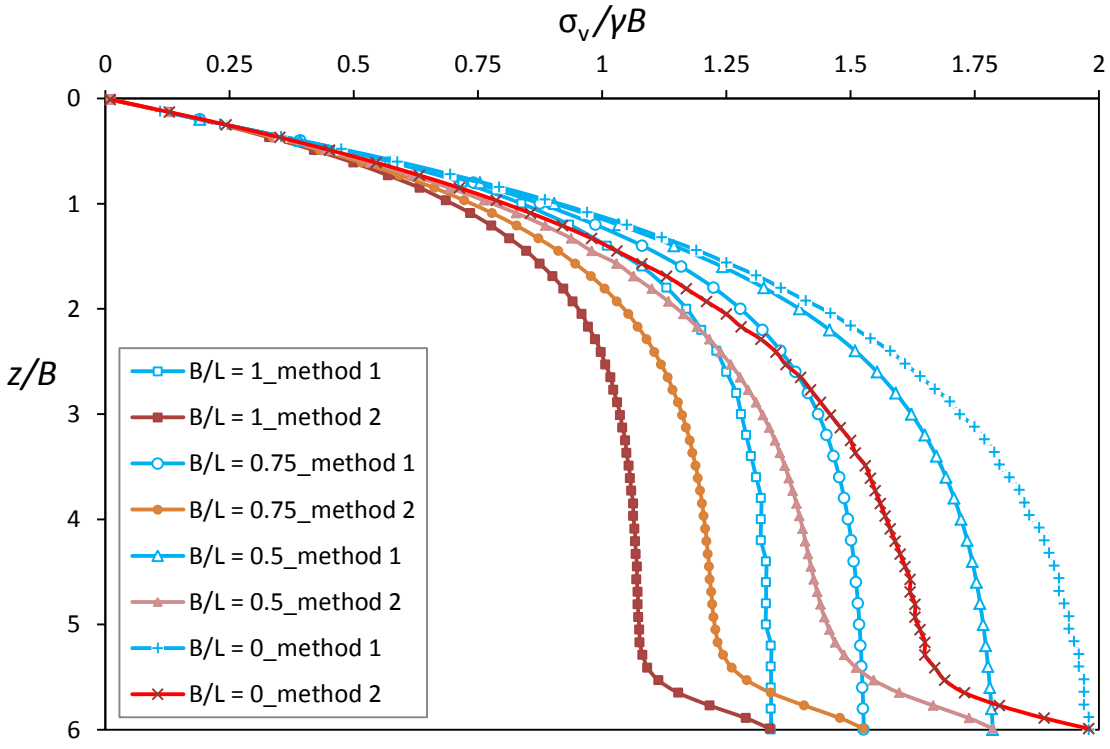

Figure 3.10. Maximum vertical stress variation for horizontal cross sections, B/L=1 - square stope, B/L= 0 - narrow stope: E = 50 MPa, ν = 0.2 and γ = 14.675 kN/m³

Most numerical modelling work related to mine stopes, reported in the literature, adopt method 2 when calculating vertical stress. If loadings on the barricade at the bottom of the mine stope or the loads onto a buried conduit at the bottom of a backfilled trench are required, method 1 is preferable because, method 1 models the situation more realistically. Therefore, FLAC results from method 1 are used for comparison with laboratory test results. Often the average stress is used with analytical equations, but most of in situ vertical stress data presented as vertical stress at a point. Therefore in numerical simulations, it is conservative to consider the maximum vertical stress, which is the vertical stress at the centre.

3.7 Results from laboratory tests and FLAC for backfilled mine stopes

When the wall is very rough, the wall friction angle (δ) can be taken as equal to the friction angle (ϕ). Equation 3.15 and 3.16 are used with K as either K_o or K_a. Moreover, the $K\tan\delta$ would not change with φ for the range of 25° to 45° as shown in Figure 3.11. Therefore the analytical equations would estimate similar vertical stresses, for the range of φ from 25° to 45° and subjected to change with the input of lateral pressure coefficient.

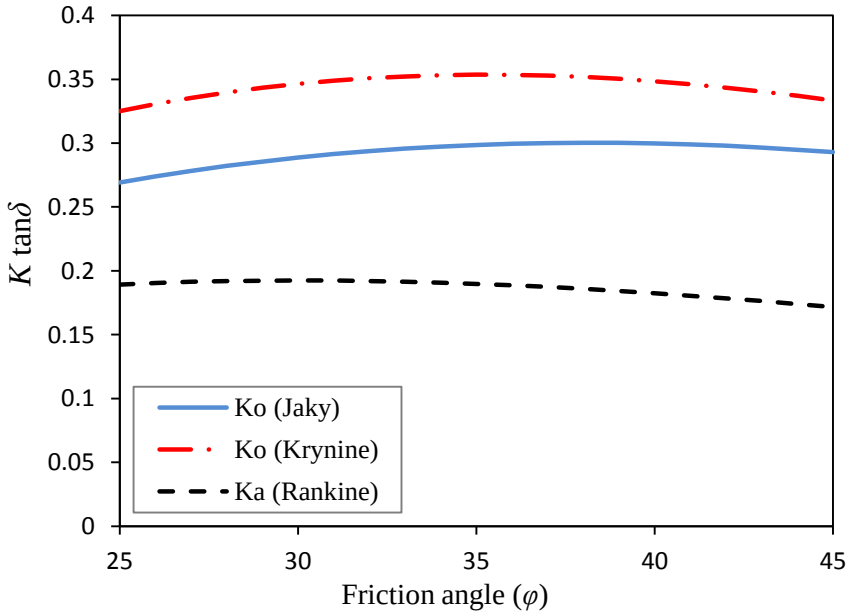

Figure 3.11. Variation of $K\tan\delta$ with when definitions for K_o and K_a is considered for rough walls

The frictional properties (φ and δ) are nearly the same for sand as well as HFs, at low relative densities (Table 3.1). Therefore, the same analytical equation in arching theory is used to compare laboratory test results for both materials with K_o and K_a.

The following terminology was used to identify laboratory tests.

- Letter of C, S or R - to represent the stope shape; C - circular, S - square and R - rectangular
- 100 or 150 - to represent the stope width in millimetres
- A or B – for wall roughness conditions; A for medium rough walls and B for rough walls

Therefore S150B identifies the test data related to 150 mm wide square stope with rough walls.

3.7.1 Vertical stress variation

The variation of the vertical stress with depth, for circular and square stopes of width 150 mm, is presented in Figure 3.12. The dashed lines show the variation of the average vertical stress, with $K = K_o$ and $K = K_a$ depth based on Equation 3.15, where the vertical stress is substantially reduced with arching. The vertical stress reaches an asymptotic value relatively quickly, at depths of $3B$ - $4B$. The degree of arching will be less in the case of a trench (i.e. plane strain loading) where the frictional resistance is provided only by the two sides, as opposed to the four sides in the case of the square cross section in the example.

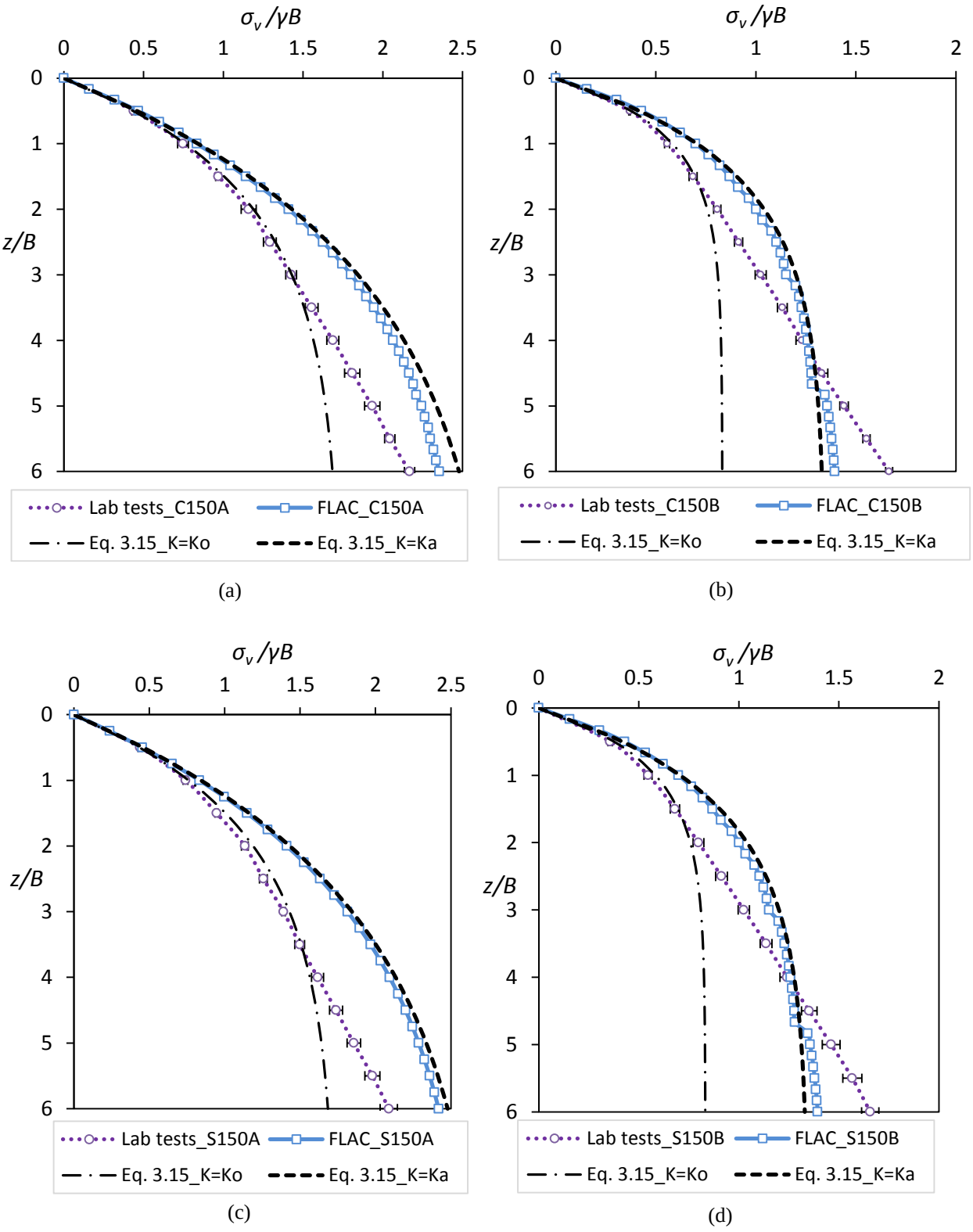

Figure 3.12. Vertical stress variation from laboratory tests and FLAC simulations are compared with analytical equations; a) circular 150 mm diameter stope with medium rough walls, b) circular 150 mm diameter stope with rough walls, c) square 150 mm wide stope with medium rough walls and d) square 150 mm wide stope with rough

At shallow depths (upto $z = 2B - 3B$), the vertical stress from laboratory tests agree with the analytical equation with $K = K_o$ (Figure 3.12). However, the vertical stress variation deviates from analytical equations at depths beyond 3*B*. And, this later behaviour is more likely a linear increase of vertical stresses with depth, which is not expected with analytical equations (e.g. Equation 3.15). For analysis, the vertical stress variation is divided into two regions as;

Region 1- depths from top to 3*B*, and

Region 2- depths beyond 3*B*

3.7.2 Vertical and shear stress variation within region 1

The vertical stress variation follows analytical equation ($K = K_o$) in region 1, but then deviates and shows a linear increase in region 2. Shear stress acting along the wall is calculated and presented in Figure 3.13a. The shear stress, in laboratory test results, follows the analytical equation in region 1 and reaches a maximum. Therefore shear stress does not increase in region 2. The normalised horizontal stress, termed as horizontal stress hereafter, is calculated with shear stress and tanδ, and included in Figure 3.13b. As with shear stress variation, the horizontal stress also reaches a maximum within region 1.

The vertical stress and horizontal variation in region 1 can be explained by considering the soil grain matrix. At lower depths, the soil matrix is capable of holding the self-weight, remains intact and acts like a continuum, and hence the stress variation follows the analytical equation. This is evident with the horizontal stress variation as well, which follows the analytical equation. At the end of region 1, the shear stress and the horizontal wall stress are increased to attain the maximum values. But analytical equations predict shear and horizontal stresses greater than the recorded in tests (Figure 3.13).

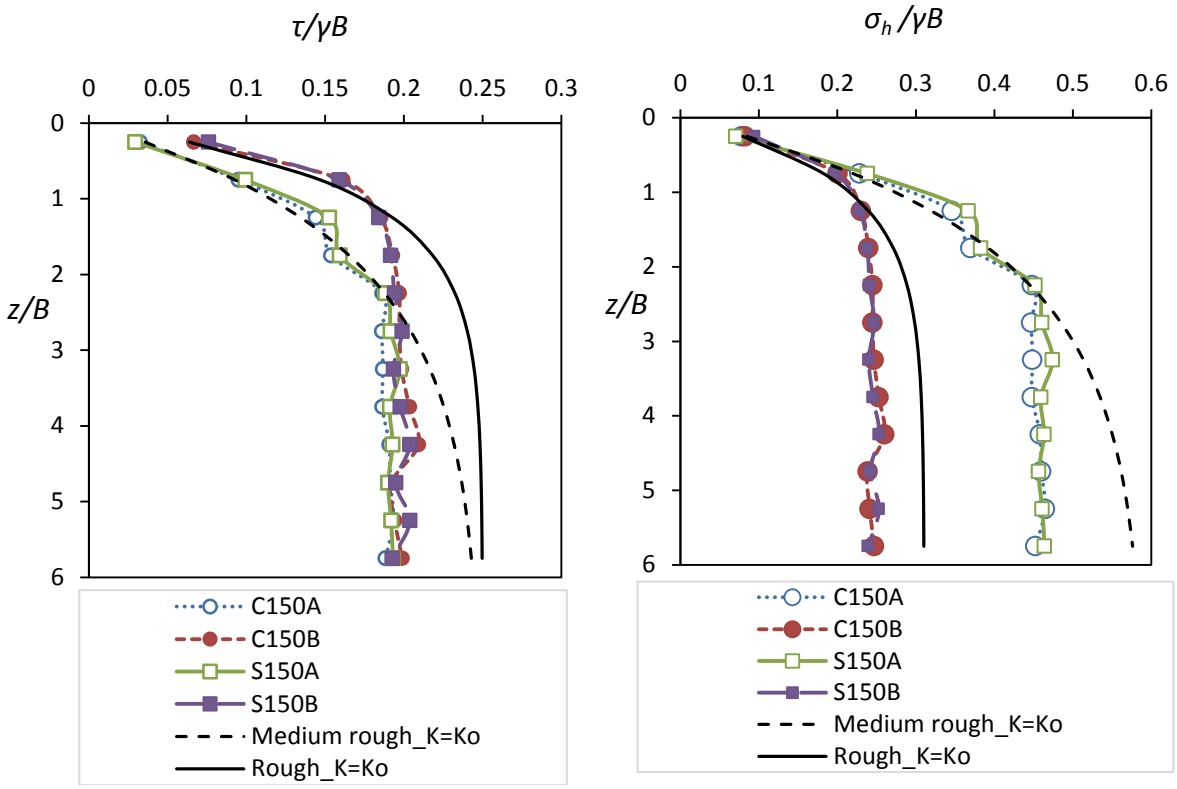

Figure 3.13. Stress variation from laboratory tests are compared with analytical equations for circular and square stope of 150 mm width; (a) shear stress variation and (b) horizontal stress variation

3.7.3 Vertical and shear stress variation within region 2

When a container is filled in layers, the added weight is transferred to the underlying layers well as to the wall. The mobilisation of friction along the wall controls the vertical stress variation felt at bottom. When the horizontal stress variation with depth is considered, the horizontal stress becomes asymptotic at a relatively shallow depth, within region 1, as seen in the laboratory tests (Figure 3.13b).

As the horizontal stress becomes maximum, the shear stress also reaches the maximum (Figure 3.13a). But, the maximum horizontal stress and shear stress in laboratory tests are less than what is estimated from analytical equations (Figure 3.13). This implies that the shear forces have not fully developed, such that shear force is

capable of carrying the weight from the addition of fill mass. But this is contrary with analytical equations, in which the additional weight is totally balanced by shear forces, in region 2 and hence the vertical stress reaches an asymptote. Therefore, further down the stope, the addition of load from the top makes it difficult for the soil matrix to carry the entire load without slipping and transfers the some of the load to bottom. As this weight portion of the new layer transferred continuously to base, the vertical stress shows a linear increase, without reaching an asymptote, in region 2.

Confinement between the grains in soil matrix develops in region 1, and enables the horizontal and shear stresses to increase. But in region 2, the wall friction is mobilized to the maximum, and therefore shear stress cannot increase further. Then the rest of the load is transferred to bottom, making the vertical stress to increase in a liner trend and not reaching an asymptote. The same pattern is observed by Ting (2011), where the vertical stresses do not reach an asymptote; rather they tend to increase with depth (Figure 2.11). This is considered as the major difference between the actual particulate behaviour shown in granular material and theoretical continuum approach.

3.7.4 Sand and hydraulic fills - vertical stress variation

The vertical stress variation, for both sand and HFs when filled to a 150 mm wide square container, is shown in Figure 3.14. Both the sand and HFs have nearly the same internal friction angle at low relative densities, as obtained from direct shear tests (Table 3.1). This allows comparing vertical stress variation results in the same graph, alongside with Equation 3.15.

As seen in the Figure 3.14, vertical stress variation in both cases neither matches the analytical equations nor reaches any asymptote. Interestingly, in the case of both sand and HFs vertical stresses tend to increase even after a depth of 6B and the rate of increase is higher with sand (Figure 3.14). And in region 2, vertical stress shows a linear increase for both sand and HFs. The lateral forces have not fully developed and hence a linear increase of vertical stress is observed in region 2, and the vertical stress increase rate is higher for sand, compared with HFs.

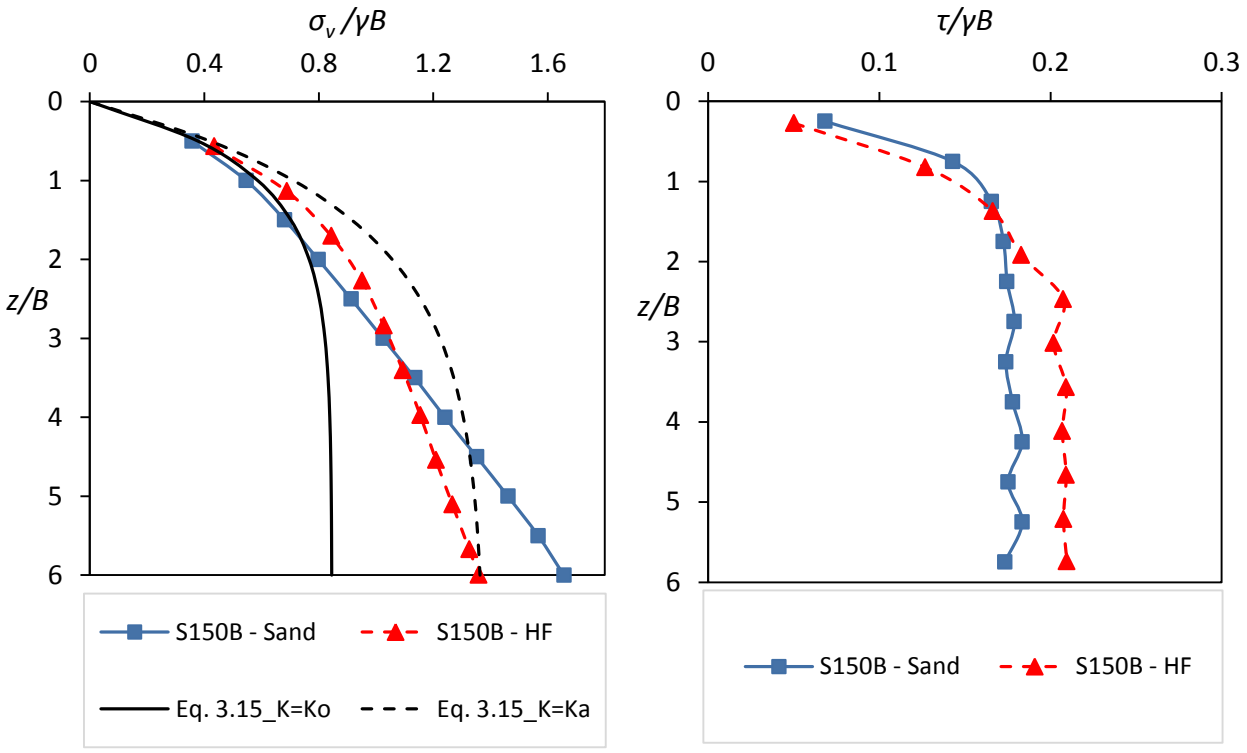

(a) (b)

Figure 3.14. Variation of stress for sand and HFs, when filled to a 150 mm wide square stope; (a) vertical stress and (b) shear stress

HFs are freshly crushed materials and consist of angular particles. HF grains interlock, due to angular freshly crushed grains, and therefore transfer a considerable load to walls and therefore the increase of vertical stress is less. In contrast, the grain interlocking is less for sand, where the grains are rounded or sub-rounded, and less shear stresses are recorded (Figure 3.14b). Grain interlocking can be further deduced with Scanning Electron Microscope (SEM) images, in which HFs show more angular grains than compared with sand (Figure 3.15).

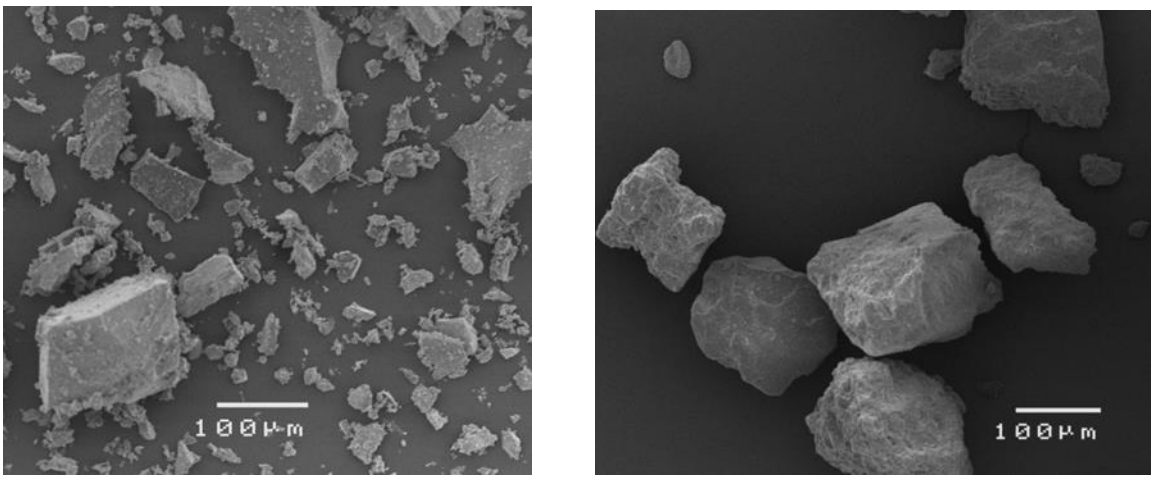

(a) (b)

Figure 3.15. Grain shape analysis through SEM; (a) highly angular grains in HFs and (b) rounded to sub-rounded grains in sand

3.7.5 Vertical stress variation with the size of the stope

Both the medium rough as well as rough walls are included in two sizes for circular containments. Stopes of 100 mm and 150 mm widths were instrumented and vertical stress variation was obtained (Figure 3.16). The vertical stresses show agreement in tests when the diameter of stope is changed, as they are presented in terms of dimensionless variables. This agreement shows the possibility of extending the predictions of vertical stress variation to containments with significantly larger diameters. Furthermore, the shapes of the plots in region 1 and region 2 are quite distinct, as identified earlier with Figure 3.12. Region 1 shows a reasonable agreement with the analytical equation with $K = K_o$. However, in region 2, a linear increase of vertical stress with depth is observed with laboratory tests. Hence the laboratory test results do not match the analytical equation for the entire height. The numerical simulation results are same for both 100 mm and 150 mm stopes (Figure 3.16), as both used the continuum approach and the zone size to width ratio was the same, in both models. The vertical stress variation shown with laboratory tests is the same as discussed for Figure 3.12, and therefore the analysis given for region 1 and region 2 variation is valid for different sizes of stopes too.

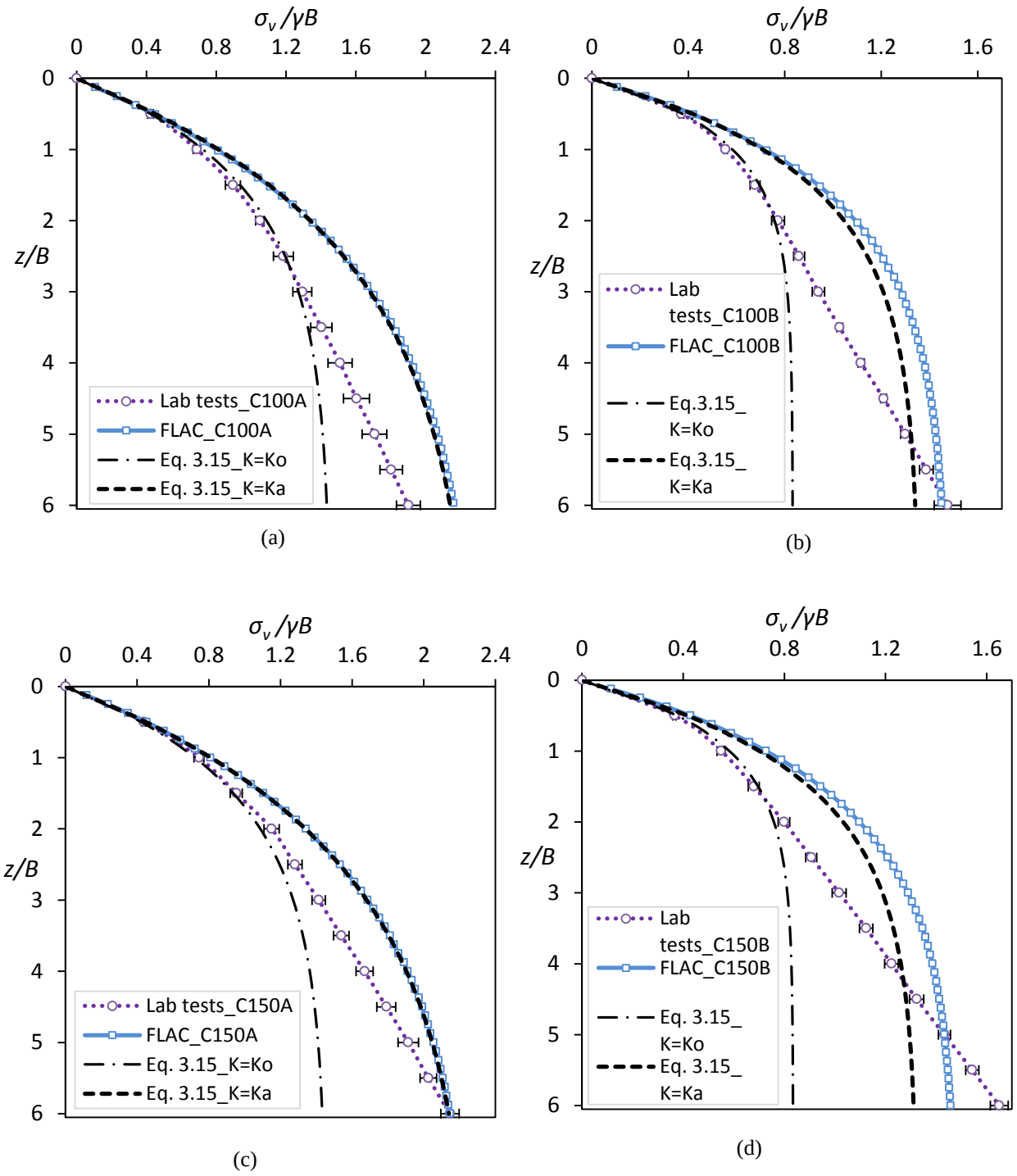

Figure 3.16. Vertical stress variation from laboratory tests and FLAC simulations are compared with analytical equations; (a) circular 100 mm diameter stope with medium rough walls, (b) circular 100 mm diameter stope with rough walls, (c) circular 150 mm diameter stope with medium rough walls and (d) circular 150 mm diameter stope with rough walls

3.8 Calculated lateral pressure coefficient (K_{calc})

Vertical stress variation does not match the analytical equations and numerical simulation results (Figures 3.12 and 3.16). A 'varying lateral pressure coefficient', in which the K is taken as a function of depth, can be suggested as an alternative to match test results with analytical equations. K should be varying instead maintaining as a constant value, to agree with theoretical vertical stresses (Lenczner 1963). The laboratory tests conducted for this dissertation, enabled the vertical and horizontal stresses be measured independently and therefore, a K_{calc} value was obtained with Equations 3.22 and 3.24, for each layer. The test data with HFs suggested that the 'K_{calc}' is not a unique curve for test, and varies with the filling material as well as the wall roughness condition (Figure 3.17).

The 'K_{calc}' is not the same for sand and HFs (Figure 3.17). The grain size distribution and the interlocking of granular particles affect the calculated value of lateral earth pressure coefficient. These results again highlight that K is not a constant and subject to change with the backfill depth and backfill material.

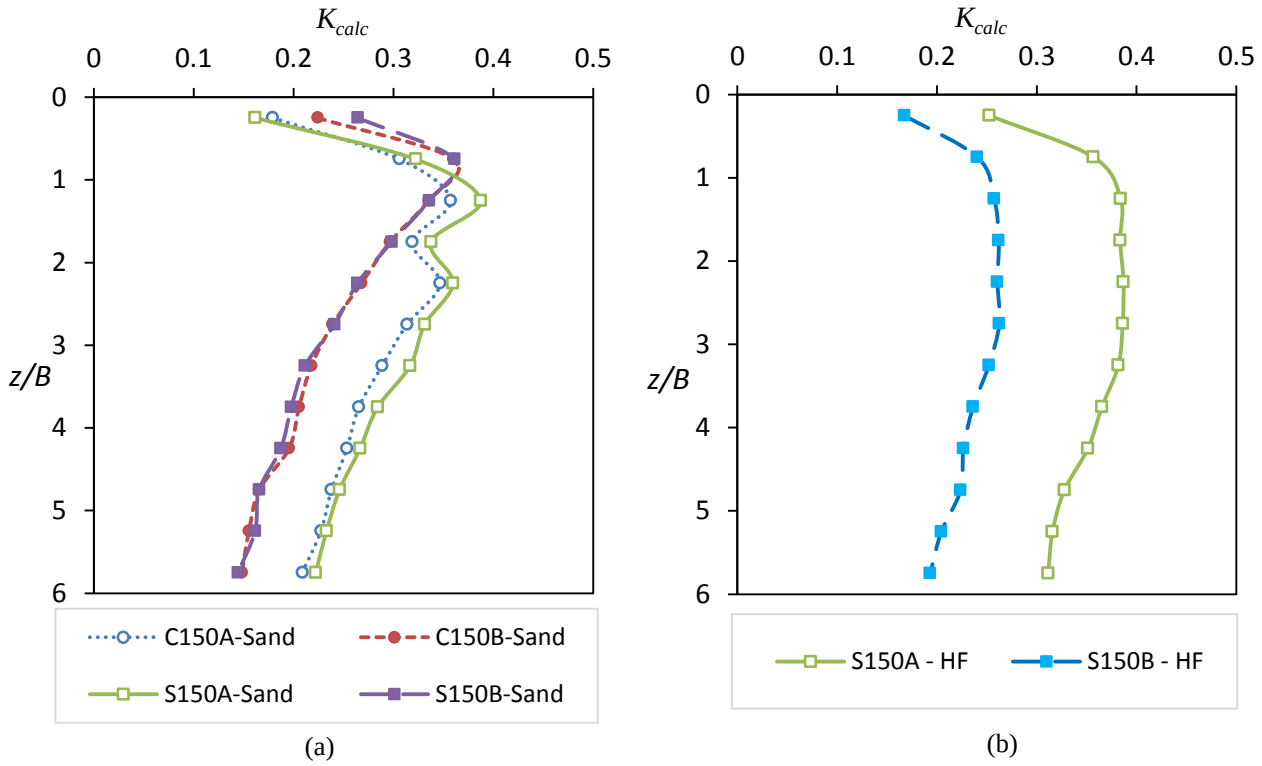

Figure 3.17. Calculated K value (K_{calc}) from laboratory tests; (a) sand and (b) HFs

3.9 Estimation of vertical stress variation for plane strain conditions

Understanding the effect of width to length ratio (B/L) on the vertical stress variation is an important part of this study, as many different cross sectional shapes are encountered for backfilling. Most of analytical equations (Marston and Anderson 1913; Handy 1985) are derived for plane strain conditions, in which the length is infinite compared to the width, as in the case of long trenches. However, laboratory testing of a model stope under plane strain conditions is not feasible and an attempt is made to build a rectangular stope, in which the length is 5 times the width. The vertical stress variation and the shear stress variation were obtained for filling the rectangular stopes. The results from square as well as rectangular stopes were used to extrapolate the vertical stresses for a narrow stope representing plane strain situation.

Fahey et al. (2009) and Sivakugan and Widisinghe (2013) highlighted that the cross sectional area to the perimeter ratio influences the stress development when all other factors (e.g. properties of the fill) remain the same in backfilled mine stopes. This ratio, often called as hydraulic diameter, is the same for square and circular cross sections, implying that the average vertical stresses would be the same for both cross sections. Both square and circular stopes have same B/L ratio of 1.0. This effect is evident from the results shown in Figure 3.12, that the vertical stress variation is nearly the same for both the square and circular stopes.

Mine backfilling is also carried out with rectangular shaped stopes, and a methodology is developed to interpolate the vertical stress for a stope of $B/L \neq 1$. A rectangular laboratory test model (B/L ratio of 0.2) is available in JCU and both the square stope and rectangular stope are used to obtain the vertical stress variation and extrapolation was done for region 1 and region 2 separately as both regions show distinct curvature. Region 1 shows an exponential variation of vertical stress with depth, while region 2 demonstrates a linear variation. Therefore, region 1 was analysed based on an exponential curve fitting technique and region 2 was analysed as a linear variation. The estimation of average vertical stress for other containment shapes was

introduced considering the B/L ratio, based on laboratory results for square (B/L = 1) and rectangular stopes (B/L = 0.2), with 0 and 1 being the two extremes. Normalised depth, z/B, was considered as the first independent variable and the B/L ratio was considered as the second independent variable.

A linear regression is applied for the region 1, for square and rectangular stopes, taking z/B as the independent variable (Figure 3.18). Then an exponential variation is fitted for the vertical stress in region 1, as a function of z/B for the different B/L values (Figure 3.19). Both, the linear and exponential, regressions show an R-squared value close to 1, implying a reasonable agreement with the fitted curves. Then the second independent variable, B/L, is considered. Then the relationship of $\sigma_v/\gamma B$ and z/B with respect to B/L was considered. At the end, the following equations were obtained with linear and exponential regression:

Region 1

$$\frac{\sigma_v(region1)}{\gamma B} = \left[-0.429\frac{B}{L}+0.796\right].\ln\left(\frac{z}{B}\right)+\left[-0.22\frac{B}{L}+0.882\right] \tag{3.25}$$

Region 2

$$\frac{\sigma_v(region2)}{\gamma B} = \left[-0.184\frac{B}{L}+0.287\right].\frac{z}{B}+\left[-0.246\frac{B}{L}+0.998\right] \tag{3.26}$$

Application of B/L = 0, will result the vertical stress estimation for plane stain backfilling, which cannot be obtained from laboratory tests. The vertical stress calculated for plane strain condition is given in Figure 3.20, along with vertical stress variations for square and rectangular stopes.

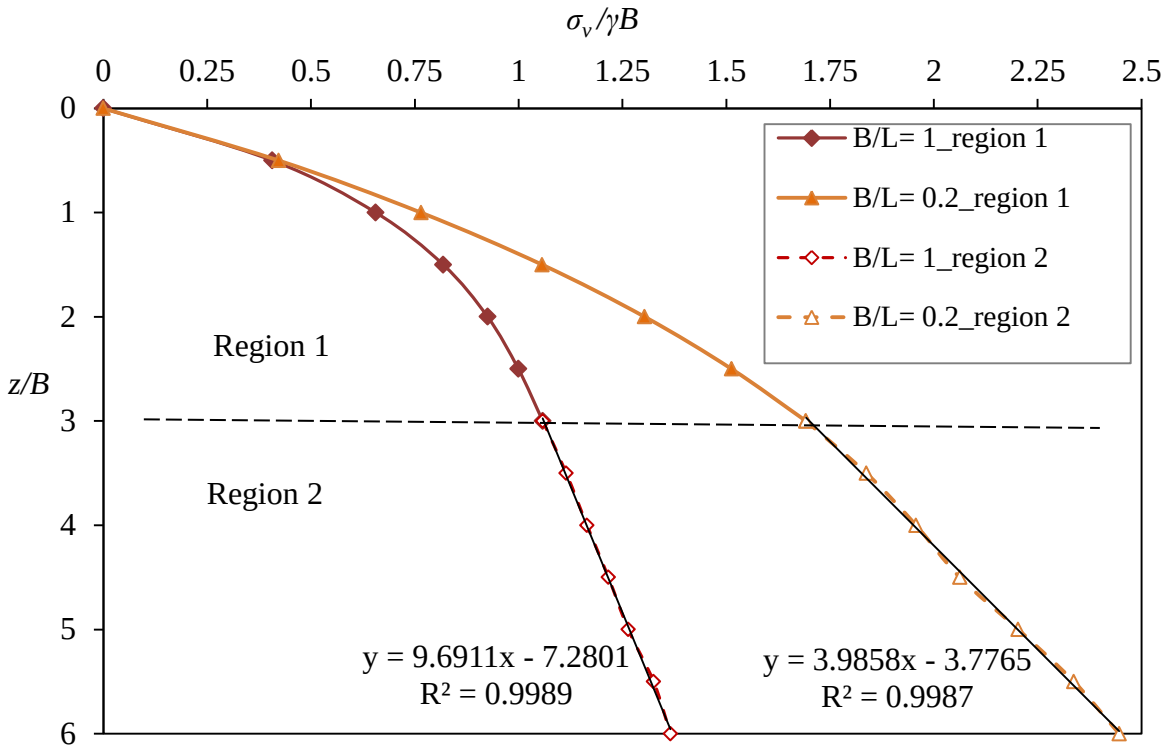

Figure 3.18. Vertical stress variations for square and rectangular stopes, and a linear regression is indicted for region 2

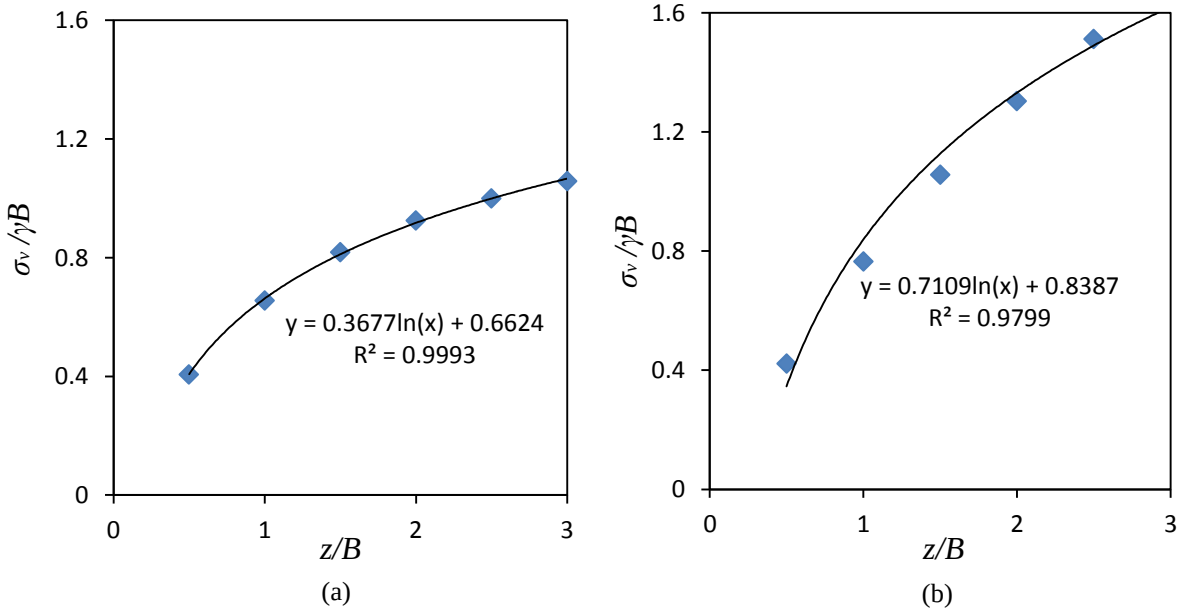

Figure 3.19. Regression for region 1; for (a) B/L = 1 (square stopes) and (b) B/L = 0.2 (rectangular stopes)

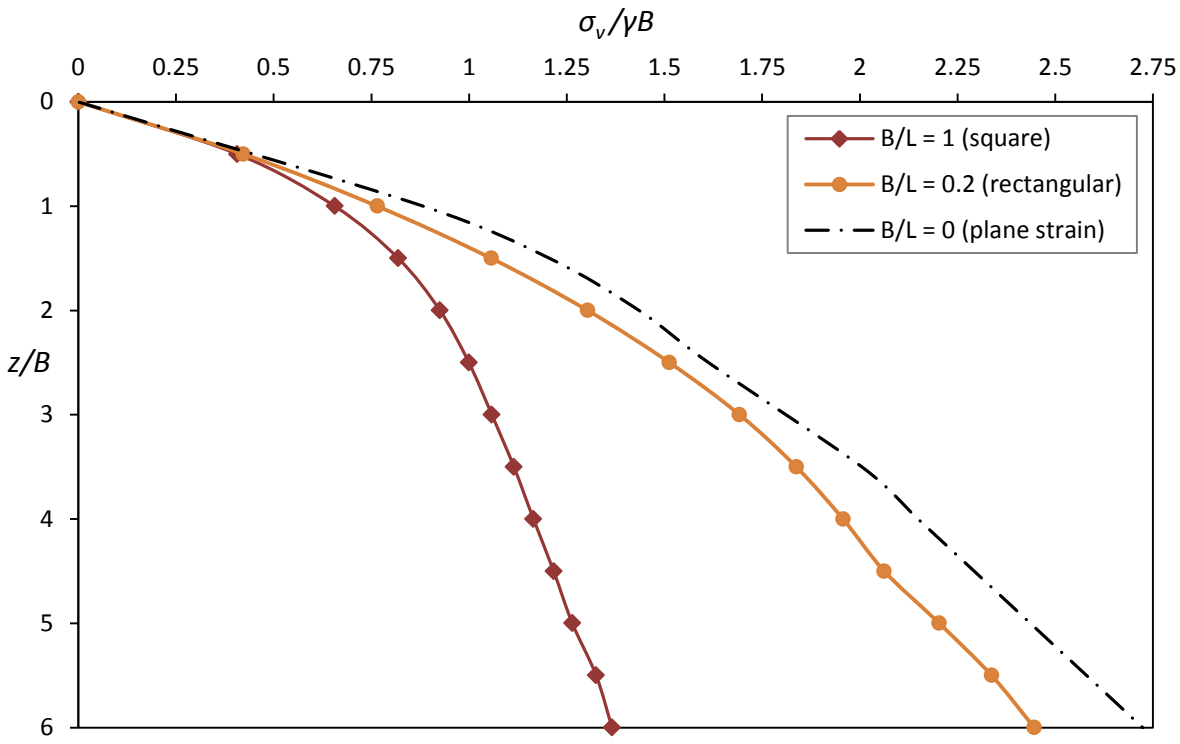

Figure 3.20. Estimated vertical stress variation for plane strain conditions, based on laboratory test results

3.10 Summary and conclusions

Arching occurs within granular backfill behind retaining walls, backfills in trenches, underground mine stopes and grain storage silos. Three different approaches for studying the effects of arching within granular soils, analytical, laboratory model tests and numerical simulations were taken in this dissertation. A generalised equation for vertical stress is presented where the stope perimeter and the cross-sectional area are considered as geometry inputs. Laboratory model tests were carried out to obtain the average vertical stress and shear stress variation with depth. Also the laboratory models were numerically simulated with FLAC and FLAC^{3D}. A significant scatter was observed for vertical stress at depths larger than 3B (region 2) for above three approaches. The vertical stress variation with depth, as determined from the laboratory tests, becomes linear in region 2, thus deviating from analytical and numerical solutions,

which suggest the vertical stresses become asymptotic at large depths in the order of 4-5*B* (Figure 3.11).

Granular materials, encountered in soil mechanics, are often treated as a continuum and modelled accordingly. Continuum behaviour can be considered as a lower bound solution for the vertical stresses within a system of cohesionless granular materials, in which the arching is expected to develop, thus reducing the vertical stresses. The analytical and numerical models based on continuum approach suggest that the vertical normal stress becomes asymptotic in region 2 (larger depths) in a granular fill contained within vertical walls. In well-established arching theory (Janssen 1895; Marston 1930), a horizontal layer element is considered for derivation of an expression for the average vertical stress. This horizontal layer acts as a single block, which carries a portion of load via interaction with wall. The interface friction is assumed to be fully mobilised along the walls as the stope is filled in RD of 30 %. After a depth, the shear forces are expected to carry the additional weight and therefore the vertical stress reaches an asymptote within the region 2 in the analytical equations. However, the laboratory test results show that the vertical normal stress increases steadily even at very large depths and does not become asymptotic even at depths as high as 6*B*. As the granular material is not cemented and consists of grains, it has less interlocking. As a result, vertical stress variation in region 2 has shown a linearly increasing trend, which is common for both sand and HFs, in both containments of width 150 mm. Grain re-arrangement within the matrix and capability to hold the grain matrix and carry the loads to walls from matrix affects this vertical stress variation.

In continuum approach the horizontal stress increased proportionally with the vertical stress (i.e., constant *K*). the lateral stress ratio, 'K_{calc}' is calculated from the model test data and proves that the *K* is not a constant and vary with depth as laboratory test results do not match the analytical equations, an alternative of varying *K* is suggested to use with analytical solutions.

The vertical normal stress σ_v variation with depth z can be computed in two separate ways, with numerical simulations, "method 1" and "method 2" as discussed. Method 1 tracks the stress at the bottom of the stope while filling progresses and the σ_v at bottom is used in determining the σ_v-z variation. Method 2 uses the values of σ_v at various depths, recorded at the end of filling, in determining the σ_v-z plot. The two different procedures used for determining the vertical stress profile, gave different values of stresses, except for at the top and bottom of the stope. The difference is attributed to fixing the bottom of the stope, implying zero displacement in any direction. The reasons were discussed and recommended that the method commonly used in numerical modelling (method 2) is not necessarily the better of the two. When the stresses or loadings at the bottom of the stopes are required for determining the lateral stresses into the barricade while the filling progresses, method 1 is more suitable. This is true even for backfilling trenches with buried conduits at the bottom. In addition, method 1 mimics the model laboratory test procedure discussed previously, and can be a better validation tool. In reality, the vertical stress near the buried structure at the bottom of the trench, such as barricade or buried pipe that is of interest to the designer and not the vertical stress profile. Further, in a situation such as mine backfilling that takes a relatively long time for the filling process, consideration of the vertical normal stresses throughout the filling process is desirable. The proposed "method 1" models the field situation better, when the loadings at the bottom during filling are required, and gives the same stress profile for all stopes with any aspect ratio.

An empirical equation to estimate vertical stress in plane strain conditions is obtained based on laboratory test results from model stopes with square (B/L = 1) and rectangular (B/L = 0.2) cross sections. As a distinct variation of vertical stress was identified with depth, the extrapolation for the vertical stress in plane strain conditions (B/L = 0) are carried out, combining the exponential regression for region 1 and the linear regression for region 2. The average vertical stress variation for a backfilled narrow stope of plane stain situation was deduced, considering B/L and z/B as independent variables. In conclusion of this chapter, the continuum approach to describe

the granular backfilled scenarios is not sufficient as observed with the laboratory tests. Large vertical and horizontal stress deviations were observed when laboratory test results are compared with those from analytical and continuum methods.

Chapter 4

Vertical Stress Isobars for Backfilled Structures

4.1 General

Industries such as chemical, mining, agriculture, electric power generation, food processing and pharmaceuticals use silos to store agricultural grains, pharmaceutical powders, chemical pellets, coal and other minerals, etc. The failure rate of silos is comparatively higher when silos are compared with other industrial structures (Theimer 1969; Carson 2000; Dogangun et al. 2009). Overlapping of pressure bulbs and first time loading of silos erected in clay foundations have caused problems (Bozozuk 1976). Therefore, the vertical stress distribution is prerequisite for foundation/support designs to ensure the stability of the structure when in operation. Noting the seriousness of the problem and the necessity of estimating the vertical stresses within a granular soil contained within a vessel, there had been several attempts from as early as end of 18th century.

The mine stopes having plan dimensions of 20 m to 60 m and heights as much as 200 m, are backfilled with crushed waste rock or mine tailings. When filled with hydraulic fills, barricades are subjected to loads from backfill slurry. Failure of the barricades can result in the in-rush of the slurry into the drives during the early stages of filling, which can be a solemn concern, placing the miners and the machinery at risk. Therefore, reasonable estimates of vertical stresses within backfilled stopes are essential for the progress of mining operations and designs of the barricades with confidence. In both scenarios, silos and backfilled mines stopes, the filling granular material is not compacted and subjected to self-weight only. But in the case of hydraulic fills, the tailings are poured into the stope as slurry and excess water drains out with time. For the simplicity of creating vertical stress isobars, the backfills are assumed to be dry.

Arching theories (Janssen 1895; Marston and Anderson 1913) as well as laboratory tests (Jarrett et al. 1995; Pirapakaran and Sivakugan 2007b; Ting et al. 2012a) were aimed at understanding the *average* vertical stress at a depth, neglecting the lateral variations. But the principal stress orientations suggest that the vertical

stresses vary horizontally as well (Figure 4.1) (Fahey et al. 2009). The interfacial friction makes the principal stresses not vertical or horizontal anymore.

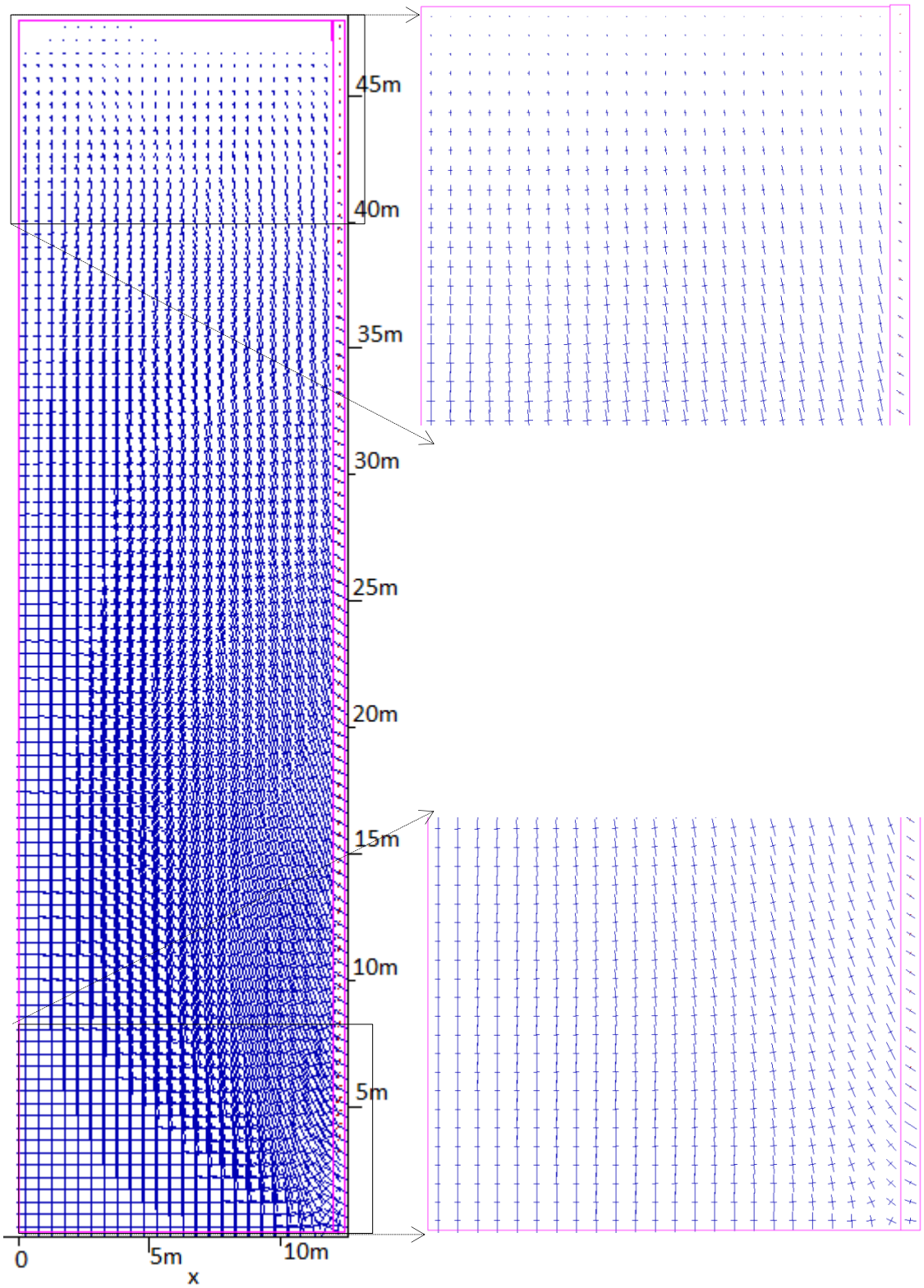

Figure 4.1. Orientation of principal stress directions for a narrow backfilled structure, as output with FLAC simulations

There are analytical equations developed to evaluate the lateral variation of vertical stresses in silos, bins, backfilled trenches and mine stopes (Walker 1966; Handy 1985; Drescher 1991; Singh et al. 2011). However, no analytical equation have been derived to estimate vertical stresses at any point for square stopes or silos because shape of silos/stopes introduce additional geometry related parameters when trying to derive an analytical equation.

Also limited literature of in situ measurements of stress in backfilled mine stopes (Belem et al. 2004; Helinski et al. 2011; Thompson et al. 2012) and in silos (Blight 1986; Ooi et al. 1990) are available currently. However, few have reported the lateral variation of vertical stress, such as Robertson et al.(1986), who clearly identified an in situ lateral variation of vertical stress in backfill, with a penetrating tool to measure the stresses. O'Neal and Hagerty (2011) showed that the vertical stress decreases significantly near the walls when confined with vertical walls in road embankment backfills. Additionally, with difficulties of obtaining in situ measurements of vertical stresses in this type of backfilling situations, numerical simulations provide a viable alternative to estimate the lateral variations of vertical stresses. Li and Aubertin (2008) proposed expressions for lateral stress variation using limit analysis and numerical simulations and further verified their proposal with FLAC simulations. Additionally, Li and Aubertin (2009) discussed the effect of stope width, stope height and material internal friction angle on the vertical stress variation, but have not included the effect of Poisson's ratio, which will be analysed in this chapter.

Pressure isobars or vertical stress contours beneath a uniformly loaded square or strip footing are found in most geotechnical textbooks (e.g. (Sivakugan and Das 2010). This is a simple and effective tool that can be used for quick determination of the vertical stress increase beneath a footing at any location. The isobars developed for silos, mine stopes and trenches are similar in principle and the way they are applied. An attempt is made to address all relevant input parameters in backfilling scenario and discuss their effect on estimating the vertical stresses within granular backfills

surrounded by vertical walls, under axisymmetric and plane strain conditions. These isobars can be used for determining the vertical stress at a specific location in a silo or stope of any dimensions, with due consideration to arching. The objective of this chapter is to present a simple method using vertical stress isobars, for determining the vertical stress at any point within the granular fill, contained within vertical walls.

4.1 Sensitivity study for parameters used with simulations

Geological materials are naturally non-uniform. The density the backfill material is a prime input parameter for numerical models. Filling method is important for the stress distribution as it governs the lateral pressure coefficient within the fill (Michalowski 2005). Though the density could be slightly different with the funnel filling, the assumption of uniform density is made for model simplicity and numerical solution efficiency (Karlsson et al. 1998). The influence of other input parameters, such as friction angle, Young's modulus, Poisson's ratio, interfacial friction angle, dilation angle and cohesion was identified through a systematic sensitivity analysis.

A 24 m wide (B) and 144 m high (H) (i.e., height/width = 6) structure was chosen and divided into square zones throughout. The horizontal bottom boundary as well as the vertical boundary on the non-symmetrical axes are fixed for displacements in both X and Y directions. Interface elements were included to simulate the interaction between the backfill and structure. Table 4.1 summarises the selected cases and the different parameters used in these cases.

Table 4.1. Summary of material properties used in the sensitivity study

Case	E (MPa)	v	δ	ψ , c (kPa)	number of layers
A	50	0.20	40°	0°,0	240
B	10	0.20	40°	0°,0	240
C	3000	0.20	40°	0°,0	240
D	50	0.25	40°	0°,0	240
E	50	0.30	40°	0°,0	240
F	50	0.20	30°	0°,0	240
G	50	0.20	20°	0°,0	240
H	50	0.20	10°	0°,0	240
J	50	0.20	40°	5°, 0	240
L	50	0.20	40°	10°,0	240
M	50	0.20	40°	0°,0	8
N	50	0.20	40°	0°,0	48
R	50	0.20	40°	0°,50	240
S	50	0.20	40°	5°, 50	240

4.1.1 Influence of friction angle

Friction angles of granular backfills depend on the relative density and can vary from 30° for loose state to as high as 45° for dense state. The friction angle of hydraulic fills used commonly for backfilling underground stopes can be in the range of 29° to 45°, depending on the relative density (Pirapakaran and Sivakugan 2007b). Therefore, it is required to evaluate the effect of friction angle on vertical stress and, friction angles in the range of 30° to 45° were considered in this analysis.

Variation of normalised vertical stress $\sigma_v / \gamma B$ with normalised depth z/B along the centre line, determined from numerical simulations shown in the Figure 4.2. Here, it is assumed that the granular backfill is a Mohr-Coulomb material with E = 20 MPa, ν = 0.2, and γ = 20.0 kN/m^3 for these simulations. The vertical stresses are significantly less than the overburden pressures computed as the product of the unit weight and depth (Figure 4.2). For example, at depth of 6B, the vertical stress is 42% of the overburden pressure, clearly showing the arching effect. Moreover, the vertical stress varies within a narrow band for the friction angle range of 30° to 45° and it appears that, the friction angle has little influence on the magnitude of the vertical stress.

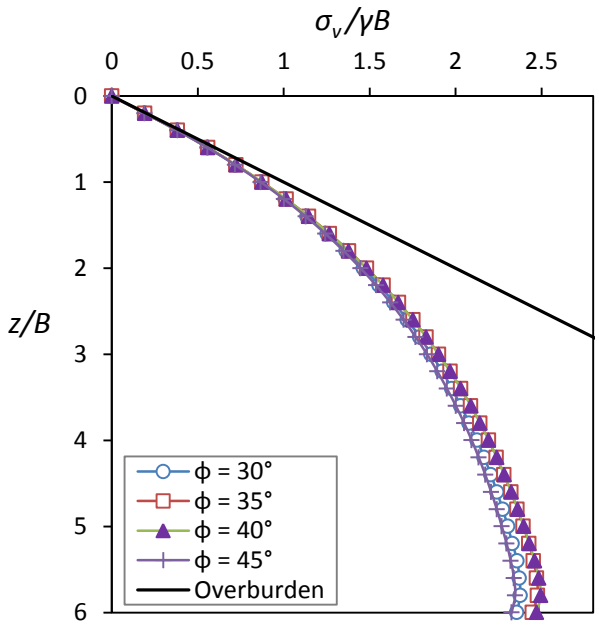

Figure 4.2. Variation of average vertical stress with depth for various friction angles E = 20 MPa, ν = 0.20, and γ = 17.65 kN/m³

The influence of the friction angle on the vertical stress was further analysed by investigating the stress values at 15 different locations within the right half of the fill. The points were located at horizontal distances of 0.15*B*, 0.25*B* and 0.35*B*, and at vertical depths of *B*, 1.5*B*, 2*B*, 2.5*B* and 4*B*, giving 15 grid points in total. The variations of σ_v with ϕ at these 15 locations are shown in Figure 4.3.

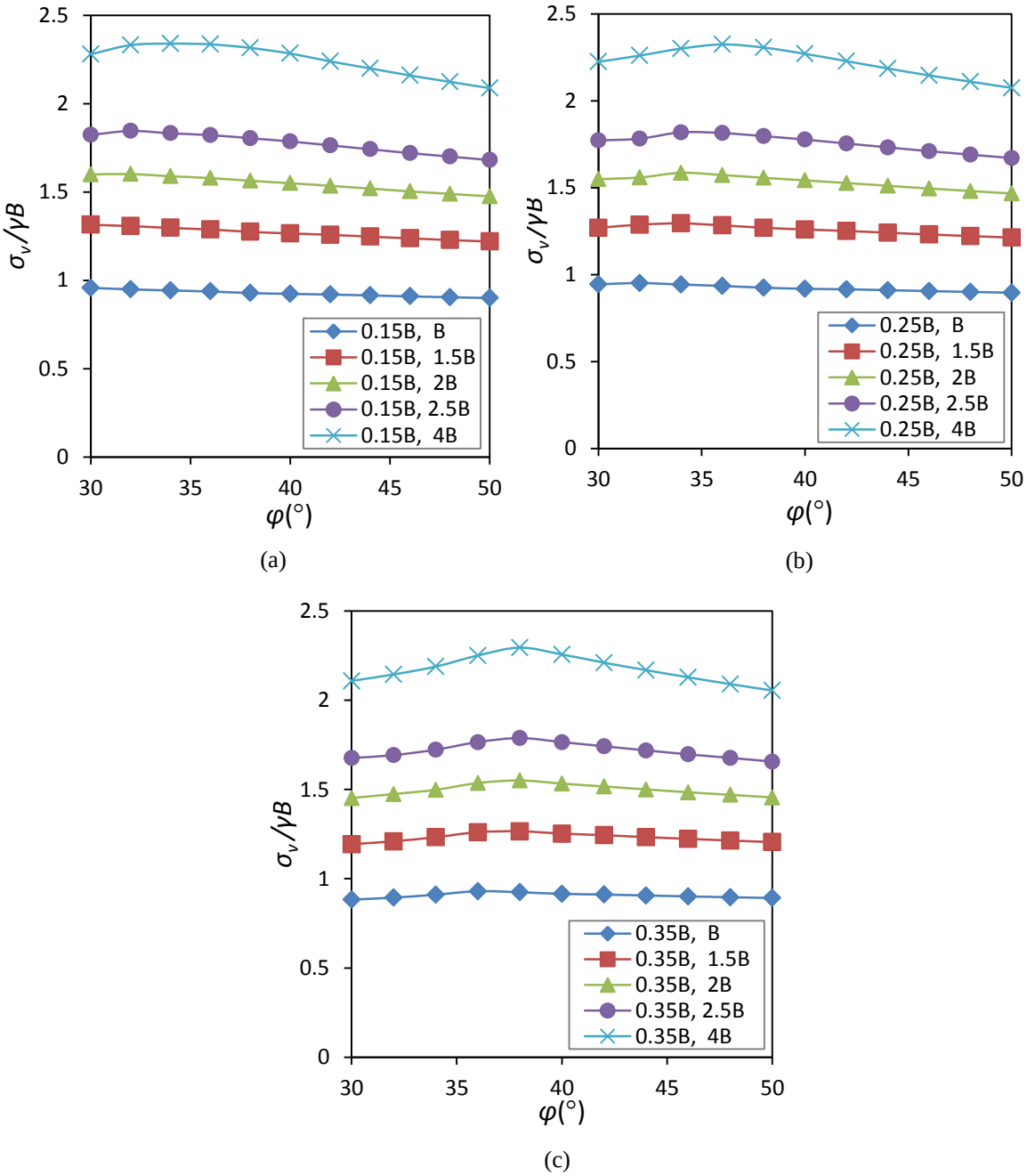

Figure 4.3. Vertical stresses for selected 15 points within the fill for friction angles 30° to 50° and E = 20 MPa, ν = 0.20, and γ = 17.65 kN/m^3; (a) width 0.15*B* from the centre, (b) width 0.25*B* from the centre and (c) width 0.35*B* from the centre.

As shown in Figure 4.3, the vertical stress (σ_v) is insensitive to ϕ in the range of 30° to 50°. Therefore, in developing the isobars proposed herein, ϕ is taken as 40°, which represents the stress values across the range of 30° to 50°. The error in assuming ϕ = 40° for all fills is studied further. The error is defined as the difference between $\sigma_{v,\phi}$ and $\sigma_{v,40}$, divided by $\sigma_{v,40}$, and expressed as a percentage. Here, $\sigma_{v,\phi}$ and $\sigma_{v,40}$ are the vertical stress values computed at friction angles of ϕ and 40° respectively. The error histogram is presented in Figure 4.4 and the error is less than 9% for any of the 165 points. Therefore, the isobars were developed with friction angle of 40° and they can be used to evaluate the vertical stress for any friction angle between 30° and 45°, with maximum error of 9%.

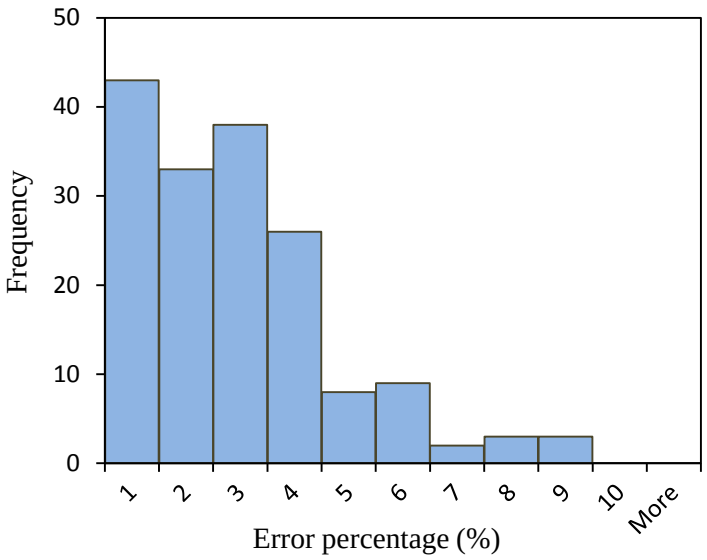

Figure 4.4. Error distribution when 40° selected as the reference friction angle to estimate vertical stress within a backfilled structure

4.1.2 Young's modulus and Poisson's ratio

Stiffness properties are also often used as input parameters when a numerical simulation is carried out. First the effect of Young's modulus for the vertical stress along the centre line was studied. Figure 4.5 shows the variation of normalised vertical stress $\sigma_v/\gamma B$ with normalised depth z/B, along the vertical centre line, for different

values of Young's modulus (E), ranging from 10 MPa to 3000 MPa. It is evident, from the Figure 4.5, that the Young's modulus has no influence on the vertical stress variation. This agrees with the observation made by Li and Aubertin (2009b) for E ranging from 30 MPa to 300 MPa. When the Young's modulus is high, less shear strain is required to fully mobilise the shear strength. However, with a low stiff (soft) material large shear strains are required to fully mobilise the shear strength. As a result, the change of Young's modulus would not influence the vertical stress.

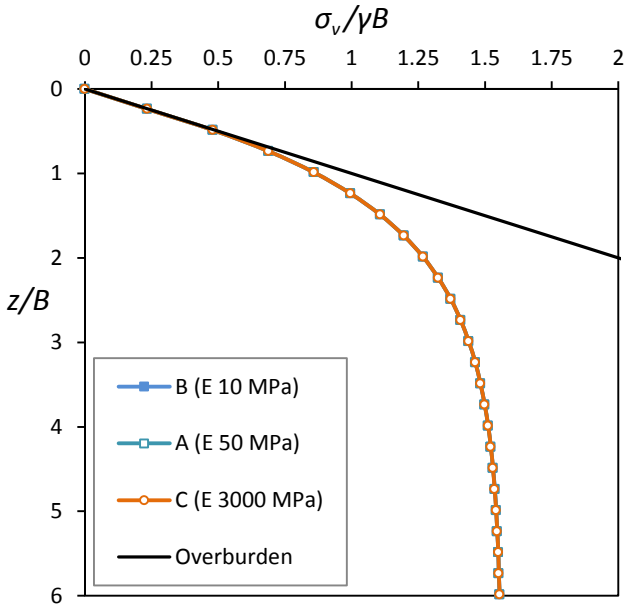

Figure 4.5. Vertical stress variation along centre with Young's modulus, when the model filled in layers; ν = 0.25 and γ = 17.65 kN/m³

Next, the effect of Poisson's ratio (ν) was studied. FLAC simulations were carried out with Poisson's ratio varying in the range of 0.2 - 0.3 and the variation of $\sigma_v / \gamma B$ versus z/B is shown in Figure 4.6, assuming γ = 17.65 kN/m^3 and E = 50 MPa. A significant change in vertical stress, at centre, is observed when the Poisson's ratio is changed (Figure 4.6a). Li and Aubertin (2009) observed that the vertical stress is higher when ν = 0.2, and lower when ν = 0.4. The horizontal stress at wall and the stress ratio (horizontal stress at wall to vertical stress at centre) is considered in Figure 4.6b and 4.6c, respectively, to elaborate the effect of Poisson's ratio on arching and stress variations within the fill.

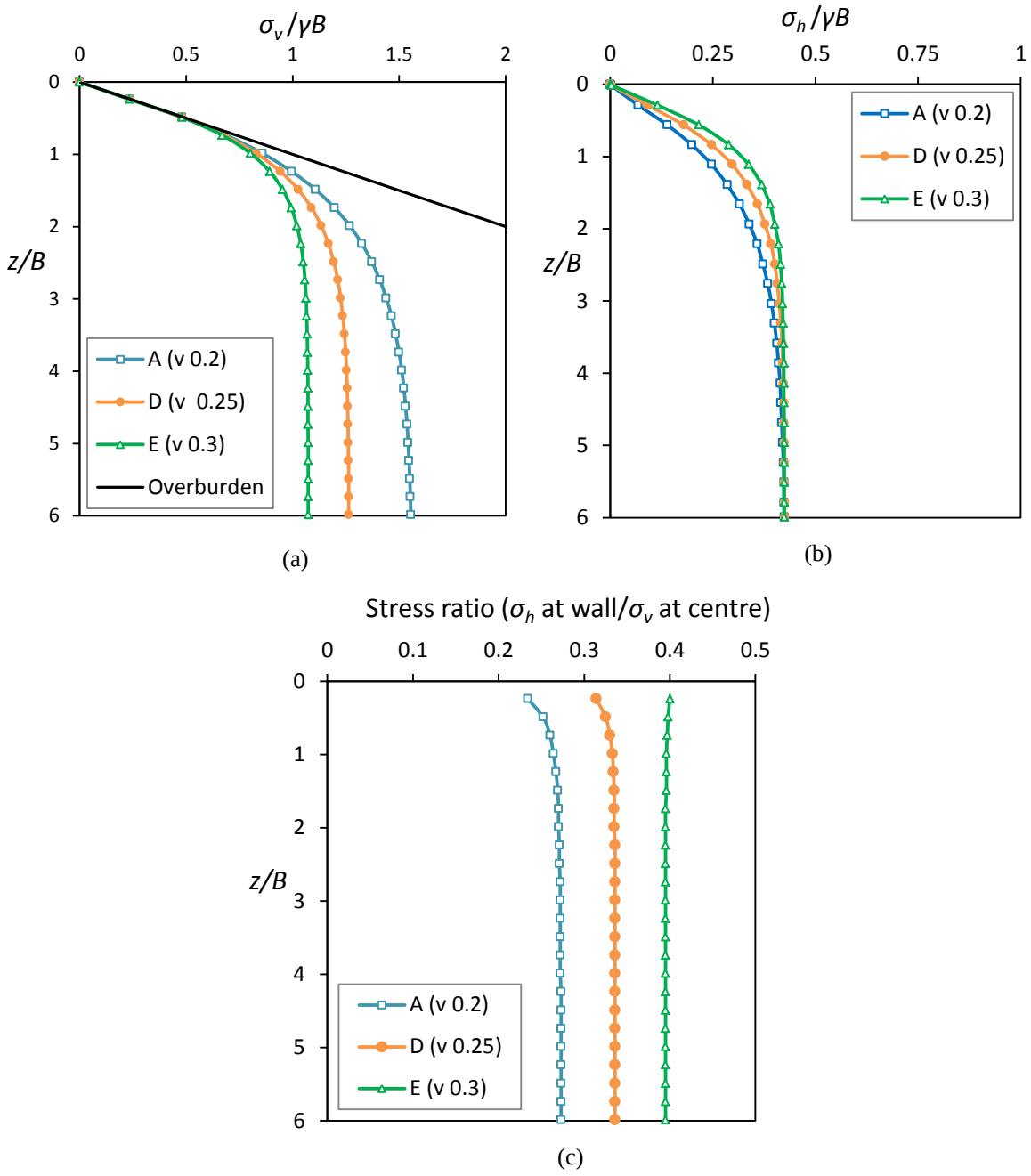

Figure 4.6. Stress variations for different Poisson's ratio, when the model filled in layers, E = 50 MPa and γ = 17.65 kN/m³; (a) vertical stress at centre, (b) horizontal stress at wall and (c) horizontal stress at wall to vertical stress at centre ratio

The horizontal stress at wall, is varied with Poisson's ratio at lower depths ($z/B < 3$), when the arching is not fully developed. Later, the arching is fully developed, and the horizontal stress at the wall does not vary with the Poisson's ratio (Figure 4.6b). However, the horizontal stress to vertical stress ratio changes with the Poisson's ratio

and mostly constant for the specified Poisson's ratio for the model (Figure 4.6c). Moreover, the stress ratio is increased with the increase of input ν. This can be explained with definition for lateral pressure coefficient at rest; 'elastic K_o' value (Equation 4.1) and the ratio of bulk modulus to shear modulus.

When the granular material is treated as a linear elastic continuum, the coefficient of earth pressure at rest is related to the Poisson's ratio as follows;

$$K_0 = \frac{\nu}{1-\nu} \tag{4.1}$$

The 'elastic-K_o' value increases with the Poisson's ratio (Figure 4.7). This increase of elastic-K_o' reduces the vertical stress at depths more than 3*B*. However, the horizontal stress remains the same for depths more than 3*B*, when an elastic material is considered (Figure 4.6b).

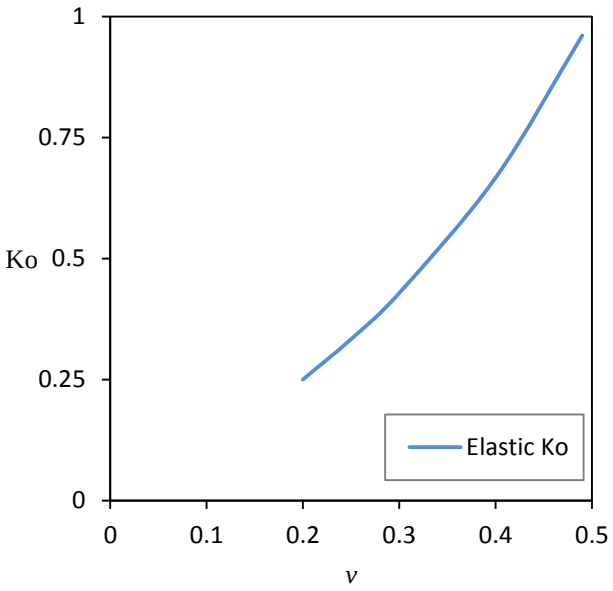

Figure 4.7.Variation of 'elastic K_o', with Poisson's ratio

On the other hand, the ratio of Bulk modulus to Shear modulus (the modulus ratio) in isotropic elastic materials can be directly related to the Poisson's ratio (Greaves et al. 2011). This is evident in Equation 4.2, where the modulus ratio only consists of *v*;

$$\text{Bulk modulus/ Shear modulus} = \frac{2(1+\nu)}{3(1-2\nu)} \tag{4.2}$$

Bulk modulus dictates compression and shear modulus dictates distortion. Therefore, the modulus ratio is an indication of whether the material favours compression or shearing. When Poisson's ratio is small, the modulus ratio also small and, the material is easily compressed than sheared. Loose material, with lower *ν*, undergoes larger compression with addition of mass from the top than shearing. However, the medium dense material has higher *ν* (e.g., 0.3), implying the modulus ratio is large, and therefore material favours shearing than the compression. When the material in favour of shearing, the shear strength tends to fully mobilise at a lower depth and therefore arching is more prominent, and that leads to lower vertical stresses at the bottom. Hence, the *ν* decides whether the compression or the shearing is more apparent within the material when filled between rigid walls, and also the vertical stress reductions with arching.

Next, either Elastic or Mohr-Coulomb constitutive models can be used for backfill in FLAC simulation models. The vertical stress variation with elastic constitutive models are arranged with legend 'Elastic, ν = 0.2' and 'Elastic ν = 0.3'). Mohr-Coulomb constitutive models are used with different *φ* values and the results are given in legend under 'Mohr-Coulomb'. The average stress variation of Mohr-Coulomb material models with $\varphi = 40°$, closely matches to elastic models when $\nu = 0.2$ (Figure 4.8).

Furthermore, the average vertical stresses are compared with analytical equations (Equation 3.19) with different K values. The analytical results are given under the legend '$K = K_0$', '$K = K_a$' and 'K = elastic K_0'. The average vertical stress variation with FLAC elastic model closely matches with the estimations from Equation 3.19, when the K is taken as K_a or elastic K_0 (Figure 4.8). This implies that the elastic constitutive model would output results that are agree with analytical equations as well as the results from Mohr-Coulomb constitutive model, with given parameters and input

values. Therefore, the vertical stress isobars are produced with FLAC simulations, including elastic constitutive model for the backfill.

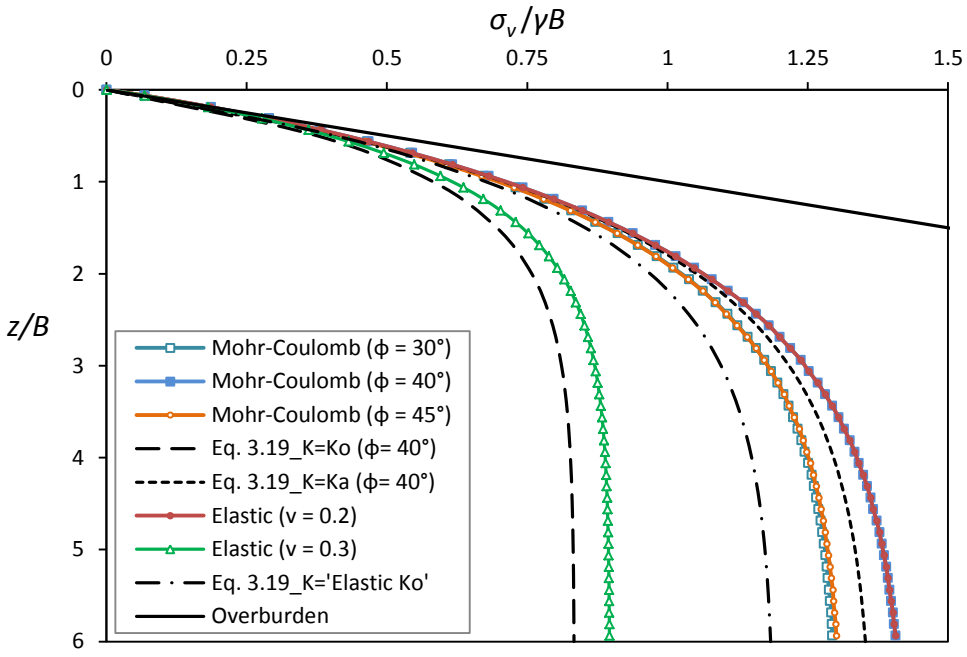

Figure 4.8. Variation of average vertical stress for Mohr-Coulomb material and for elastic material. Analytical equation estimations are also included with K_o, K_a and 'elastic K_o'

4.1.3 Interfaces and interfacial friction angle

Interfacial friction angle (δ) is included in arching theory and the influence of wall friction angle on the stress variation has been identified early and discussed by many researchers in the form of analytical equations similar to Equation 3.19 (Marston and Anderson 1913; Handy 1985; Paik and Salgado 2003; Goel and Patra 2008; Singh et al. 2011) and also in numerical simulations (Li and Aubertin 2009b; Ting et al. 2011). Shear stresses lead to arching and result vertical stress reductions and therefore, the interfacial friction angle has an impact on the vertical as well as horizontal stress variation.

The walls, in mine stopes, are formed after explosive blasts and highly irregular with fully rough conditions. Therefore, the shear failure does not occur at the interface

between backfill and rock wall, but occurs inside backfill, where several grain diameters away from the wall (Borgesson 1981; Singh et al. 2010). Figure 4.9 shows the wall of a freshly blasted stope wall in an underground mine and the rough wall surface, seen in Figure 4.9, justifies the assumption of wall-fill interfacial friction angle as the same as the friction angle of the fill. This is common with backfilled trenches, where the excavated soil surface is rough and hence a fully rough wall at the interface can be assumed. Therefore any vertical slip will take place few grains away from the rock wall. However, in grain containers, such as silos, the walls often consist of construction materials, such as concrete, metal etc. and therefore those walls can be assumed as medium rough.

Figure 4.9. A photograph showing the wall roughness in a mine stope (courtesy of Mr. Patrick Wilson, Ravenswood mine, Queensland).

Within backfilled mine stopes, trenches or filled silos, the granular material interacts with the surrounding and modelling of this soil-structure interaction would be vital. FLAC and FLAC^{3D} contain built-in interface elements, which can be used effectively to model this interaction. Interface elements follow the Mohr-Coulomb criterion with specified tension cut-off. The displacement and force transfer between

boundary and the fill is modelled through normal (K_n) and shear (K_s) stiffness for the interface. However, the stiffness properties of interface, K_n and K_s, are not readily defined and the empirical values suggested by FLAC user manual (Itasca 2011), were used with simulations.

Four simulations with different interfacial friction angles (cases A, F, G and H; δ = 10°- 40°) were conducted. Figure 4.10 shows the variation of $\sigma_v/\gamma B$ versus z/B for different values of the wall-fill interfacial friction angle (δ), while all other parameters remained the same. The interfacial friction angle has significant influence on the vertical stresses within the fill, and the vertical stress is decreased with the increase of δ (Figure 4.10). Shearing at the boundary (rock, soil or concrete) leads to stress redistribution and transfers a significant amount of fill load to walls. With rough walls (e.g. mine stopes), a larger fraction of the fill weight is transferred to the wall and lesser load is transferred to the base resulting in lower values of vertical stress. For very smooth walls (i.e. δ = 0), the variation of vertical stress is same as the overburden stress, which is simply the product of the unit weight of the fill and the depth. Here, the entire fill weight is transferred to the base, without arching.

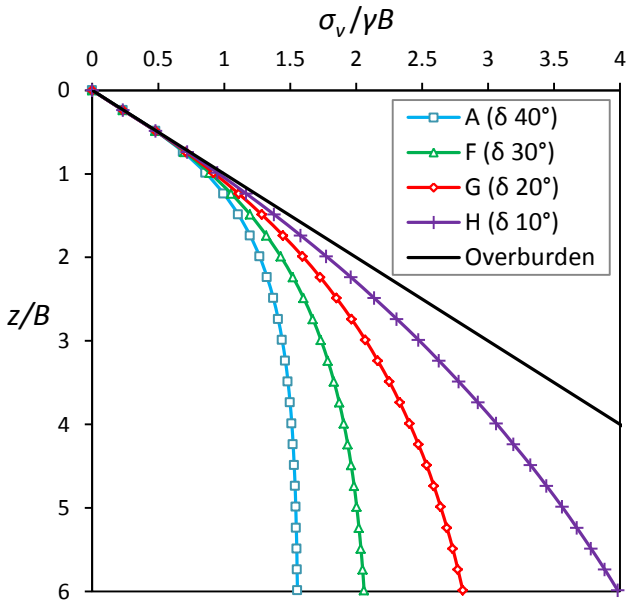

Figure 4.10. Vertical stress variation along the centreline for different values of interfacial friction angle (E = 50 MPa, ν =0.20 and γ = 17.65 kN/m³)

4.1.4 Dilation angle and cohesion

Dilation affects the interface behaviour, and can be included as a property of interface elements. A non-associated flow rule is used for granular materials, where the dilation angle is relatively small and would be less than the internal friction angle in backfilled masses (Jenike and Shield 1959; Karlsson et al. 1998). Few simulations (cases J, L, R and S) were conducted for different dilation and fill cohesion values. Figure 4.11 shows the variation of $\sigma_v / \gamma B$ against z/B for different values of dilation angle (ψ) and cohesion (c). The vertical stresses decrease with increasing values of ψ from 5° to 10°. Dilatant fill material induces a horizontal thrust, onto the wall via the interface elements, resulting higher normal stresses to the wall and leads to higher arching.

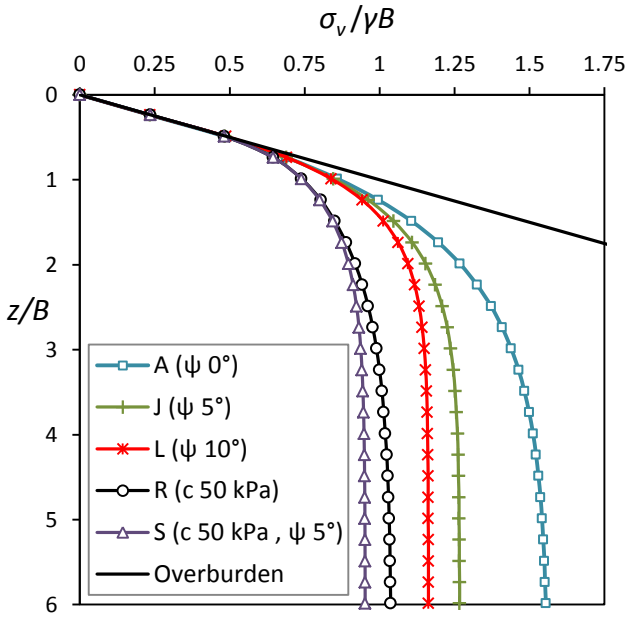

Figure 4.11. Vertical stress variation along the centreline for different values of dilation angle (ψ) and cohesion (c) of the fill (E = 50 MPa, ν = 0.20 and γ = 17.65 kN/m³)

When cohesion is included in the interface, the vertical stress at centre was decreased (Figure 4.11 - case R). Cohesion increases the shear stress and leads to arching resulting lower vertical stress at bottom. Therefore, cohesion enables a substantial fraction of the fill load to be carried by the wall, as it improves the shear

strength and hence vertical stress is significantly reduced the within the fill. Additionally, when the fill has both dilating and cohesion properties, the stress transfer is intensified, as both arching effects are superimposed and therefore the vertical stresses tends to be even less (Figure 4.13 – case S). However, the simulations considered herein for stress isobars, dilation angle is assumed to be zero, because the fill is loosely placed hence not dense enough to cause any dilation during shear.

4.2 FLAC simulation procedure

The numerical models show that there is lateral variation of the vertical stress at all levels, and the variation is more significant at larger depths where shear strength is fully mobilised, i.e. arching effects are more predominant for the stress developments in larger depths. Ting et al. (2011) showed that in plane strain conditions (i.e. trenches), the vertical stress σ_v reaches an asymptotic value, at a depth of 5B. Therefore, the isobars are developed only for depths up to 6B, beyond which there will be very little increase in σ_v. The exact values of vertical stresses within the backfill during filling were derived using FLAC, and are presented in the form of vertical stress isobars. Therefore, the vertical stress variation along the width or the vertical stress at any point within the fill can be obtained from this proposed vertical stress isobars charts. In the absence of such chart, it would require numerical simulations to determine these exact values.

A 24 m wide structure was chosen and a half-width of 12 m and a height of 6 times the width are modelled with a square mesh of 0.3 m × 0.3 m, which has 40 zones across the half-width. The horizontal bottom boundary is fixed for displacements in both X and Y directions. Material property parameters and values for the numerical simulations are listed in Table 4.2. It is assumed that the fill is dry and is surrounded by rock or concrete wall. The boundary or the surrounding material may be deformed before the filling takes place which depends on the construction material for silos or the ground stress conditions when backfilled mine stopes are considered. However, a

general case is considered here and wall deformation before the filling is not accounted when developing the isobars. The granular fill and wall material are both assumed to follow linear elastic constitutive model for the simplicity and simulations were carried out with $\delta = \varphi$ for very rough wall and $\delta = 0.5\varphi$ for medium rough wall.

The model was filled in 240 layers (layer height of 0.6 m), and the system was brought to equilibrium after each layer was placed. The vertical stress values at bottom were recorded into the array through a FISH code, according to method 1 as described in Chapter 3.5. The array, which consists of vertical stress of zones at bottom, is used to plot stress isobars chart.

Table 4.2. Parameters used with FLAC simulations to generate stress isobars

Property	**Granular fill**	**Rock/ Concrete**
Constitutive model	Linear elastic	Linear elastic
Unit weight (kN/m³)	17.65	26.48
Young's modulus (MPa)	50	20 000
Poisson's ratio	0.2 and 0.3	0.3
Friction angle (°)	40	-
Cohesion (MPa)	0	0
Interfacial friction angle	40° and 20°	
Interface stiffness K_n,K_s (MPa/m)	1850 , 2250	
Interface cohesion (MPa)	0	
Interface dilation angle (°)	0	

(a)

Stress isobar values are normalised with the unit weight and the width of the structure (Figure 4.12). The stress isobar values were normalized, so that these isobars can be used for any application like a silo filled with grains or a mine stope filled with backfills, where different unit weights and structure dimensions are encountered. Therefore, the vertical stress at any location within the granular material contained within the structure can be estimated using stress isobar charts and Equation 4.3.

$$\sigma_v(kPa) = isobar\ value \times \gamma\ \left(\frac{kN}{m^3}\right) \times B(m) \tag{4.3}$$

Continuous lines and dashed lines were used for stress isobars, where continuous lines represent ν = 0.2 and dashed lines represent ν = 0.3. Noting the two different sets of isobars for ν = 0.2 and 0.3, interpolation is possible for Poisson's ratio values within that range. The contour interval was maintained as 0.05γB, for the entire height of 6B with stress isobars, for the sake of clarity in the isobars chart. A clutter of lines near the walls might occur if a finer contour interval is introduced and therefore the same contour interval was maintained with stress isobars charts presented herein. The distance between successive contours increases with z/B, implying that the rate of increase in the stresses reduces with depth, because of arching. However, these isobars can be used for any width and any height up to six times the width only.

4.3 Stress isobars for plane strain conditions and validation

The backfilled trenches or narrow mine stopes are assumed considerably long, and are treated as plane strain problems. Then stress isobars were developed with plane strain configuration in FLAC simulations. Half of the model was simulated because of the symmetry and a roller boundary was applied along the centre. The other end of the model was connected to the walls with interface elements. As backfilled tranches or narrow mine stopes were considered, it is reasonable to assume that $\delta = \phi$ and the isobar chart for plane strain configuration is presented in Figure 4.12, where the heights from 0 - 2B, 2B - 4B and 4B - 6B were separated for clarity.

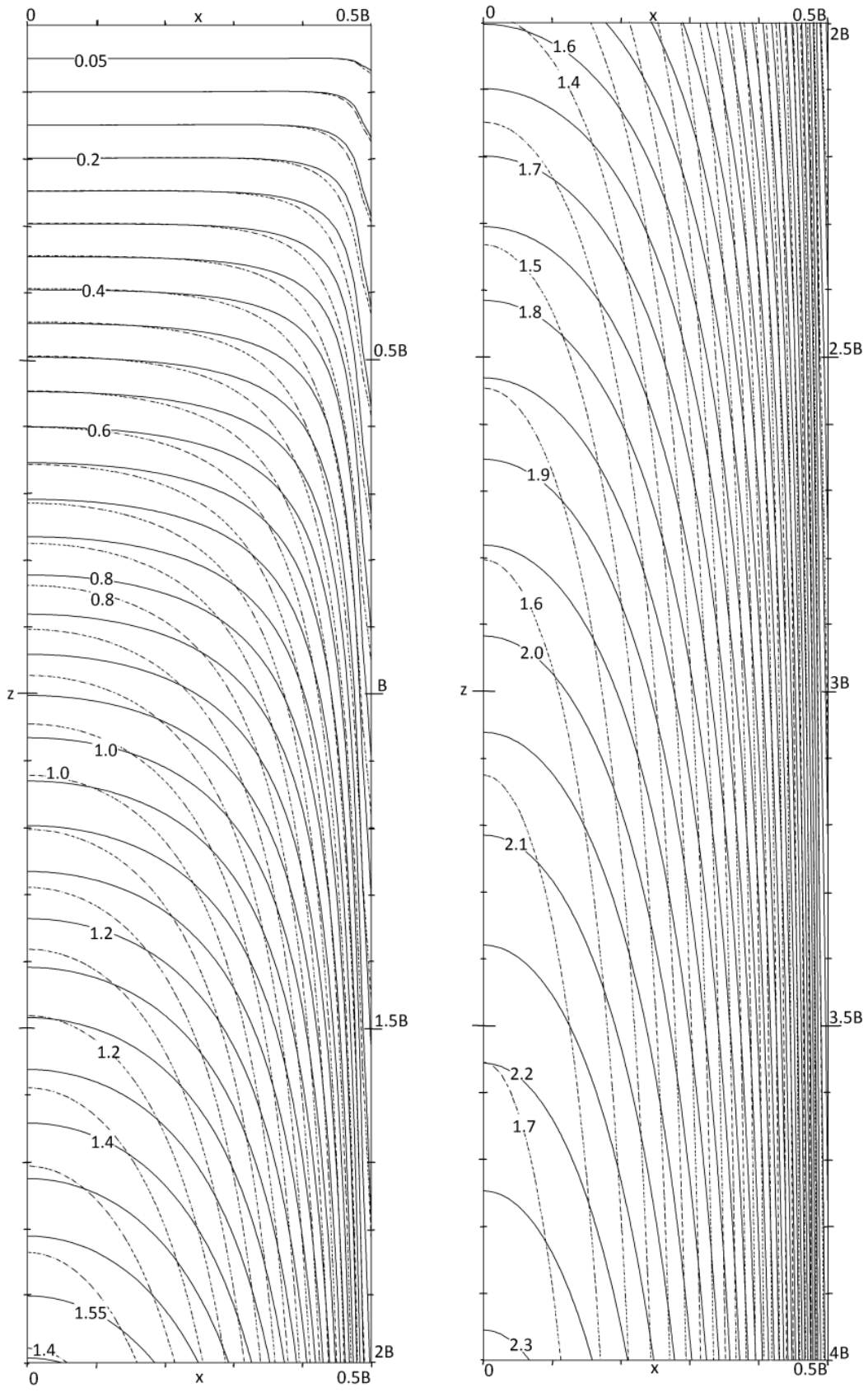

(a) (b)

Figure 4.12. Stress isobars for plane strain conditions- trenches for (a) z = 0-2*B*, and (b) z = 2*B*-4*B*

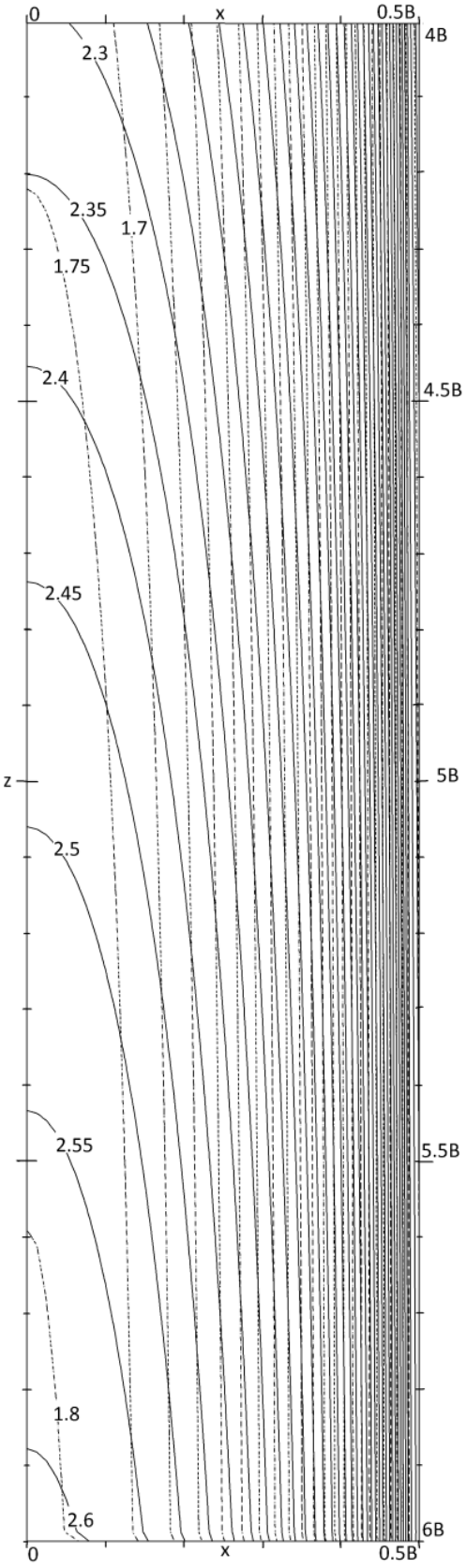

(c)

Figure 4.12. Stress isobars for plane strain conditions- trenches for (c) z = 4B-6B

The proposed isobars for plane strain conditions were validated against 36 scenarios with randomly selected dimensions and Poisson's ratios that are representative of field situations as in Table 4.3. As the width and height of the backfilled structure is considered according to cases in Table 4.3, the vertical stresses were computed using 36 FLAC simulations. Then, the vertical stresses were also determined using the isobars and Equation 4.3 for given 36 scenarios. The vertical stresses determined from above two approaches, are compared in Figure 4.13, where the stress estimated with stress isobars chart is matching to the stresses determine from FLAC simulations (i.e., all the points are in the close vicinity of the line of equality). The comparison in Figure 4.13 shows an excellent agreement, reinforcing the validity of the isobars for determining the vertical stress within a granular fill contained in a trench or a mine stope.

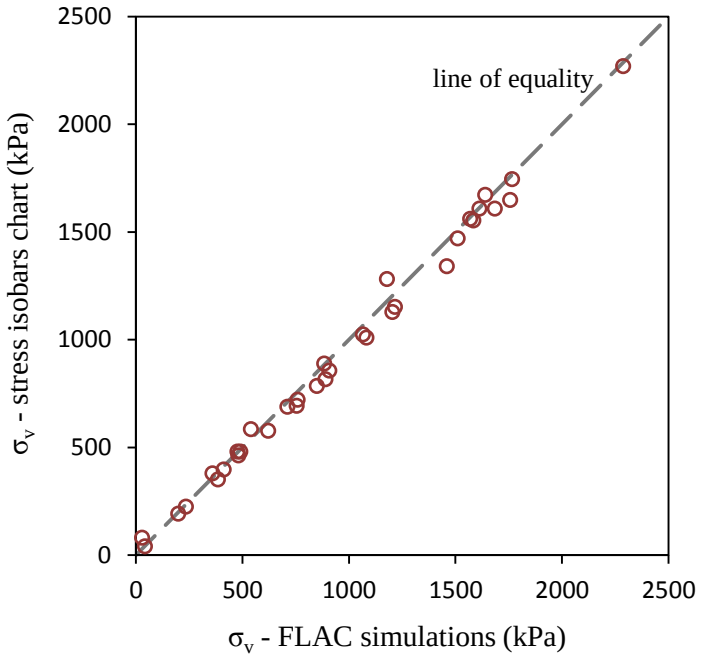

Figure 4.13. Comparison of vertical stresses estimated for selected random cases in Table 4.3 with plane strain stress isobar charts and individual FLAC simulations

Table 4.3. Scenarios used for verification of plane strain stress isobar charts

Scenario	Width (B)	Height (H)	ν
1	11	37.86	0.2
2	14	47.84	0.2
3	14	61.80	0.2
4	6	30.45	0.3
5	6	29.51	0.2
6	15	20.40	0.3
7	5	122.48	0.3
8	14	31.35	0.2
9	6	13.75	0.2
10	12	53.72	0.2
11	11	29.41	0.2
12	13	51.38	0.3
13	12	62.15	0.3
14	13	82.18	0.3
15	9	37.83	0.2
16	10	9.72	0.3
17	13	23.75	0.2
18	15	113.28	0.2
19	15	56.12	0.2
20	8	64.13	0.2
21	13	58.50	0.3
22	9	21.17	0.2
23	15	9.25	0.2
24	7	73.80	0.2
25	10	38.50	0.3
26	10	59.10	0.2
27	9	60.35	0.3
28	13	63.65	0.3
29	8	8.38	0.3
30	10	16.40	0.3
31	10	135.13	0.3
32	8	26.13	0.2
33	7	34.60	0.2
34	11	26.26	0.3
35	15	31.90	0.2
36	11	27.43	0.2

4.4 Stress isobars for axisymmetric conditions and validation

The hydraulic diameter, which is the ratio of cross sectional area to the perimeter, plays a significant role when the filled material is subjected to arching. For square and circular cross sections of the same width, the cross sectional area to perimeter ratio (A/P) is same. Also the vertical stress profiles are similar for the two (Equations 3.14 and 3.16). The vertical normal stress variations along three vertical lines (i.e. x = 0, $B/4$ and $B/2$ where B is the width and x is measured from centre) on the vertical plane of symmetry of circular silo and a square mine stope compared in order to understand the similarity (Figure 4.14). Axisymmetric configuration was used for modelling the silos, and only the vertical radial plane is modelled. FLAC^{3D} was used for modelling the stopes with square cross section with brick zones of 0.3 m sides. In both simulations, the backfill was connected to the walls with interface elements.

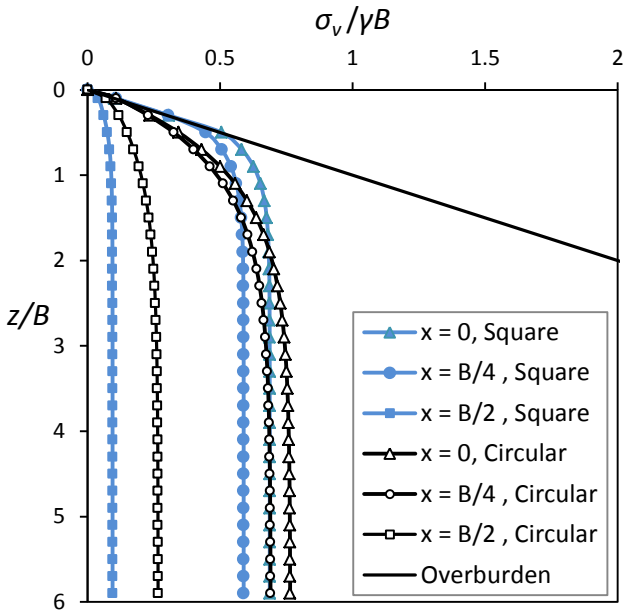

Figure 4.14. Vertical stress variation at x = 0, $B/4$ and $B/2$ for square and circular structures filled with granular materials (E = 50 MPa, ν = 0.20 and γ = 17.65 kN/m³)

As seen in the Figure 4.14, the vertical stress at the centre closely follows each other. But closer to the wall, the vertical stresses may have large error in assuming that square and circular cross sections give the same results. Therefore, the vertical stress isobar for axisymmetric conditions can be used for square cavities with vertical walls (e.g. mine stopes) backfilled with granular materials, but the error would be higher when estimating stresses near the edge.

Stress isobars for interfacial wall frictions of $\delta = \varphi$, $\delta = 0.5\varphi$ are given in Figures 4.15 and 4.16 respectively. As the walls within silos are not rough, stress isobar charts with $\delta = 0.5\varphi$ (Figure 4.16) are more suitable to be used with silos. Additionally, with interpolation, Figures 4.15 and 4.16 can be used for determining the stress isobar values another interfacial friction angle, for δ in the range of 0.5φ to φ.

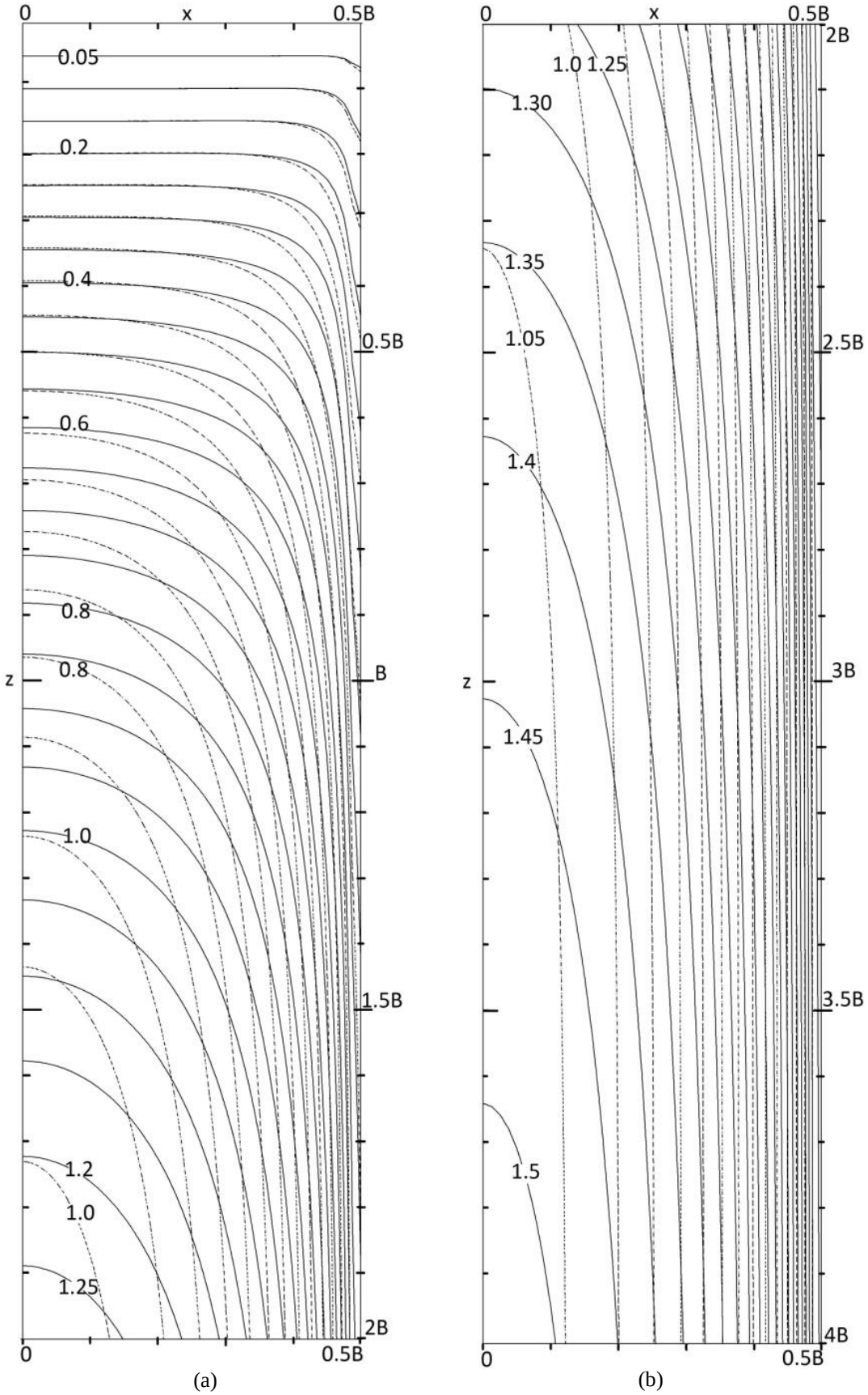

Figure 4.15. Axisymmetric vertical stress isobars for $\delta = \varphi$;

(a) z = 0 - 2*B*and (b) z = 2*B* - 4*B*

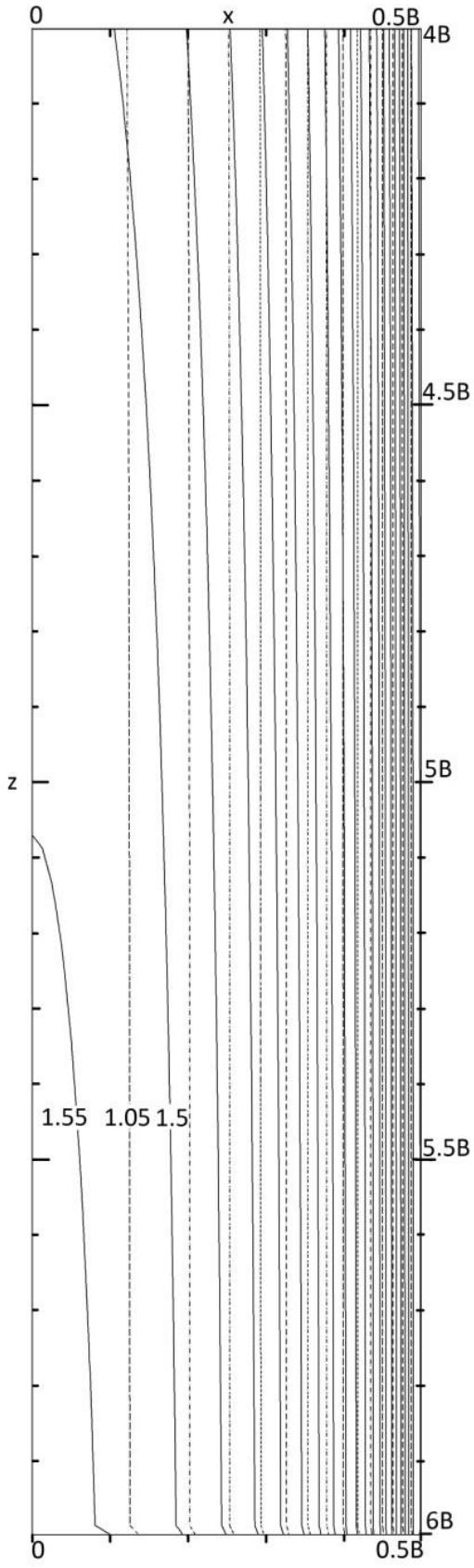

(c)

Figure 4.15. Axisymmetric vertical stress isobars for $\delta = \varphi$;

(c) z = 4*B* - 6*B*

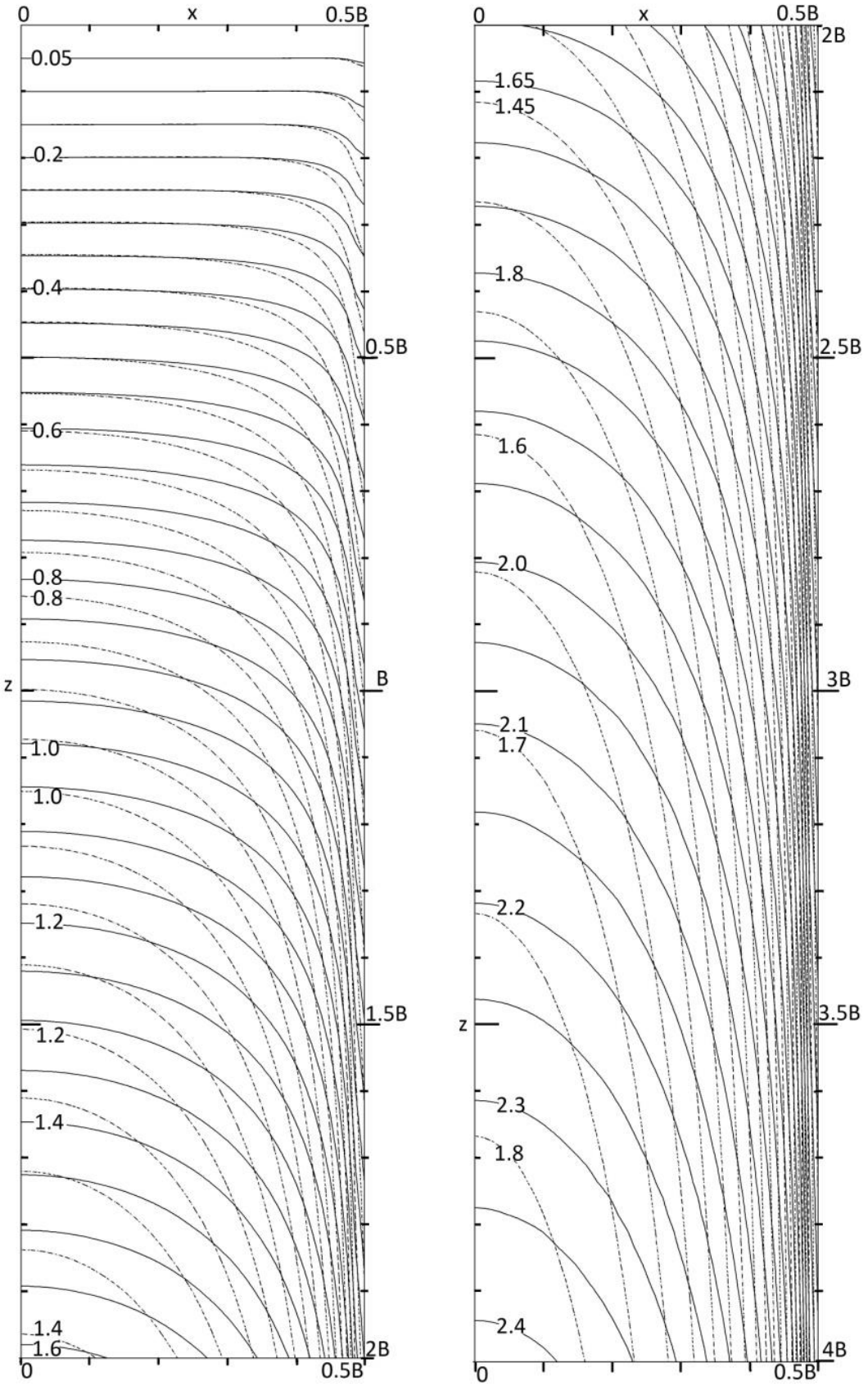

Figure 4.16. Vertical stress isobars for $\delta = 0.5\,\varphi$; (a) z = 0 - 2B, (b) z = 2B - 4B, and (c) z = 4B - 6B

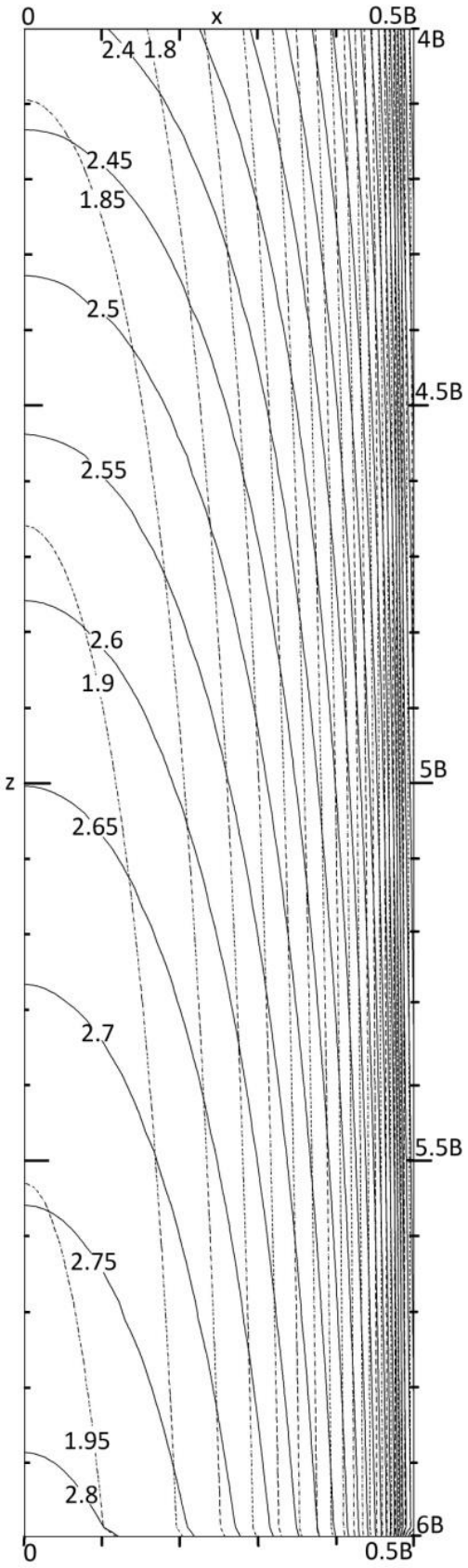

(c)

Figure 4.16. Vertical stress isobars for $\delta = 0.5\,\varphi$; (a) $z = 0$ - $2B$, (b) $z = 2B$ - $4B$, and (c) $z = 4B$ - $6B$

To validate stress isobars proposed for silos and square mine stopes, 36 cases were randomly selected for silos of various dimensions, at different stages of filling (Table 4.4). Poisson's ratios of 0.2 or 0.3, and interfacial friction angle of φ or 0.5φ were also randomly chosen for these cases. Here, each case was a different combination of width, depth and Poisson's ratio. Rest of the parameters were the same as those in Table 4.2. The normal stress values were computed using numerical simulations and were also estimated using isobars given in Figures 4.15 and 4.16. Then the vertical stress estimations were compared in Figure 4.17. It can be seen that all the points are in the close vicinity of the line of equality. Therefore comparison in Figure 4.17 shows an excellent agreement between the use of stress isobars to estimate vertical stresses and simulate each and individually simulated scenarios in FLAC for axisymmetric cases.

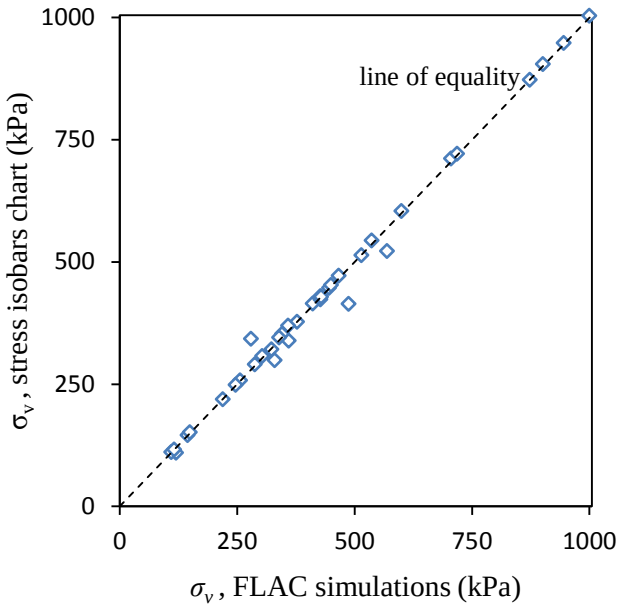

Figure 4.17. Comparison of vertical stresses estimated for selected random cases with axisymmetric stress isobars and individual FLAC simulations

Table 4.4. Scenarios used for verification of axisymmetric stress isobar charts

Scenario	**Width (*B*)**	**Height (*H*)**	***v***	***δ* (°)**
1	18	27.0	0.2	20
2	15	18.0	0.2	40
3	24	61.8	0.2	20
4	21	30.5	0.3	20
5	22	125.4	0.3	40
6	16	20.4	0.2	40
7	23	122.5	0.2	40
8	6	31.4	0.3	40
9	10	13.8	0.3	20
10	18	37.8	0.2	40
11	15	72.0	0.3	20
12	15	51.4	0.2	40
13	22	62.2	0.2	40
14	19	82.2	0.2	20
15	17	37.8	0.2	40
16	20	42.0	0.2	40
17	19	23.8	0.2	20
18	23	113.3	0.3	40
19	5	15.0	0.2	40
20	19	64.1	0.3	40
21	18	58.5	0.2	40
22	17	71.4	0.3	20
23	22	33.0	0.3	20
24	24	73.8	0.2	20
25	22	38.5	0.3	20
26	13	74.1	0.2	20
27	17	60.4	0.3	40
28	19	63.7	0.2	40
29	5	8.4	0.3	20
30	8	16.4	0.2	20
31	23	135.1	0.3	20
32	19	26.1	0.3	20
33	8	34.6	0.3	40
34	13	19.5	0.2	40
35	22	31.9	0.3	20
36	9	48.6	0.2	20

The error percentages for these validation exercises were arranged as histograms in Figure 4.18 for plane strain and axisymmetric scenarios. The error in 83% of the cases is less than 4% for axisymmetric isobars and 80% of the cases the error is less than 8% for PS isobars. Again, few large errors were recorded when estimating the vertical stresses near the wall. The stress isobar charts, created using FLAC numerical modelling, verified with individual FLAC simulations, which consist of a circular argument. This procedure was followed because of the lack of in situ stress data related to backfilled stopes. However, in overall Figures 4.18 reinforce the validity of the isobars for determining the vertical stress in a granular fill contained within rigid walls.

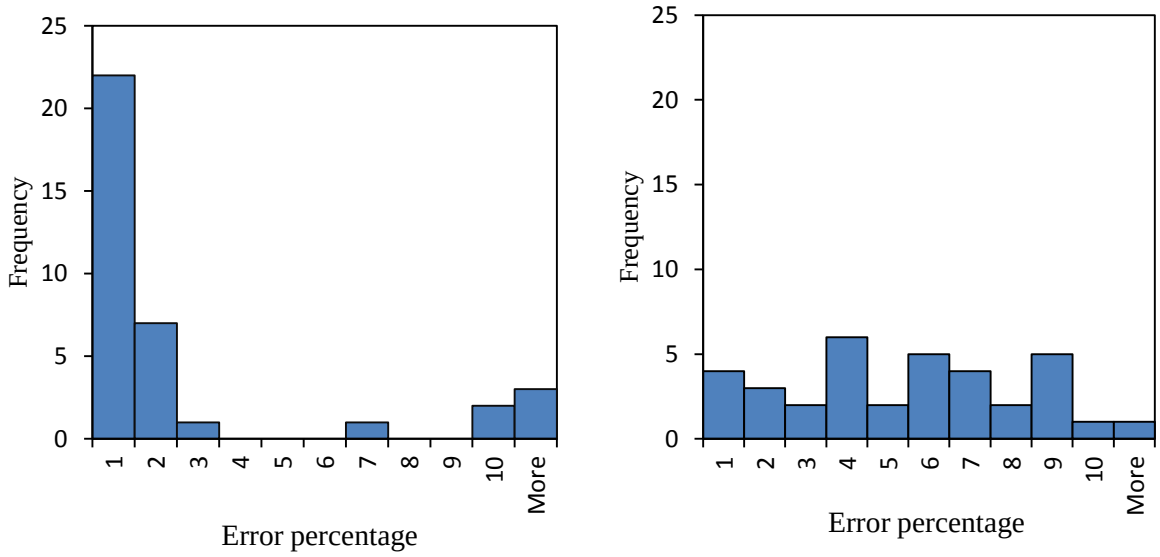

(a) (b)

Figure 4.18. Error of estimation, when stress isobar charts were used to estimate vertical stresses for scenarios; (a) plane strain stress isobars chart used for scenarios given on Table 4.3 and (b) axisymmetric stress isobars chart used for scenarios for given on Table 4.4.

4.5 Summary and conclusions

A thorough parametric study was carried out through numerical simulations, in an attempt to identify the parameters influencing the vertical stresses within the granular fill. The conclusions are summarised as;

- The vertical stresses at similar locations within a column of granular backfill surrounded by a rigid wall are approximately the same for square and circular cross sections.
- The internal friction angle (φ = 30° to 50°) has a minimal effect on the vertical stress variation along the centre line. Moreover, the lateral variation of vertical stress also considered for the above friction angles and the error of considering the φ = 40° is considered and found that the most of the error is less than 5%, if the friction angle for fill is assumed as 40°.
- The Young's modulus of the fill has no influence on the vertical stresses for the range of 10 MPa to 3000 MPa.
- Poisson's ratio has significant influence on the vertical stresses within the fill. Larger the Poisson's ratio, lower is the vertical stress transferred to the bottom, provided the other parameters remain the same.
- The use of interface elements to represent the fill-wall interface in the numerical simulations is effective, but it is necessary to choose appropriate values for K_n and K_s.
- Presence of dilation and cohesion within the fill lowers the vertical stress transferred to the bottom.
- It is understood that granular materials often follow the Mohr-Coulomb constitutive model. Within this exercise, presentation of a simple set of curves was expected and therefore simple linear elastic model was used.

- The lateral variation of the vertical stress at any depth within the fill estimation is possible with the proposed vertical stress isobar charts. However, this is a limitation with widely used Marston's equation and its extensions.

While Marston's equation gives the average value of the vertical stress at a depth, the proposed isobars enable one to determine the exact vertical stress at any point within the fill mass. Therefore the lateral variation of the vertical stress at any depth within the fill can be calculated. The method is simple, quick and is reasonably accurate. The vertical stress variation with the fill friction angle and stiffness is discussed and suitably treated, when deriving these proposed isobars. The Poisson's ratio has some effects on the magnitude of the vertical stresses. Therefore different isobar curves for $v = 0.2$ and $v = 0.3$ are given in the isobar charts. The design charts provided in the form of isobars, are similar to the pressure isobars available in the literature for uniformly loaded strip and square footings. There are several practical situations where containments are filled with granular materials. The proposed stress isobar charts can be used to estimate the vertical stresses within narrow, long and deep backfilled mine stopes, as well as square stopes.

The proposed isobars for plane strain and axisymmetric scenarios are validated in a systematic manner and the stress isobars have shown a good agreement with the numerical models when determining the vertical stresses for trenches, silos or mine stopes. The isobars for circular/square cannot be used for rectangular ones. However, by having the two cases (plane strain and axisymmetric), it is possible to interpolate the values for a vertical stope with rectangular cross section. If the backfilled stope cross section is a square or a circle ($B/L = 1$) as well as narrow trench ($B/L = 0$), these isobar charts can be used. However, for rectangular cross sections (e.g. $0 < B/L < 1$), one can only estimate the isobar value by interpolating from the values from axisymmetric ($B/L = 1$) and plane strain ($B/L = 0$) cases.

Chapter 5

Stress Developments within a Backfilled Drive and the Lateral Loading on the Barricade

5.1 General

Stress conditions in stopes have been monitored in situ (Mitchell et al. 1975; Knutsson 1981; Belem et al. 2004; Helinski et al. 2011; Thompson et al. 2012), as well as studied through laboratory tests (Pirapakaran and Sivakugan 2007b; Ting et al. 2012a). The distance along the drive from the stope brow or the stope entrance is called as the offset distance in backfilling practice. An exponential lateral stress reduction within the backfilled drive is predicted with the offset distance in analytical equations, where elastic behaviour with a vertical shear plane method is assumed (Kuganathan 2002; Li and Aubertin 2009a). However, the force propagation from the stope to drives, and ultimately the stresses onto the barricades are not well understood in to-date research literature. Understanding the load to the barricade is a concern in the mine backfilling operations. It is expected that the normal stress to the barricade should be kept below 100 kPa to avoid failure (Thompson et al. 2014). However, an evaluation of the stress state along the drive is necessary for adequate barricade designs and also to determine the corresponding filling procedure.

Earth Pressure Cells (EPC) have been successfully used to measure the stresses in the backfills (Take and Valsangkar 2001; Belem et al. 2004; Thompson et al. 2009; Helinski et al. 2011). For example, Belem et al. (2004) measured the lateral pressure on barricades in paste fill stopes, which included a plug, and a total pressure cell (TPC) attached to the barricade. In Belem et al. (2004) measurements, the barricade stress increased to gain a maximum and later decreased as the paste fill cures. Yumlu and Guresci (2007) described an in situ stress monitoring program for paste filled stope at Turkey and concluded that overpressure condition, that occurs with tight filling of backfill within the drives, is responsible for most of the failures. Thompson et al. (2009; 2012) presented in situ stress monitoring results for stopes and barricades in CPB filled mines in Canada and Turkey. Helinski et al. 2011 reported the results of barricade stress measurements in two paste backfilled mines in Australia, and observed very different stress behaviours for different cemented paste backfill mixtures. Most of the recent in

situ stress monitoring has been carried out for cemented backfills. However, this dissertation focuses on uncemented backfills and, therefore, the studies on uncemented fills are discussed in detail.

Grice (1989) reports a field study of barricade stresses monitoring by loading the barricade in undrained conditions to check the failure. The results showed 4 m × 4 m brick barricade cracked at a pressure of 220 kPa. Later, a discussion by Duffield et al. (2003) on recent barricade failures mentioned that the anticipated stresses can be different if the barricade dimensions are different from Grice's (1989) results. However, in situ monitoring of backfilling is an expensive process because of the high cost of monitoring equipment and the instrument is also not retrievable (Dunnicliff 1988). Therefore, this study aimed to delve into the mechanisms of stress transfer from mine stope to the barricade, where EPCs have been used in the laboratory test setup.

Mitchel et al. (1975) carried out barricade pressure monitoring with rubber 'sandwich' cells and piezometers. Afterwards, model studies on backfill stability (Mitchell et al. 1982) and centrifuge tests have been reported for backfills (Smith and Mitchell 1982; Mitchell and Roettger 1984; Mitchell 1989). Mitchell (1992) studied the lateral stress on temporary barricades for two offset distances. The results showed significant arching development within the drives and an exponential stress reduction, concluding that the anticipated stresses of around 105 kPa for a 3 m × 3 m barricade when placed at the stope entrance (Mitchel 1992). However, Mitchell (1992) has not given details of the stope dimensions for this estimated barricade stress. Even though, the tests conducted by Mitchell (1992) were a good initiative into the study of barricade stress and stress variation, following deficiencies can be identified with the test setup:

- Stope dimensions and the drive dimensions were equal – e.g., 0.2 m
- Depth of the model stope was only 1.5 times the drive height- model height is not sufficient to study the barricade load variation when the backfill is subjected to arching

- Load to the barricade is obtained for 0 and 100 mm distance from stope brow and variation of stress along the drive position has not been analysed

Reduction of lateral load acting on the barricade with offset distance encourages miners to install the barricade as far as possible from the stope brow (Li and Aubertin 2009a). However, the drainage decreases with offset distance, leaving the fill to take longer time to develop the effective stresses (Kuganathan 2002). Therefore, the current industrial practice is to build the barricade one drive height away from stope brow (Kuganathan 2005). This study aimed to analyse the effect of offset distance on the loading on the barricade.

5.2 Laboratory test design

Initial laboratory tests were done at JCU with an apparatus developed in-house, to study the stresses within the stopes. The apparatus consists of a model stope, made of Perspex, with circular and square cross sections and a supporting assembly with a load cell. Details of these tests are given in Chapter 3.3. The aim is to evaluate stress conditions within the drive. Backfilled mine stopes are 15 m to 20 m wide, and depths can be larger than 100 m and the normal stress reaches an asymptote after a certain depth. For example, the asymptotic vertical stress within the stope, determined from Equation 3.15 for a 15 m wide square stope, is 250 kPa. Practically, higher stresses are not experienced in laboratory model tests (1:100 scaled down), and sometimes the system may have low stresses (for example 5 kPa) (Pirapakaran and Sivakugan 2007b; Ting et al. 2012a). Therefore, testing a regular model stope within the laboratory conditions may not generate stresses as much as encountered in situ. Hence, a uniformly distributed load (UDL) is applied through the MTS Universal Testing Machine (called as MTS herein) at the top of the model and a horizontal plate, which is placed on the top of the model stope, distributes the applied load uniformly from the MTS (Figure 5.1). The MTS is capable of applying a pre-programmed load, which is then held for a specified duration of time.

The stress at a height within the backfilled stope estimated by Equation 3.15, is the same for a square and a circular cross section with the same width (Fahey et al. 2009; Sivakugan and Widisinghe 2013). The ratio of cross sectional area to the perimeter of a horizontal layer element, dictates the vertical stress variation throughout the stope, thus the vertical stress variations in both square and circular stopes should be the same. Therefore, a model stope was developed with a thick-walled stainless steel tube, with an inner diameter of 310 mm, representing the stope width. Considering that the circular and square cross sectional stopes may generate the same stress conditions when backfilled, a circular cross section was selected for the stope, since it facilitates easy manufacturing and setting up.

Relative dimensions of the stope and drives influence the lateral loading to the barricade, and a change in dimensions of the barricade may significantly affect the resistance capacity of the barricade (Kuganathan 2001; Duffield et al. 2003). According to Duffield et al. (2003), a barricade of 5 m by 5 m may experience large stresses compared to a barricade of 4 m by 4 m (Grice 1989), considering the HF barricade failure at Bronzewing mine (Torlach 2000). Barricade dimensions, those are the same as drive dimensions, were varied in this testing program to study the loadings. Four drives with widths 75 mm, 100 mm, 125 mm and 150 mm were attached to the main stope and the normal stress to the barricade was measured by EPCs.

Four drives with widths of 75 mm, 100 mm, 125 mm and 150 mm represent barricade to stope width ratios of 0.25, 0.33, 0.416 and 0.5 respectively (Figure 5.1). The barricade was made out of tempered wood, with a grooved recess to insert the EPC, in such a way that the EPC is flushed with HF when the stope is filled. Two bolts were installed at the back of the barricade, so the offset distance could be varied with the movement of bolt as well as the barricade was kept fixed while the test takes place (Figure 5.1).

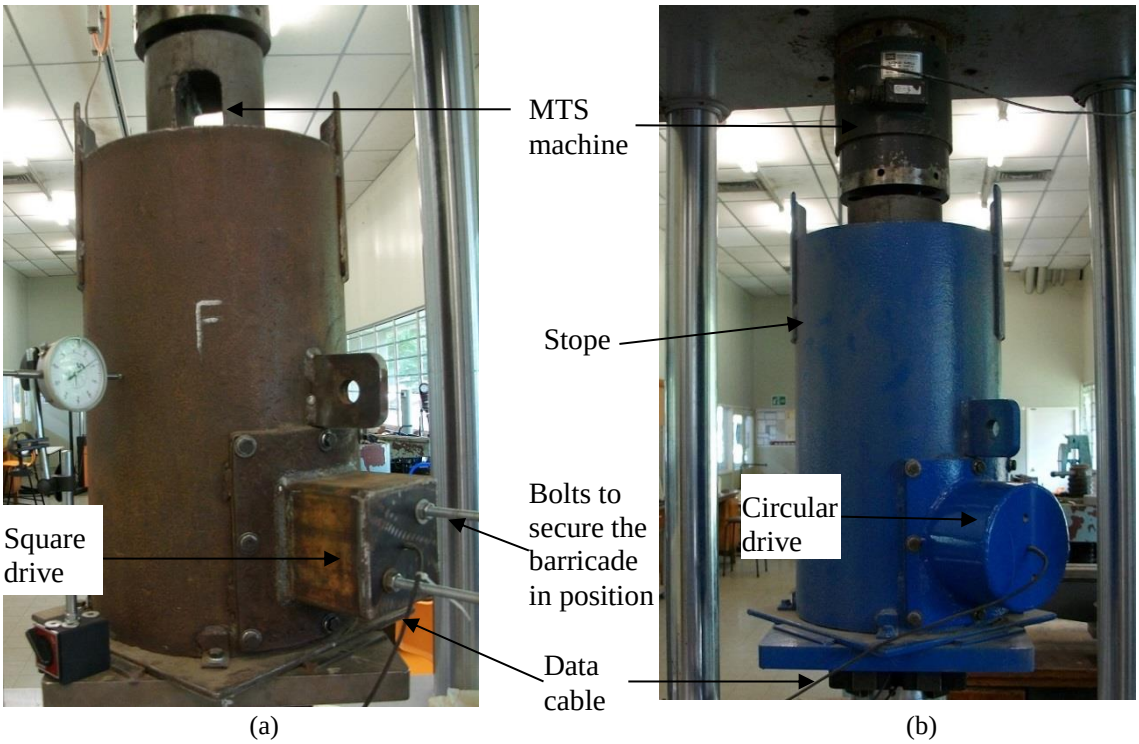

(a) (b)

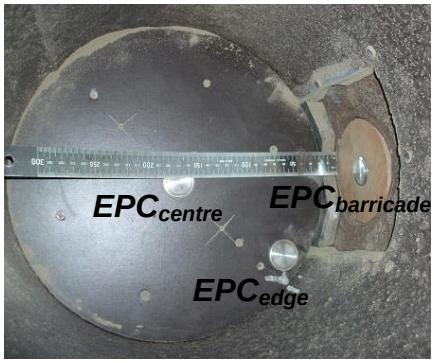

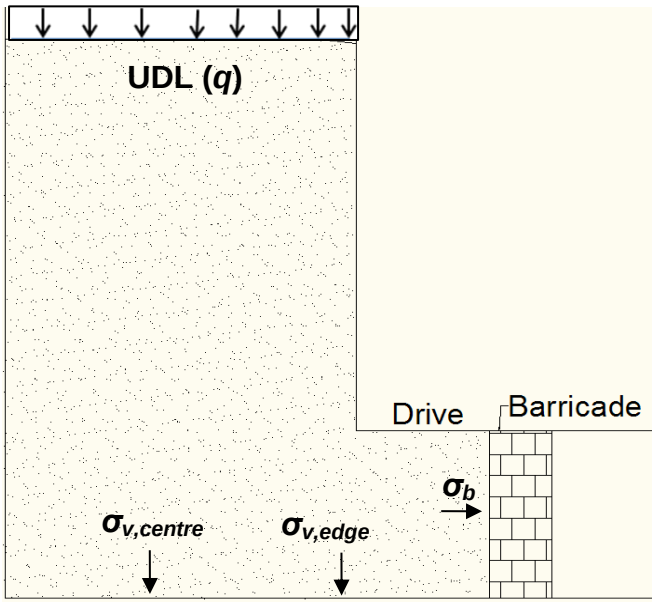

(c) (d)

Figure 5.1. Arrangement of the test setup; (a) with square drive, (b) with circular drive, (c) EPC arrangement and (d) schematic of UDL application from MTS

5.2 Earth pressure cells – installation and calibration

Barricade contact pressure was measured with EPCs in this study. Many operational factors (stress history, temperature, data recording, etc.) are required to consider with the use of EPC, or with pressure transducers. The stress history affects the EPC reading and should be considered with stress readings (Talesnick 2005). With the tests carried out during the present work, EPC was attached to the stope that was filled with HF and UDL (surcharge) was applied with the MTS. Thereafter, the HF was dumped to clean the apparatus before the next test. Therefore, the stress history dependency was not considered in these tests, as the EPC was subjected to one loading cycle.

Many types of stress transducers are commercially available. In addition, there has been many attempts to construct pressure transducers, for example Trollope and Lee (1961) and Askegaard (1963), among others. Furthermore, Labuz and Theroux (2005) developed pressure transducers and, the pressure sensed on the diaphragm was analytically expressed with shear plane method. Talesnick (2005) introduced null-pressure gauges, in which the diaphragm deflection is brought to zero by pumping air from an external air pressure regulator. Though, Talesnick (2013) showed linear calibration curves with null pressure gauges, they are often not commercially viable for an experiment which involves few pressure gauges, since they may require a considerable instrumentation work (Jardine 2010).

5.2.1 Earth pressure cells installation

The EPCs can be installed either embedded in soil or flushed with the boundary. Insertion of a pressure transducer in soil disturbs the existing stress field (Harris and Seager 1973; Clayton and Bica 1993; Talesnick 2005) and may induce either stress concentrations or reliefs depending on the EPC thickness. This stress redistribution and the change of void ratio in the vicinity of the stress transducer can seriously affect the accuracy of readings. The stress measurement within the soil is of great difficulty,

compared to the installation of transducers to measure the stresses at the boundary. Therefore, the stress at a face of a structural element can be measured with a greater accuracy than within the soil mass. Hence, the former installation technique, flushing with the boundary, is more accurate, and was used with barricade stress measurements in this study.

Cell action factor, which indicates the accuracy of transducer, is defined as "the ratio of the normal stress measured by the cell to that which would have existed in the absence of the transducer" (Clayton and Bica 1993). The cell action factor is lowest for dense and high modulus material and therefore, the loose material would incur a higher cell action factor as well as the backfill placement density affects the accuracy of readings (Clayton and Bica 1993). Hence a low relative density is used in the laboratory tests with HFs. Also Take and Valsangkar (2001) have mentioned that the EPC diaphragm should be about 20 times larger than the average grain size. In HFs tested, the ratio of EPC diaphragm to grain size is more than 20. Although, suitable correction factors should be used to adjust the temperature variation with EPC readings (Daigle and Zhao 2004), as all the tests were conducted under temperature controlled laboratory conditions, a temperature correction was not required for EPC readings.

5.2.2 Calibration of earth pressure cells

The calibration factor, is given by the manufacturer for a particular EPC, which is often obtained from a test performed under a uniform fluid pressure. If the calibration is not performed under the conditions identical to the testing, the resulting readings may be of very limited importance (Dunnicliff 1988). Calibration within the test conditions and calibration for the expected stress range are essential for reliable EPC readings.

There are three methods available to calibrate an EPC as follow:

1. Placing a dead weight placed on the diaphragm
2. A fine layer of test material placed above the EPC and then various dead weights placed on top of the fine layer of test material

3. An air pressure or oil pressure on the EPC (homogeneous fluid pressure)

Latter two methods are commonly used to calibrate EPCs, as in the first method, dead weights on the diaphragm, may disturb diaphragm deformations and damage the diaphragm. Take and Valsangkar (2001) calibrated EPCs with a soil layer and a homogenous fluid pressure, and obtained comparable results with both the methods. However, according to Wachman and Labuz (2011) when a fluid is used for calibration, the pressures are over-estimated by around 15% which highlights the necessity of calibrating the EPC within a similar material which intended to carry out the stress measurements. Moreover, the test results of Ramirez et al. (2010) showed linear calibration coefficients for 'Deadweights and Wheat' calibration, where a fine layer of wheat has been placed on the EPC and followed by deadweights (Figure 5.2).

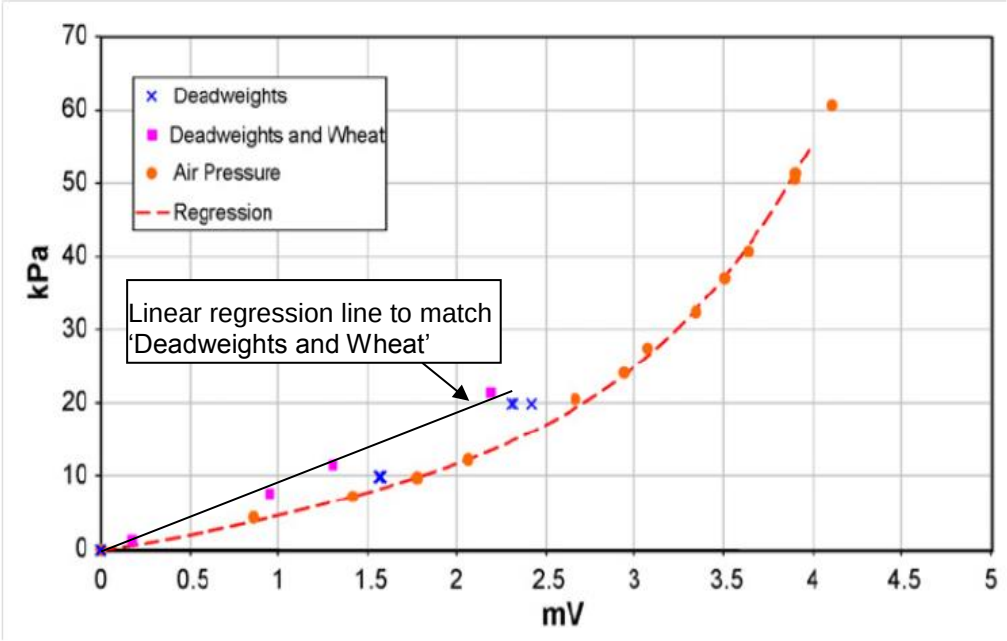

Figure 5.2. The calibration charts by Ramirez et al. (2010) and a linear calibration drawn for readings of 'deadweights and wheat'

This study used three different KYOWA EPCs (BED-A), those are capable of measuring pressures up to 200 kPa, 500 kPa and 1 MPa. An apparatus was developed in JCU Geomechanics laboratory to calibrate the above EPCs (Figure 5.3). An aluminium mould was machined to the size of EPCs and a slot was left for the EPC cable. Then, the EPC was placed on mould and a fine layer of sand was applied on top of it (Figure 5.3). After that, the mould was placed on the direct shear test structure, where the top loading plate was used to apply the dead weight (Figure 5.3b). Dead weights were increased and the normal stress was calculated taking into account the total mass of ball, loading plate, hanger and dead weights. Four trials were conducted for each EPC, and the mean pressure readings with applied pressure and the calibration coefficients for each EPC are shown in Figure 5.4.

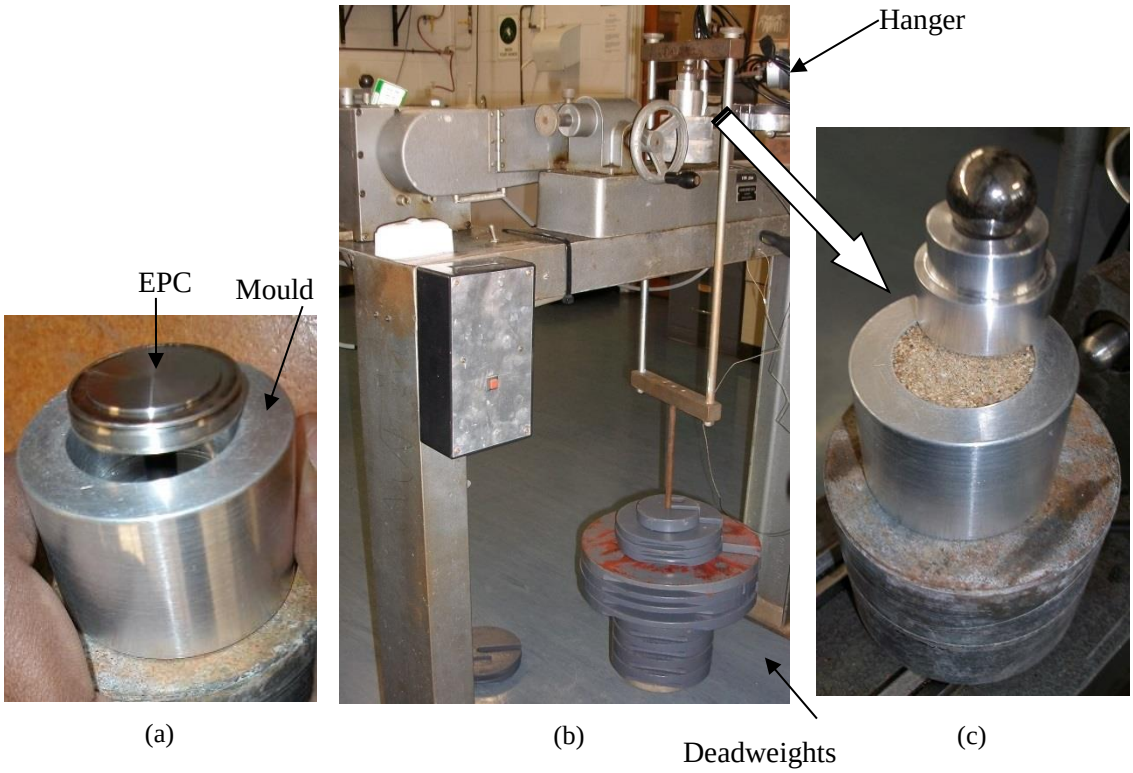

Figure 5.3. The mould and setup used to calibrate EPCs; (a) close-up view with the mould and the EPC, (b) EPC loaded with dead weights after placing a fine layer and (c) details of the setup

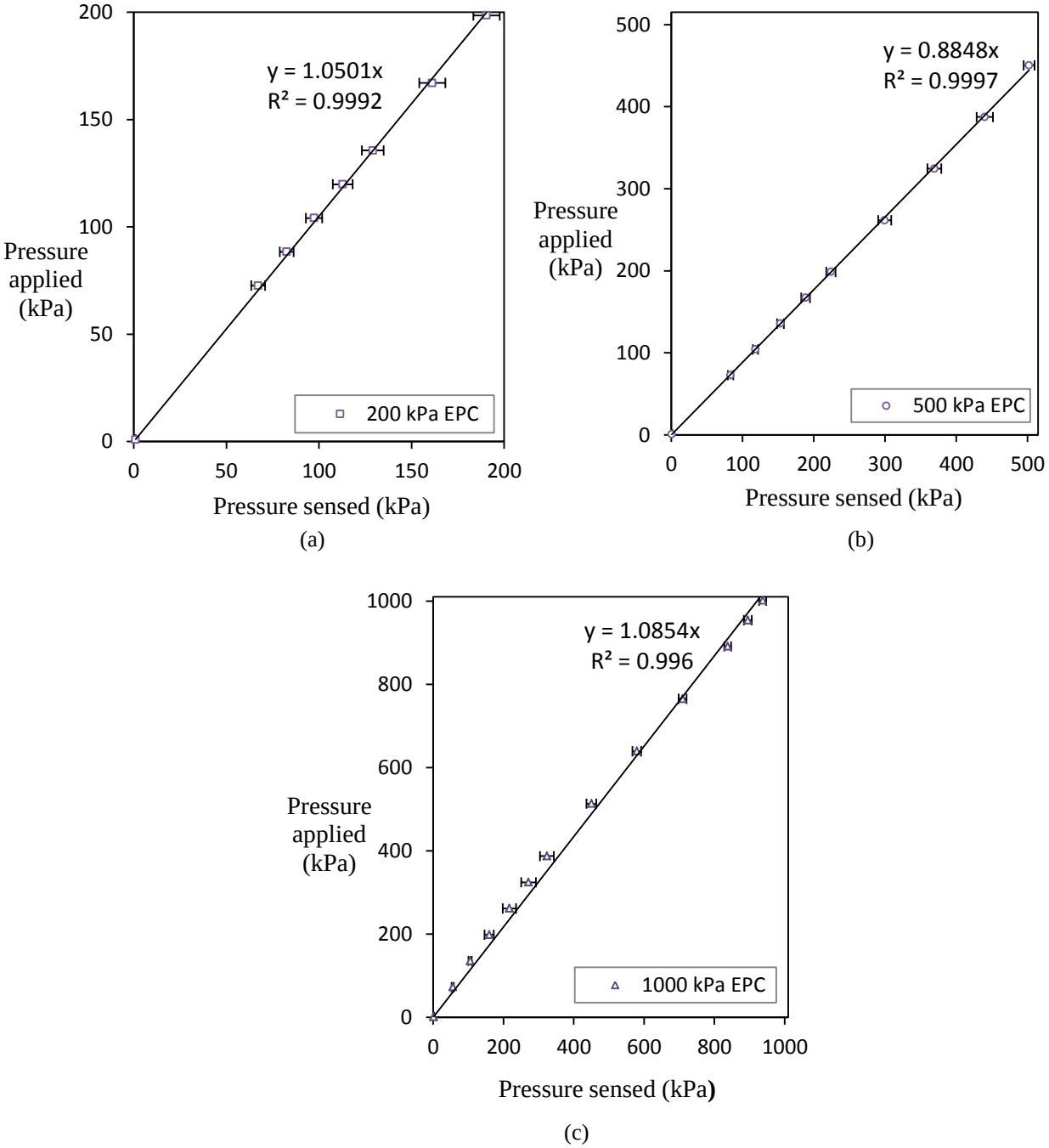

Figure 5.4. EPC Calibration results shown with calibration coefficients s and R-squared values for; (a) EPC1-200 kPa, (b) EPC2-500 kPa and (c) EPC3-1 MPa

According to the results EPC1 and EPC3 underestimated the stresses (Figures 5.4a and 5.4c) and EPC2 overestimated the stresses (Figure 5.4b). The calibration tests were repeated for four trials and the reproducibility of the results were excellent among trials. The linear calibration factors, for each EPC, are displayed within Figure 5.4.

5.3 Laboratory test methodology

5.3.1 Methodology to evaluate the variation of vertical stress

Analytical equations assume that the vertical stress distribution across the stope depth is uniform (Marston and Anderson 1913). However, to date understanding of arching and numerical simulation results confirm it is not the case (Chapter 4). Shear strength mobilization along the walls causes the stress arch to form, in which the vertical stress at the centre is higher than that at the wall. To quantify this variation, EPC3 (1 MPa) was installed at the centre of the stope and the EPC2 (500 kPa) was installed at the edge of the stope. Moreover, EPC1 (200 kPa) was placed in flush with the barricade and the barricade was stationed at zero offset distance, such that it measures the horizontal stress at walls corresponding to a particular vertical stress. In this manner, EPC3 reads the vertical stress at centre and EPC2 measures the vertical stress near the wall. The EPC1 reading makes it possible to evaluate the lateral pressure coefficient near the bottom, at the perimeter.

5.3.2 Methodology to evaluate the barricade stress variation with offset distance

The setup was arranged to measure the horizontal stress on the barricade, with barricade situated at various offset distances. The barricade was moved to offset distances of 25 mm, 50 mm and 75 mm and fixed at the particular location with the bolts (Figure 5.1). The variation of barricade stress with offset distance can be estimated with this setup.

5.3.3 Methodology to evaluate the barricade stress variation with drive dimensions

The dimensions of the stopes and the drives vary within the same mine (Sivakugan et al. 2006b). Therefore, consideration of the barricade stress variation with barricade dimension is essential. Hence four drives with widths of 75 mm, 100 mm,

125 mm and 150 mm were attached to the stope (Figure 5.1). Then the barricade was positioned at 0, 25 mm, 50 mm and 75 mm offset distances and the stope was filled to obtain the stresses on the barricade with EPCs as described below.

5.3.4 Methodology to evaluate the barricade stress variation with drive shape

The effect of drive shape was analysed with circular and square drives. The variations of stress distribution patterns with circular and square drive shapes were studied to understand the effect of the concept of hydraulic diameter, cross sectional area to perimeter ratio, on arching and the loads onto the barricade.

EPCs were installed on the barricades, and the barricade was stationed at appropriate offset distances. Then the stope was filled with HFs up to 465 mm with a 20 mm aperture funnel. After filling the stope, all data cables from EPCs were connected to the TDS-602 (Tokyo Sokki Kenkyujo Co., Ltd) data logger. Next, the system was subjected to uniform pressures of 36 kPa, 69 kPa, 101 kPa, 134 kPa, 264 kPa, 393 kPa, 524 kPa, 654 kPa, 783 kPa and 913 kPa consecutively, with the UDL applied through MTS. For each loading, the load was held for 5 minutes and then was increased to the next loading level. EPC readings were recorded to data logger throughout the test. Finally, the actual stress at the barricade was obtained after correcting the recorded EPC stress data using the calibration coefficients. Additionally, the displacement of the loading plate was recorded in the computer that controls the MTS, which continuously monitors the displacement of the rammer.

5.4 Analytical equations to estimate stresses on barricade

Most of the analytical equations, related to arching, are based on the equilibrium of horizontal or vertical layer elements, which is also known as the shear plane method. A detailed analysis about the attempts to analytically determine the load on the barricade is given below.

Lateral stress on the barricade were first studied by Mitchell et al. (1975), who proposed an expression considering the full overburden conditions. The lateral pressure coefficient at rest, K_o has been taken as 0.5.

$$\sigma_b = \gamma H K_o \tag{5.1}$$

where, σ_b- lateral stress on barricade

H - stope height

This equation (Equation 5.1) over predicted the requirements for barricades. As the understanding of arching evolved, Smith and Mitchell(1982) incorporated arching to their empirical formulation:

$$\sigma_b = 0.4\gamma H\left(1 - 0.6\frac{L}{h}\right) \tag{5.2}$$

where, L - offset distance of barricade from the stope

h - width of drive

In this empirical equation, if the *L/h* ratio becomes 5/3, then the load on barricade becomes zero. Therefore the analytical equations have been further modified.

The drive itself can be considered as a miniature stope. The lateral stress near the stope brow, acts horizontally on drive and can consider as the internal surcharge on the drive. Kuganathan (2002) analytically obtained the stress on the barricade (σ_b) for fully drained conditions:

$$\sigma_b = \sigma_o \times exp\left(\frac{P_d\, K_o\, tan\varphi}{A_d}.L\right) \tag{5.3}$$

where, σ_o- horizontal stress at the stope entrance

P_d - perimeter of drive

A_d - cross sectional area of the barricade

Later, Li and Aubertin (2009a) proposed another equation to evaluate the stress acting on a point within the barricade considering many factors, such as different earth pressure coefficients along longitudinal and transverse directions within the drive.

$$\sigma_b = \left[\frac{h'}{H_d}.\sigma_{hT0} + \left(1 - \frac{h'}{H_d}\right).\sigma_{hB0}\right]\left\{exp\left[-L.\frac{2\,tan\delta}{K_{dl}}\left(\frac{1}{H_d} + \frac{K_{dt}}{h'}\right)\right]\right\} \quad (5.4)$$

where, σ_{hB0} , σ_{hT0} - horizontal stress at base and top of the stope entrance, respectively

h', H_d - height considered and total height of the drive respectively

K_{dl} - earth pressure coefficient in longitudinal direction within the drive

K_{dt} - earth pressure coefficient in transverse direction within the drive

5.4.1 Derivation of analytical equation to estimate the barricade stress

An analytical solution for the barricade stress was derived from first principles, and the derivation is similar to the derivation given in Section 3.1. The terminology related to derivation is illustrated in Figure 5.5.

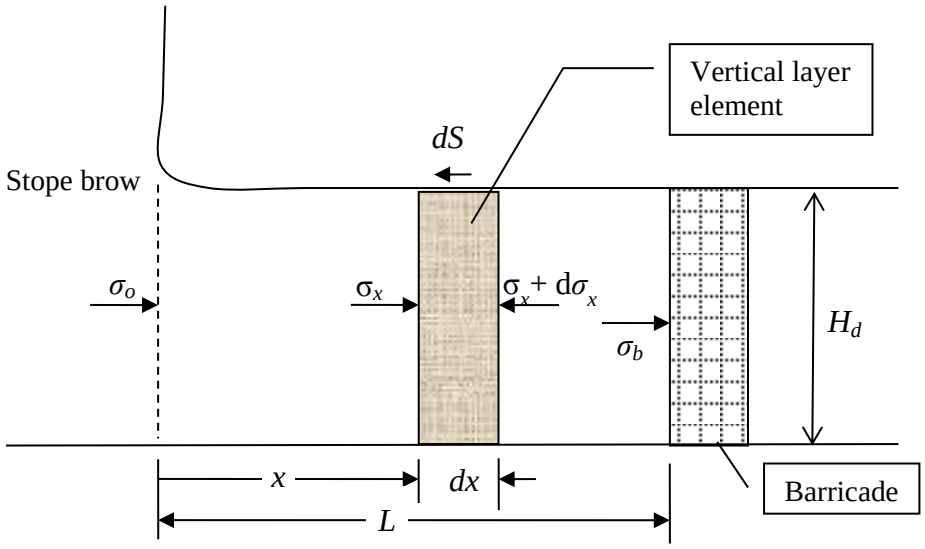

Figure 5.5. The notation showing the barricade height and offset distance along with other parameters

Let A_d - cross sectional area of the vertical layer element

P_d - perimeter of the vertical layer element

The shear force on vertical layer element;

$$dS = (K\sigma_x \tan\delta + c_a)\, P_d dx \tag{5.5}$$

For equilibrium of vertical layer element,

$$\sigma_x\, A_d = (\sigma_x + d\sigma_x)A_d + (K\ \sigma_x \tan\delta + c_a)P_d dx \tag{5.6}$$

$$d\sigma_x = -(K\ \sigma_x \tan\delta + c_a)\frac{P_d}{A_d}dx \tag{5.7}$$

$$\frac{d\sigma_x}{dx} = \left(-\frac{P_d}{A_d}c_a\right) - \left(K\ \tan\delta\frac{P_d}{A_d}\right)\sigma_x \tag{5.8}$$

Let $X' = -\frac{P_d}{A_d}c_a$ and $Y' = K\ tan\delta\frac{P_d}{A_d}$, both of which are constants that depend on the dimensions and fill parameters, to simplify next few steps.

Therefore,

$$\frac{d\sigma_x}{dx} = X' - Y'\sigma_x \tag{5.9}$$

$$\int_{\sigma_o}^{\sigma_b} \frac{d\sigma_x}{X' - Y'\sigma_x} = \int_0^L dx \tag{5.10}$$

$$\left[-\frac{1}{Y'}\ln(X' - Y'\sigma_x)\right]_{\sigma_o}^{\sigma_b} = [x]_0^L \tag{5.11}$$

$$\therefore \frac{X' - Y'\sigma_b}{X' - Y'\sigma_o} = e^{-Yx} \tag{5.12}$$

$$\sigma_b = \frac{X'}{Y'}\left(1 - e^{-Y'x}\right) + \ \sigma_o\, e^{-Y'x} \tag{5.13}$$

i.e., the general expression for the barricade stress, at a offset distance of *L* becomes:

$$\sigma_b = \frac{\left(-\frac{P_d}{A_d}c_a\right)}{\left(K\ \tan\delta\frac{P}{A_d}\right)}\left(1 - e^{-K\ tan\delta\frac{P_d}{A_d}L}\right) + \ \sigma_o\, e^{-K\ tan\delta\frac{P_d}{A_d}L} \tag{5.14}$$

For a cohesionless fill: $C_a = 0$;

$$\sigma_b = \frac{A_d}{(K\tan\delta P_d)}\left(1 - e^{-K\tan\delta\frac{P_d}{A_d}L}\right) + \sigma_o\, e^{-K\tan\delta\frac{P_d}{A_d}L} \tag{5.15}$$

Term 1 Term 2

The term 1 has little influence on the barricade stress, because the value of $(A_d/K\tan\delta P_d)$ is smaller compared to σ_o. The term 2 has significant influence on barricade stress as the lateral stress at stope brow is higher. Therefore the Equation 5.15 can be simplified to term 2 as;

$$\sigma_b = \sigma_o\, e^{-K\tan\delta\left(\frac{P_d}{A_d}\right)L} \tag{5.16}$$

The simplified Equation 5.16, is same as Kuganathan's (2002) Equation 5.3. Therefore, Equation 5.3, is used for comparison with laboratory test results herein.

5.5 Numerical (FLAC^{3D}) simulations for laboratory tests

A detailed description of numerical simulation packages including those used in this dissertation is given on Chapter 3 and Chapter 4. The simulation procedure, related to tests with MTS machine, is outlined herein. A square stope with one drive was modelled using FLAC^{3D} to compare with laboratory results. Constitutive model parameters, interface parameters and properties for hydraulic fills and barricade are tabulated in Table 5.1. The stope, drive and barricade were simulated with equi-dimensional block elements (5 mm × 5 mm × 5 mm), and only half of the model was simulated due to symmetry (Figure 5.6a). Interface elements were included to the model as given in Figure 5.6b. Here the barricade was assumed as a rough planer structure and interface elements were used between (i) the stope and fill, (ii) barricade and fill, and (iii) drive walls and fill. Then the stope was filled with minefill in 10 layers. After the initial model reaches to equilibrium state, the surcharge was applied on top of the stope, via a FISH function, in which the load was increased in 10 steps. After the surcharge

was applied for each step, the model was iterated and to equilibrium. The stresses at the barricade, at stope centre and at stope edge were recorded, into an array with a FISH routine. Later with each surcharge, the array was updated. A sample FLAC^{3D} simulation code is included in Appendix A3.

Table 5.1. Geomechanical properties used with FLAC^{3D} model for barricade bricks, rock surrounding, HF and interface

Material	**Property/modelling parameter**	
Barricade bricks	Young's modulus	*1.99 GPa
	Poisson's ratio	*0.2
	Density	*1,927 kgm^{-3}
Rock surrounding	Young's modulus	*20 GPa
	Poisson's ratio	*0.3
	Density	*2,700 kgm^{-3}
HF	Young's modulus	*50 MPa
	Poisson's ratio	*0.25
	Density	1,800 kgm^{-3}
	Internal friction angle	39°
Interface	Interfacial friction angle	38°
	Normal and shear stiffness	*2,689 GPa
	Dilation angle	0°

*Used with available data in literature and with the FLAC^{3D} user manual

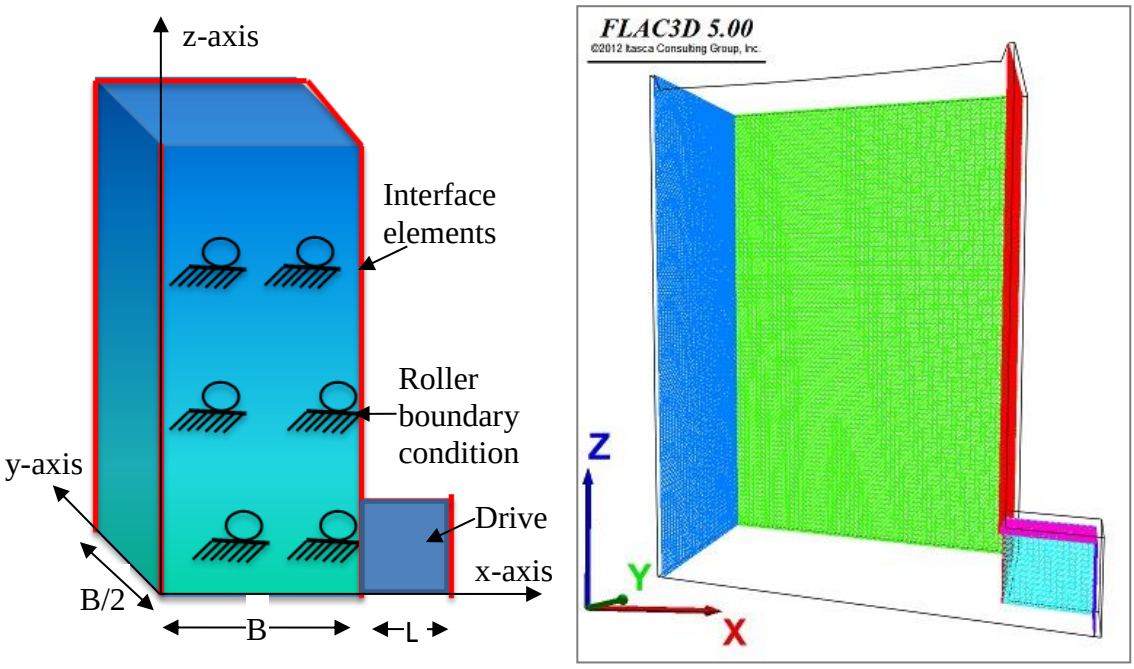

(a) (b)

Figure 5.6.FLAC^{3D} model to simulate the tests conducted with MTS; (a) numerical modelling parameters and boundary conditions, and (b) interfaces used in model

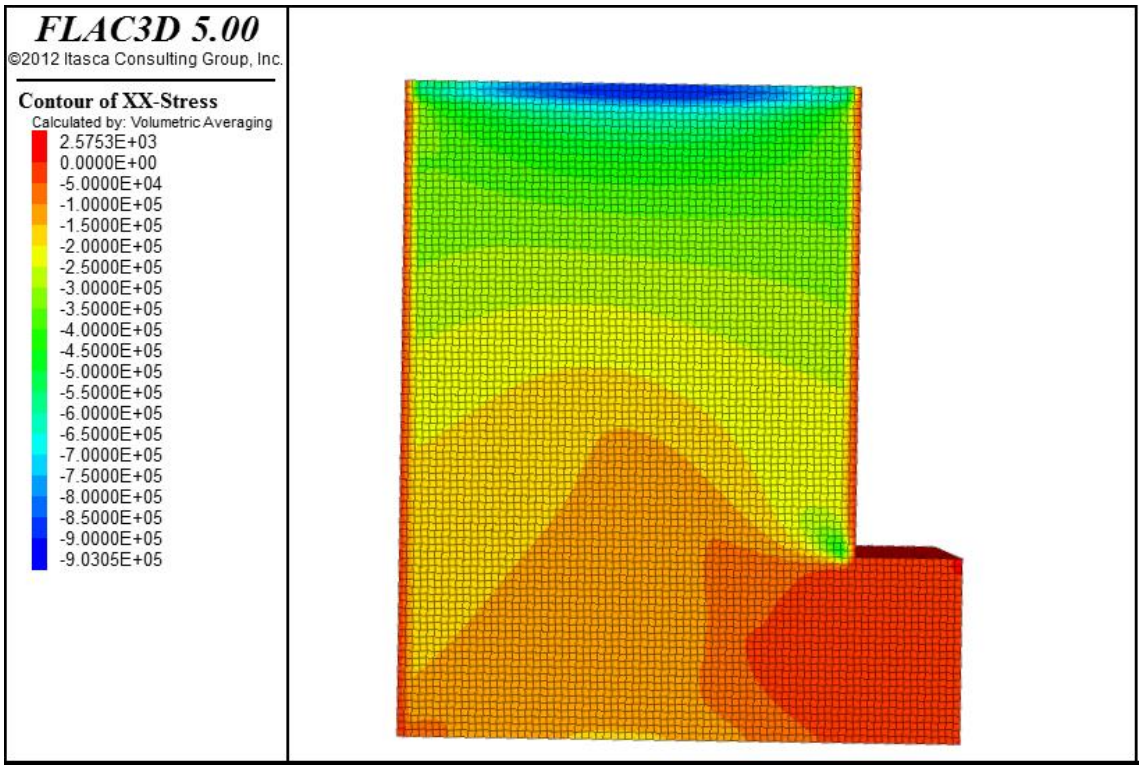

Figure 5.7. The lateral stress variation when the SD_125_75 model stope is subjected to a surcharge of 913 kPa

5.6 Results and analysis

The following notation was used to identify each test:

- CD or SD to identify drive shape; CD - circular drives or SD - square drives
- Digits following CD or SD to identify the drive width in millimetres
- Last digits to identify the offset distance in millimetres.

Therefore a symbol such as CD150_75 denotes a circular drive of 150 mm and the offset distance is 75 mm. The repeatability, of tests with MTS, was analysed with four CD150_0 and four CD150_75 tests. CD150_0 tests resulted similar EPC1 and EPC2 stresses (Figure 5.8a). However, when the offset distance is increased the EPC1 recorded lower stresses than the EPC2 (Figure 5.8b). The precision was high for all EPC stress readings (Figure 5.8). Higher precision was obtained as the filling and load application were conducted methodically and this suggests that the other tests would also be highly repeatable.

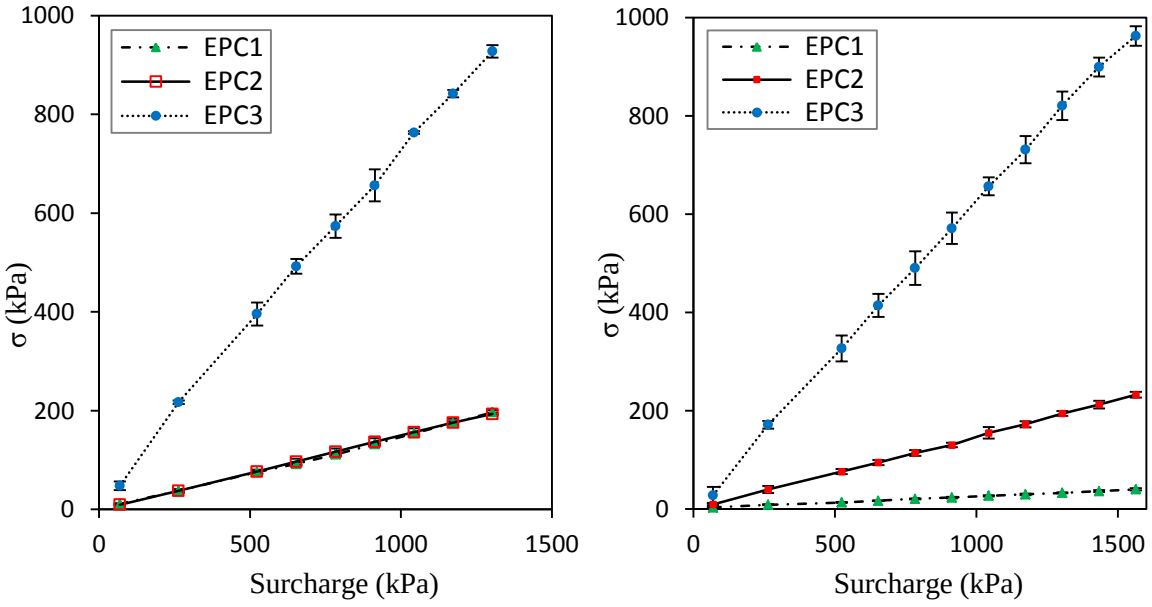

(a) (b)

Figure 5.8. The repeatability of tests, conducted with MTS, as analysed with four trials; (a) CD150_0 test results (b) CD150_75 test results

5.6.1 Variation of vertical stress at bottom and lateral stress ratio

The vertical stress at the centre of the stope bottom and horizontal stress at stope wall were considered in computing the lateral stress ratio. The barricade was installed at the stope brow, and therefore the EPC on barricade would record the horizontal stress to the wall. Additionally, the vertical stress at stope edge was recorded and used to evaluate the lateral variation of vertical stress at bottom.

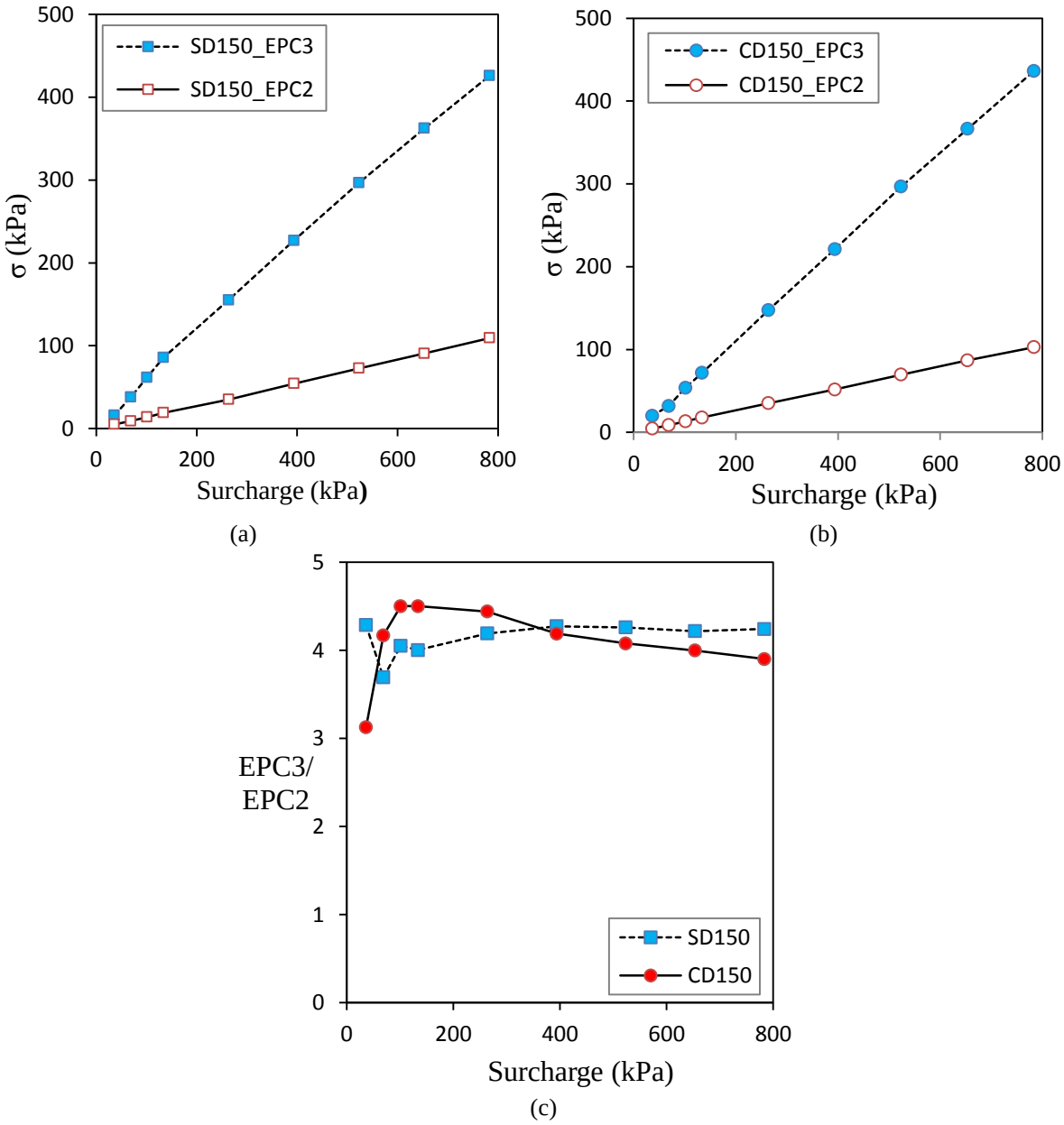

Figure 5.9. Vertical stress recorded at stope centre and stope edge with applied surcharge; (a) square drive attached, (b) circular drive attached, and (c) comparison of stress at centre to stress at edge

The lateral variation of vertical stress is significant and the vertical stress on stope centre is considerably higher than the vertical stress at stope corner (Figure 5.9). This is further highlighted when comparing the ratio of vertical stress at centre to the vertical stress at corner (Figure 5.9c). The ratio is higher than one, and remains around four for all applied surcharges. This confirms that, it is not safe to assume an average vertical stress. Therefore, the vertical stress at centre (i.e., the maximum vertical stress) is recommended to be considered in designs.

Theoretical equations (e.g.,(Marston and Anderson 1913)) assume the ratio of horizontal stress at wall to average vertical stress as K_a, K_0 ,.etc. A lateral pressure coefficient near stope walls can be computed with the vertical stress at stope edge and horizontal stress at barricade. This lateral pressure coefficient was introduced by Krynine (Handy 1985; Iglesia et al. 2014) and is denoted as $K_{krynine}$. The average vertical stress is taken as the average of vertical stress at stope centre and stope edge. The following lateral pressure coefficients were calculated using horizontal and vertical stresses recorded. The K_1, K_2 and K_3 are calculated from the model test results for square and circular shaped drives and compared with theoretical lateral pressure coefficients in Figure 5.10.

$$K_1 = \frac{Horizontal\ stress\ at\ wall}{Average\ vertical\ stress\ at\ bottom} \tag{5.17a}$$

$$K_2 = \frac{Horizontal\ stress\ at\ wall}{Vertical\ stress\ at\ stope\ bottom\ edge} \tag{5.17b}$$

$$K_3 = \frac{Horizontal\ stress\ at\ wall}{Vertical\ stress\ at\ stope\ bottom\ centre} \tag{5.17c}$$

The K_1 and K_3 are of the same order as K_a, K_0 and $K_{krynine}$ for both square and circular drives (Figure 5.10). Furthermore, K_3 lies between K_0 and K_a, but K_1 is close to $K_{krynine}$. However, the lateral pressure coefficient K_2, calculated with stope bottom edge vertical stress, is not comparable with the theoretical K. Low vertical stress, compared to the stope centre, exists at stope bottom edge as shown in Figure 5.9, and therefore a higher K_2 is shown in Figure 5.10. The edge near the walls may not be tightly filled up

with granular material and inadequate confinement may occur near the edge. However, these conditions would not rise with continuum analysis (e.g., FLAC^{3D} simulations), where a uniform confinement is assumed throughout the continuum.

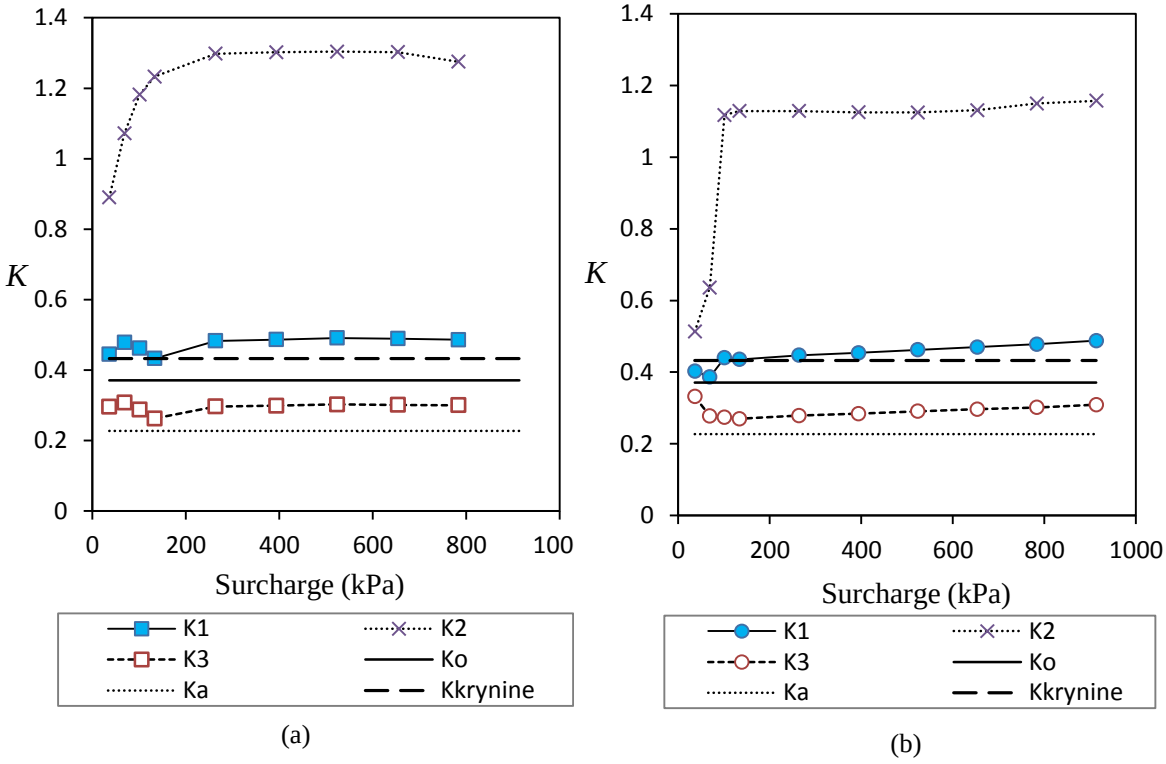

Figure 5.10. The theoretical and calculated lateral pressure coefficient values are compared; (a) 75 mm wide square drive attached and (b) 75 mm wide circular drive attached

5.6.2 Barricade stress variation with offset distance

The barricade stress variation with offset distance, for both square and circular drive shapes, was analysed. The offset distance was divided by the drive width and a normalised offset distance (L/h) was used along the x-axis. The lateral stress on barricade was normalised with the vertical stress at stope centre and the normalised barricade stress (σ_b / σ_z) is presented on y-axis. The variations of normalised barricade stress with normalised offset distance, for square shaped drives of widths 75 mm and for circular shaped drives of widths 75 mm, are given in Figure 5.11, where a curve fitting is also given for the average of stresses.

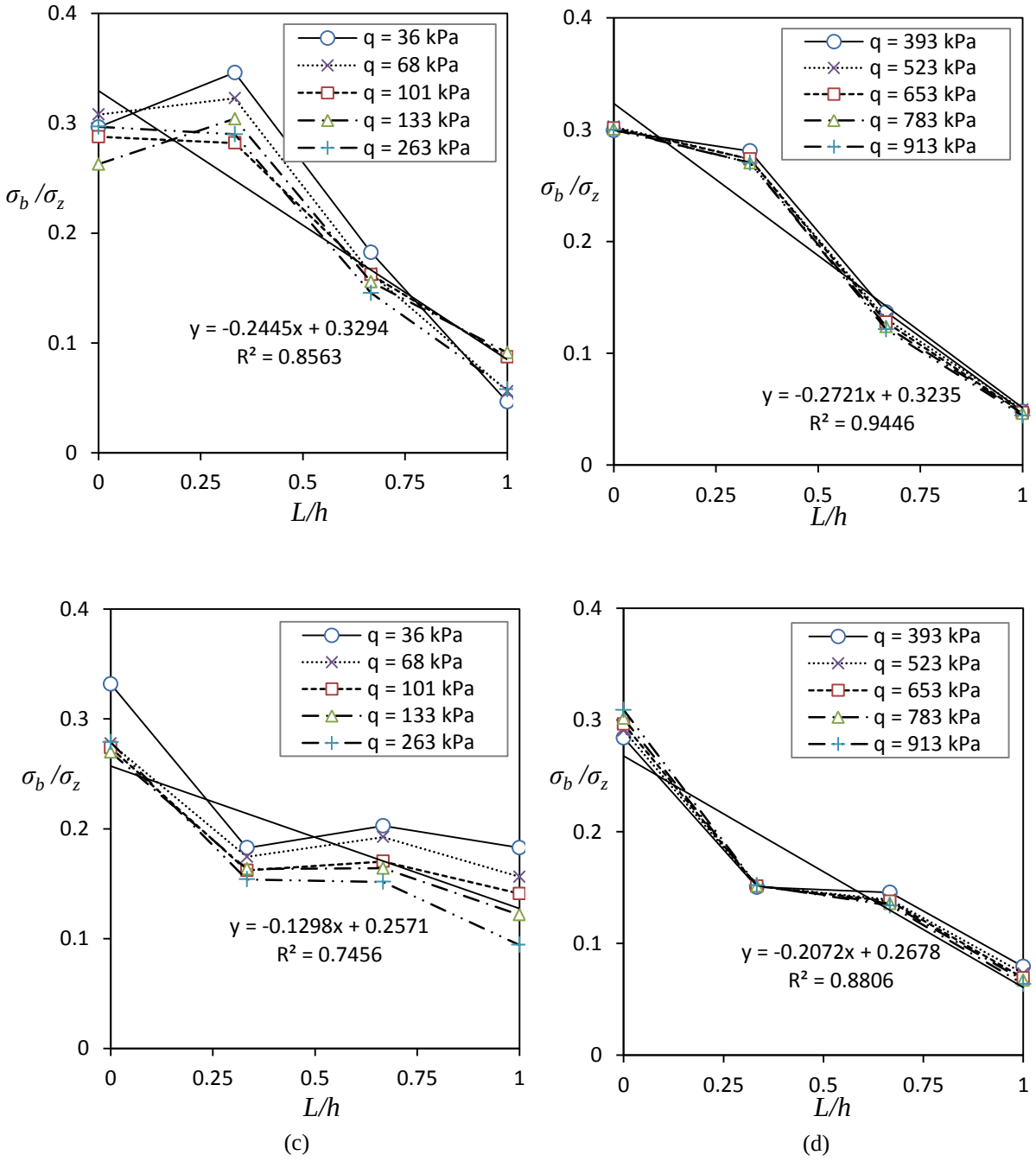

Figure 5.11. Barricade stress variation with offset distance and the best fit curve; (a) and (b) 75mm wide square drive, (c) and (d) 75 mm wide circular drive

In both square and circular drives, the highest barricade stress was obtained when the barricade is at zero offset distance, or flushed with the stope. When the normalised offset distance is one (L/h = 1), the normalised barricade stress is at the minimum. As the offset distance increases, more surface area along the drive contributes to arching and hence the stress on the barricade is greatly reduced

(Figure 5.11). However, the stress reduction pattern is identified by drawing the best fit curve. A linear function of offset distance can estimate the barricade stress for square drive and circular drives. Overall, the barricade stress variation can be considered as a decreasing function with the offset distance. Additionally, when the surcharge is higher, the barricade stress in both square and circular drives shows a steeper decrease. The increase of normalised offset distance from 0 to 1 reduces the stress at the barricade to about 76% for circular drives (Figure 5.11c and 5.11d).

The pattern of decreasing barricade stress with offset distance is inconsistent in some tests, as shown in below (Figure 5.12). The barricade stress is increased for offset distance of 0.6 of SD125 tests (Figure 5.12a). Also in CD150 tests, the barricade stress increased at offset distance of 0.2 or 0.33 (Figure 5.12b). The barricade stress should decrease with offset distance due to arching and stress transfer to drive walls. As the stope is filled after each test, the relative density variations with filling and handling might have caused these variations.

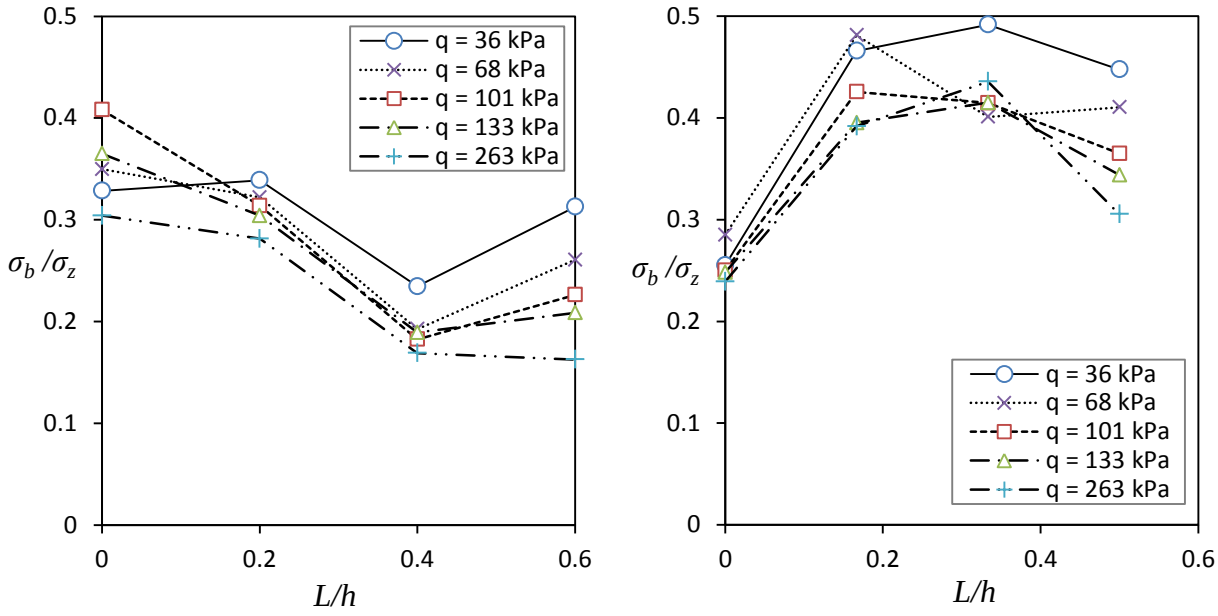

Figure 5.12. Barricade stress variations, highlighting few increased stresses, as the offset distance increased; (a) for SD125 tests and (b) for CD150 tests

The different relative densities occur with placement and especially with handling the stope with MTS. This difference of relative density may influence the deviations of barricade stress as given in Figure 5.12. Although measures were taken to place the mine fill in such a way that the relative density is maintained constant at all locations, such as keeping the funnel at the same height and using the same mechanism to bring the filled stope to MTS machine, the loading plate displacement was not uniform for all the cases (Appendix A1). The uneven loading plate displacements imply a difference of particle packing within the stope.

5.6.3 Variation of barricade stress with drive dimensions

The variation of the lateral loading on barricade with barricade width, for a offset distance of 25 mm is shown in Figure 5.13. Here the results are given for a higher range of surcharges and the rest of the data are included in Appendix A2.

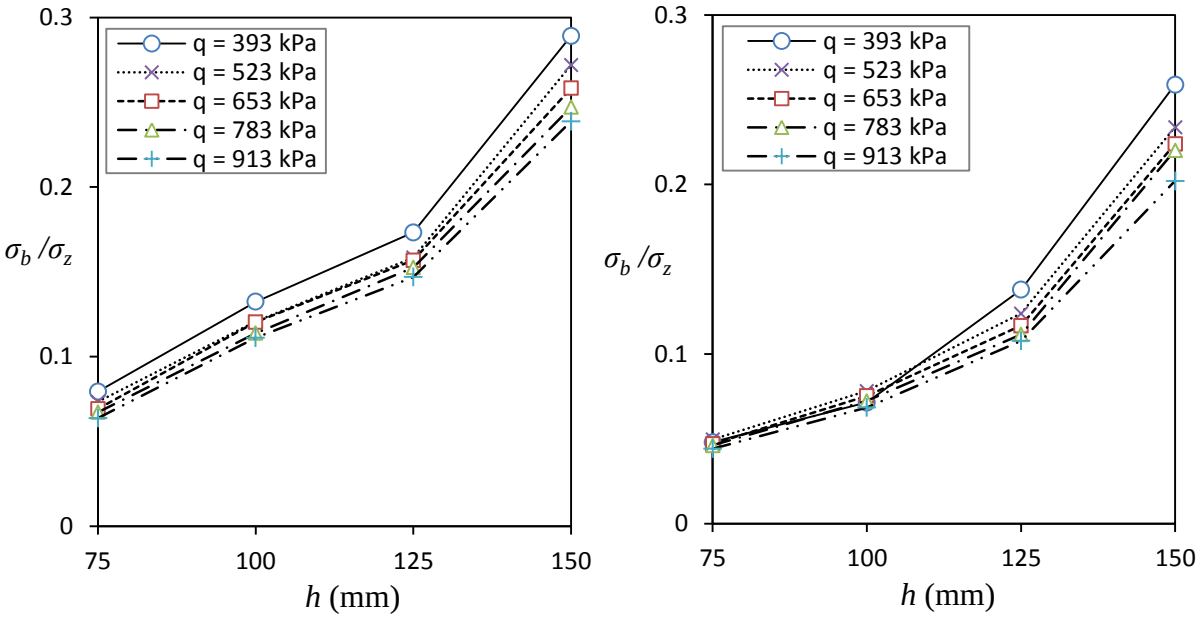

Figure 5.13. Barricade stress variation with barricade width, for offset distance of 25 mm; (a) square drives and (b) circular drives

The normalised stress on the barricade is increasing with drive width (Figure 5.13). This implies that a large load is transferred to barricade, when the drive dimensions are larger. Wide drive provides a path to transfer more load from the stope to the barricade, than in the case of a confined pathway in a smaller drive. Overall, the trend was to increase the barricade stress with drive dimension. Therefore, the expected load or the stress to the barricade increases with the drive dimension in backfilling stopes and this aspect is recommended to be considered in fill monitoring and filling activities.

5.6.4 Variation of barricade stress with drive shape

Both square shaped and circular shaped drives were used in the tests and the barricade stresses were compared among the different drive shapes. The barricade stress variation was compared for offset distance of 25 mm and different surcharge values, as shown in Figure 5.14.

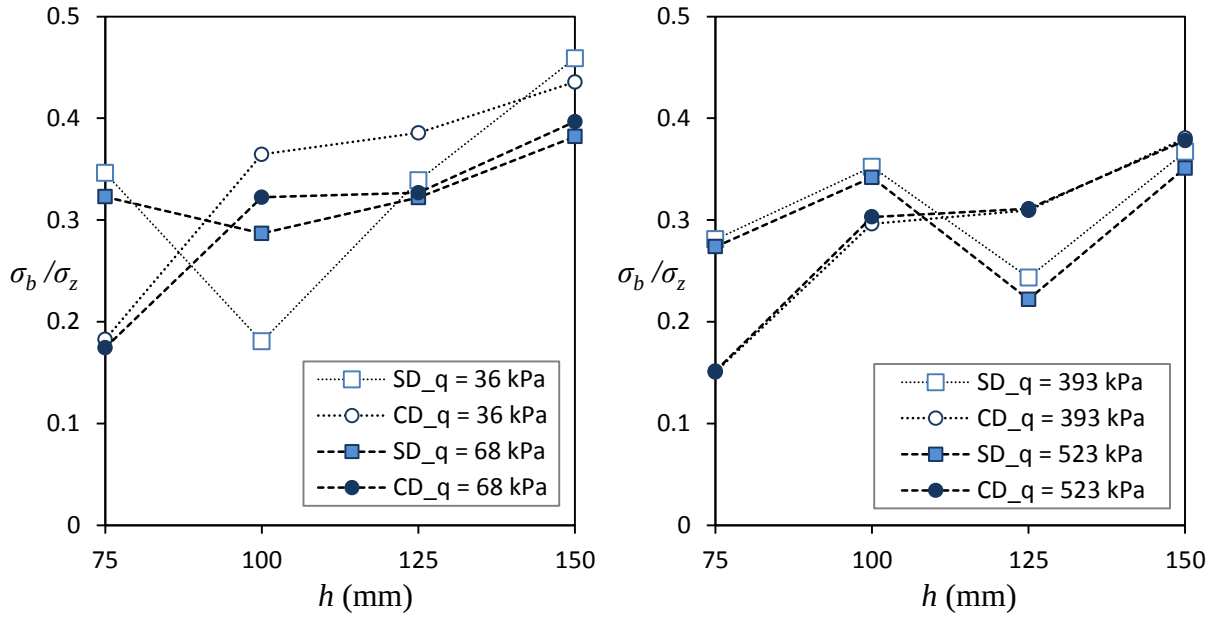

(a) (b)

Figure 5.14. Barricade stress variation when shape of the drive is changed and the offset of 25 mm: (a) for surcharges of 36 kPa and 68 kPa, and (b) surcharges of 393 kPa and 523 kPa

The barricade stress is increasing with the drive width for both circular and square drives (Figure 5.14). As the surcharge increased, the barricade stress variation fluctuated within a narrow range (σ_b / σ_z = 0.18 to 0.45). Figure 5.14b shows a drop in barricade stress with drive width of 125 mm for square drives. The different relative densities, with filling and handling, can be identified as the main reason for the stress decrease. The packing density, particularly within and in the vicinity of the drive affects the force propagation from stope to drive in this specific case (Figure 5.14b).

5.6.5 Comparison of barricade stress estimated with analytical equations, numerical simulations and laboratory tests

Square drives and circular drives, were tested in laboratory, and the same trend in the variation of barricade stresses were observed as shown in Figure 5.14. The circular drive could not be attached to the stope with FLAC^{3D}, to replicate the test condition, as the surrounding material could not be merged between the stope and drive. Therefore, the test results were compared with FLAC^{3D} simulation results for square drives and with Equation 5.3, and are shown in Figure 5.15 and Figure 5.16. The laboratory test results are indicated under the 'Lab test_EPCs' title in legend.

The FLAC^{3D} stresses at offset distance of zero are higher than the stresses estimated with laboratory tests (Figure 5.15). FLAC^{3D} predicts a large stress at stope brow, because a larger horizontal stress is recorded on walls with assumed continuum approach. Also the assumed continuum layer, the analytical equations use an average vertical stress at stope bottom (Equation 5.3). Therefore, the vertical stresses estimated with analytical equations, are high than predicted by FLAC^{3D}, which is again reflected with barricade stresses (Figure 5.15).

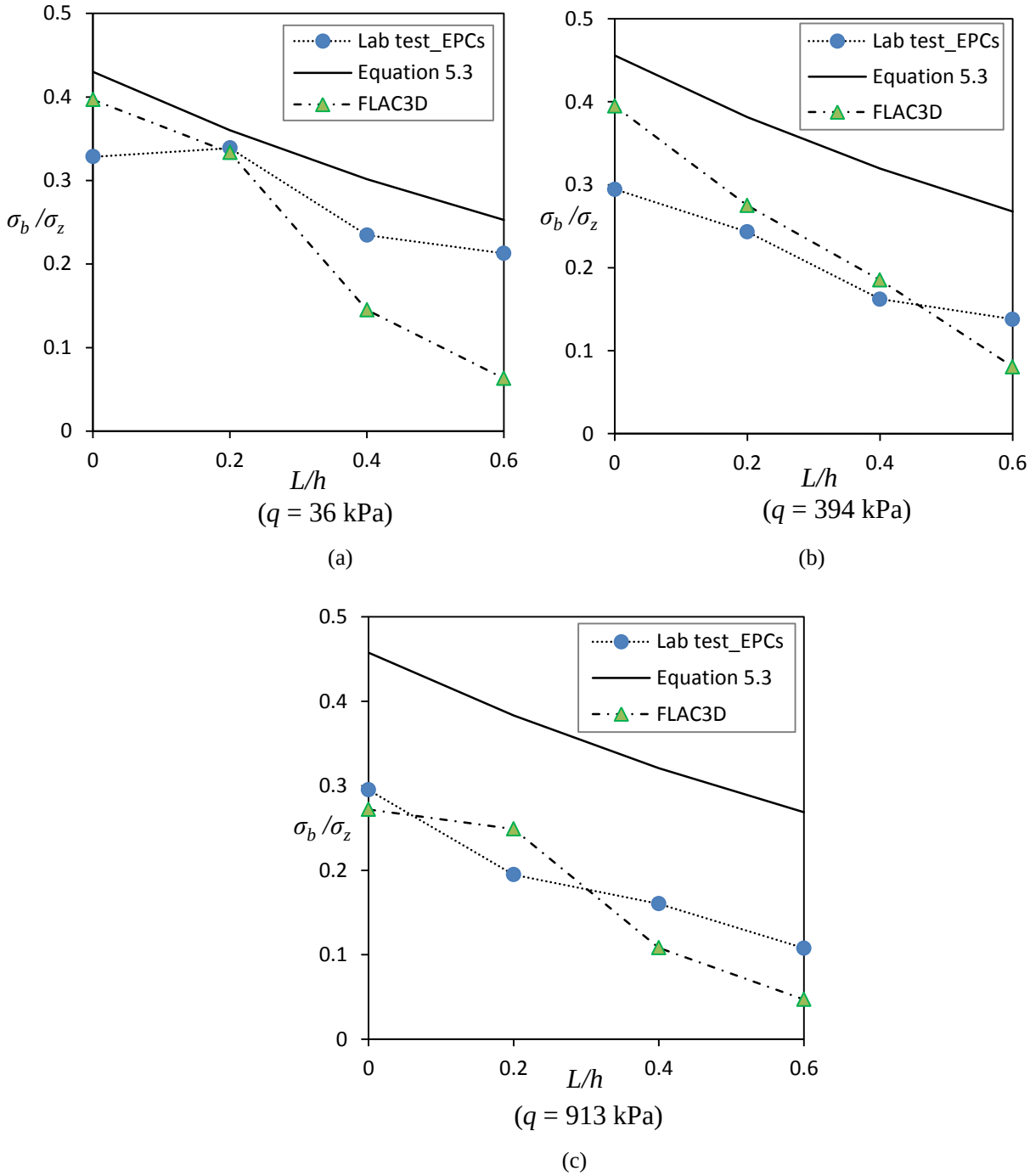

Figure 5.15. Variation of barricade stress with offset distance as compared in different surcharges; (a) q = 36 kPa, (b) q = 394 kPa and (c) q = 913 kPa

As the offset distance is increased, or when the barricade is moved away from the stope brow, arching distributes the fill loads to drive walls and therefore, the barricade stress decreased with offset distance (Figure 5.15). Larger surface area along the drive contributes to arching as the offset distance is increased, and hence the stress

on the barricade is reduced. FLAC^{3D} simulations suggest a decrease of the barricade stress with the offset distance (Figure 5.15). The barricade stresses estimated by Equation 5.3 and the EPC stresses are of the same order in magnitude, with the analytical equations giving higher values in all cases. Nevertheless, barricade stresses, from FLAC^{3D} simulations are comparable to laboratory tests (Figure 5.15).

Next, the barricade stress variation with respect to the drive width, based on the three different approaches, is presented. In Figure 5.16, the normalised barricade stress variation at zero and 75 mm offset distances is included for two surcharge pressures.

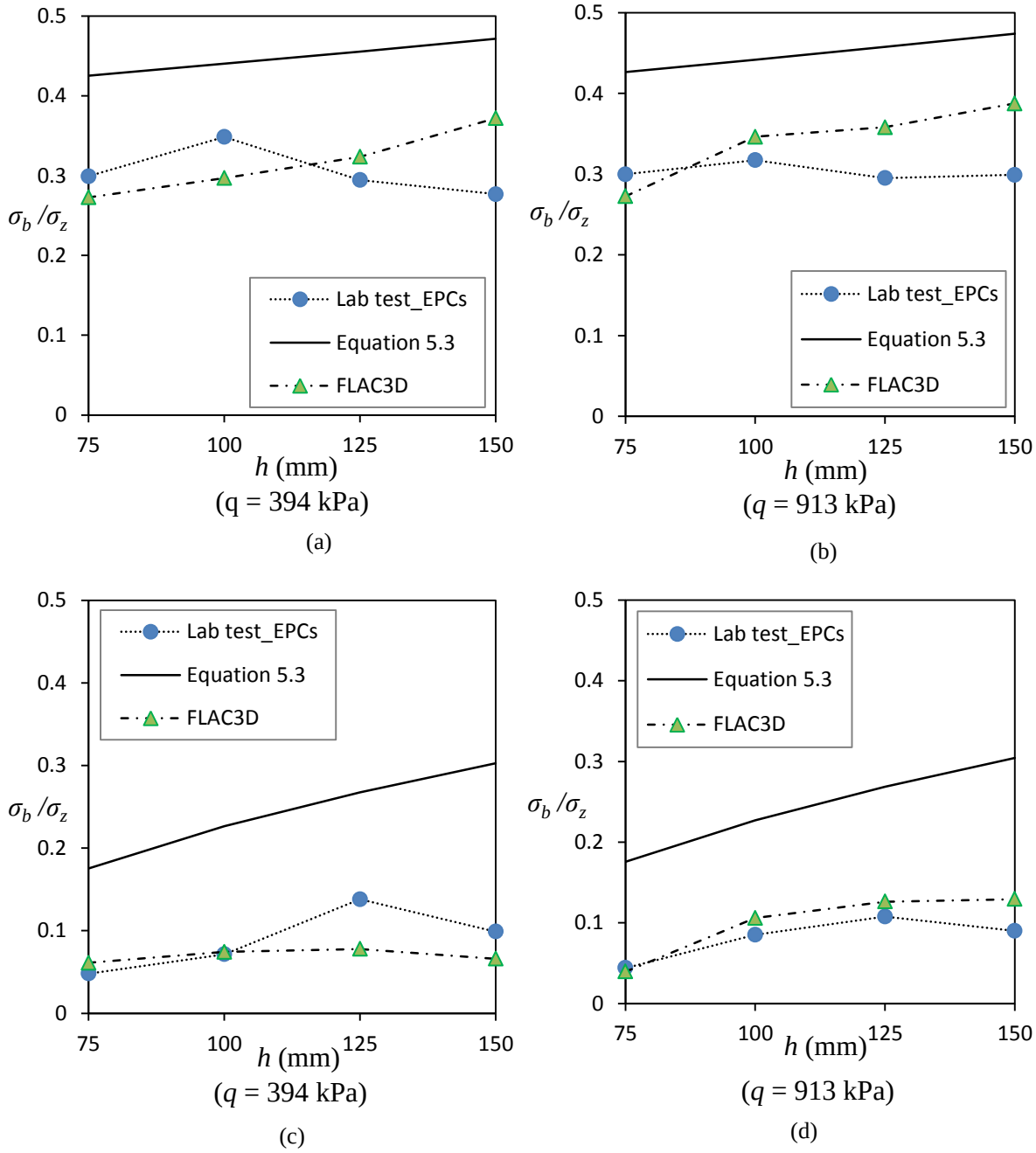

Figure 5.16. The variation of barricade stresses with the drive width from analytical, numerical and laboratory test results; (a) q = 394 kPa and L = 0, (b) q = 913 kPa and L = 0, (c) q= 394 kPa and L = 75 mm and (d) q =913 kPa and L = 75 mm

The analytical equation over-estimates stresses at stope brow for all of the surcharges (Figures 5.16). FLAC^{3D} simulations predicted the lateral stresses relatively better, with good agreement with laboratory model tests (Figure 5.16). As the width of the drive was increased, the barricade stress was also increased (Figure 5.16). Larger

drive width allows a larger quantity of fill to act as the medium to transfer stresses through the drive. The analytical equation overestimates the loads on barricade within backfilled stopes. The reason, for the barricade stress deviations from three approaches, is the average vertical stress at bottom used in analytical equations. This average vertical stress continuum assumption, forces the vertical stress variation to reach the asymptotic stress quickly, even at the presence of a large surcharge on the top.

5.7 Extension of simulations to full scale mine stopes

The possibility of extending the test results into full scale mine stopes was considered. These barricade stresses do not replicate any field conditions, but indicate normalised barricade stress with respect to the vertical stress at the stope bottom centre. The proposed solution is based on the maximum vertical stress which occurs at the stope centre. However, the laboratory model test applies a surcharge to a short stope, and the surcharge can be seen as a force applied from a large column of fill above this short stope. The equivalent surcharge applied from a tall large stope at a certain height is determined with the stress isobar charts proposed in Chapter 4. Stress isobar charts have been proposed for narrow stopes (plane strain conditions) and square stopes (approximated with axisymmetric geometry) and the vertical stress at a certain height can be determined with stress isobar charts.

All the barricade stresses obtained through laboratory testing program, are given in Figure 5.17. The barricade stress was normalised with the vertical stress at stope bottom (σ_z) and used as the *y*-axis, while with the normalised offset distance used as the *x*-axis. The estimations from analytical equation (Equation 5.13) also shown for the comparison and it shows that the range of variation shown with laboratory tests could not estimate with analytical equation. The barricade stresses vary over a wide range and the maximum values are considered herein, conservatively. The maximum of normalised barricade stresses within the range of offset distance less than 0.4 can be considered as fixed at 0.3789 and beyond it shows a logarithmic decrease with the

normalised offset distance (Figure 5.17). The maximum barricade stress can be related to normalised offset distance as,

$$\frac{\sigma_b}{\sigma_z}(for\ 0 < \frac{L}{h} \leq 0.4) = 0.3789 \tag{5.18}$$

$$\frac{\sigma_b}{\sigma_z}(for\ 0.4 < \frac{L}{h} < 1) = -0.312 \ln\left(\frac{L}{h}\right) + 0.0565 \tag{5.19}$$

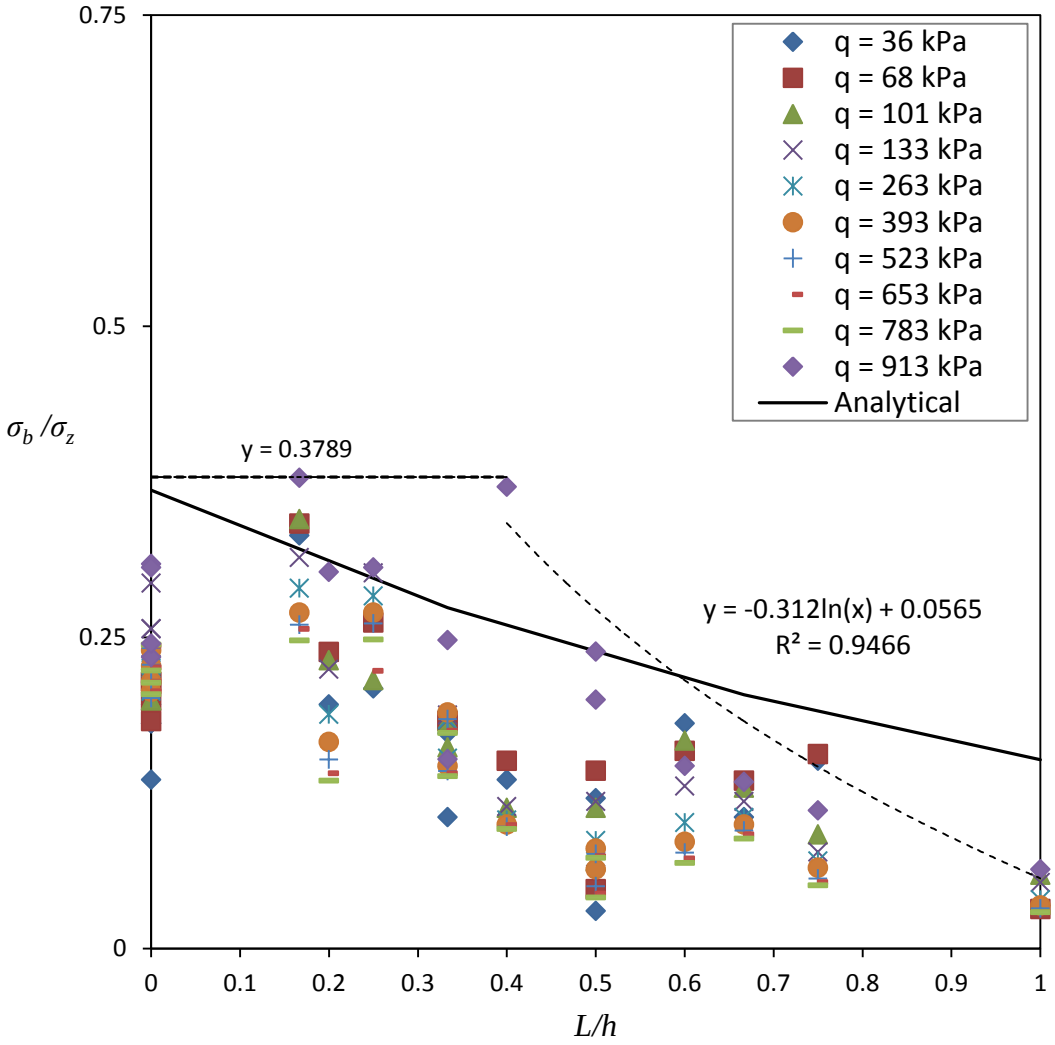

Figure 5.17. The normalised barricade stress, with respect to the offset distance, from all laboratory tests with drives of 75 mm, 100 mm, 125 mm and 150 mm widths

The calculation of barricade stress for a full scale stope is shown in an example. This example assumes the following parameters for a mine stope filled with HFs.

Table 5.2. The parameters considered for the calculation of barricade stress from the proposed empirical equation (Equations 5.18 and 5.19)

Input data	
Stope shape	square
Stope width (*B*)	15 m
Stope height (*z*)	65 m
Drive width (*h*)	5 m
Offset distance (*L*)	3 m
Unit weight of HF (γ)	20 kN/m^3
Poisson's ratio of HF (v)	0.2

The stress isobar chart of Figure 4.15c is chosen to estimate the vertical stress at stope centre, as the z/*B* ratio of stope is 4.33. Then the influence factor (*I*), for *z*/*B* of 4.33 and *x*/*B* of 0, is 1.5.

Maximum vertical stress at stope bottom (σ_z) = $I.\gamma.B$ = 1.5×20×15 = 450 kPa

And the normalised offset distance, L/h is 0.6.

Therefore from Equation 5.19, $\frac{\sigma_b}{\sigma_z} = -0.312\ln(0.6) + 0.0565$

The stress on barricade (σ_b) = 0.215×450 kPa

$$\sigma_b = 97 \text{ kPa}$$

The given calculation is simple and a competent miner would be able to estimate stresses on the barricade, if the stress isobar charts are available.

5.8 Summary and conclusions

Barricade stress estimation is important for reliable barricade design and fill monitoring activities. Three approaches, such as laboratory model tests, analytical equations and numerical simulations were considered in this study. Laboratory tests were conducted to find a relationship between the stress at the stope bottom and the horizontal stress on the barricade. In the laboratory model, the drives were made out to widths of 75 mm, 100 mm, 125 mm and 150 mm, and were attached to the 310 mm in diameter model stope. As the results are readily available for a considerable range of drive width to stope width ratios, interpolation could be used to determine the loads acting on barricades of other drive sizes.

Predictions from the analytical equations were compared with the laboratory test results. The analytical solution tends to underestimate the barricade stresses, which are obtained from the laboratory tests. Moreover, the stope with barricade was modelled with FLAC^{3D}, as the geometry with the inclusion of drive in simulations makes it a three dimensional problem. FLAC^{3D} outputs higher stress on the barricade at the stope brow and the barricade stress rapidly decreases with increasing offset distance. Moreover, the same range of barricade stresses are predicted by laboratory test results as well as numerical simulations at higher offset distances. The overall pattern is that the normalised barricade stress is decreasing with normalised offset distance. However, some deviations were observed and predicted because the HFs packed differently with funnel filling and this was further confirmed by MTS machine plate displacement data, which are not uniform for all the tests.

Finally an empirical equation was proposed to estimate the barricade stress, considering the maximum recorded barricade stresses from laboratory tests. In this proposed application, the stress on the barricade was expressed with respect to the vertical stress at the stope centre and the vertical stress at stope centre is determined by the stress isobar charts, given in Chapter 4. This attempt combined stress isobar charts and laboratory test results. Finally, different situations may exist in field, such as

different geometries, different fill material and different material properties. A general case was considered and derived stress relationships, but additional data may be required to adopt this general form to any other backfilling situation.

Chapter 6

Estimation of Stresses within Backfilled Containments: An Analytical Approach

6.1 General

> "The way out of the difficulty lies in dropping the old fundamental principles and starting again from the elementary fact that sand consists of individual grains" (Terzaghi 1920).

Marston and Anderson (1913) derived the expression for vertical stress in a narrow backfilled trench after a series of full scale tests conducted with clay, yellow clay and mixed clay. However, the cohesion has been neglected in Marston and Anderson's calculations but has been included in re-calculations done by Scarino (2003). Cohesion makes a significant contribution towards arching and stress developments as it aids to hold the material together. The cohesive materials behave nearly as a continuum and this continuum behaviour has been considered in deriving most of the analytical solutions. The well-established analytical equations, for example, Janssen's (1895) equation and Marston's (1930) equation, and their modifications are considered as the arching theory herein and the relevant analytical equations are given as Equations 3.9 and 3.15.

The arching theory has been validated through a few studies (Knutsson 1981; Take and Valsangkar 2001). However, deviations from the arching theory have also been reported in a few cases. For example, Lenczner (1963) observed a disagreement of the vertical stress variation with the arching theory when sands were tested. Moreover, Vanel and Clément (1999) who measured the average vertical stress variation in a cylindrical tube filled with glass beads also observed a linear increase in the average vertical stress, which differs from the asymptotic stress estimated with the arching theory.

As discussed in Section 3.7, the vertical stress variations obtained through laboratory model tests for sand as well as for HFs may not agree with the arching theory. In the laboratory tests the average vertical stress increased with depth which is contrary to the arching theory (Figure 3.7) in which an asymptotic vertical stress is expected at large depths. Furthermore, two distinct vertical stress variations were

identified: (i) exponential curve up to depths of 3*B* and (ii) a linear increase of vertical stresses from depth 3*B* onwards. Therefore, alternative calculation schemes are considered to describe the laboratory test results in this chapter. Additionally, the assumptions in the arching theory are revisited, and an alternative analytical solution is proposed.

6.1 Theoretical assumptions with continuum approach

Although many theoretical improvements have been suggested to the arching theory, the widely scattered stress measurements observed in the field and laboratory have not been explained to-date (Blight 1986; Blight 1990; Vanel and Clément 1999). In the analytical equations (Equations 3.15 and 3.19) of the arching theory, the only parameters that can be changed are K and tan δ, and those are functions of φ. However, the packing structure or the packing density which influences the lateral stresses and hence shear stresses has not been considered in above mentioned equations. For example, densely packed sand dilates with shearing, but loosely placed sand does not dilate and may not lead to full mobilization of friction. This affects the force transfer at walls and induces different vertical stresses at the bottom, which is not expected with the arching theory (Section 3.7). Therefore, the grain packing influences the vertical stress variation especially when granular fills are considered (Vanel and Clément 1999). However, the grain packing condition has not been considered in the continuum approach and hence has not been accounted for within the arching theory. Moreover, the assumptions made in arching theory have often been subjected to questions. Therefore in the present study these assumptions are critically evaluated focusing on the particulate nature of the granular material.

6.1.1 Horizontal layer element and uniform vertical stress

In the arching theory, the granular material is analysed considering a horizontal layer element, which acts as a single block that interacts with the wall. The vertical stress throughout this layer element is considered uniform. However, the granular

material is not cemented and consists of cohesionless grains. Unlike the assumed continuum, the cohesionless grains are not bonded and hence possess less interlocking. Therefore, when shearing occurs at the wall, the shear strains near the wall are higher than those at the middle. These differences of shear strains in a particular layer can induce different horizontal and vertical stresses within the backfill. As a result, the vertical stress may not be uniform along the horizontal layer element. Analytical equations have been proposed by Walker (1966), Handy (1985), Li and Aubertin (2008) and Singh et al. (2011) to estimate the variation of vertical stress along the width for a backfill in a fixed wall structure.

According to the arching theory, with the full mobilization of friction, the load of an added fill layer is completely balanced by shear forces after a certain large depth. This results in an asymptotic vertical stress, at the particular height and beyond. However, in laboratory tests, a continuous increase of vertical stress was observed since additional load was still being transferred to the base after the placement of every fill layer (Figure 3.7). Moreover, the laboratory test results have shown that the lateral stresses are lower than what is estimated from the arching theory (Figure 3.13). This is because the cohesionless grains are loosely packed and may not induce large lateral stresses, as expected with the arching theory. Therefore, the grain packing within the granular fill should be considered when calculating the lateral stresses and the assumption of uniform vertical stress throughout the layer element may not be correct.

6.1.2 The lateral pressure coefficient -K

Theoretically, the lateral pressure coefficient (K) is defined for a point within the soil mass. However, with the arching theory the horizontal stress at wall to the average vertical stress at bottom is considered as K, which is clearly not defined for a specific point. The lateral pressure coefficient used in the arching theory assumes both σ_h and σ_v remain the same across the width. The lateral stress to vertical stress ratio may change with the material, grain size distribution, grain angularity, filling method, compaction effort and etc. Lenczner (1963) concluded that K varies linearly with depth for H/B of 0-

4 and hyberbolically after H/B ratio of 4. Take and Valsangkar (2001) also suggested that K changes with depth depending on the lateral wall movement. Therefore, the assumption of a constant lateral pressure coefficient is incorrect.

A comprehensive definition for K has not been reached so far with the continuum approach. As a result, rather than just assuming a continuum, the trend of considering the macro scale properties of granular mass is increasing (Cundall 2001; Andò et al. 2012). The macroscopic behaviour of granular systems has not yet been fully explored and understood (Agnolin and Roux 2007). Hence the alternatives to describe the granular behaviour, such as discrete element approach, higher-order continua (e.g. second gradient models that allow to differ the stresses within the continuum (Chambon 2011)), and multi-scale computations (micro-scale was explicitly simulated, e.g. (Nitka et al. 2011) and (Andrade et al. 2011)) are currently being used.

Within the continuum it is postulated that the major stresses are accompanied by the corresponding deformations. i.e. deformation is the leading factor for arching and stress development (Trollope and Burman 1980). Ideally if deformations are absent in a continuum, no stress changes can be derived. But in discontinua, as in the case of granular materials, grain re-arrangements can occur without noticeable deformations (Trollope and Burman 1980). The grains tend to re-arrange and accept loads, without showing a visible overall deformation to the outside. The stress strain response of a given geomaterial depends on relative density, effective stress state and the fabric (Salgado et al. 2000). Therefore the grain arrangement and the fabric within the structure need to be considered in developing alternative solutions that account for the arching within a granular system.

6.2 Modified Butterfield (1969) solution for particulate approach

There has been significant interest in the past in understanding the behaviour of granular soils by considering an array of disks. Trollope (1957) has considered a granular wedge with disk arrangements in laboratory tests and presented theoretical equations. Moreover, regularly packed uniform disks have also been used to derive

expressions for dilation relationship (for example (Rowe 1962)). Later, the solution proposed by Butterfield (1969) with a disk arrangement to represent grains addressed the stress anomalies that occur in silos or similar structures. Furthermore, Trollope and Burman (1980) have formulated a discrete stiffness model (DSM) including disks with shearless contacts (contacts that would not generate any shear forces) to analyse the results from sand piles.

Butterfield (1969) proposed an analytical solution that considers the summation of all forces within a uniform disk arrangement. Similarly, in the present study statistical equilibrium of a systematically packed array of smooth, mono-sized, rigid spheres was considered. The disks were assumed to have no friction among themselves and transfer the load directly to the disks underneath or to the walls. Deformations of disks were neglected in this simple model, considering the stress ranges undergone by grains in this type of a filling. The numerical simulation of the physical behaviour of geomaterial is often complicated and hence it requires consideration of numerous micro-mechanical aspects. Therefore a simple array of disks and the forces between disks are considered in the proposed solution. Matlab program (MathWorks 2012) was used to calculate the disk forces, according to the equation derived in this scheme. The analytical procedure presented herein is similar to Butterfield's (1969) model, but has advantages, such as the possibility of calculating the vertical or horizontal stress at any location throughout the depth.

6.2.1 Contacts and contact angle

In the continuum approach each unit is assumed to be fully connected to the surrounding units (mostly these units are of square/rectangular or trapezoidal shapes). However, a given granular grain can have only a limited number of connections with surrounding grains. For example, Smith et al. (1929) have shown that the average number of contacts in a packing of lead shots were six to eight in three dimensions. Also, Bernal and Mason (1960) observed an average number of contacts of 5.5 to 6.5, in

three dimensional randomly packed spheres through laboratory tests. Moreover, the simulations by Makse et al. (2000) show four to six contacts on average per particle.

The simplest disk clastic model can be developed with six contact forces around the disk, where all lines of action pass through the centroid (Trollope 1957; Rowe 1962; Butterfield 1969). But the existence of six contacts around the disk can be considered as a special scenario, where the disks would be arranged in an orthogonal structure. The inclination of the line connecting the centres of disks to the horizontal is considered as the contact angle and denoted by 'α' (Figure 6.1). When this contact angle is 60°, the hexagonal packing occurs and it is a rare situation because the disks can re-arrange and even a slightest decrease in the contact angle may break the orthogonal structure.

As the contact angle decreased from 60°, horizontal forces are broken and the number of contacts around the disk reduces to four (Figure 6.1). This packing condition is more probable to exist within a disk assembly and therefore the results in the present study are presented for a disk assembly having a contact angle less than 60° where each disk is subjected to four forces from surrounding disks and vice versa (Figure 6.1). However, the equations and the results for contact angle of 60° are also presented for completeness of the proposed analytical solution in Appendix B.

Force distribution among disks

Every disk was subjected to four forces l, m, L, and M, which act in a direction making an angle of α to the horizontal (Figure 6.1a). Additionally, the weight of the disks was replaced by two equivalent forces (*f*) along the direction of α to horizontal (Figure 6.1b).

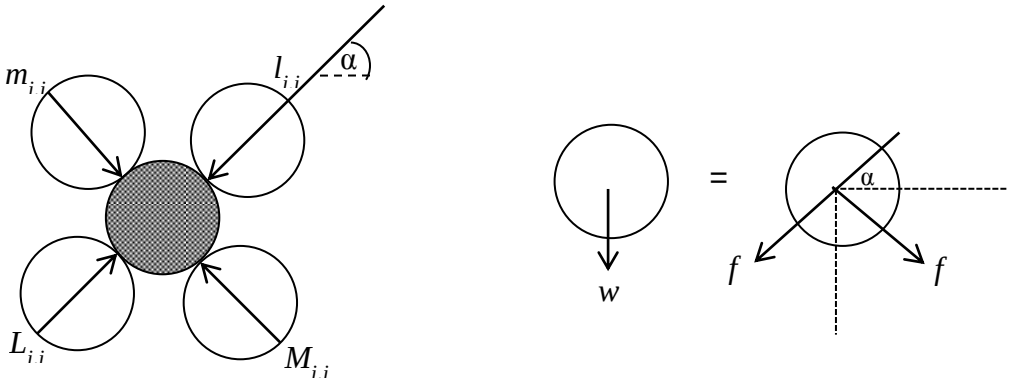

Figure 6.1. The forces in the disk assembly; (a) forces from surrounding disks and (b) the weight represented with two equal forces f

6.2.2 Arching factor- *F*

Butterfield (1969) emphasized the need to address the stress anomalies that occur in silos or similar structures. The stresses existing in silos may not be that less as predicted with the existing arching theory (Section 3.7). This is because the inter-particle forces within a grain arrangement may not be always uniform as assumed in the arching theory. The possibility to relax or tighten the inter-particle forces within a granular material can be modelled with an arching factor (*F*). The arching factor reflects the status of forces between the disks in such a way that $F = 0$ means that all the forces surrounding disks are uniform and the forces from overlying disks are evenly distributed, and $F = 1$ means full arching to the left side, where the forces are increased towards the left side. The intermediate arching ($0 < F < 1$) can model the presence of uneven distribution of inter-particle forces those represent the force transfer possibilities that can exist in a granular material fill.

The arching factor is defined as follows,

$$\frac{M}{L} = (1 - F)\frac{(m + f)}{(l + f)} \tag{6.1}$$

The *L* and *M* forces are calculated as follows,

$$L = \frac{(l+f)(l+m+2f)}{(l+f)+\{(1-F)(m+f)\}} \tag{6.2}$$

$$M = \frac{(m+f)(1-F)(l+m+2f)}{(l+f)+\{(1-F)(m+f)\}} \tag{6.3}$$

Force transmission at walls

As a rigid walled container is filled with granular material, the arching would transfer loads to the walls by means of shear stress. Similarly, within a disk assembly, the shear stresses are generated only at the points, where the disks make contact with walls (Figure 6.2). The force transfer at the wall considering shear forces is calculated as follows;

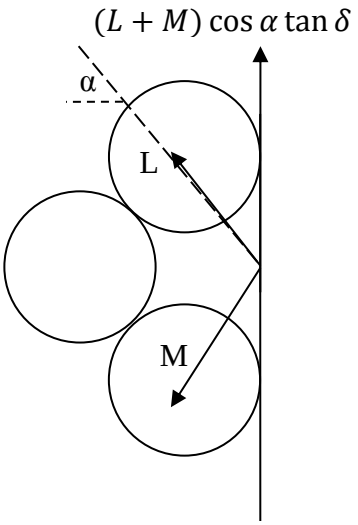

Figure 6.2. The force transmission at walls, when α <60°

Considering the equilibrium at the touching point (Figure 6.3),

$$M\sin\alpha = L\sin\alpha + (L'+M')\cos\alpha\tan\delta \tag{6.4}$$

Then, $M' = L' \times \frac{[\tan\alpha - \tan\delta]}{[\tan\alpha + \tan\delta]}$ (6.5)

6.2.3 Derivation of analytical solution

A structure of width (*B*) and height (*H*) was chosen for the derivation of the proposed solution. Then mono-sized disks were assumed to be packed within this

structure, such that width contains ‘s’ number of disks and height consists of ‘*p*’ number of disks (Figure 6.3). The disk diameter is denoted by ‘*d*’. As a plane strain situation was considered herein, a unit length of disk diameter was used along the length (Figure 6.3). The distance between two adjacent disk centres is 2dcosα (Figure 6.3). The disk weight and disk diameter were calculated from the given input values of model width, model height, bulk density, number of disks on height, number of disks on width and contact angle.

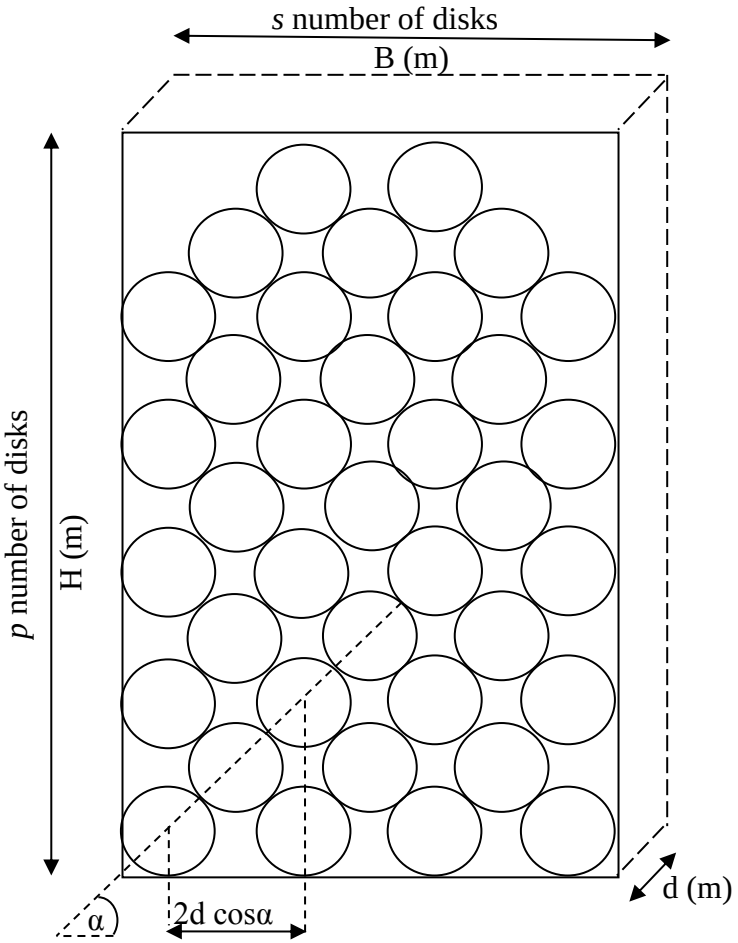

Figure 6.3. Disk arrangement in 2D space and relevant parameters

The vertical stress and horizontal stress on the walls were calculated considering the disk arrangement as idealised in Figure 6.4. The forces from two nearby disks to the walls of the structure were considered in order to calculate the vertical and lateral stresses. The vertical stress throughout the bottom wall was averaged when calculating the average vertical stress.

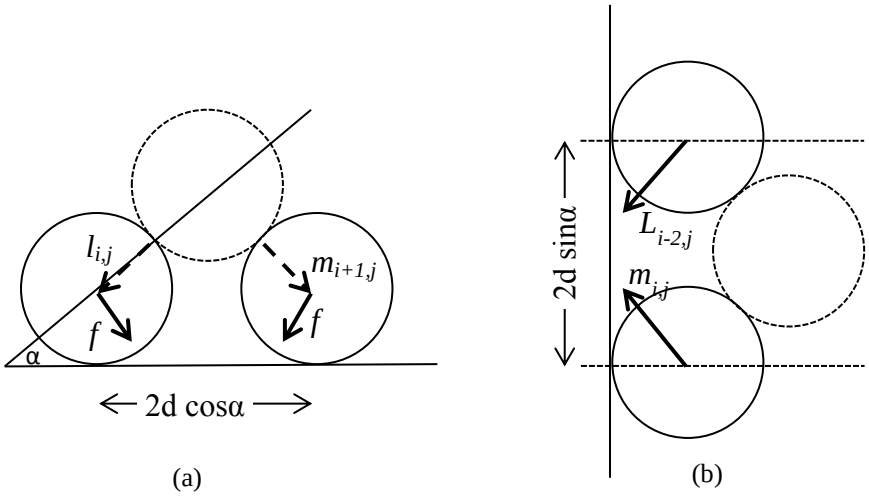

Figure 6.4. Disk arrangement to calculate (a) the vertical stress and (b) the horizontal stress

$$(\sigma_v)_{i,j} = \frac{\left(l_{i,j} + m_{i,j+1}\right)\sin\alpha + 2f\sin\alpha}{2d^2\cos\alpha} \tag{6.6}$$

$$(\sigma_h)_{i,j} = \frac{\left(L_{i-2,j} + m_{i,j}\right)\cos\alpha}{2d^2\sin\alpha} \tag{6.7}$$

6.3 Analytical equations for inter-disk forces

The following assembly of disks was considered for the derivation of inter-particle forces. The row number (n_i) increases with depth and the column number (n_j) increases towards the centre. Only the right half of the model was considered because of symmetry (Figure 6.5). The forces around a particular disk can be simplified into 8 cases, for the model considering the *i, j* position of a disk within the disk assembly. The computations of the forces *l*, *m*, *L* and *M* for each case are given below.

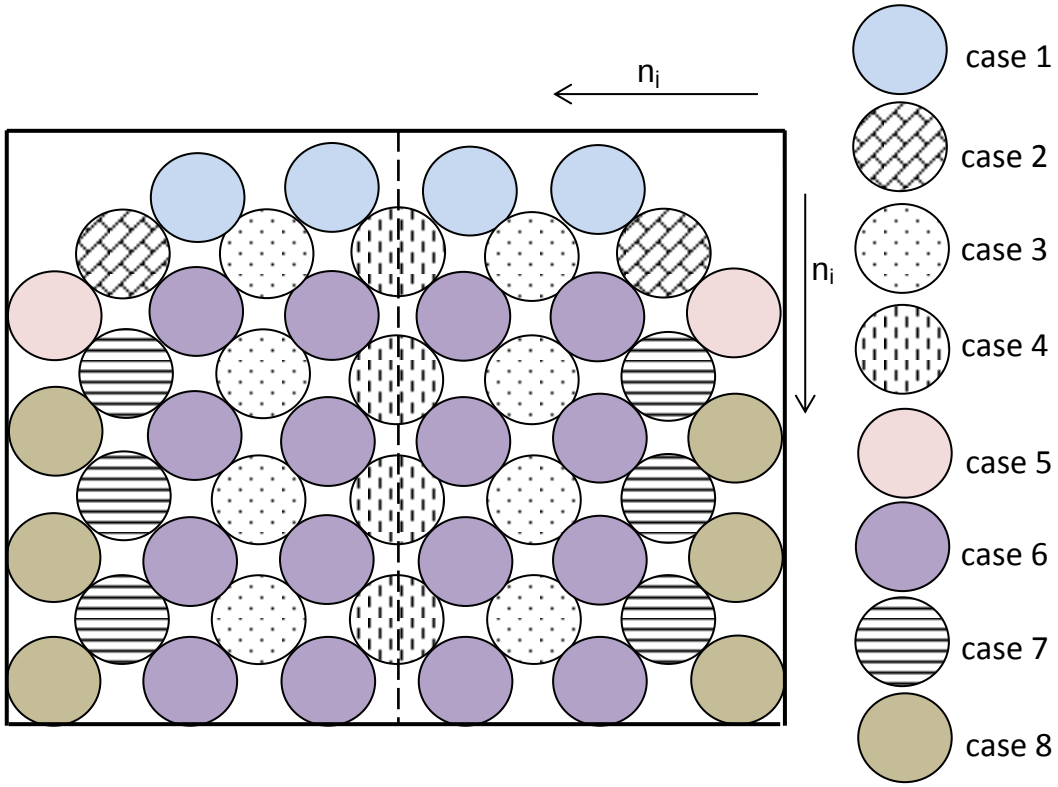

Figure 6.5. The disk arrangement highlighting the cases considered for calculations; each disk is identified with the respective *i,j* location

Case 1. for, $i = 1$

$$l_{i,j} = m_{i,j} = 0 \tag{6.8a}$$

$$L_{i,j} = M_{i,j} = f \tag{6.8b}$$

Case 2. for, $i = 2$ and $j = 1$

$$l_{i,j} = 0 \tag{6.9a}$$

$$m_{i,j} = M_{i-1,j+1} \tag{6.9b}$$

$$L_{i,j} = \frac{(l_{i,j} + f)(l_{i,j} + m_{i,j} + 2f)}{\{(l_{i,j} + f) + (1 - F)(m_{i,j} + f)\}} \tag{6.9c}$$

$$M_{i,j} = \frac{(1 - F)(m_{i,j} + f)(l_{i,j} + m_{i,j} + 2f)}{\{(l_{i,j} + f) + (1 - F)(m_{i,j} + f)\}} \tag{6.9d}$$

Case 3. for, $i = 2, 4, 6..$ and $j \neq 1$ and $j \neq n_j$

$$l_{i,j} = L_{i-1,j} \tag{6.10a}$$

$$m_{i,j} = M_{i-1,j+1} \tag{6.10b}$$

$$L_{i,j} = \frac{(l_{i,j} + f)(l_{i,j} + m_{i,j} + 2f)}{\{(l_{i,j} + f) + (1 - F)(m_{i,j} + f)\}} \tag{6.10c}$$

$$M_{i,j} = \frac{(1 - F)(m_{i,j} + f)(l_{i,j} + m_{i,j} + 2f)}{\{(l_{i,j} + f) + (1 - F)(m_{i,j} + f)\}} \tag{6.10d}$$

Case 4. for, $i = 2, 4, 6..$ and $j = n_j$

$$l_{i,j} = L_{i-1,j} \tag{6.11a}$$

$$m_{i,j} = l_{i,j} \tag{6.11b}$$

$$L_{i,j} = l_{i,j} + f \tag{6.11c}$$

$$M_{i,j} = m_{i,j} + f \tag{6.11d}$$

Case 5. for, $i = 3$ and $j = 1$

$$l_{i,j} = 0 \tag{6.12a}$$

$$m_{i,j} = M_{i-1,j} \tag{6.12b}$$

$$L_{i,j} = \frac{(l_{i,j} + f)(l_{i,j} + m_{i,j} + 2f)}{\{(l_{i,j} + f) + (1 - F)(m_{i,j} + f)\}} \tag{6.12c}$$

$$M_{i,j} = \frac{(1-F)\left(m_{i,j}+f\right)\left(l_{i,j}+m_{i,j}+2f\right)}{\left\{\left(l_{i,j}+f\right)+(1-F)\left(m_{i,j}+f\right)\right\}} \tag{6.12d}$$

Case 6. for, $i = 3$ and $j \neq 1$

$$l_{i,j} = L_{i-1,j-1} \tag{6.13a}$$

$$m_{i,j} = M_{i-1,j} \tag{6.13b}$$

$$L_{i,j} = \frac{\left(l_{i,j}+f\right)\left(l_{i,j}+m_{i,j}+2f\right)}{\left\{\left(l_{i,j}+f\right)+(1-A)\left(m_{i,j}+f\right)\right\}} \tag{6.13c}$$

$$M_{i,j} = \frac{(1-F)\left(m_{i,j}+f\right)\left(l_{i,j}+m_{i,j}+2f\right)}{\left\{\left(l_{i,j}+f\right)+(1-F)\left(m_{i,j}+f\right)\right\}} \tag{6.13d}$$

Case 7. for, $i = 4, 6, 8..$ and $j = 1$

$$l_{i,j} = L_{i-1,j} \tag{6.14a}$$

$$m_{i,j} = M_{i-1,j+1} \tag{6.14b}$$

$$L_{i,j} = \frac{\left(l_{i,j}+f\right)\left(l_{i,j}+m_{i,j}+2f\right)}{\left\{\left(l_{i,j}+f\right)+(1-F)\left(m_{i,j}+f\right)\right\}} \tag{6.14c}$$

$$M_{i,j} = \frac{(1-F)\left(m_{i,j}+f\right)\left(l_{i,j}+m_{i,j}+2f\right)}{\left\{\left(l_{i,j}+f\right)+(1-F)\left(m_{i,j}+f\right)\right\}} \tag{6.14d}$$

Case 8. for, $i = 5, 7, 9..$ and $j = 1$

$$l_{i,j} = \frac{[\tan\alpha - \tan\delta]}{[\tan\alpha + \tan\delta]} \times M_{i-2,j} \tag{6.15a}$$

$$m_{i,j} = M_{i-1,j} \tag{6.15b}$$

$$L_{i,j} = \frac{\left(l_{i,j}+f\right)\left(l_{i,j}+m_{i,j}+2f\right)}{\left\{\left(l_{i,j}+f\right)+(1-F)\left(m_{i,j}+f\right)\right\}} \tag{6.15c}$$

$$M_{i,j} = \frac{(1-F)\left(m_{i,j}+f\right)\left(l_{i,j}+m_{i,j}+2f\right)}{\left\{\left(l_{i,j}+f\right)+(1-F)\left(m_{i,j}+f\right)\right\}} \tag{6.15d}$$

The equations were written to a Matlab program file and executed to output the vertical stresses and horizontal stresses. The complete calculation algorithm is included in Appendix B.

6.4 Sensitivity of the model

The effect of arching factor (F) and the disk diameter (d) on the vertical stress is discussed in this section. Figure 6.6 shows the average vertical stress variation with depth for various F values. The average vertical stress was calculated for depth using the equations 6.8 to 6.15.

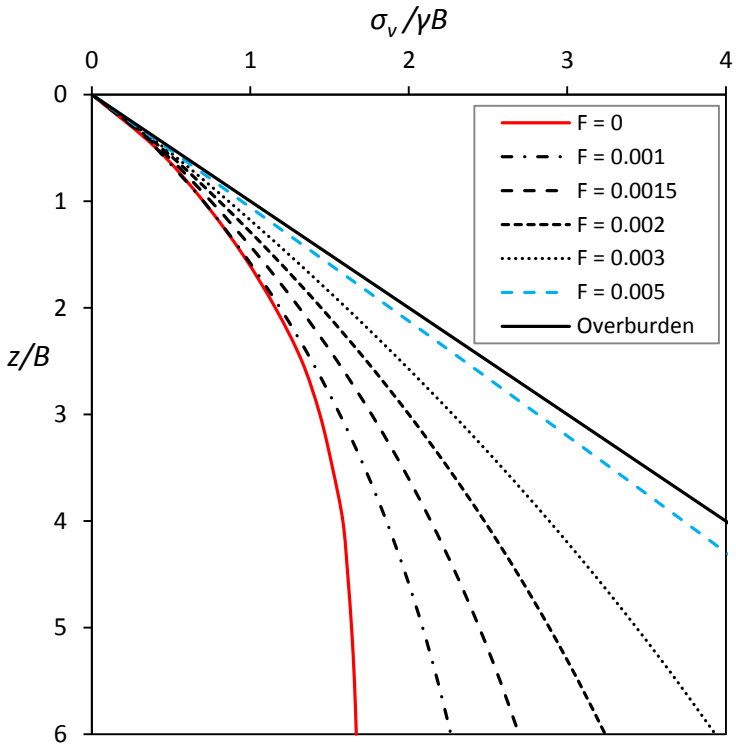

Figure 6.6. Sensitivity of F on average vertical stress variation

According to the defintion, the F values can range from 0 to 1. However, when F = 0.005, the vertical stress variation becomes closer to the overburden stress (Figure 6.6). Further increase in F would result vertical stresses similar to the overburden stress. Therefore, only the vertical stress variations determined within the range of $F = 0.005$ to $F = 0$ are shown in Figure 6.6 for comparison. The average vertical stress on bottom is significantly reduced when F is less than 0.005 (Figure 6.6). When $F = 0$, i.e., uniform L and M forces, the vertical stress decreases showing significant arching and the average vertical stress variation becomes asymptotic as expected with the arching theory. However, the intermediate values of F would output a

range of vertical stresses for the given system and these vertical stresses show an increase with depth, unless $F = 0$ (Figure 6.6).

The number of disks used in the model affects the vertical stress variation. In the present study, 3 million, 12 million and 48 million disks were considered and the corresponding vertical stress variation is given in Figure 6.7. The model dimensions were considered as width of 100 mm and height of 600 mm and maintained for all cases throughout the comparison. The higher number of disks within the model resulted in reduced disk diameter to be able to accommodate within the given dimensions. The disk diameters and the recorded maximum vertical stresses for considered models are given in Table 6.1.

The vertical stress is higher when 48 million disks are used in the model compared to 3 million disks. The magnitude of lateral stress onto the wall impacts on the arching and the highest lateral stresses on walls may result in the lowest vertical stresses at the bottom. When less number of disks (i.e. larger diameters) were used in the model, higher lateral stresses occurred which resulted ultimately lower vertical

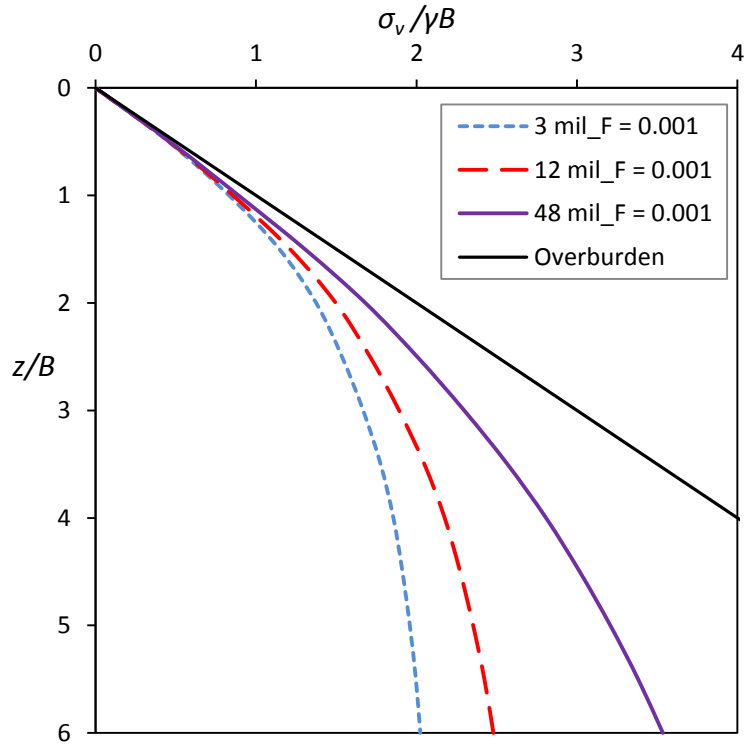

Figure 6.7. Variation of vertical stress with number of disks used in the model

stresses at the bottom. On the other hand, when large number of disks was used in the model the lateral stress at the wall was decreased and higher vertical stress at bottom was observed. Therefore, depending on the number of disks used in the model, the lateral stress may vary which results in varying vertical stress at bottom.

Table 6.1. The maximum average vertical stress compared with the number of disks used in the model

Number of disks (0.5s*p)	**Disk diameter (μm)**	**Maximum average vertical stress ($\sigma_v/\gamma B$)**
500*6000 = 3 million	87.18	2.02
1000*12000 = 12 million	43.59	2.47
2000*24000 = 48 million	21.79	3.53

6.4.1 Vertical stress outputs and comparison with arching theory

The vertical stress variations from the developed analytical solution and from the arching theory were compared in Figure 6.8. Two lateral pressure coefficients ($K = K_0$ and $K = K_a$) were used for the arching theory and the resulting vertical stress variations are included in Figure 6.8.

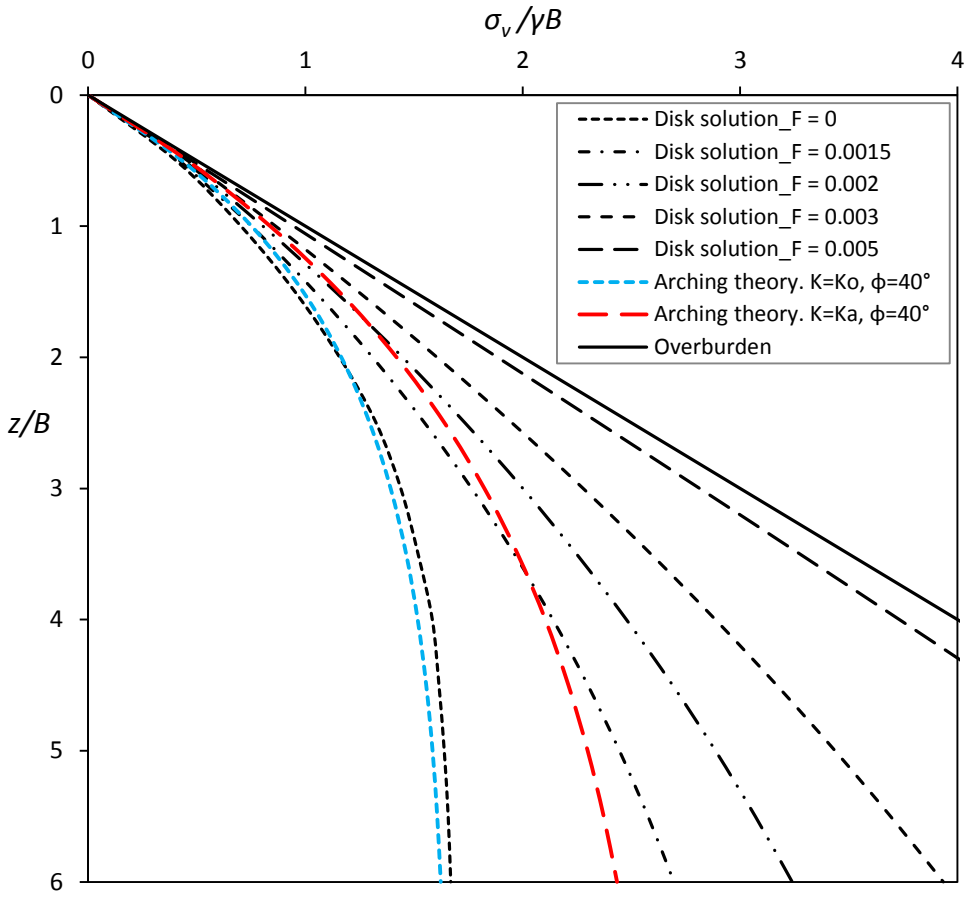

Figure 6.8. Variation of vertical stress from the proposed analytical equation is compared with arching theory

Both vertical stress estimations from arching theory shown in Figure 6.8 are varying exponentially. The vertical stresses estimated with arching theory (when $K = K_0$) and proposed analytical solution (when $F = 0$) are similar. When $F = 0$, the disks are subjected to uniform L and M forces and therefore, the vertical stress variation closely matches the arching theory with $K = K_0$. However, with intermediate F values ($0 < F < 0.005$), the presented analytical solution outputs vertical stress variations that are not usually estimated with the arching theory. While the vertical stresses derived from the arching theory reach asymptotic values at z/B greater than 4, those determined with the present study by considering an assembly of disks show that the vertical stress continue to increase even at depths as high as $6B$ with no sign of reaching any asymptotic value.

6.4.2 Lateral variation of vertical stress

The vertical stress at any point along the width can be calculated with Equation 6.6 as the inter-disk forces are readily available. The vertical stress variation along the width at a depth of 6*B* is presented for different values of *F* in Figure 6.9. The distance from the centreline is considered as *x* and normalised with the width *B*.

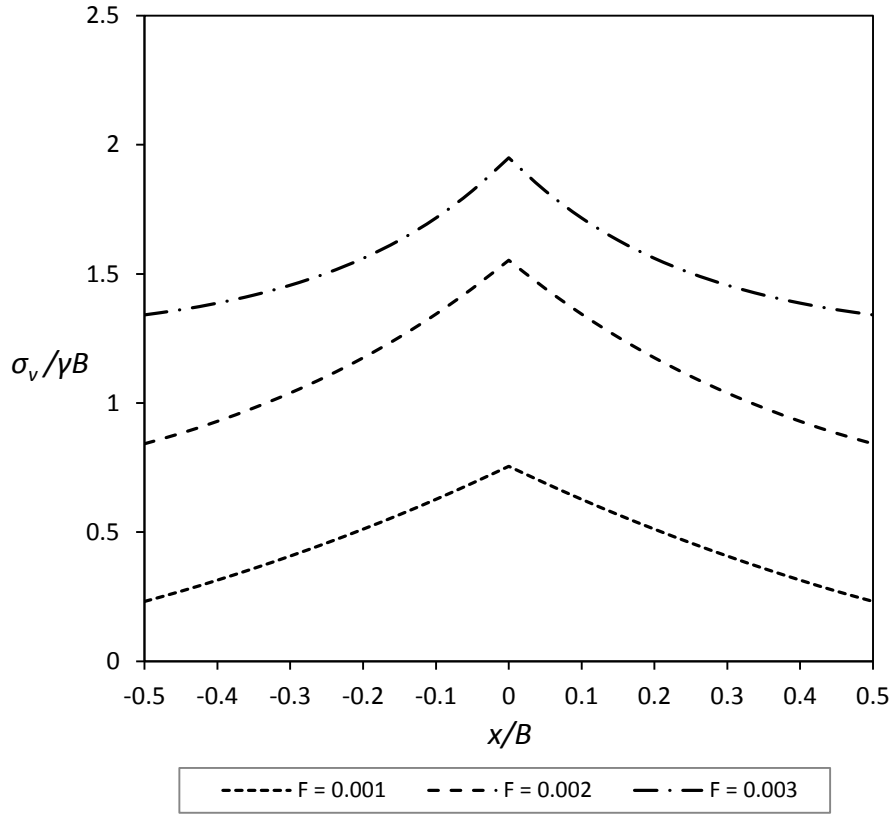

Figure 6.9. Variation of vertical stress along the width, for various arching factors, at a depth of 6B

The vertical stress increases towards the centre in Figure 6.9, irrespective of the value of *F*. Lower F values show a linear increase of vertical stress towards the centre, but when F is increased the vertical stresses are increased non-linearly towards the centre. This implies that the *L* forces are increased and M forces are decreased with the increase of *F* when right half of the container is considered. Moreover, this proposed solution results in non-zero vertical stresses close to the wall at depths like 6*B* (Figure 6.9). As the disk forces in the material below are calculated based on the

overlying disk forces and the inter-disk forces close to the wall remain non-zero, in the proposed analytical solution.

Next, the lateral variation of the vertical stress at different depths was studied. The vertical stress variation at heights of 2*B*, 4*B* and 6*B* for F = 0.002 is shown in Figure 6.10.

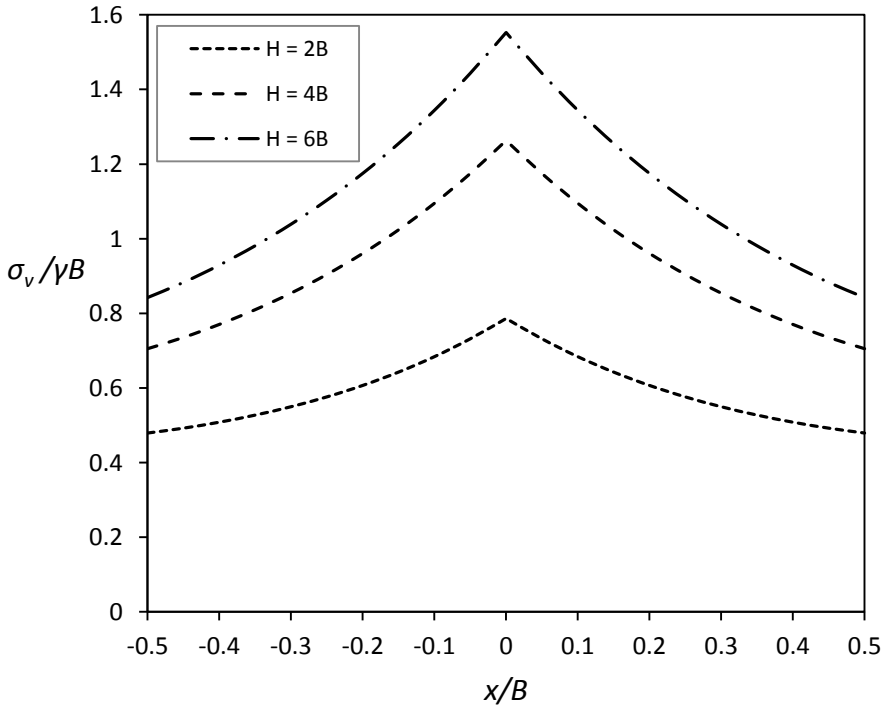

Figure 6.10. Lateral variation of average stress at depths of 2*B*, 4*B* and 6*B*; (*F* = 0.002)

As shown in Figure 6.10, the vertical stress is minimum at the fill and wall boundary (*x*/*B* = -0.5 and 0.5). The vertical stress increases non-linearly and reaches the maximum at the centre (*x*/*B* = 0). Moreover, the rate of increase in the vertical stress increases with the depth in such a way that the depth of 6*B* (maximum depth used in the model) shows the steepest increase in the vertical stress. For a given point (For example at *x*/*B* = 0, centre) the increase of vertical stress is not proportional to the increase of the depth (Figure 6.10). As the depth increases, the rate of increase of vertical stress at the

centre decreases (Figure 6.10). This reduction of rate of increase of vertical stress shows the arching effect within the system.

6.4.3 Variation of lateral pressure coefficient

The defined K_1 (Equation 5.17a) is synonymous to the K used in the arching theory. The value of K_1 can be calculated with the proposed analytical solution. The calculated K_1 at various depths for three different F values is given in Figure 6.11.

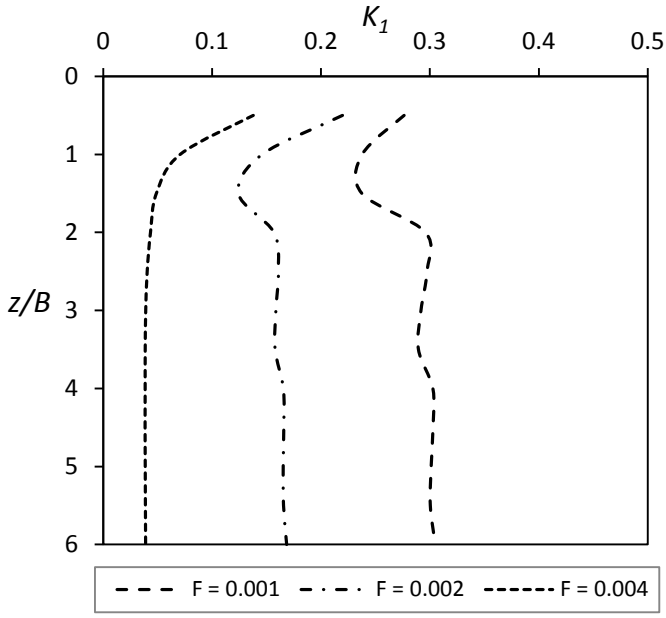

Figure 6.11. Variation of calculated lateral pressure coefficient (K_1) with depth for different F values

The K_1 values are not constant either with depth or with the input F value (Figure 6.11). Additionally, the K_1 is decreased with the F value assumed. Previously, the K_1 varied with depth in laboratory test results and this is also evident in the presented analytical solution. Though the variation of calculated K values with laboratory tests (Figure 3.10) are not similar to the K_1 values from the presented solution, overall the lateral pressure coefficient K_1 can be concluded as a varying parameter.

6.5 Comparison of laboratory tests with analytical solution

The average vertical stress from the presented analytical solution is compared with the laboratory model test results (Figure 6.12). The narrow rectangular stope of $B/L = 0.2$ was used for the comparison, because the laboratory test results for sand (Figure 2.1) and HFs are readily available (Figure 3.18) for this narrow rectangular stope.

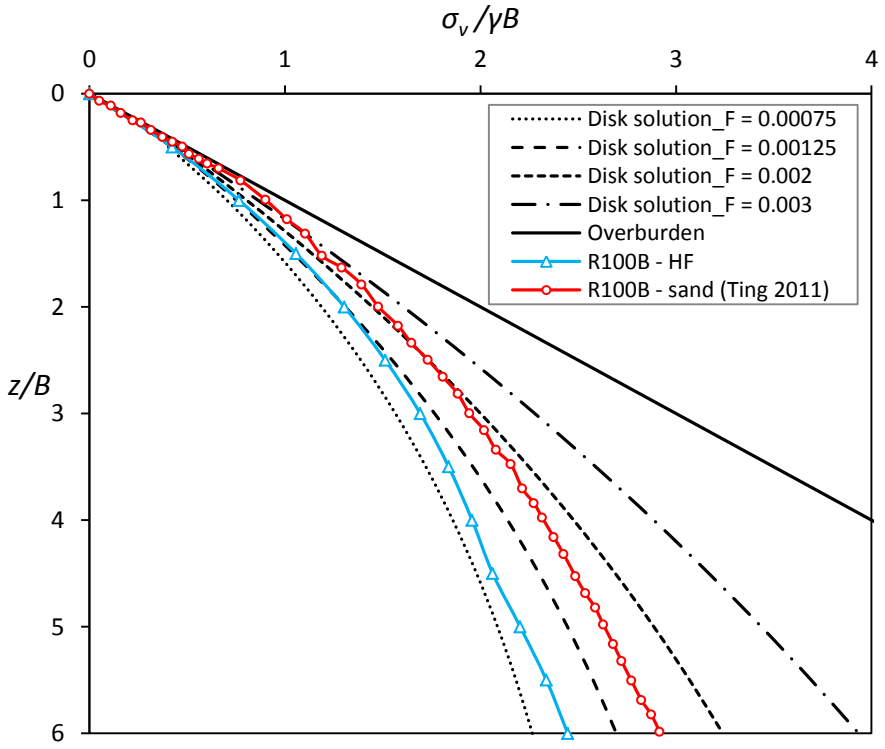

Figure 6.12. The laboratory test results for B/L = 0.2 model are compared with the proposed analytical solution

In laboratory tests the vertical stress variation for HFs and sand shows a linear increase after a depth of 3*B*. The presented analytical procedure predicts vertical stresses close to the values observed in the laboratory tests and also shows a linear increase in the vertical stress after a depth of 3*B* (Figure 6.12). Moreover, the vertical stresses do not reach an asymptotic stress both in the laboratory tests and in the presented analytical solution.

Next, the laboratory test results with B/L = 0.2 container were best fitted by the proposed analytical solution by varying the input of arching factor (F). The resulting vertical stress variations are shown in Figure 6.13 with the results for sand as well as HF.

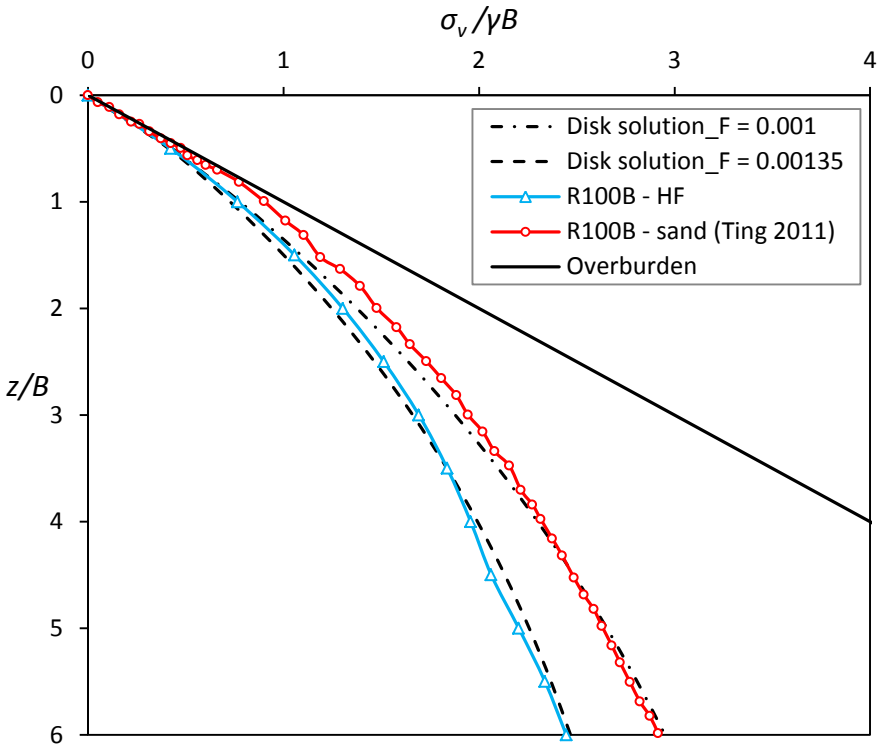

Figure 6.13. The proposed analytical solution is matched with laboratory model test results with B/L = 0.2

The analytical solution, when F = 0.00135 matched the test results for sand whereas F = 0.001 matched the test results for HFs in narrow rectangular stope. The vertical stress variation from laboratory tests when depths larger than 3B, matched the proposed analytical solution (Figure 6.13). Overall HFs showed lower vertical stresses than sand as the interlocking of grains is higher in HF materials. Therefore the HF tends to interlock more and induce higher lateral stresses onto the walls. As the vertical stress variations are matched, the existance of different lateral stresses onto the walls can be estimated using appropriate input values for F (Figure 6.13).

Next, the vertical stress derived from the analytical solution matched the proposed extrapolation of vertical stresses that were obtained when HF was filled to a

narrow stope as given in Section 3.8 (Figure 6.14). As the extrapolation was conducted for upper section of the stope (region1) and lower section of the stope (region 2), the resulted curve is not smooth in the range of $z = B$ to $4B$. According to Figure 6.14, at large depths the vertical stress from analytical solution with $F = 0.00125$ shows a good match with the laboratory test results.

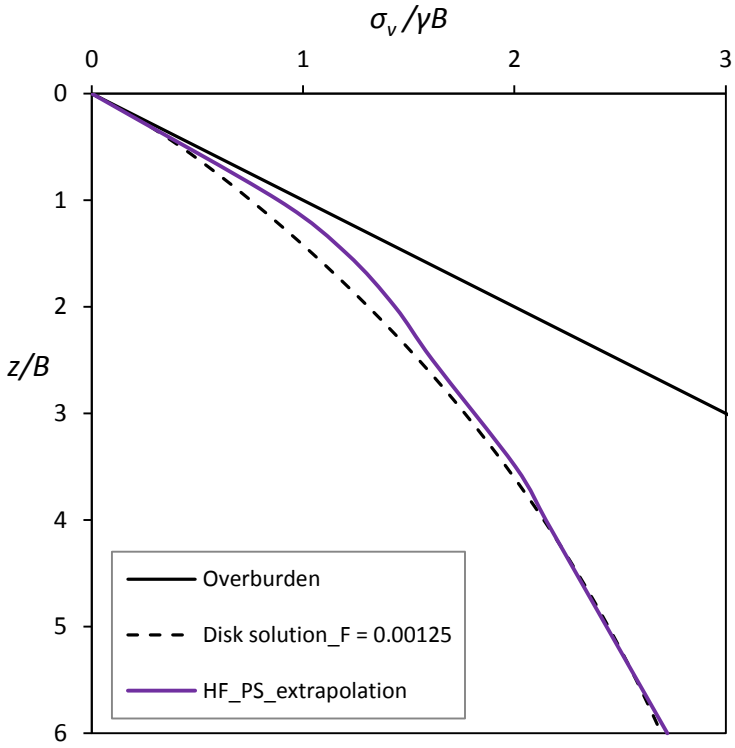

Figure 6.14. The derived vertical stress variation with laboratory tests is matched with the proposed analytical solution

6.7 Advantages and limitations of proposed numerical approach

As the stress distribution within a granular fill is dictated by several other factors not considered in the continuum approach, such as grain size distribution, grain angularity, filling method etc., the arching theory does not provide a realistic picture especially when used on dry granular medium. However, the proposed analytical solution is capable of reasoning the existence of a range of vertical stresses within a granular filled containment. The arching factor (F) introduced here distributes the inter-particle forces unevenly and therefore the solution outputs vertical stress variations that

are similar to what was observed with the laboratory tests. The Matlab program is capable of handling a reasonable number of disks in proposed model calculations. For example, a model with 12 million disks could be solved within 3 minutes. However, the memory demand and model runtime may increase with the increasing number of disks.

Moreover, granular grains rearrange with the load applied and this re-arrangement can be analyse with an inter-disk contact angle (Duran et al. 1998). However, the contact angle of disks is a fixed input condition within the proposed solution. The proposed solution can be further modified by introducing a variation factor for the contact angle with the forces on the disks within the system. Furthermore, most of the grains within a granular material do not contribute towards carrying the forces and are termed as 'rattlers' since they are free to rattle. Agnolin and Roux (2007) have defined the rattlers as particles having less than four contacts with the surrounding. Only the rest of the grains (heavily loaded grains) contribute to bear the force and to form axially loaded columns or force columns (Drescher and de Josselin de Jong 1972; Vanel and Clément 1999). Although the proposed analytical solution does not model force columns or rattlers, it aims to present the idea of force calculations for individual grains. It is the particulate nature of the granular material that is responsible for developing the above mentioned rattlers as well as force columns. Although the proposed solution did not explicitly show the existence of axially loaded columns or rattlers, the lateral variation of vertical stresses shown in Figure 6.9 suggest that the vertical stress is higher towards the centre. Therefore, the proposed analytical solution estimates the lateral stress variation occurring within the granular material to a reasonable extent.

The discrete element simulation packages (Particle Flow Code: PFC (Itasca 2012)) are more sophisticated discrete elements models and are capable of detecting breaking and forming of grain contacts as well as the grain shearing. The Discrete Element Method (DEM) considers the equilibrium of contact forces and the displacements of an assembly of disks are found through a series of calculations tracing

the movements of the individual grains. Though the proposed analytical solution is not as sophisticated as DEM, it highlights the calculation of inter-particle forces and their interaction to a reasonable extent. Additionally, the proposed analytical solution is an improvement to the Butterfield (1969) solution and the use of Matlab allows outputting location specific and detailed calculations to study the lateral variation of vertical stress as given in Figures 6.9 and 6.10. The possibility to calculate the horizontal and lateral stresses at any point within the model can be considered as an advantage of this model.

The shearing among the disks or the inter-disk friction is not modelled with the proposed analytical solution. The inclusion of inter-disk friction would require more iterations as the shearing would change the force distributions throughout the system. Moreover, the disks were assumed to be mono-sized to avoid a complex calculation scheme. However, the inclusion of different-sized disks with inter-disk shearing may output highly comparable results to the laboratory tests, but may require complex algorithms.

6.8 Summary and conclusions

A continuum approach can be assumed to model cohesive materials such as clays, but may not be suitable to describe the stress variations within cohesionless granular materials. Discreteness and randomness of force distributions make it difficult to implement a continuum approach for such material. Continuum behaviour can be considered as a lower bound solution for a granular system. But the upper bound can be subjected to change with other granular parameters (for example, packing density, filling method, etc). Most of the developed analytical equations assume uniform stress distribution across a particular height, but this condition is only a realistic upper limit of the force re-distributions (Trollope and Burman 1980).

The continuous increase of vertical stress was observed in laboratory tests, as well as in the analytical solution proposed in this chapter based on particulate approach,

even at large depths (Figure 6.13). When a filling of granular material is considered the arching theory implies higher lateral stresses, and as a result the vertical stress reaches an asymptote. However, the lateral stresses within a granular system, are not as high as expected with the arching theory and therefore, weight of the added layer may not be balanced by the shear forces, which may result in a portion of the additional layer weight to be transferred to the base. This makes the vertical stress to increase even after depths of 6B. When the grain confinement is low, the lateral stresses on the walls are low and hence it will lead to less arching. The relaxation or increase of inter-particle forces is modelled with an appropriate input parameter *F*. The presence of intermediate arching factor values (*F*) would result in less lateral forces than expected with arching theory and closely match the vertical stress profiles determined from laboratory tests.

The vertical stress variations shown with HFs and sand are different during the laboratory studies (Figure 3.14). The internal friction angle is almost equal for HFs and sand, and therefore the similar vertical stress variations are postulated in the arching theory. However, a difference in the vertical stresses for HFs and sand was observed because the granular parameters and grain interactions would affect the force transfer as observed with the laboratory tests. The angular shaped grains in HFs interlock and transfer more forces to walls, whereas the sand with sub-rounded grains interlocks less than HFs and transfer comparatively less forces to walls. Although the presented analytical solution cannot explicitly model the interlocking of grains, the given α and *F* parameters are capable of estimating a range of vertical stress for a particular granular backfill. Therefore, a range of vertical stress may be expected with granular filling, as suggested by Butterfield (1969), Blight (1986) and many others, depending on the grain packing and force distributions among grains.

Finally, the analytical solution presented in this chapter is similar to Butterfield (1969) solution, but has numerous advantages as the individual particle forces are calculated. The possibility to calculate the vertical or lateral stress at any point within the fill makes it possible to evaluate the lateral or vertical variation of stresses within the

fill. Additionally, the number of disks used in the Butterfield (1969) solution is a fixed parameter for a container with certain dimensions, whereas the proposed solution makes it possible to model disks with various diameters within the same stope dimensions.

Chapter 7

Summary, Conclusions and Recommendations for Future Research

7.1 Summary

Mine backfilling is a vital process within the mining cycle. The understanding about the backfill load redistributions inside the stope as well in the drive would pave the path to optimise barricade designs. The literature review consists of two sections, first discussing the geotechnical properties of backfills and the barricade failure mechanisms that have been identified in the literature. The failures related to barricades are identified as being dependent on the quality of construction, backfill quality control and management of fill pours. However, there is a lack of research and understanding on the variation of loads on the barricade with the offset distance. The latter section of the literature review critically analyse the arching theories and identifies a scatter of vertical and horizontal stresses from in situ stress measurements and from laboratory model tests that is not supported by the arching theory.

In Chapter 3, a generalised analytical equation to determine the vertical stresses within a backfilled structure is presented, considering the stope perimeter (P) and the cross-sectional area (A) as geometry inputs. Limit equilibrium analysis with a horizontal layer element is used for the derivation of this generalised analytical equation. Laboratory model tests for backfilled structures were performed and the measured average vertical stress variation deviated from the estimated vertical stresses from arching theory. Two distinct trends in the vertical stress variations were observed with laboratory tests, such that in shallow depths (region 1: $z/B < 3$) the vertical stress varied exponentially and at large depths (region 2: $z/B > 3$) the vertical stress was increased linearly. Moreover, the horizontal stress exerted on the walls were also measured within the laboratory setup and the results show that the horizontal stresses become asymptotic at a shallow depth, i.e. reaching a maximum horizontal stress and will not increase beyond. As the laboratory model stope is filled in layers, the additional weight from new layers is partially balanced by the shear forces and the rest is transferred to the bottom as vertical forces. At shallow depths the granular matrix within the cohesionless granular media holds the arch (transfer a large proportion of the load to walls via shear

forces). But as the depth increases, with the addition of load from above, the shear forces reach a maximum and transfer the rest of the load of the fill layer to bottom. Therefore a linear increase of vertical stress was observed for large depths ($z/B > 3$). This can be considered as the major difference in the stress variation observed between the laboratory tests and the arching theory developed from a continuum approach.

A constant lateral pressure coefficient is used with the arching theory, such that the horizontal stress increases proportionally with the vertical stress. As the laboratory model is equipped to measure the average vertical stress as well as the horizontal stress on walls, the lateral stress coefficient (K_{calc}) was calculated and shown that it is not a constant along the depth. Therefore, the variation of the lateral earth pressure ratio must be considered in designs and a range of vertical stresses may be expected within a structure backfilled with cohesionless granular material.

Laboratory tests were conducted for square ($B/L = 1$) and rectangular ($B/L = 0.2$) backfilled model stopes. Since a plane strain model of a backfilled stope, or a very long narrow stope cannot be built within laboratory conditions, an empirical equation to estimate vertical stress in plane strain conditions is developed with extrapolation. As the vertical stress variation from laboratory tests shows two different trends in the stress variations with depth, the extrapolation for the vertical stress in plane strain conditions is also carried out, combining the exponential regression for region 1 and the linear regression for region 2 and considering B/L and z/B as independent variables. The proposed vertical stress variation is distinct to the stress variation proposed by the arching theory.

Towards the end of Chapter 3, two interpretations for the vertical normal stress σ_v variation with depth z have been identified with numerical simulations. Method 1 tracks the stress at the bottom of the stope while filling progresses and this σ_v at bottom is used in determining the σ_v variation. The other method, method 2, records the σ_v values at various depths at the end of filling to determine the σ_v variation. The two different procedures used for determining the vertical stress profile give different values

of stresses, except for at the top and bottom of the stope. The difference is attributed to fixing the bottom of the stope, implying zero displacement in any direction. Additionally, method 1 provides an interpretation about the variation of the vertical stress at the bottom throughout the filling process and method 2 outputs the vertical stress variation within a filled stope. This study identified that the often used approach in numerical modelling (method 2) is not necessarily the better of the two stress interpretation methods. When the stresses or loadings at the bottom of a structure are required for determining the lateral stresses into the barricade while the filling progresses, method 1 appears to be more appropriate.

Vertical stress isobars are a novel concept, which presents an estimate of the vertical stress for a particular backfill within rigid walls. As the stress isobars have been developed with a two-dimensional simulation package, the vertical stresses within plane strain or axisymmetric backfills can be estimated. However, interpolation can be used to estimate the vertical stresses within a rectangular backfill. The presented stress isobars in Chapter 4 were labelled with the normalised vertical stress values, such that the stress isobar charts can be used to estimate the vertical stresses within any other cohesionless backfill and within a structure of any width. Moreover, the height of the structure was also presented as a normalised variable and therefore these stress isobars can be used for a structure of height up to 6*B*.

In Chapter 5, a laboratory test setup was designed and assembled to measure the barricade stresses with respect to the vertical stress at the stope centre. The loading conditions on the barricade may be different depending on the full draining or impermeable conditions of the barricade. Chapter 5 was focused on determining a general relationship of the barricade stress with the barricade dimensions and the offset distance. Earth pressure cells were used as pressure transducers to measure the stresses on the barricade, at the stope centre and at the stope edge. A uniform load was applied from MTS loading machine to subject the fill within the drive to a large stress conditions as experienced in the prototype structure. Four drive widths were tested and

four offset distances were tested for each drive width. Drives were made out to widths of 75 mm, 100 mm, 125 mm and 150 mm, and attached to the 310 mm in diameter model stope. The surcharge was applied in stages, and the barricade load, the vertical stress at the centre and the edge were recorded using a data logger.

FLAC^{3D} was used to simulate the laboratory tests with drives, because the inclusion of drive makes the model a three-dimensional problem. In terms of the simulation results, FLAC^{3D} gives a relatively higher stress on the barricade when placed at the stope entrance and the barricade stress decreases with an increase in the offset distance. However, a similar level of decay in the barricade stresses is predicted by the laboratory test results. On the other hand, the analytical equations overestimate the stresses on the barricade. Therefore, based on the barricade stresses from the laboratory tests, an empirical equation was proposed for the barricade stress variation with offset distance. In this empirical equation, the stress on the barricade was expressed in terms of the vertical stress at the stope centre. The vertical stress at the stope centre can be determined by using the stress isobar charts given in Chapter 4. The application of the proposed empirical procedure combines the stress isobar charts and laboratory test results.

In Chapter 6, an analytical solution was proposed considering the statistical equilibrium of a regular assembly of mono-sized disks. The limit equilibrium analysis of the arching theory may not be suitable to describe the stress variations within the cohesionless granular materials. Discreteness and randomness of particle interactions make it difficult to implement a continuum approach. Therefore, the continuum behaviour can be considered as an upper bound solution for a granular system, or the extreme case of development of uniform forces on every particle, but the lower bound is subjected to change with other granular parameters, such as the grain size, grain interlocking, etc. As an alternative, an analytical solution was proposed based on inter-particle forces within a regular assembly of mono-sized disks.

The proposed analytical solution in Chapter 6 considers the force distribution among disks and the uneven force distributions are modelled with an input parameter called arching factor (F). By definition, $F = 0$ indicates uniform forces around a disk and $F = 1$ indicates that forces are maximised to the left side, which is also called as full arching to the left side condition. The introduced arching factor visualises the possibility to exist less lateral stresses that are obtained with the laboratory tests. Also it is showen in this study that the stress variation for a particular disk assembly would vary with the number of disks used within the model.

7.2 Conclusions

The study has been carried out to understand the stress developments within backfilled mine stopes and the stress transfer from stopes to the drives. The conclusions that are drawn during the study can be categorised as follows.

Numerical simulations and stress isobars

- The internal friction angle has a minimal effect on the variation of the vertical stress within the range of 30°- 50°. However, the wall friction significantly affects the vertical stress variation and separate stress isobar charts were presented for $\delta = \varphi$ and $\delta = 0.5\varphi$.
- The Young's modulus does not have an effect on the vertical stress variation, within the range of 10 MPa to 3000 MPa. However, the Poisson's ratio has a significant effect on the vertical stress variation with numerical simulations, as the Poisson's ratio dictates whether the material is predominantly in compression or shearing (bulk modulus to the shear modulus ratio). Therefore, the stress isobars were presented for $\nu = 0.2$ and $\nu = 0.3$.
- The use of interface elements is effective with backfill numerical models. The failure at the fill boundary can be elaborately modelled with interface elements, which are built into the FLAC simulation packages.
- The inclusion of cohesion and dilation angle to the interface would result in differences in the vertical stress variation within the backfill.
- The use of normalized dimensionless variables offers greater flexibility to adopt stress isobar charts for any backfill situation, where the height is less than or equal to $6B$ or for another granular material.

Tests for barricade loads and stress variation within drives

- The maximum vertical stress within the stope or the vertical stress at the stope centre should be considered when estimating the loads on the barricade.

- The horizontal stress to the average vertical stress ratio closely matches the lateral pressure coefficient - $K_{krynine}$.
- The normalised barricade stress decreases linearly with the normalised offset distance.
- The normalised barricade stress increases with the drive width.
- The barricade stress varies within a close range when calculated from three approaches, analytical, numerical simulations ($FLAC^{3D}$) and laboratory tests. However, the analytical equation overestimates the stress on the barricade because it considers the average vertical stress at the bottom to calculate the horizontal stress at the stope entrance.

This study was conducted on dry hydraulic fill to understand the stress variations within the drive when backfilled. Additionally, this study sheds light on the arching along the drives and hence the reduced loads acting on the barricade. The normalised stress on the barricade is given as an empirical equation, consisting of the offset distance and the vertical stress at the stope centre. Finally, different situations may exist in field, such as different geometries, different fill material and different material properties. Therefore, the use of the proposed empirical equation may need to adopt this general form to any other backfilling situation with suitable technical competency.

Conclusions from laboratory tests on backfill structures and the proposed analytical model

- The arching theory gives a basis to estimate the vertical stresses in granular filled containments, but is not sufficient. The average vertical stress within the laboratory model does not reach an asymptote even at depths of 6*B*, whereas arching theory estimates that the vertical stress reaches the asymptote value at depths less than 6*B*.

- In the laboratory setup, the filled weight is partially taken by the walls and the rest is transmitted to bottom. The measured shear forces or horizontal stress reach a maximum value in laboratory tests. Additionally, the horizontal stress measured from laboratory tests is less than the estimated value with the arching theory.
- Arching theory uses a constant K (K_0, K_a or $K_{krynine}$) to estimate the stress variations. Additionally, in the arching theory it is considered that the lateral stress ratio is a constant such that the horizontal stress increased proportionally with the vertical stress along the depth. However, it was shown that the ratio of the horizontal stress to the average vertical stress is not a constant and varies with the depth.
- Sand and minefills show distinct variation in the vertical stress profile when filled into a laboratory model stope. The grain interlocking may cause the deviations as sand consists of sub-rounded grains and angular grains in minefills would incur more grain interlocking However, both sand and minefills have shown almost the same internal friction angles and interfacial friction angles with rough walls. Therefore, the arching theory gives a similar vertical stress variation for both sand and HFs. This confirms that the analytical equations related to arching theory are not capable of estimation of vertical stress differences that have occurred because of grain interlocking differences.
- The analytical model developed with regular array of disks successfully replicates the laboratory results for the vertical stress variation, with various arching factor inputs for the model. F = 0.005 outputs a vertical stress variation close to the overburden stress and therefore the F values in between 0 and 0.005 were considered in this proposed analytical solution with a mono-sized disk assembly.
- The vertical stress variations from the laboratory tests from HFs were matched to the proposed analytical model when F = 0.001. Also the vertical stress variations from the laboratory tests for sand were matched with the proposed analytical model when F = 0.00135.

7.3 Recommendations for future research

The aim of the research was to critically assess the arching and stress developments within backfilled stopes and drives and to develop a methodology to estimate the vertical stresses within a stope and also the loads on barricades based on analytical, numerical and laboratory test approaches. The following recommendations are made for future research to further revisit the assumptions used and to develop the proposed analytical model.

Development of the understanding on the loads onto barricades

The empirical equation for the barricade load is proposed in this dissertation on the basis that the drives and barricades are square and circular in cross section. As mining would encounter drives of irregular shapes (for example, horseshoe shape), a study that would analyse the drive shape may be useful. Moreover, the three dimensional nature of the mining stopes and drives would limit the flexibility of the solution developed. However a reasonable solution would assist the mining geomechanics community to estimate loads on barricades and construct barricades as well as control the fill pours accordingly.

Furthermore, numerical ($FLAC^{3D}$) simulations can be developed with including fluid mechanical interactions (stress developments with consolidations) within the fill. This would aid to further understand the development of effective stress within the slurry backfill. The use of three-dimensional simulation software is highly recommended in future studies, as it would relax the assumptions and gives more realistic picture about the stress developments within the drive.

Development of a modified analytical model for disk assembly

The following modifications are suggested to the proposed analytical model with a disk assembly:

- Packing of disks with two different diameters will allow the porosity to be reduced within the model and the vertical stress variations can be further studied with porosity changes, as the variation of relative density is not accounted for in the arching theory or numerical simulations.
- Incorporating inter-particle shearing to the disk assembly would enable one to represent the granular shearing and further to understand the mechanics related to granular material.
- The results from square shaped laboratory scale stopes may be replicated with regular three-dimensional sphere assembly, where the force calculations with three dimensions are accounted for with three-dimensional arrays in Matlab software.
- A comprehensive model, which includes inter particle shearing and irregular particle sizes would be suitable to study the relationship of F and v.

Development of DEM or hybrid DEM numerical simulations

DEM modelling is sophisticated to include a range of particles and to simulate the granular system. However, the computational limitations in a way restrict the applicability of PFC models to backfills as PFC models may need reasonable computer memory capacity to include a reasonable number of granular particles to replicate the backfills. In hybrid models, discrete element domain is included in a small area within a large finite difference domain. And in hybrid models, the surrounding reactions from rocks or other forces are simulated with the finite difference model and the area of interest is modelled with discrete elements. Therefore with DEM or hybrid DEM/FLAC models, the following studies can be conducted:

- The variation of stresses, with changes in the porosity or particle packing
- The effect of particle shearing, rather than assuming shearless contacts between particles, on the stress developments

References

Agnolin, I. and Roux, J.-N. (2007). Internal states of model isotropic granular packings. I. Assembling process, geometry, and contact networks. *Physical Review E, 76*(6), 061302.

Andò, E., Hall, S. A., Viggiani, G., Desrues, J. and Bésuelle, P. (2012). Experimental micromechanics: grain-scale observation of sand deformation. *Géotechnique Letters, 2*(3), 107-112. doi: 10.1680/geolett.12.00027

Andrade, J. E., Avila, C. F., Hall, S. A., Lenoir, N. and Viggiani, G. (2011). Multiscale modeling and characterization of granular matter: From grain kinematics to continuum mechanics. *Journal of the Mechanics and Physics of Solids, 59*(2), 237-250. doi: 10.1016/j.jmps.2010.10.009

Archibald, J., De Souza, E. and Beauchamp, L. (2009). Compilation of industry practices for control of hazards asso-ciated with backfill in underground mines-Part II underground transport and stope placement. In Diederichs, M. & Grasselli, G. (Ed.), 3rd CANUS Rock Mechanics Symposium. Toronto:

AS1289.5.5.1. (1998). soil compaction and density tests - determination of the minimum and maximum dry density of a cohesionless material - standard method *Methods of testing soils for engineering purposes*: STANDARDS AUSTRALIA.

AS1289.6.2.2. (1998). Soil strength and consolidation tests- Determination of the shear strength of a soil- Direct shear test using a shear box *Methods of testing soils for engineering purposes*: STANDARDS AUSTRALIA.

Askegaard, V. (1963). Measurement of pressure in solids by means of stress cells. *Bulletin No.17, Strutural Research Laboratory, Technical University of Denmark,* Copenhagen.

Aubertin, M., Li, L., Arnoldi, S., Belem, T., Bussière, B., Benzaazoua, M. and Simon, R. (2003). Interaction between backfill and rock mass in narrow stopes. In Culligan, P. J. & Whittle, A. J. (Ed.), 12th Pan American Conference on Soil Mechanics and Geotechnical Engineering (pp. 1157-1164). Boston, Massachusetts, USA: MIT.

Barrett, J. R., Coulthard, M. A. and Dight, P. M. (1978). Determination of fill stability. In (Ed.), Mining with Backfill—12th Canadian Rock Mechanics Symposium (pp. 85-91). Sudbury, Ontario, Canada Canadian Institute of Mining and Metallurgy

Belem, T., Harvey, A., Simon, R. and Aubertin, M. (2004). Measurement and prediction of internal stresses in an underground opening during its filling with cemented fill. In Villaescusa, E. & Potvin, Y. (Ed.), Ground support in Mining and Underground construction: Ground Support 2004 (pp. 28–30). Perth, Western Australia: Taylor & Francis group, London.

Bentler, J. and Labuz, J. (2006). Performance of a Cantilever Retaining Wall. *Journal of Geotechnical and Geoenvironmental Engineering, 132*(8), 1062-1070. doi: 10.1061/(ASCE)1090-0241(2006)132:8(1062)

Bernal, J. D. and Mason, J. (1960). Packing of Spheres: Co-ordination of Randomly Packed Spheres. *Nature, 188*, 910-911. doi: 10.1038/188910a0

Berndt, C. C., Rankine, K. J. and Sivakugan, N. (2007). Materials properties of barricade bricks for mining applications. *Geotechnical and Geological Engineering, 25*(4), 449-471. doi: 10.1007/s10706-007-9122-y

Bishop, A. W. (1958). Test Requirements for Measuring the Coefficient of Earth Pressure at Rest",. In (Ed.), Conference on Earth Pressure Problems (pp. 2-14). Brussels

Blight, G. E. (1986). Pressures exerted by materials stored in silos part I, coarse materials. *Geotechnique, 36*, 33-46. doi: 10.1680/geot.1986.36.1.33

Blight, G. E. (1990). Defects in accepted methods of estimating design loading for silos. *Proceedings of the ICE, 88*(88), 1015-1036.

Bloss, M. L. (1992). *Prediction of cemented rock fill stability design procedures and modelling techniques.* (PhD Thesis), University of Queensland, Brisbane.

Bloss, M. L. (2014). An operational perspective of mine backfill. In Potvin, Y. & Grice, A. G. (Ed.), Minefill 2014: 11th International Symposium on Mining with Backfill (pp. 15-30). Perth: Australian Centre For Geomechanics.

Bloss, M. L. and Chen, J. (1998). Drainage research at Mt Isa Mines Limited 1992-1997. In (Ed.), Minefill '98 International symposium of mining with backfill (pp. 111-116). Brisbane: AusIMM.

Borgesson, L. (1981). Mechanical properties of hydraulic backfill. In (Ed.), Application of Rock mechanics to Cut and Fill mining. Lulea, Sweden.: Institution of Mining and Metallurgy, London.

Bozozuk, M. (1976). CB-177. Tower Silo Foundations. *Canadian Building Digests*. Retrieved from http://archive.nrc-cnrc.gc.ca/eng/ibp/irc/cbd/building-digest-177.html website:

Brady, B. and Brown, E. (1985). *Rock mechanics for underground Mining*: George Allen & Unwin Ltd. Pages

Bridges, M. (2003). A new era in fill-retaining barricades. *AMC's newsletter "Digging Deeper" on current events and modern mining methodology.* Retrieved 05 Sept 2011

Brinkgreve, R. B. J., Broere, W. and Waterman, D. (2004). PLAXIS finite element code for soil and rock analysis, 2D (Vol. Version 8.6). Delft, Netherlands: Plaxis bv.

Brooker, E. W. and Ireland, H. O. (1965). Earth Pressures at Rest Related to Stress History. *Canadian Geotechnical Journal, 2*(1), 1-15.

Butterfield, R. (1969). A theoretical study of the pressures developed in a silo containing single-size particles in a regular packing. *International Journal of Rock Mechanics and Mining Sciences, 6*(2), 227-247. doi: 10.1016/0148-9062(69)90037-0

Carson, J. W. (2000). Silo Failures: Case Histories and Lessons Learned. In Levy, A. & Kalman, C. J. (Ed.), Third Israeli conference for conveying and handling of particulate solids (pp. 153-166). Dead sea, Israel.: Elsevier Science B.V.

Celeste, L. (2000). Three miners trapped in West Australian gold mine. Retrieved 05 Sept 2011

Chambon, R. (2011). Instability and bifurcation for inelastic geomaterials. In Bonelli, S., Dascalu, C. & Nicot, F. (Ed.), Advances in Bifurcation and Degradation in Geomaterials (pp. 362). Porquerolles, France.: Springer,New York.

Clayton, C. and Bica, A. (1993). The design of diaphragm-type boundary total stress cells. *Geotechnique, 43*(4), 523-535. doi: 10.1680/geot.1993.43.4.523

Coulthard, M. A. (1999). Applications of numerical modelling in underground mining and construction. *Geotechnical and Geological Engineering, 17*(3), 373-385.

Cowling, R., Grice, A. and Isaacs, L. (1988). Simulation of hydraulic filling of large underground mining excavations. In Swoboda (Ed.), Numerical methods in geomechanics (pp. 1869-1876). Innsbruck: Balkema, Rotterdam.

Cowling, R., Voboril, A., Isaacs, L., Meek, J. and Beer, G. (1989). Computer models for improved fill performance. In (Ed.):

Cundall, P. A. (2001). A discontinuous future for numerical modelling in geomechanics? *Proceedings of the ICE - Geotechnical Engineering, 149*(1), 41-47. doi: 10.1680/geng.2001.149.1.41

Daigle, L. and Zhao, J. Q. (2004). The influence of temperature on earth pressure cell readings. *Canadian Geotechnical Journal, 41*(3), 551-559. doi: 10.1139/t04-004

Das, B. M. (2010). *Principles of Geotechnical Engineering* (7th ed.): Cengage learning. Pages 424-426

De Souza, E., Archibald, J. and Dirige, A. (2003). Economics and perspectives of underground backfill practices in Canadian mining. In (Ed.), minebackfill:

Dogangun, A., Karaca, Z., Durmus, A. and Sezen, H. (2009). Cause of Damage and Failures in Silo Structures. *Journal of Performance of Constructed Facilities ASCE, 23*(2), 65-71. doi: 10.1061/(ASCE)0887-3828(2009)23:2(65)

Drescher, A. (1991). *Analytical methods in Bin-load analysis* (Vol. 36). Amsterdam: Elsevier Science Publishers Pages 255

Drescher, A. and de Josselin de Jong, G. (1972). Photoelastic verification of a mechanical model for the flow of a granular material. *Journal of the Mechanics and Physics of Solids, 20*(5), 337-340. doi: 10.1016/0022-5096(72)90029-4

Duffield, C., Gad, E. and Bamford, W. (2003). Investigation into the Structural Behaviour of Mine Brick Barricades. *AusIMM Bulletin, 2*(2,Mar/April), 44-50.

Dunnicliff, J. (1988). *Geotechnical Instrumentation for monitoring field performance*. New York: John Wiley and Sons. Pages

Duran, J., Kolb, E. and Vanel, L. (1998). Static friction and arch formation in granular materials. *Physical Review E, 58*(1), 805-812.

El-Sohby, M. A. and Andrawes, K. Z. (1972). Deformation Characteristics of Granular Materials Under Hydrostatic Compression. *Canadian Geotechnical Journal, 9*(4), 338-350. doi: 10.1139/t72-038

El Mkadmi, N., Aubertin, M. and Li, L. (2014). Effect of drainage and sequential filling on the behavior of backfill in mine stopes. *Canadian Geotechnical Journal, 51*(1), 1-15. doi: 10.1139/cgj-2012-0462

ERA. (2003). Jabiluka Uranium Mining Project (Northern Territory, Australia). from http://www.wise-uranium.org/upjab.html

Evans, R., Ran, J. and Allan, R. (2007). Application of Mine Fill at Barrick Gold. In Hassani, F., Archibald, J. & Nantel, J. (Ed.), Minefill 2007: : 9th international symposium on mining with backfill. Montreal: Canadian Institute of Mining, Metallurgy and Petroleum.

Fahey, M., Helinski, M. and Fourie, A. (2009). Some aspects of the mechanics of arching in backfilled stopes. *Canadian Geotechnical Journal, 46*(11), 1322-1336. doi: 10.1139/T09-063

Fall, M. and Nasir, O. (2010). Mechanical behaviour of the interface between cemented tailings backfill and retaining structures under shear loads. *Geotechnical and Geological Engineering, 28*(6), 779-790.

Federico, A., Elia, G. and Germano, V. (2008). A short note on the earth pressure and mobilized angle of internal friction in one-dimensional compression of soils. *Journal of GeoEngineering, 3*(1), 41-46.

Frydman, S. and Keissar, I. (1987). Earth Pressure on Retaining Walls Near Rock Faces. *Journal of Geotechnical Engineering, 113*(6), 586-599. doi: 10.1061/(ASCE)0733-9410(1987)113:6(586)

Goel, S. and Patra, N. (2008). Effect of Arching on Active Earth Pressure for Rigid Retaining Walls Considering Translation Mode. *International Journal of Geomechanics, 8*(2), 123-133. doi: 10.1061/(ASCE)1532-3641(2008)8:2(123)

Grabinsky, M. W., Cheung, D., Bentz, E., Thompson, B. D. and Bawden, W. F. (2014). Advanced structural analysis of reinforced shotcrete barricades. In Potvin, Y. &

Grice, A. G. (Ed.), Minefill 2014: 11th International Symposium on Mining with Backfill (pp. 135-149). Perth: Australian Centre for Geomechanics.

Greaves, G. N., Greer, A. L., Lakes, R. S. and Rouxel, T. (2011). Poisson's ratio and modern materials. *Nature Materials, 10*(11), 823-837. doi: 10.1038/nmat3134

Grice, A. (1989). Fill research at Mount Isa mines limited. In (Ed.), Fourth International symposium on mining with backfill (pp. 15–22). Montreal, Canada:

Grice, A. (1998a). Underground mining with backfill. In (Ed.), 2nd annual summit-Mine tailings disposal systems. Brisbane:

Grice, A. (2003). Mining with Backfill. *AMC's newsletter "Digging Deeper" on current events and modern mining methodology.* Retrieved 04 Sep 2011

Grice, A. G. (1998b). Stability of Hydraulic Backfill Barricades. In Bloss, M. L. (Ed.), Sixth International symposium on Mining with Backfill (pp. 117-121). Brisbane: Australian Institute of Mining and Metallurgy.

Grice, T. (2001). recent minefill developments in Australia. In Stone, D. (Ed.), seventh international symposium on mining with backfill. Seattle, Washington: Society for Mining, Metallurgy and Exploration.

Handy, R. L. (1985). The arch in soil arching. *Journal of Geotechnical Engineering, 111*(3), 302-318. doi: 10.1061/(ASCE)0733-9410(1985)111:3(302)

Harris, G. W. and Seager, J. S. (1973). Pressure measurement in sand model experiments and the use of pressure-sensitive transistors. *International Journal of Rock Mechanics and Mining Sciences & Geomechanics, 10*(6), 613-622. doi: 10.1016/0148-9062(73)90008-9

Harrop-Williams, K. (1989). Arch in Soil Arching. *Journal of Geotechnical Engineering, 115*(3), 415-419. doi: 10.1061/(ASCE)0733-9410(1989)115:3(415)

Hartlen, J., Nielsen, J., Ljunggren, L., Martensson, G. and Wigram, S. (1984). The Wall Pressure in Large Grain Silos (Vol. Document D2). Stockholm: Swedish Council for Building Research.

Helinski, M. (2007). *Mechanics of mine backfill.* (PhD Thesis), University of Western Australia, Perth.

Helinski, M., Fahey, M. and Fourie, A. (2010). Coupled two-dimensional finite element modelling of mine backfilling with cemented tailings. *Canadian Geotechnical Journal, 47*(11), 1187-1200. doi: 10.1139/t10-020

Helinski, M., Fahey, M. and Fourie, A. (2011). Behavior of Cemented Paste Backfill in Two Mine Stopes: Measurements and Modeling. *Journal of Geotechnical and Geoenvironmental Engineering, 137*(2), 171-182. doi: 10.1061/(ASCE)GT.1943-5606.0000418

Henderson, A., Newman, P., Landriault, D. and Antoniazzi, P. (1997). The cost advantage of using paste as a backfill. In (Ed.), (pp. 15-23): Golder paste technology ltd, Sudbury, Ontario.

Iglesia, G., Einstein, H. and Whitman, R. (2014). Investigation of Soil Arching with Centrifuge Tests. *Journal of Geotechnical and Geoenvironmental Engineering, 140*(2), 04013005. doi: 10.1061/(ASCE)GT.1943-5606.0000998

Itasca. (2011). FLAC 2D, version 7.0 User Guide. In Cundall, P. (Ed.): Itasca Consulting Group, Minnepolis, Minnesota.

Itasca. (2012). Partcile Flow Code: PFC. Minneapolis, United States.: Itasca Consulting Group, Inc.

Jaky, J. (1944). The coefficient of earth pressure at rest. *Journal of the Society of Hungarian Architects and Engineers, 7*(2), 355-358.

Janssen, H. (1895). Versuche uber Getreidedruck in Silozellen. *Zeitschrift des Vereines deutscher Ingenieure, 39*, 1045-1049.

Jardine, R. J. (2010). Experimental arrangements for investigation of soil stresses developed around a displacement pile, The use of miniature soil stress measuring cells in laboratory applications involving stress reversals (Closure). *SOILS AND FOUNDATIONS, 50*(3), 448-449. doi: 10.3208/sandf.50.448

Jarrett, N. D., Brown, C. J. and Moore, D. B. (1995). Pressure measurements in a rectangular silo. *Geotechnique, 45*(1), 95-104. doi: 10.1680/geot.1995.45.1.95

Jayasree, P., Rajagopal, K. and Gnanendran, C. (2012). Influence of Sidewall Friction on the Results of Small-Scale Laboratory Model Tests: Numerical Assessment. *International Journal of Geomechanics, 12*(2), 119-126. doi: 10.1061/(ASCE)GM.1943-5622.0000120

Jenike, A. W. and Shield, R. (1959). On the plastic flow of Coulomb solids beyond original failure. *Journal of the Mechanics and Physics of Solids, 18*, 319.

Karlsson, T., Klisinski, M. and Runesson, K. (1998). Finite element simulation of granular material flow in plane silos with complicated geometry. *Powder Technology, 99*(1), 29-39. doi: 10.1016/S0032-5910(98)00087-4

Keen, M., Fehrsen, M. and Cooke, R. (2007). Boulby Mine Backfill System: Operational Experience. In Hassani, F., Archibald, J. & Nantel, J. (Ed.), Minefill 2007: : 9th international symposium on mining with backfill. Montreal: Canadian Institute of Mining, Metallurgy and Petroleum.

Knutsson, S. (1981). Stresses in the hydraulic backfill from analytical calculations and in situ measurements. In (Ed.), Application of Rock mechanics to Cut and Fill mining (pp. 261-268). Lulea, Sweden: Institution of Mining and Metallurgy, London.

Krynine, D. P. (1945). Discussion of 'stability and stiffness of cellular cofferdams' by K. Terzaghi. *Transactions of American Society of Civil Engineers, ASCE, 110*, 1175-1178.

Kuganathan, K. (2001). Mine backfilling, backfill drainage and bulkhead construction–a safety first approach. *Australian Mining Monthly, February*58–64.

Kuganathan, K. (2002). A method to design efficient mine backfill drainage systems to improve safety and stability of backfill bulkheads and fills. In (Ed.), 8th Underground operators' conference, growing our underground operations (pp. 181–188). Townsville: AUSIMM, Carlton, Vic.

Kuganathan, K. (2005). Hydraulic Fills. In Potvin, Y., Thomas, E. D. & Fourie, A. (Eds.), *Handbook on Mine Fill* (pp. 23-47). Perth: Australian Centre for Geomechanics.

Labuz, J. F. and Theroux, B. (2005). Laboratory Calibration of Earth Pressure Cells. *Geotechnical Testing Journal ASTM, 28*(2), 1-9. doi: 10.1520/GTJ12089

Ladanyi, B. and Hoyaux, B. (1969). A study of the trap-door problem in a granular mass. *Canadian Geotechnical Journal, 6*(1), 1-14. doi: 10.1139/t69-001

Lenczner, D. (1963). An investigation into the behaviour of sand in a model silo. *The Structural Engineer, 41*(12), 389-398.

Li, L. and Aubertin, M. (2008). An improved analytical solution to estimate the stress state in subvertical backfilled stopes. *Canadian Geotechnical Journal, 45*(10), 1487-1496. doi: 10.1139/t08-060

Li, L. and Aubertin, M. (2009a). Horizontal pressure on barricades for backfilled stopes. Part I: Fully drained conditions. *Canadian Geotechnical Journal, 46*(1), 37-46.

Li, L. and Aubertin, M. (2009b). Numerical investigation of the stress state in inclined backfilled stopes. *International Journal of Geomechanics, 9*(2), 52-62. doi: 10.1061/(ASCE)1532-3641(2009)9:2(52)

Li, L., Aubertin, M. and Belem, T. (2005). Formulation of a three dimensional analytical solution to evaluate stresses in backfilled vertical narrow openings. *Canadian Geotechnical Journal, 42*(6), 1705-1717. doi: 10.1139/t05-084

Li, L., Aubertin, M., Simon, R., Bussière, B. and Belem, T. (2003). Modeling arching effects in narrow backfilled stopes with FLAC. In (Ed.), 3rd International symposium on FLAC and FLAC^{3D} numerical modelling in geomechanics (pp. 211–219). Ontario, Canada:

Makse, H. A., Johnson, D. L. and Schwartz, L. M. (2000). Packing of Compressible Granular Materials. *Physical Review Letters, 84*(18), 4160-4163. doi: 10.1103/PhysRevLett.84.4160

Marston, A. (1930). The theory of external loads on closed conduits in the light of the latest experiments. *Bulletin 96 of the Iowa Engineering Experiment Station*, 138-170.

Marston, A. and Anderson, A. O. (1913). The theory of loads in pipes and ditches, and tests of cement and clay drain tile and sewer pipe. In Marston, A. (Ed.), *Bulletin number 31* (Vol. xi, pp. 30-88). Ames, Iowa.: Engineering Experiment Station, Iowa State College of Agriculture and Mechanic Arts.

MathWorks. (2012). Matlab. Massachusetts, United States: The MathWorks, Inc.

McCarthy, D. (2007). *Essentials of soil mechanics and foundations:basic geotechnics* (7th ed.): N.J.Perason/Prentice Hall. Pages

Mesri, G. and Hayat, T. M. (1993). The coefficient of earth pressure at rest. *Canadian Geotechnical Journal, 30*(4), 647-666. doi: 10.1139/t93-056

Michalowski, R. (2005). Coefficient of Earth Pressure at Rest. *Journal of Geotechnical and Geoenvironmental Engineering, 131*(11), 1429-1433. doi: 10.1061/(ASCE)1090-0241(2005)131:11(1429)

Mitchell, R. (1992). Centrifuge model studies of fill pressures on temporary bulkheads. *CIM Bulletin, 85,(960)* 48-54.

Mitchell, R., Olsen, R. and Smith, J. (1982). Model studies on cemented tailings used in mine backfill. *Canadian Geotechnical Journal, 19*(1), 14-28. doi: doi: 10.1139/t82-002

Mitchell, R. and Roettger, J. (1984). Bulkhead pressure measurements in model fill pours. *CIM Bulletin, 77*(888), 50-55.

Mitchell, R., Smith, J. and Libby, D. (1975). Bulkhead pressures due to cemented hydraulic mine backfills. *Canadian Geotechnical Journal, 12*(3), 362-371.

Mitchell, R. J. (1989). Model studies on the stability of confined fills. *Canadian Geotechnical Journal, 26*(2), 210-216. doi: 10.1139/t89-030

Mkadmi, E. N., Aubertin, M. and Li, L. (2011). The effect of transient drainage on the stress state in backfilled mine stopes. In (Ed.), Pan-Am CGS Geotechnical conference. Toronto:

Moya, M., Ayuga, F., Guaita, M. and Aguado, P. J. (2002). Mechanical properties of granular agricultural materials considered in silos design. In (Ed.), 15th ASCE Engineering mechanics conference. Columbia University, NY:

Nantel, J. (1998). Recent developments and trends in backfill practices in Canada. In (Ed.), The Mining Cycle (pp. 11-14). Mt Isa.: AusIMM.

Nitka, M., Combe, G., Dascalu, C. and Desrues, J. (2011). Two-scale modeling of granular materials: a DEM-FEM approach. *Granular Matter, 13*(3), 277-281. doi: 10.1007/s10035-011-0255-6

O'Neal, T. S. and Hagerty, D. J. (2011). Earth pressures in confined cohesionless backfill against tall rigid walls — a case history. *Canadian Geotechnical Journal, 48*(8), 1188-1197. doi: 10.1139/t11-033

Ooi, J. Y., Pham, L. and Rotter, J. M. (1990). Systematic and random features of measured pressures on full-scale silo walls. *Engineering Structures, 12*(2), 74-87. doi: 10.1016/0141-0296(90)90012-h

Paik, K. H. and Salgado, R. (2003). Estimation of active earth pressure against rigid retaining walls considering arching effects. *Geotechnique, 53*(7), 643-653. doi: 10.1680/geot.2003.53.7.643

Pirapakaran, K. (2008). *Load-deformation characteristics of minefills with particular reference to arching and stress developments.* (PhD Thesis), James Cook University, Townsville.

Pirapakaran, K. and Sivakugan, N. (2007a). Arching within hydraulic fill stopes. *Geotechnical and Geological Engineering, 25*(1), 25-35. doi: 10.1007/s10706-006-0003-6

Pirapakaran, K. and Sivakugan, N. (2007b). A laboratory model to study arching within a hydraulic fill stope. *Geotechnical Testing Journal ASTM, 30*(6), 496-503. doi: 10.1520/GTJ103693

Potvin, Y. (2005). Introduction. In Potvin, Y., Thomas, E. D. & Fourie, A. (Eds.), *Handbook on Mine Fill* (pp. 3-10). Perth: Australian Centre for Geomechanics.

Potvin, Y., Thomas, E. and Fourie, A. (2005). *Handbook on mine fill*: Australian Centre of Geomechanics, The University of Western Australia. Pages

Ramírez, A., Nielsen, J. and Ayuga, F. (2010). Pressure measurements in steel silos with eccentric hoppers. *Powder Technology, 201*(1), 7-20. doi: 10.1016/j.powtec.2010.02.027

Rankine, K. J. (2005). *An investigation into the drainage characteristics and behaviour of hydraulically placed mine backfill and permeable minefill barricades.* (PhD Thesis), James Cook University, Townsville.

Rankine, R. M. (2004). *The geotechnical characterisation and stability analysis of BHP Billiton's Cannington Mine paste fill.* (PhD Thesis), James Cook University, Townsville.

Revell, M. and Sainsbury, D. (2007a). Advancing Paste Fill Bulkhead Design Using Numerical Modeling. In Hassani, F., Archibald, J. & Nantel, J. (Ed.), Minefill 2007: : 9th international symposium on mining with backfill. Montreal: Canadian Institute of Mining, Metallurgy and Petroleum.

Revell, M. and Sainsbury, D. (2007b). Paste bulkhead failures. In Hassani, F., Archibald, J. & Nantel, J. (Ed.), Minefill 2007: : 9th international symposium on mining with backfill. Montreal: Canadian Institute of Mining, Metallurgy and Petroleum.

Robertson, A. M., AS, M. and WR, N. (1986). A Simple Tool to Measure Stress in Mine Backfill. In (Ed.), Symposium on mining technology. West Virginia:

Rowe, P. W. (1962). The Stress-Dilatancy Relation for Static Equilibrium of an Assembly of Particles in Contact. *Proceedings of the Royal Society of London. Series A. Mathematical and Physical Sciences, 269*(1339), 500-527. doi: 10.1098/rspa.1962.0193

Salgado, R., Bandini, P. and Karim, A. (2000). Shear Strength and Stiffness of Silty Sand. *Journal of Geotechnical and Geoenvironmental Engineering, 126*(5), 451-462. doi: 10.1061/(ASCE)1090-0241(2000)126:5(451)

Scarino, J. (2003). Reappraisal of Marston's Formula. *Journal of Transportation Engineering, 129*(6), 703-712. doi: 10.1061/(ASCE)0733-947X(2003)129:6(703)

Simpson, J. (2007). Mount Isa Mines continues to expand. In Smith, M. (Ed.), *Mining Methods in Underground Mining* (pp. 99-104). Örebro, Sweden,: Ulf Linder, Atlas Copco Rock Drills AB.

Singh, S. (2009). *Drainage and settlement characteristics of hydraulic fills.* (PhD Thesis), James Cook University.

Singh, S., Shukla, S. and Sivakugan, N. (2011). Arching in inclined and vertical mine stopes. *Geotechnical and Geological Engineering, 29*(5), 685-693. doi: 10.1007/s10706-011-9410-4

Singh, S., Sivakugan, N. and Shukla, S. K. (2010). Can soil arching be insensitive to phi? *International Journal of Geomechanics, ASCE, 10*(3), 124-128. doi: 10.1061/(ASCE) GM.1943-5622.0000047

Sivakugan, N. (2008). Drainage issues and stress developments within hydraulic fill mine stopes. *Australian Journal of Civil Engineering, 5*(1), 61(11).

Sivakugan, N. and Das, B. M. (2010). *Geotechnical Engineering ; A practical problem solving approach*: J. Ross Publishing, Inc. Pages 1-485

Sivakugan, N., Rankine, K. J. and Rankine, R. M. (2005). Geotechnical aspects of hydraulic filling of underground mine stopes in Australia. In Indraratna, B. & Chu, J. (Eds.), *Elsevier Geo-Engineering Book Series* (Vol. 3, pp. 513-538): Elsevier.

Sivakugan, N., Rankine, K. J. and Rankine, R. M. (2006a). Permeability of Hydraulic Fills and Barricade Bricks. *Geotechnical and Geological Engineering, 24*(3), 661-673. doi: 10.1007/s10706-005-2132-8

Sivakugan, N., Rankine, R. M., Rankine, K. J. and Rankine, K. S. (2006b). Geotechnical considerations in mine backfilling in Australia. *Journal of Cleaner Production, 14*(12-13), 1168-1175.

Sivakugan, N. and Widisinghe, S. (2013). Stresses Within Granular Materials Contained Between Vertical Walls. *Indian Geotechnical Journal, 43*(1), 30-38. doi: 10.1007/s40098-012-0029-z

Sivakugan, N., Widisinghe, S. and Wang, V. (2014). Vertical Stress Determination within Backfilled Mine Stopes. *International Journal of Geomechanics, 14*(5), 06014011. doi: 10.1061/(ASCE)GM.1943-5622.0000367

Smith, J. and Mitchell, R. (1982). Design and control of large hydraulic backfill pours. *CIM Bulletin, 75,(838)* 102-111.

Smith, W. O., Foote, P. D. and Busang, P. F. (1929). Packing of Homogeneous Spheres. *Physical Review, 34*(9), 1271-1274.

Spangler, M. G. and Handy, R. L. (1973). *Soil Engineering* (3rd ed.): Intext Educational Publishers. Pages

Take, W. A. and Valsangkar, A. J. (2001). Earth pressures on unyielding retaining walls of narrow backfill width. *Canadian Geotechnical Journal, 38*(6), 1220-1230. doi: 10.1139/cgj-38-6-1220

Talesnick, M. (2005). Measuring soil contact pressure on a soil boundary and quantifying soil arching. *Geotechnical Testing Journal, 28*(2), 1-9. doi: 10.1520/GTJ12484

Talesnick, M. (2013). Measuring soil pressure within a soil mass. *Canadian Geotechnical Journal, 50*(7), 716-722. doi: 10.1139/cgj-2012-0347

Terzaghi, K. (1920). Old earth-pressure theories and new test results. *Engineering News-Record, 85*(13), 632-637.

Terzaghi, K. (1943). *Theoretical soil mechanics*: John Wiley & Sons, New York. Pages 66-99

Theimer, O. F. (1969). Failures of reinforced concrete grain silos. *Transactions of the ASME*, 460-477.

Thomas, E. G. (1969). *Characteristics and Behaviour of Hydraulic Fill Material.* (PhD Thesis), University of Queensland, Brisbane.

Thompson, B. D., Bawden, W. F. and Grabinsky, M. W. (2012). In situ measurements of cemented paste backfill at the Cayeli Mine. *Canadian Geotechnical Journal, 49*(7), 755-772. doi: 10.1139/t2012-040

Thompson, B. D., Grabinsky, M. W., Bawden, W. F. and Counter, D. B. (2009). In situ measurements of cemented paste backfill in long-hole stopes. In Diederichs, M. & Grasselli, G. (Ed.), ROCKENG09; 3rd CANUS Rock Mechanics Symposium. Toronto:

Thompson, B. D., Hunt, T., Malek, F., Grabinsky, M. W. and Bawden, W. F. (2014). In situ behaviour of cemented hydraulic and paste backfills and the use of instrumentation in optimising efficiency. In Potvin, Y. & Grice, A. G. (Ed.), Minefill 2014: 11th International Symposium on Mining with Backfill (pp. 337-350). Perth: Australian Centre for Geomechanics.

Ting, C. H. (2011). *Arching in granular materials with particular reference to inclined mine stopes.* (Ph.D. Thesis), James Cook University, Townsville, Australia.

Ting, C. H., Shukla, S. K. and Sivakugan, N. (2011). Arching in soils applied to inclined mine stopes. *International Journal of Geomechanics, 11*(1), 29-35. doi: 10.1061/(ASCE)GM.1943-5622.0000067

Ting, C. H., Sivakugan, N. and Shukla, S. K. (2012a). Laboratory simulation of the stresses within Inclined stopes. *Geotechnical Testing Journal ASTM, 35*(2), 1-15. doi: 10.1520/GTJ103693

Ting, C. H., Sivakugan, N., W., R. and Shukla, S. K. (2012b). Analytical Method to Determine Vertical Stresses within a Granular Material Contained in Right Vertical Prisms. *International Journal of Geomechanics, 12*(1), 74-79. doi: 10.1061/(ASCE)GM.1943-5622.0000110.

Torlach, J. (2000). *Potential hazards associated with Mine fill*. Perth: Mineral house, The Government of Western Australia.

Trollope, D. H. (1957). The Systematic Arching Theory Applied to the Stability Analysis of Embankments. In (Ed.), Fourth International Conference on Soil Mechanics and Foundation Engineering (pp. 382-388). London: Butterworths Scientific Publications.

Trollope, D. H. and Burman, B. C. (1980). Physical and numerical experiments with granular wedges. *Geotechnique, 30*(2), 137-157. doi: 10.1680/geot.1980.30.2.137

Trollope, D. H. and Lee, I. K. (1961). The measurement of soil pressures. In (Ed.), 5th International Conference on Soil Mechanics and Foundation Engineering (pp. 493-499). Paris:

Trollope, D. H., Rosengren, K. J. and Brown, E. T. (1965). The Mechanics of Brown Coal. *Geotechnique, 15*, 363-386. http://www.icevirtuallibrary.com/content/article/10.1680/geot.1965.15.4.363

Vanel, L. and Clément, E. (1999). Pressure screening and fluctuations at the bottom of a granular column. *The European Physical Journal B, 11*, 525-533. doi: 10.1007/s100510050965

Veenstra, R. L. (2013). *A Design Procedure for Determining the In Situ Stresses of Early Age Cemented Paste Backfill.* (PhD Thesis), University of Toronto. Retrieved from http://hdl.handle.net/1807/36027

Villaescusa, E. (2003). Global Extraction Sequences in Sublevel Stoping. In (Ed.), Twelfth International Symposium on Mine Planning and Equipment Selection (MPES 2003). Kalgoorlie: AusIMM.

Wachman, G. S. and Labuz, J. F. (2011). Soil-Structure Interaction of an Earth Pressure Cell. *Journal of Geotechnical and Geoenvironmental Engineering, 137*(9), 843-845. doi: 10.1061/(ASCE)GT.1943-5606.0000501

Walker, D. M. (1966). An approximate theory for pressures and arching in hoppers. *Chemical Engineering Science, 21*(11), 975-997. doi: 10.1016/0009-2509(66)85095-9

Yumlu, M. and Guresci, M. (2007). Paste backfill bulkhead failures and pressure monitoring at Cayeli mine. *CIM Bulletin, 100*1-10.

APPENDICES

APPENDIX A

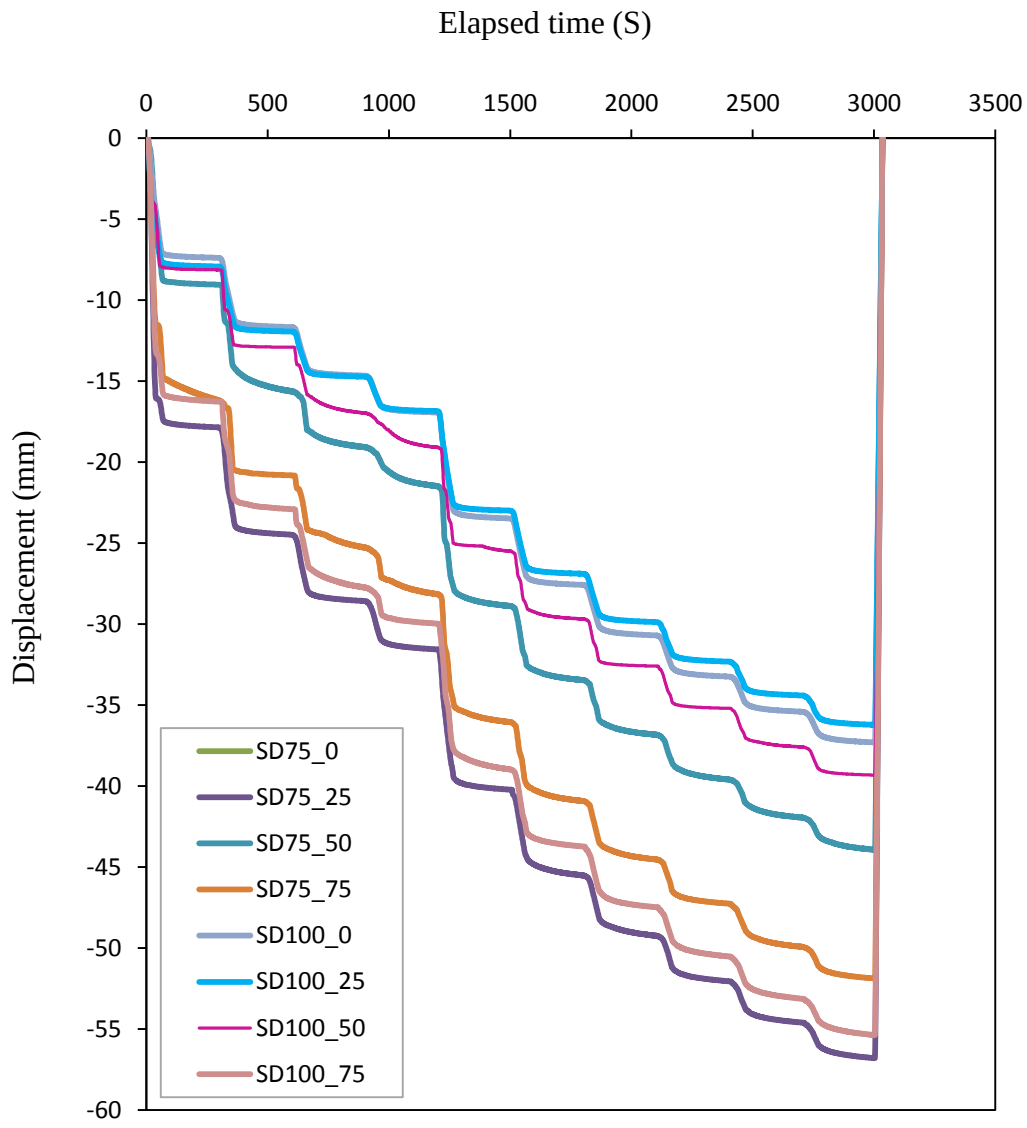

Figure A1. Load plate displacement results for tests with square drives for 75 mm and 100 mm wide drives

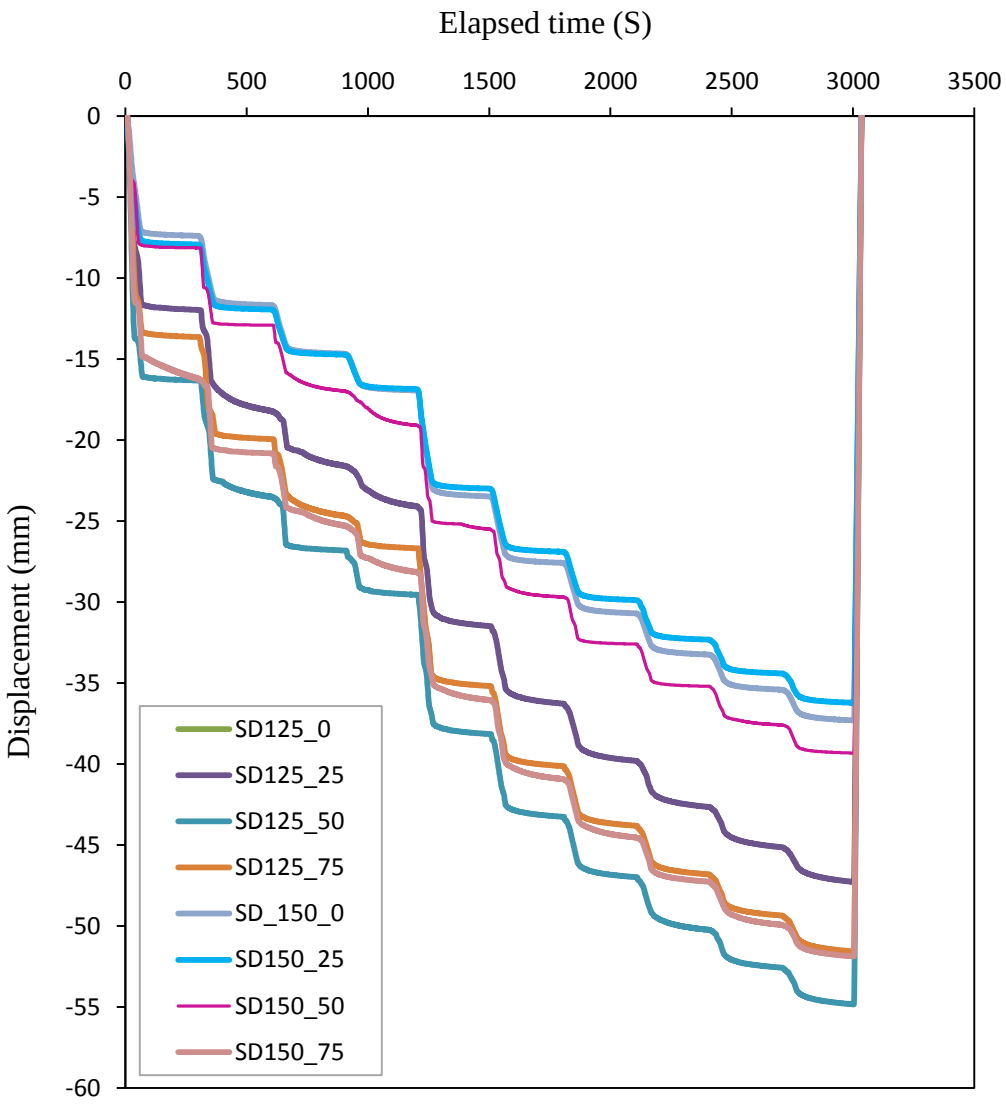

Figure A2. Load plate displacement results for tests with square drives for 125 m and 150 mm wide drives

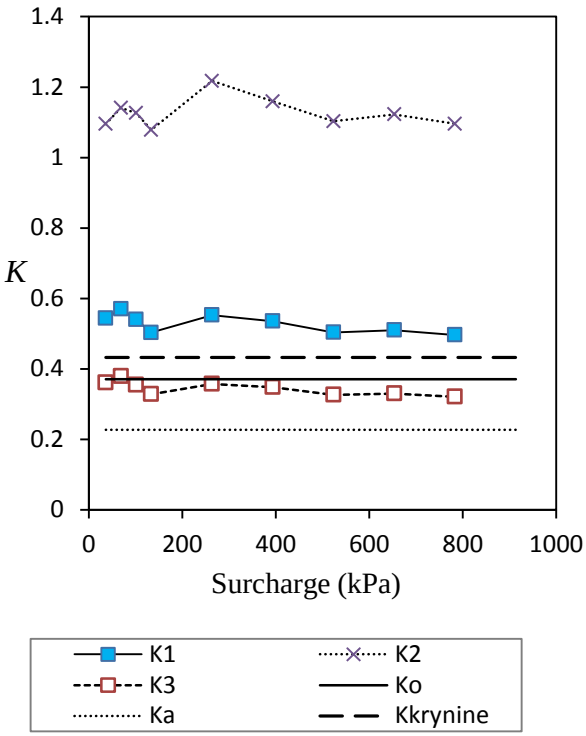

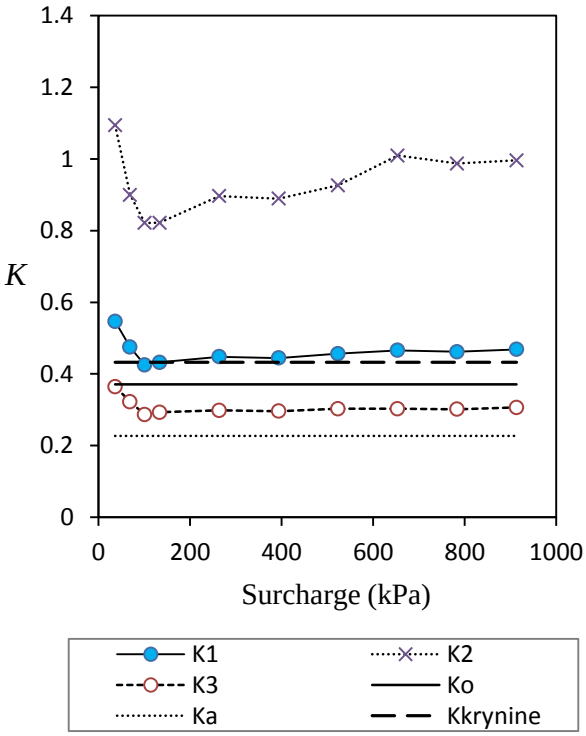

Figure A3. The calculated lateral pressure coefficient values are compared with theoretical values; (a) 100 mm wide square drive is attached, (b) 100 mm wide circular drive is attached

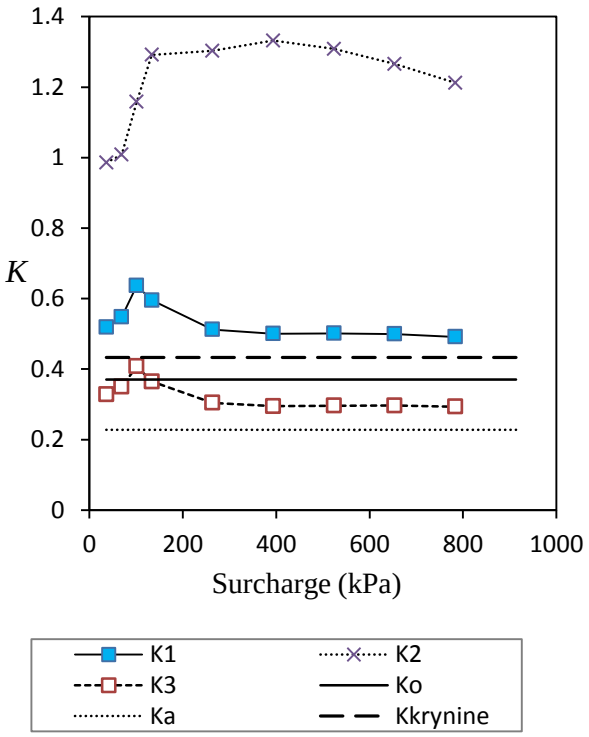

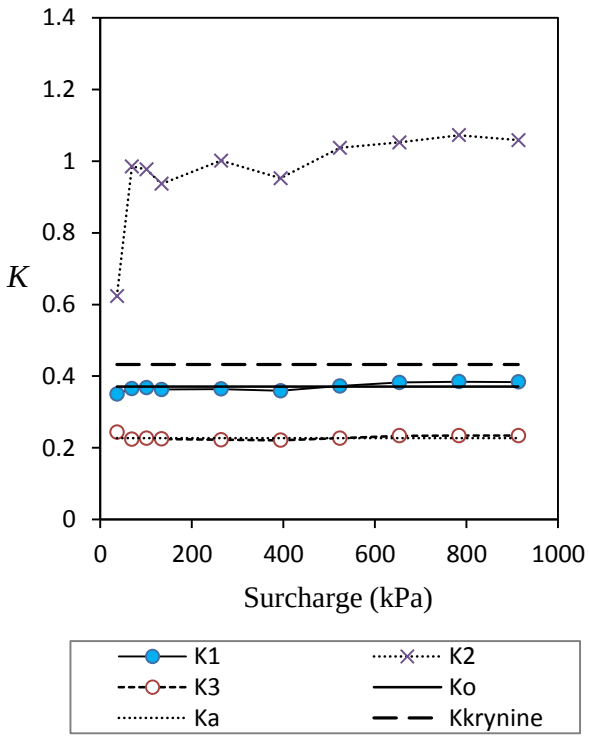

Figure A4. The calculated lateral pressure coefficient values are compared with theoretical values; (a) 125 mm wide square drive is attached, (b) 125 mm wide circular drive is attached

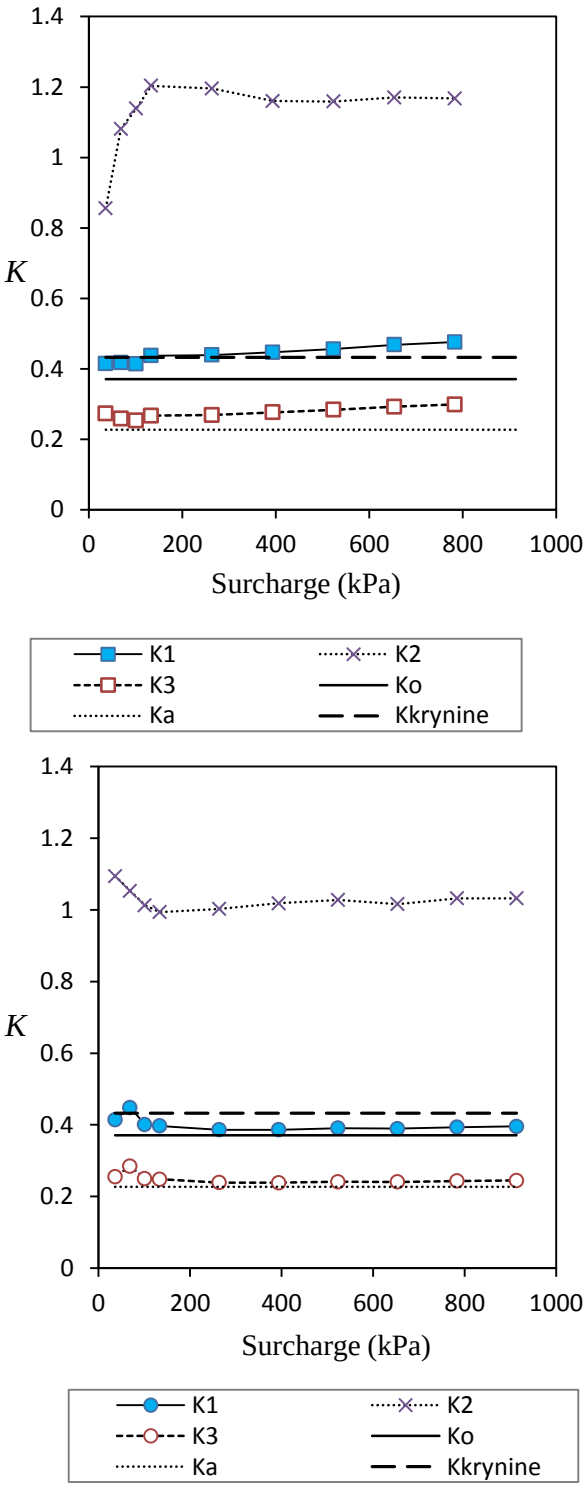

Figure A5. The calculated lateral pressure coefficient values are compared with theoretical values; (a) 150 mm wide square drive is attached, (b) 150 mm wide circular drive is attached

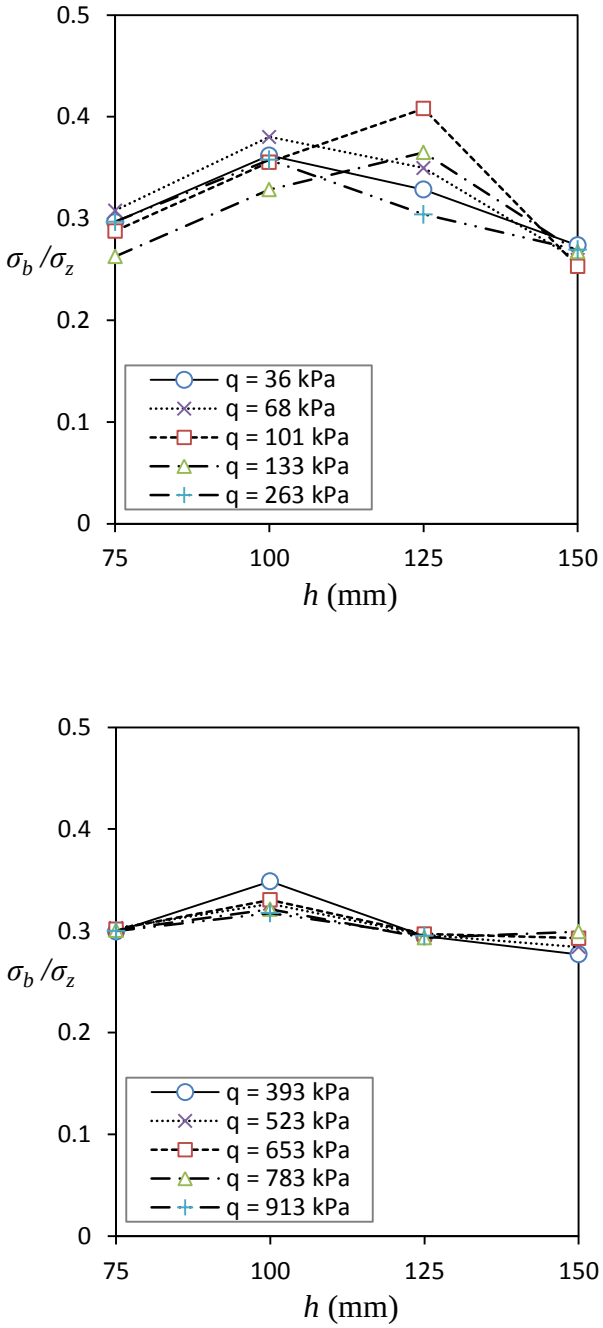

Figure A6. Barricade stress variation with drive width at zero offset distance on square drives

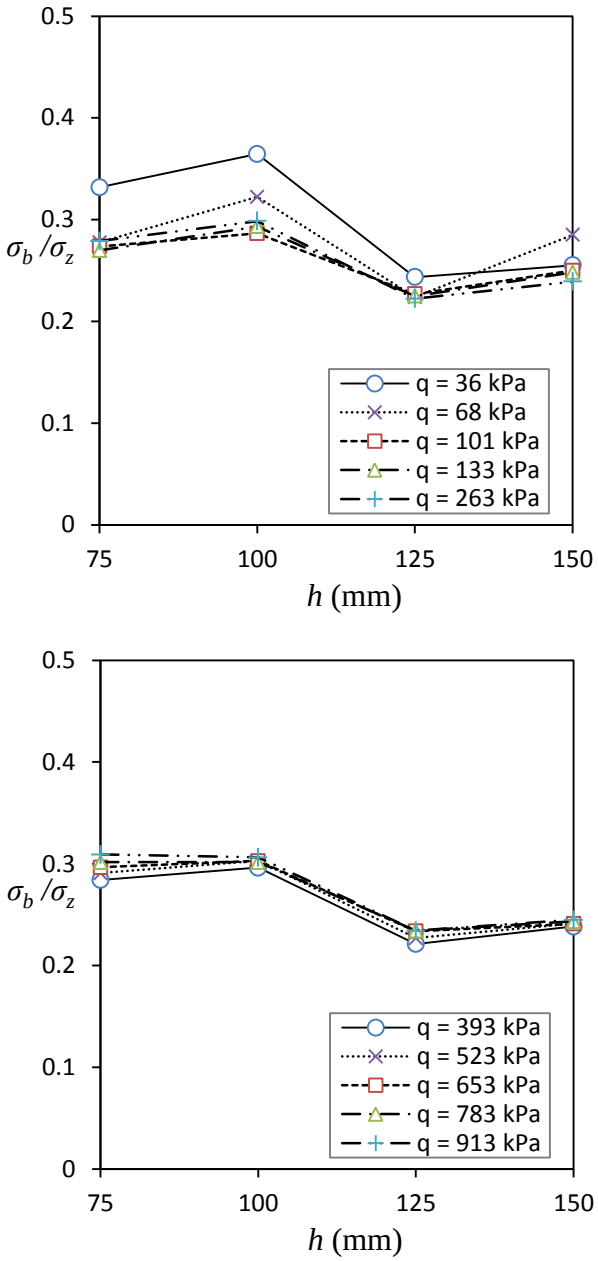

Figure A7. Barricade stress variation with drive width at zero offset distance on circular drives

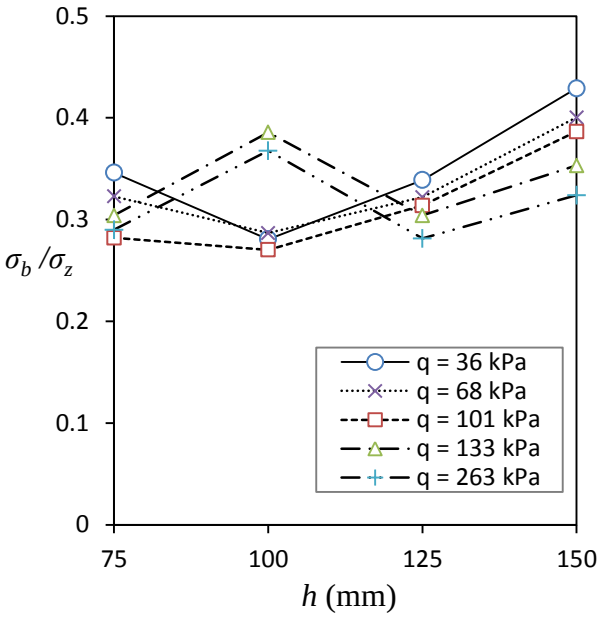

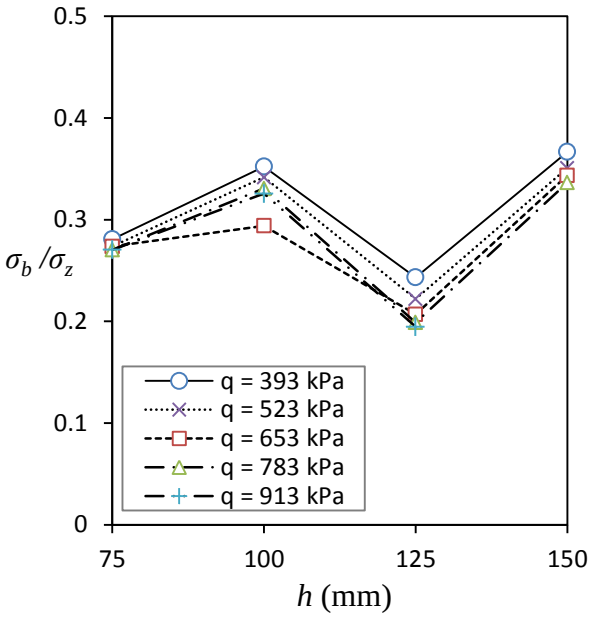

Figure A8. Barricade stress variation with drive width, for offset distance of 25 mm on square drives

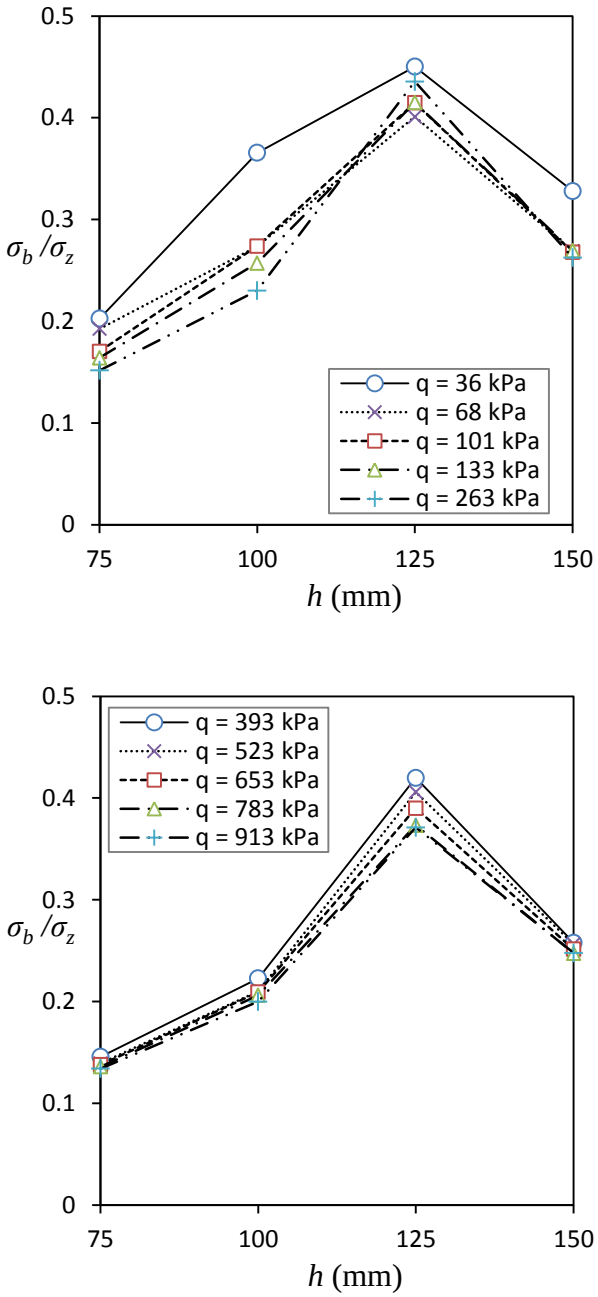

Figure A9. Barricade stress variation with drive width, for offset distance of 50 mm on square drives

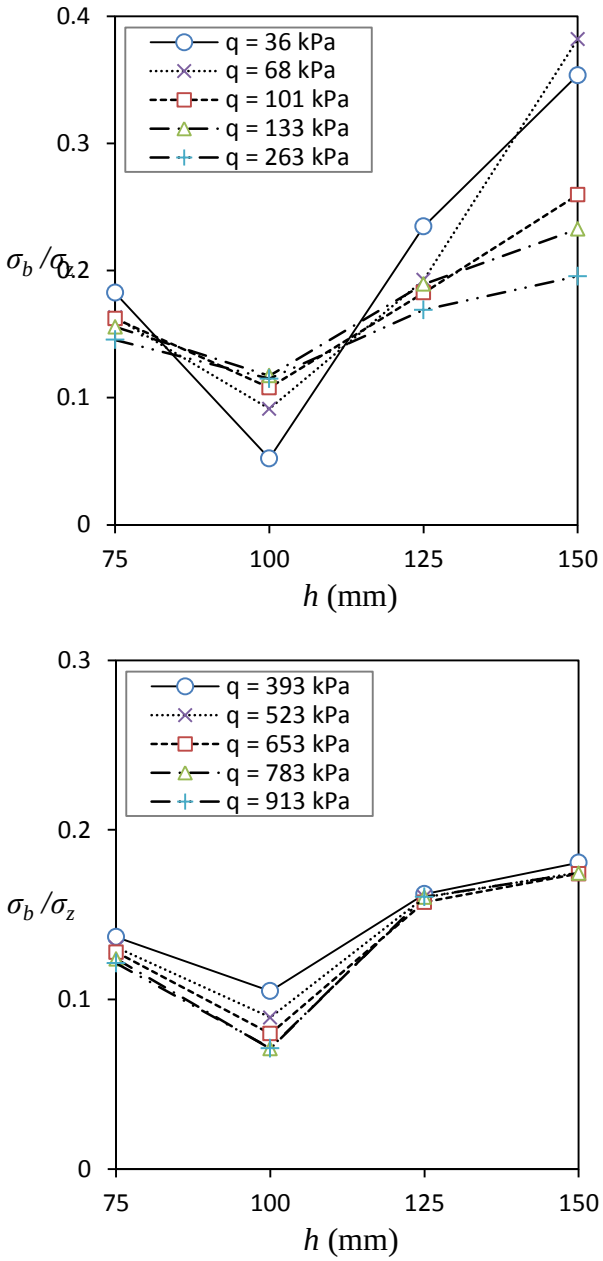

Figure A10. Barricade stress variation with drive width, for offset distance of 50 mm on circular drives

The FLAC3D code used to simulate laboratory studies

```
;-----------------------------------------------------
; ---- Simulation of a square minestope- ---
;-----------------------------------------------------
SET cust1 'Sankha Widisinghe'
SET cust2 'James Cook University'
new

; Quater of the square stope is concerned
;calculation of shear and bulk moduli

def inputparameters
 ;s-shear b-bulk y-youngs_modulus pr- poisson ratio
ybrick = 1.99e9
prbrick = 0.2
dbrick = 1927                          ; brick properties from Berndt et al_2007
y1  = 2e10
pr1 = 0.2
drock = 2700.0
y2  = 5e7                              ; fill properties
pr2 = 0.3
dfill = 1800.0
ffill = 38.0
delta = 23.0
dangle = -5.0
gamma = dfill*9.81
        srock = y1 / (2*(1+pr1))       ; rock
        brock = y1 / (3*(1-2*pr1))
        sfill = y2 / (2*(1+pr2))       ;hydraulic fill
        bfill = y2 / (3*(1-2*pr2))
        sbrick = ybrick / (2*(1+prbrick))  ;barricade bricks
        bbrick = ybrick / (3*(1-2*prbrick))
        int_stif = 1e8
        ;int_stif = (10/0.5)* (brock + 1.33*srock)
end
```

```
@inputparameters

;define all the geometry and other constants
def mod_parameters
size = 0.005
width = 0.310
depth = 0.155                    ; half of the depth side
height = 0.460                   ; 92 elements
size_h = int(height / size)      ; number of zones in height
size_w = int(width / size)       ; number of zones in width
size_d  = int(depth / size)      ; number of zones in depth
h       = 0.115                  ; layer height, for the first layer
ele     = 23                     ; number of  layer elements
h1      = 0.115                  ; for other layers
ele1    = 23                     ; for other layers
twidth = width*2
;--------------------drive parameters
drivewidth      = 0.075
dwidth = width + drivewidth
ddepth  = 0.040
dheight = 0.075
gap     = 0.005                  ; for the rock crust, thickness of crust
ngap    = -0.005
gw      = width + gap
gd      = depth + gap
gdw     = dwidth + gap
gdd     = ddepth + gap
gdh     = dheight + gap
remdepth        = depth - gdd
size_remdepth  = (int(remdepth/size))
remheight       = height - gdh
size_remheight = int(remheight / size)
size_gap  = 1
size_dw= int(drivewidth / size)
size_dd = int(ddepth / size)
size_dh = int(dheight / size)
```

```
size_gdw = size_dw + size_gap
size_gdh = size_dh + size_gap
size_gdd = size_dd + size_gap
end
@mod_parameters

define boundries
dis_1    = 0.0000001
dis_2    = -0.0000001
pwidth = width + dis_1
nwidth = width + dis_2
pdepth = depth + dis_1
ndepth = depth + dis_2
pdheight = dheight + dis_1
ndheight = dheight + dis_2
pddepth          = ddepth + dis_1
nddepth  = ddepth + dis_2
pdwidth = dwidth + dis_1
ndwidth = dwidth + dis_2
pbarricade = gdw + dis_1
nbarricade = gdw + dis_2
pheight = height + dis_1
nheight = height+ dis_2

end
@boundries

;----------------------find gridpoints at bottom of stope-----------
def find_add
global top_head = null
global gp_pnt = gp_head
loop while gp_pnt # null
if gp_zpos(gp_pnt) < size then
        if gp_xpos(gp_pnt) <= width then
                if gp_ypos(gp_pnt) <= depth then
                        local mem_head = get_mem(2)
```

```
                                mem(mem_head) = top_head
                                mem(mem_head+1) = gp_pnt
                                top_head = mem_head
                        end_if
                end_if
        endif
        gp_pnt = gp_next(gp_pnt)
        endloop
        end

        ;----------------------creation of rock grid----------------------
        GEN zone brick size @size_gap @size_d @size_h ratio 1 1 1 &
        p0(@ngap 0 0) p1(0 0 0) p2(@ngap @depth 0) p3(@ngap 0 @height)
                ; 1, crust, end of width towards centre
        GEN zone brick size @size_w @size_gap @size_h ratio 1 1 1 &
        p0(0 @depth 0) p1(@width @depth 0) p2(0 @gd 0)       p3(0 @depth @height)
                ; 2, width side crust parallel to fill
        GEN zone brick size @size_gap @size_gap @size_h ratio 1 1 1 &
        p0(@ngap @depth 0) p1(0 @depth 0) p2(@ngap @gd 0)          p3(@ngap      @depth
@height)                ; 3, junction of width side end, x axis
        GEN zone brick size @size_gap @size_gap @size_h ratio 1 1 1 &
        p0(@width @depth 0) p1(@gw @depth 0) p2(@width @gd 0)   p3(@width     @depth
@height)                ; 4, junction of width  and depth side near the drive

        GEN zone brick size @size_gap @size_remdepth @size_gdh ratio 1 1 1 &
        p0(@width @gdd 0) p1(@gw @gdd 0) p2(@width @depth 0)    p3(@width       @gdd
@gdh)           ; 5, check this, depth side crust at drive height
        GEN zone brick size @size_gap @size_d @size_remheight ratio 1 1 1 &
        p0(@width 0 @gdh) p1(@gw 0 @gdh) p2(@width @depth @gdh)         p3(@width   0
@height)        ; 6, depth side crust above drive height
        GEN zone brick size @size_gdw @size_dd @size_gap ratio 1 1 1 &
        p0(@width 0 @dheight) p1(@gdw 0 @dheight) p2(@width @ddepth @dheight)
p3(@width 0 @gdh)     ; 7,top layer of drive
        GEN zone brick size @size_gdw @size_gap @size_dh ratio 1 1 1 &
        p0(@width @ddepth 0) p1(@gdw @ddepth 0) p2(@width @gdd 0) p3(@width
@ddepth @dheight)     ; 8, depth side layer of drive
        GEN zone brick size @size_gdw @size_gap @size_gap ratio 1 1 1 &
        p0(@width @ddepth @dheight) p1(@gdw @ddepth @dheight) p2(@width @gdd
@dheight) &
```

```
p3(@width @ddepth @gdh)
; 9, junction of height  n depth side of drive
GROUP zone rock
GEN zone brick size @size_gap @size_dd @size_dh ratio 1 1 1 &
p0(@dwidth 0 0) p1(@gdw 0 0) p2(@dwidth @ddepth 0) p3(@dwidth 0 @dheight)
        ; barricade
GROUP zone barricade range group rock not
GEN zone brick size @size_w @size_d @size_h ratio 1 1 1 &
; inifill in stope
p0(0 0 0) p1(@width 0 0) p2(0 @depth 0)          p3(0 0 @height)
GEN zone brick size @size_dw @size_dd @size_dh ratio 1 1 1 &
; inifill in drive
p0(@width 0 0) p1(@dwidth 0 0) p2(@width @ddepth 0)          p3(@width          0
@dheight)
GROUP zone inifill range group rock not group barricade not


range name = rock group rock
range name = inifill group inifill
range name = barricade group barricade
GROUP gp top_surface range x @dis_2 @width y @dis_2 @depth z @nheight
@pheight
range name = top_surface group top_surface


MODEL mech elastic range group rock
PROP density=@drock shear=@srock bulk=@brock range rock
MODEL mech elastic range group inifill
PROP density=@drock shear=@srock bulk=@brock range inifill
MODEL mech elastic range group barricade          ;elastic          model          assigned
initially
PROP bu=@bbrick de=@dbrick sh=@sbrick  range barricade
;----------------------boundary conditions------------------------
fix x y z range z @dis_1 @dis_2
fix   y   range y @dis_1 @dis_2
fix x y z range rock
fix x y z range x @nbarricade @pbarricade
@find_add
SET gravity= 0 0 -9.81
STEP 100
```

```
;----------------------excavation of inifill----------------------
MODEL mech null range inifill
SET gravity= 0 0 -9.81
STEP 10

INTERFACE 1 face range x @dis_1 @dis_2                    ;    x    side
interface
INT 1 PROP kn=@int_stif ks=@int_stif fric=@delta dil=@dangle
INTERFACE 2 face range y @ndepth @pdepth                  ; y side interface
INT 2 PROP kn=@int_stif ks=@int_stif fric=@delta dil=@dangle
INTERFACE 3 face range x @nwidth @pwidth                  ; x side , end of width
interface
INT 3 PROP kn=@int_stif ks=@int_stif fric=@delta dil=@dangle
INTERFACE 4 face range y @nddepth @pddepth                ;    drive,    y    side
interface
INT 4 PROP kn=@int_stif ks=@int_stif fric=@delta dil=@dangle
INTERFACE 5 face range z @ndheight @pdheight              ;    y    side
interface
INT 5 PROP kn=@int_stif ks=@int_stif fric=@delta dil=@dangle
INTERFACE 6 face range x @ndwidth @pdwidth                ; x side , barricade
interface
INT 6 PROP kn=@int_stif ks=@int_stif fric=@delta dil=@dangle


;-------------------------------------------------------------------------------------------
;**********************************backfilling                                    in
layers**************************************
;layer 1
GROUP zone fill1 range z 0 @h group rock not group barricade not
range name = fill1 group fill1
MODEL mech mohr range fill1          ;MC model assigned to fill
PROP density=@dfill shear=@sfill bulk=@bfill fric=@ffill range fill1

SET gravity= 0 0 -9.81
SET mech force = 1
SET large
STEP 5000
```

```
;----------------------stress recording after 1 layer----------
define stress_record
global width = width
global Unit_weight = gamma
local ad = top_head
local zftot = 0.0
loop while ad # null
        gp_pnt = mem(ad+1)
        local zf = gp_zfunbal(gp_pnt)
        zftot = zftot + zf
        ad = mem(ad)
endloop
global total_zforce = zftot
global total_area = width*depth
global av_stress = total_zforce / total_area
global norm_stress = -av_stress / (Unit_weight*twidth)
global zone_1 = z_near (0.0025,0.0025,0.0025)   ; for maximum stress
global zone_2 = z_near (0.3075,0.0025,0.0025)   ; for hor stress at bottom
global zone_3 = z_near (0.3075,0.0025,0.050)    ; for hor stress at midheight
maxstress = z_szz (zone_1)
h_stress1 = z_sxx (zone_2)
h_stress2 = z_sxx (zone_3)
max_stress = -maxstress/(twidth*unit_weight)
hor_stress1 = -(h_stress1)/(twidth*unit_weight)
hor_stress2 = -(h_stress2)/(twidth*unit_weight)
global h_B = 5/(width*2)
table (1,h_B)= norm_stress
table (2,h_B)= hor_stress1
table (3,h_B)= hor_stress2
table (4,h_B)= max_stress
end
@stress_record


;*******************Backfilling with 10layers***************
DEFINE filling
```

```
            local k
            loop k(2,4)
            k1 = (0.115*k) - 0.115
            k2 = 0.115*k
            k3 = k
  numfill = 'fill'+string(k)
  state   = 'fill'+string(k)+'filled with fill'
 command

GROUP zone @numfill range z @k1 @k2 group rock not group fill1 not group barricade
not
range name = @numfill group @numfill
MODEL mech mohr range @numfill                ;MC model assigned to fill
PROP density=@dfill shear=@sfill bulk=@bfill  fric=@ffill range @numfill

SET grav 0, 0, -9.81
SET mech force = 1
SET large
print @numfill
STEP 5000
;save @state
 end_command

;----------------------stress recording----------------------------
global width = width
global Unit_weight = gamma
local ad = top_head
local zftot = 0.0
loop while ad # null
            gp_pnt = mem(ad+1)
            local zf = gp_zfunbal(gp_pnt)
            zftot = zftot + zf
            ad = mem(ad)
endloop
global total_zforce = zftot
global total_area = width*depth
```

```
global av_stress = total_zforce / total_area
global norm_stress = -av_stress / (Unit_weight*width*2)
global zone_1 = z_near (0.0025,0.0025,0.0025)   ; for maximum stress
global zone_2 = z_near (0.3075,0.0025,0.0025)   ; for hor stress at bottom
global zone_3 = z_near (0.3075,0.0025,0.050)    ; for hor stress at midheight
maxstress = z_szz (zone_1)
h_stress1 = z_sxx (zone_2)
h_stress2 = z_sxx (zone_3)
max_stress = -maxstress/(twidth*unit_weight)
hor_stress1 = -(h_stress1)/(twidth*unit_weight)
hor_stress2 = -(h_stress2)/(twidth*unit_weight)

global h_B = k2/(width*2)
table (1,h_B)= norm_stress
table (2,h_B)= hor_stress1
table (3,h_B)= hor_stress2
table (4,h_B)= max_stress
end_loop                ; end of loop for filling - k
end
@filling                ; activates the loop


save MTS_S75_75_initialfill.sav

; to define a relistic layer to apply the surcharge
DEFINE top_surf_bound
top_pheight = height
top_nheight = height - 0.01
END
@top_surf_bound
GROUP gp top_surface range x @dis_1 @width y 0 @depth z @top_nheight @top_pheight
range name = top_surface group top_surface
;**********************************************************************
**********************
;Applying stress as in the MTS
```

```
;function to apply stress in 10 increments
DEF superstep(n_steps,force_inc)
        loop ns (1,n_steps)
        global cum_zforce = cum_zforce + force_inc

                command
                @increase_E
                APPLY zforce @cum_zforce range nrange top_surface
                PROP density=@dfill shear=@sfill bulk=@bfill fric=@ffill range fill1
                PROP density=@dfill shear=@sfill bulk=@bfill fric=@ffill range fill2
                PROP density=@dfill shear=@sfill bulk=@bfill fric=@ffill range fill3
                PROP density=@dfill shear=@sfill bulk=@bfill fric=@ffill range fill4
                step 5
                end_command
        end_loop
                command                         ; to bring the system to equilibrium
                STEP 3000
                call contour_plot_loop   ; plot_commands file
                end_command

        global zone_5 = z_near (0.155,0.0025,0.0025)    ; stope bottom centre - EPC 1
        global zone_6 = z_near (0.3075,0.0025,0.0025)  ; stope bottom edge - EPC 2
        global zone_7 = z_near (0.3075,0.0025,0.0375) ; stope bottom edge -hstress at
entrance
        global zone_8 = z_near (0.375,0.0025,0.0375)    ; at barricade - EPC 3



        v_stress1 = z_szz (zone_5)
        v_stress2 = z_szz (zone_6)
        h_stress1 = z_sxx (zone_7)
        h_stress2 = z_sxx (zone_8)

        table (10,-cum_zforce)= -h_stress2
        table (11,-cum_zforce)= -v_stress1
        table (12,-cum_zforce)= -v_stress2
        table (13,-cum_zforce)= -h_stress1
```

```
END                 ; end of function superstep
DEF increase_E                              ; function to increse stress with MTS load
        surcharge = 0
        y2 = y2 + E_inc
        sfill = y2 / (2*(1+pr2))            ;hydraulic fill
        bfill = y2 / (3*(1-2*pr2))
END
SET @E_inc = 7e8

SET @surcharge = 36
call plot_stages_S75_75         ; give plot names with surcharge value in kPa
@superstep(10,-9.0312e-2)       ; load applied in 10 steps

SET @surcharge = 69
call plot_stages_S75_75         ; give plot names with q value in kPa
@superstep(10,-8.1234e-2)

SET @surcharge = 101
call plot_stages_S75_75         ; give plot names with q value in kPa

@superstep(10,-8.1234e-2)

SET @surcharge = 134
call plot_stages_S75_75         ; give plot names with q value in kPa
@superstep(10,-8.1234e-2)

SET @E_inc = 2.1e9
SET @surcharge = 264
call plot_stages_S75_75         ; give plot names with q value in kPa
@superstep(10,-3.24934e-1)

SET @surcharge = 394
call plot_stages_S75_75         ; give plot names with q value in kPa
@superstep(10,-3.24934e-1)
```

```
SET @surcharge = 524
call plot_stages_S75_75          ; give plot names with q value in kPa
@superstep(10,-3.24934e-1)

SET @surcharge = 654
call plot_stages_S75_75          ; give plot names with q value in kPa
@superstep(10,-3.24934e-1)

SET @surcharge = 783
call plot_stages_S75_75          ; give plot names with q value in kPa
@superstep(10,-3.24934e-1)

SET @surcharge = 913
call plot_stages_S75_75          ; give plot names with q value in kPa
@superstep(10,-3.24934e-1)

SET @surcharge = 1043
call plot_stages_S75_75          ; give plot names with q value in kPa
@superstep(10,-3.24934e-1)

SET @surcharge = 1173
call plot_stages_S75_75          ; give plot names with q value in kPa
@superstep(10,-3.24934e-1)

SET @surcharge = 1303
call plot_stages_S75_75          ; give plot names with q value in kPa
@superstep(10,-3.24934e-1)

SET @surcharge = 1433
call plot_stages_S75_75          ; give plot names with q value in kPa
@superstep(10,-3.24934e-1)

save MTS_S75_75_top.sav
SET logfile MTS_S75_75_top.log
SET log on
```

```
; hor stress at barricade - EPC 3
print table 10

; ver stress at stope bottom centre - EPC 1
print table 11

; ver stress stope bottom edge - EPC 2
print table 12

; hor stress stope bottom edge hstress at entrance
print table 13
SET log off
```

APPENDIX B

Matlab algorithm when $\alpha < 60°$

```
clc;
clear all;
close all;

%Geometry parameters
ni=12000        ;% number of i, rows
ntot = 2000     ;% for odd numbers of rows
nj=ntot/2       ;% number of j,

%Inputs
F=-0.0005               ;%arching factor
alpha = degtorad(55)    ;%angle between disks
delta = degtorad(45)    ;%interfacial friction angles
rho=1500        ;% density in kg/m3
g=9.81          ;% g in ms-2
B=0.1           ; %width in m
H=0.6           ; %depth in m

%Derivation of properties
d=(0.5*B)/(1+(2*(cos(alpha))*(ntot-1)))     ;%diameter of disk
w=(rho*g*B*H*d)/(ntot*ni)                   ;%weight of a disk, N
f= w/(2*(sin(alpha)))                       ;% f componenet
t_fac = (tan(alpha)-tan(delta))/(tan(alpha)+tan(delta))  ;%

%Initialization
l=zeros(ni,nj);L=zeros(ni,nj);
m=zeros(ni,nj);M=zeros(ni,nj);

i=1;
for j=2:nj-1
% case 1
   m(i,j)=0;
   l(i,j)=0;
   L(i,j)=f;
   M(i,j)=f;
end

for i=2:ni
   for j=1:nj
        if mod(i,2)==0
        if i==2 && j==1
   %case 2
         l(i,j)=L(i-1,j);
         m(i,j)=0;
         L(i,j)=((1+F)*(l(i,j)+f)*(l(i,j)+m(i,j)+2*f))/((1+F)*(l(i,j)+f)+(1-F)*(m(i,j)+f));
         M(i,j)=((1-F)*(m(i,j)+f)*(l(i,j)+m(i,j)+2*f))/((1+F)*(l(i,j)+f)+(1-F)*(m(i,j)+f));
```

```
        end
         if i==2 && j~=1
    %case 3
          l(i,j)=L(i-1,j);
          m(i,j)=L(i-1,j-1);
          L(i,j)=((1+F)*(l(i,j)+f)*(l(i,j)+m(i,j)+2*f))/((1+F)*(l(i,j)+f)+(1-F)*(m(i,j)+f));
          M(i,j)=((1-F)*(m(i,j)+f)*(l(i,j)+m(i,j)+2*f))/((1+F)*(l(i,j)+f)+(1-F)*(m(i,j)+f));
        end
        if i~=2 && j==1
    %case 6
       l(i,j)=L(i-1,j);
       H1=(L(i-2,j))*t_fac;
          m(i,j)=H1;
          L(i,j)=((1+F)*(l(i,j)+f)*(l(i,j)+m(i,j)+2*f))/((1+F)*(l(i,j)+f)+(1-F)*(m(i,j)+f));
          M(i,j)=((1-F)*(m(i,j)+f)*(l(i,j)+m(i,j)+2*f))/((1+F)*(l(i,j)+f)+(1-F)*(m(i,j)+f));
        end
       if i~=2 && j~=1
    %case 7
          l(i,j)=L(i-1,j);
          m(i,j)=L(i-1,j-1);
          L(i,j)=((1+F)*(l(i,j)+f)*(l(i,j)+m(i,j)+2*f))/((1+F)*(l(i,j)+f)+(1-F)*(m(i,j)+f));
          M(i,j)=((1-F)*(m(i,j)+f)*(l(i,j)+m(i,j)+2*f))/((1+F)*(l(i,j)+f)+(1-F)*(m(i,j)+f));
       end

    end

    if mod(i,2)~=0
       %for j=1:nj
        if i~=1 && j~=nj
    %case 4
          l(i,j)=L(i-1,j+1);
          m(i,j)=M(i-1,j);
          L(i,j)=((1+F)*(l(i,j)+f)*(l(i,j)+m(i,j)+2*f))/((1+F)*(l(i,j)+f)+(1-F)*(m(i,j)+f));
          M(i,j)=((1-F)*(m(i,j)+f)*(l(i,j)+m(i,j)+2*f))/((1+F)*(l(i,j)+f)+(1-F)*(m(i,j)+f));
         end

        if i~=1 && j==nj
    %case 5
          m(i,j)=M(i-1,j);
          l(i,j)=0;
          L(i,j)=(m(i,j))+f;
          M(i,j)=0;
        end
     end
    end
end
```

The model when α = 60°

The hexagonal packing occurs when the contact angle is 60° (Figure B.1a). And the force transmission at walls is sketched in Figure B.1b.

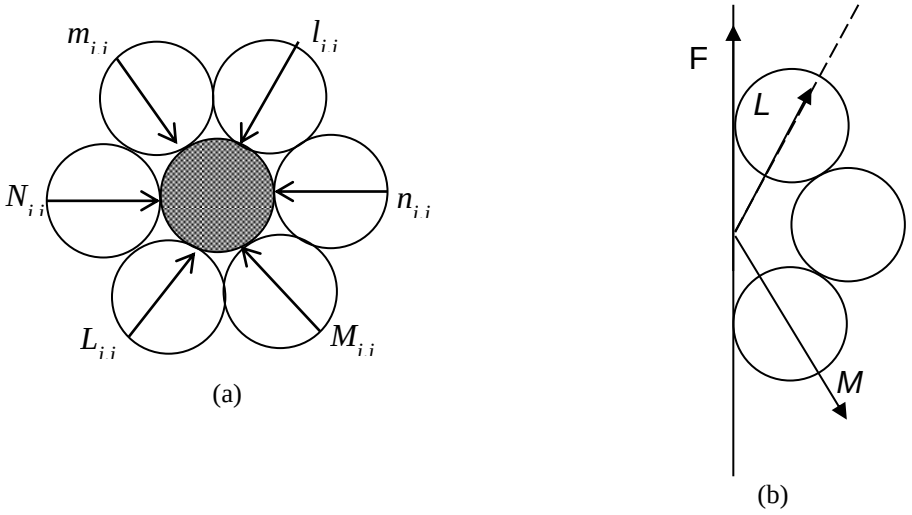

Figure B1. Forces arrangements around a disk, for contact angle of 60; (a) forces from surrounding disks and (b) force transmission at walls

Considering the force equilibrium at wall touching point;

$$M_{(i,j)} = \frac{2f\tan\alpha}{\tan\alpha+\tan\delta} + L_{(i-2,j)}\frac{(\tan\alpha-\tan\delta)}{\tan\alpha+\tan\delta} \tag{B.1}$$

Case 1. For, $i = 1$

$$l_{i,j} = m_{i,j} = n_{i,j} = N_{i,j} = 0 \tag{B.2a}$$

$$L_{i,j} = M_{i,j} = f \tag{B.2b}$$

Case 2. For, $i = 2$ and $j = 1$

$$l_{i,j} = 0 \tag{B.3a}$$

$$m_{i,j} = M_{i-1,j+1} \tag{B.3b}$$

$$n_{i,j} = 0 \tag{B.3c}$$

$$L_{i,j} = \frac{(l_{i,j} + f)(l_{i,j} + m_{i,j} + 2f)}{\{(l_{i,j} + f) + (1 - F)(m_{i,j} + f)\}} \quad \text{(B.3d)}$$

$$M_{i,j} = \frac{(1 - F)(m_{i,j} + f)(l_{i,j} + m_{i,j} + 2f)}{\{(l_{i,j} + f) + (1 - F)(m_{i,j} + f)\}} \quad \text{(B.3e)}$$

$$N_{i,j} = n_{i,j} + \cos\alpha\{(m_{i,j} - l_{i,j}) - (M_{i,j} - L_{i,j})\} \quad \text{(B.3f)}$$

Case 3. For, $i = 2$ and $j \neq 1$ and $j \neq n_j$

$$l_{i,j} = L_{i-1,j} \quad \text{(B.4a)}$$

$$m_{i,j} = M_{i-1,j+1} \quad \text{(B.4b)}$$

$$n_{i,j} = N_{i,j-1} \quad \text{(B.4c)}$$

$$L_{i,j} = \frac{(l_{i,j} + f)(l_{i,j} + m_{i,j} + 2f)}{\{(l_{i,j} + f) + (1 - F)(m_{i,j} + f)\}} \quad \text{(B.4d)}$$

$$M_{i,j} = \frac{(1 - F)(m_{i,j} + f)(l_{i,j} + m_{i,j} + 2f)}{\{(l_{i,j} + f) + (1 - F)(m_{i,j} + f)\}} \quad \text{(B.4e)}$$

$$N_{i,j} = n_{i,j} + \cos\alpha\{(m_{i,j} - l_{i,j}) - (M_{i,j} - L_{i,j})\} \quad \text{(B.4f)}$$

Case 4. For, $i = 2, 4, 6..$ and $j = n_j$

$$l_{i,j} = L_{i-1,j} \quad \text{(B.5a)}$$

$$m_{i,j} = l_{i,j} \quad \text{(B.5b)}$$

$$n_{i,j} = N_{i,j-1} \quad \text{(B.5c)}$$

$$L_{i,j} = \frac{(l_{i,j} + f)(l_{i,j} + m_{i,j} + 2f)}{\{(l_{i,j} + f) + (1 - F)(m_{i,j} + f)\}} \quad \text{(B.5d)}$$

$$M_{i,j} = \frac{(1 - F)(m_{i,j} + f)(l_{i,j} + m_{i,j} + 2f)}{\{(l_{i,j} + f) + (1 - F)(m_{i,j} + f)\}} \quad \text{(B.5e)}$$

$$N_{i,j} = n_{i,j} + \cos\alpha\{(m_{i,j} - l_{i,j}) - (M_{i,j} - L_{i,j})\} \quad \text{(B.5f)}$$

Case 5. For, $i = 3$ and $j = 1$

$$l_{i,j} = 0 \quad \text{(B.6a)}$$

$$m_{i,j} = M_{i-1,j} \quad \text{(B.6b)}$$

$$n_{i,j} = 0 \tag{B.6c}$$

$$L_{i,j} = \frac{\left(l_{i,j} + f\right)\left(l_{i,j} + m_{i,j} + 2f\right)}{\left\{\left(l_{i,j} + f\right) + (1 - F)\left(m_{i,j} + f\right)\right\}} \tag{B.6d}$$

$$M_{i,j} = \frac{(1 - A)\left(m_{i,j} + f\right)\left(l_{i,j} + m_{i,j} + 2f\right)}{\left\{\left(l_{i,j} + f\right) + (1 - F)\left(m_{i,j} + f\right)\right\}} \tag{B.6e}$$

$$N_{i,j} = n_{i,j} + \cos\alpha\left\{\left(m_{i,j} - l_{i,j}\right) - \left(M_{i,j} - L_{i,j}\right)\right\} \tag{B.6f}$$

Case 6. For, $\boldsymbol{i = 4, 6, 8..}$ $\boldsymbol{and\ j \neq 1}$

$$l_{i,j} = L_{i-1,j-1} \tag{B.7a}$$

$$m_{i,j} = M_{i-1,j} \tag{B.7b}$$

$$n_{i,j} = N_{i,j-1} \tag{B.7c}$$

$$L_{i,j} = \frac{\left(l_{i,j} + f\right)\left(l_{i,j} + m_{i,j} + 2f\right)}{\left\{\left(l_{i,j} + f\right) + (1 - F)\left(m_{i,j} + f\right)\right\}} \tag{B.7d}$$

$$M_{i,j} = \frac{(1 - F)\left(m_{i,j} + f\right)\left(l_{i,j} + m_{i,j} + 2f\right)}{\left\{\left(l_{i,j} + f\right) + (1 - F)\left(m_{i,j} + f\right)\right\}} \tag{B.7e}$$

$$N_{i,j} = n_{i,j} + \cos\alpha\left\{\left(m_{i,j} - l_{i,j}\right) - \left(M_{i,j} - L_{i,j}\right)\right\} \tag{B.7f}$$

Case 7. For, $\boldsymbol{i = 4, 6, 8..}$ $\boldsymbol{and\ j \neq n_j}$

$$l_{i,j} = L_{i-1,j+1} \tag{B.8a}$$

$$m_{i,j} = M_{i-1,j} \tag{B.8b}$$

$$n_{i,j} = 0 \tag{B.8c}$$

$$L_{i,j} = \frac{\left(l_{i,j} + f\right)\left(l_{i,j} + m_{i,j} + 2f\right)}{\left\{\left(l_{i,j} + f\right) + (1 - F)\left(m_{i,j} + f\right)\right\}} \tag{B.8d}$$

$$M_{i,j} = \frac{(1 - F)\left(m_{i,j} + f\right)\left(l_{i,j} + m_{i,j} + 2f\right)}{\left\{\left(l_{i,j} + f\right) + (1 - F)\left(m_{i,j} + f\right)\right\}} \tag{B.8e}$$

$$N_{i,j} = n_{i,j} + \cos\alpha\left\{\left(m_{i,j} - l_{i,j}\right) - \left(M_{i,j} - L_{i,j}\right)\right\} \tag{B.8f}$$

Case 8. For, $\boldsymbol{i = 5, 7, 9..}$ $\boldsymbol{and\ j = 1}$

$$l_{i,j} = \frac{2f \tan\alpha}{\tan\alpha + \tan\delta} + M_{(i-2,j)} \frac{(\tan\alpha - \tan\delta)}{\tan\alpha + \tan\delta} \tag{B.8a}$$

$$m_{i,j} = M_{i-1,j} \tag{B.8b}$$

$$n_{i,j} = 0 \tag{B.8c}$$

$$L_{i,j} = \frac{\left(l_{i,j} + f\right)\left(l_{i,j} + m_{i,j} + 2f\right)}{\left\{\left(l_{i,j} + f\right) + (1 - F)\left(m_{i,j} + f\right)\right\}} \tag{B.8d}$$

$$M_{i,j} = \frac{(1 - F)\left(m_{i,j} + f\right)\left(l_{i,j} + m_{i,j} + 2f\right)}{\left\{\left(l_{i,j} + f\right) + (1 - F)\left(m_{i,j} + f\right)\right\}} \tag{B.8e}$$

$$N_{i,j} = n_{i,j} + \cos\alpha\left\{\left(m_{i,j} - l_{i,j}\right) - \left(M_{i,j} - L_{i,j}\right)\right\} \tag{B.8f}$$